

A Dissertation

entitled

Solution-Processed Fabrication of Hybrid Organic-Inorganic Perovskites & Back  
Interface Engineering of Cadmium Telluride Solar Cells

by

Suneth C. Waththage

Submitted to the Graduate Faculty as partial fulfillment of the requirements for the  
Doctor of Philosophy Degree in Physics

---

Dr. Michael J. Heben, Committee Chair

---

Dr. Randy J. Ellingson, Committee Member

---

Dr. Yanfa Yan, Committee Member

---

Dr. Song Cheng, Committee Member

---

Dr. Terry P. Bigioni, Committee Member

---

Dr. Amanda Bryant-Friedrich, Dean  
College of Graduate Studies

The University of Toledo

December 2017

Copyright 2017, Suneth Chandana Waththage

This document is copyrighted material. Under copyright law, no parts of this document may be reproduced without the expressed permission of the author.

An Abstract of  
Solution-Processed Fabrication of Hybrid Organic-Inorganic Perovskites & Back  
Interface Engineering of Cadmium Telluride Solar Cells

by

Suneth C. Waththage

Submitted to the Graduate Faculty as partial fulfillment of the requirements for the  
Doctor of Philosophy Degree in Physics

The University of Toledo  
December 2017

Thin film solar cells based on hybrid organic-inorganic perovskites (HOIPs) have become highly attractive over the past several years due to a high solar to electric power conversion efficiencies (PCEs). Perovskite materials based on methylammonium lead iodide ( $\text{CH}_3\text{NH}_3\text{PbI}_3$ ,  $\text{MAPbI}_3$ ) possess high optical absorption coefficients, long minority carrier lifetimes and diffusion lengths, and desirable optical band gaps, and carrier collection in these materials can be highly efficient when they are paired with appropriate electron and hole transport materials (ETMs and HTMs), respectively. Additionally, perovskite solar cells (PSCs) can be fabricated via a variety of solution-based routes, which are suitable for low-cost, large area manufacturing. The combination of these attributes gives PSCs an advantage over currently available commercial photovoltaic (PV) technologies.

Understanding the nucleation and growth mechanisms, and controlling the grain size and crystallinity in the solution-processed fabrication of perovskite thin films are important to prepare electronic-quality materials for PV applications. We investigated the nucleation and growth mechanisms of  $\text{MAPbI}_3$  formed in a two-step solution process. To

prepare the MAPbI<sub>3</sub> films, PbI<sub>2</sub> films were spin-coated and then were reacted with methylammonium iodide (MAI) in the isopropanol (IPA) solution at various concentrations. We showed that the conversion rate, grain size, and morphology of MAPbI<sub>3</sub> perovskite films depend on the concentration of the MAI solution. Three distinct perovskite formation behaviors were observed at various MAI concentrations, and a tentative model was proposed to explain the reaction mechanisms.

The nucleation and growth process of MAPbI<sub>3</sub> can be significantly changed by adding divalent metal salts into the MAI solution. We showed that the incorporation of Cd<sup>2+</sup> ions significantly improved the grain size, crystallinity, and photoexcited carrier lifetime of MAPbI<sub>3</sub>. Formation of (CH<sub>3</sub>NH<sub>3</sub>)<sub>2</sub>CdI<sub>4</sub> (MA<sub>2</sub>CdI<sub>4</sub>) perovskite in the solution by reacting the MAI and Cd<sup>2+</sup> is the key for this nucleation and growth change. Devices prepared using this approach showed a significant improvement in the PCE relative to control devices prepared without Cd<sup>2+</sup> addition. The improved optoelectronic properties are attributed to a Cd-modified film growth mechanism that invokes low dimensional Cd-based perovskites. In addition to the Cd<sup>2+</sup>, Zn<sup>2+</sup> and Fe<sup>2+</sup> also have the potential to change the nucleation and growth process of MAPbI<sub>3</sub> formation, to improve the material quality.

Formation of Cd-based perovskites, once the Cd<sup>2+</sup> ions contacted with MAI, successfully applied in the cadmium telluride (CdTe) solar cell technology to form a Te layer on the CdTe surface, that would reduce the Schottky barrier height and band bending at the back contact, reducing the recombination at the back junction, and thus improve the device efficiency. We found that Cd can be selectively extracted from the CdTe surface by reacting MAI thin films with the CdTe surface, forming MA<sub>2</sub>CdI<sub>4</sub> perovskite. MA<sub>2</sub>CdI<sub>4</sub> is soluble in IPA, therefore can be rinsed out, leaving a Te layer behind on the CdTe surface.

MAI treated CdTe devices showed a reduction in the barrier height at the back contact for both Au and transparent indium tin oxide (ITO) electrodes as calculated from the temperature dependent J-V measurements, resulting higher photovoltaic parameters of open circuit voltage ( $V_{OC}$ ), fill factor (FF), and PCE relative to the control devices. In addition, only a ~6% reduction in transmittance in the near infrared (NIR) region occurred in the devices with an ITO back electrode due to the MAI treatment, indicating this can be potentially used for the fabrication of high performance transparent CdTe solar cells that use in tandem solar cell or window applications.

! තිබූ තැනක සොර සතුරන් ගත නොහොනා !  
! එසැඬි මනා වත් වතුරෙන් වල නොහොනා !  
! කෝප වුවත් රජ මැතිදුන් ගත නොහොනා !  
! උගත මනා ශිල්පයමයි මතු රැකෙනා !

Education is the only asset that will remain with you forever.

I dedicate my dissertation to my wife Sandun Kalpana, my parents, and my sister.

## Acknowledgements

First, I would like to express my sincere gratitude and appreciation to my advisor, Dr. Michael Heben, for his continuous encouragement and guidance, prudent advices and sustenance throughout my graduate research work. He has been greatly supportive and patient during obstacles and challenges in my research life as well as in personal life. I could not have hoped for a better advisor, and I sincerely recognize him for that.

I sincerely grateful to my thesis committee, Dr. Randy Ellingson, Dr. Yanfa Yan, Dr. Song Cheng, and Dr. Terry Bigioni for their valuable advice and feedback throughout this journey. My sincere thanks go to Dr. Adam Phillips and Dr. Zhaoning Song for their support and guidance since my first day in Heben group, and my graduate research journey might have been much challenging without their constant backing. I also would like to thank current members and alumni of Heben group for their support.

In addition, I would like to thank my collaborators, Niraj Shrestha and Khagendra Bhandari for their contributions to my research work. I would also like to thank Dr. Upali Jayamaha, Dr. Viranga Tillekeratne, Dr. Hasitha Mahabaduge, Dr. Udaka de Silva, and Amila Devasurendra for their inspiring discussions and contributions. Additionally, I would like to thank Dr. Richard Irving, Carl Salupo, and all the other faculty members and staff in the Department of Physics and Astronomy and the Wright Center for Photovoltaics Innovation and Commercialization (PVIC).

# Table of Contents

Abstract.....	iii
Acknowledgements.....	vi
Table of Contents.....	vii
List of Tables .....	xii
List of Figures.....	xiii
List of Abbreviations .....	xx
List of Symbols.....	xxii
1 Evolution of Perovskite Solar Cells.....	1
1.1 Introduction.....	1
1.2 Evolution of the Device Architecture .....	4
1.2.1 Liquid Electrolyte DSSC Structure.....	6
1.2.2 Solid-State Mesoscopic Structure .....	9
1.2.3 Meso-Superstructured Structure .....	11
1.2.4 The Regular Structure .....	13
1.2.5 Planar n-i-p Heterojunction Structure.....	15
1.2.6 Inverted Planar p-i-n Heterojunction Structure.....	17
1.3 Evolution of the Film Deposition Methods .....	20
1.3.1 Single-Step Solution Process .....	22
1.3.2 Two-Step Solution Deposition.....	24

1.3.3 Vapor Assisted Solution Process .....	26
1.3.4 Thermal Vapor Deposition .....	27
1.4 Advanced Device Engineering Techniques .....	28
1.4.1 Solvent Engineering.....	29
1.4.2 Deposition Process Engineering .....	31
1.4.3 Contact Materials Engineering .....	34
1.4.4 Band Gap Engineering of Perovskites .....	36
1.4.5 Perovskite Tandem Solar Cells .....	41
1.5 Outlook and Summary .....	43
1.6 Dissertation Overview .....	45
2 Understanding the Nucleation and Growth Behaviors of Methylammonium Lead Iodide Perovskites in the Two-Step Solution Process .....	47
2.1 Introduction and Motivation .....	48
2.2 Experimental Details.....	50
2.2.1 Perovskite Films and Device Fabrication .....	50
2.2.2 Thin Film Characterization .....	52
2.2.3 Device Characterization.....	53
2.3 Exploring the Degree of Conversion .....	53
2.4 Grain Size Variation .....	56
2.5 Change of Gibbs Free Energy.....	58
2.5.1 $\text{CH}_3\text{NH}_3^+$ cation concentration in solid $\text{CH}_3\text{NH}_3\text{PbI}_3$ perovskite and MAI solution.....	59
2.6 Nucleation and Growth Mechanism .....	60

	2.7 Impact on Device Performances .....	66
	2.8 Conclusion .....	69
3	Enhanced Grain Size, Photoluminescence, and Photoconversion Efficiency with Cadmium Addition During the Two-Step Growth of Methylammonium Lead Iodide .....	71
	3.1 Introduction and Motivation .....	72
	3.2 Experimental Details.....	75
	3.2.1 Perovskite Films Preparation .....	75
	3.2.2 Thin Film Characterization .....	76
	3.2.3 Device Preparation.....	77
	3.2.4 Device Characterization.....	77
	3.3 Grain Size Enhancement with the Addition of CdCl <sub>2</sub> .....	78
	3.4 Improved Degree of Crystallinity and Preferred Orientation .....	80
	3.5 Verifying the Cd <sup>2+</sup> Involvement in the Improvement in Grain Size and Crystallinity.....	83
	3.6 Effect of Cd Incorporation on the Optoelectronic Properties of the Perovskite Films .....	83
	3.7 Perovskite Formation Mechanism with Cd <sup>2+</sup> .....	86
	3.8 Impact of the Increased Grain Size and Carrier Lifetime on the Photovoltaic Device Performance.....	93
	3.9 Conclusion .....	98
4	Impact of Divalent Metal Additives on the Structural and Optoelectronic Properties of Methylammonium Lead Iodide Perovskite Prepared by the Two-	

	Step Solution Process.....	99
	4.1 Introduction and Motivation .....	100
	4.2 Experimental Details.....	101
	4.3 Grain Size Enhancement.....	102
	4.4 Impact on Crystallinity .....	104
	4.5 Impact on Optoelectronic Properties .....	107
	4.6 Conclusion .....	111
5	Selective Cd Removal from CdTe Surface for High Efficiency Te Back Contact Formation in CdTe Solar Cells .....	112
	5.1 Introduction and Motivation .....	113
	5.2 Experimental Details.....	117
	5.2.1 MAI Surface Treatment .....	117
	5.2.2 Film Characterization.....	118
	5.2.3 Solar Cell Preparation .....	119
	5.2.4 Solar Cell Characterization .....	119
	5.2.5 Low Temperature J-V Measurements.....	119
	5.3 Results and Discussion .....	120
	5.3.1 XRD spectroscopy analysis .....	120
	5.3.2 Variation of the Surface Morphology .....	121
	5.3.3 Raman Spectroscopy Analysis.....	123
	5.3.4 Formation of a Te Layer .....	124
	5.3.5 Device Performances .....	128
	5.3.6 Devices with Transparent Back Contact.....	135

	5.3.7 Back Contacts Barrier Height .....	137
	5.4 Conclusion .....	141
6	Summary and Future Research .....	143
	6.1 Thesis Summary.....	143
	6.2 Future Research .....	145
	6.2.1 Optimizing the metal addition in MAPbI <sub>3</sub> perovskite.....	145
	6.2.2 Fabrication of high efficiency transparent CdTe devices .....	146
	References.....	148
A	Supporting Information.....	174
B	List of Publications .....	175

## List of Tables

2.1	CH <sub>3</sub> NH <sub>3</sub> <sup>+</sup> cation concentrations (C) in MAI solution for different MAI concentrations .....	60
3.1	Calculated orientation index values for the XRD peaks of MAPbI <sub>3</sub> and Cd <sub>2</sub> MAPbI <sub>3</sub> perovskite films .....	82
3.2	Bi-exponential fitting time constants and mean lifetime of the carriers .....	86
3.3	Solar cell performance metric for devices made with Cd <sub>2</sub> MAPbI <sub>3</sub> and MAPbI <sub>3</sub> films .....	95
4.1	Bi-exponential fitting time constants and mean lifetime of the carriers for the Mg-, Ca-, Fe-, Co-, Cu-, Zn-, Cd- and Hg-modified, and control films .....	109
5.1	Device parameters for different reaction temperatures .....	130
5.2	Device performances for different amount of Cu .....	133
5.3	The J-V Parameters for ITO back electrode .....	136
5.4	Back contact barrier height for devices made with and without MAI treatment.	138

## List of Figures

1-1	Diagram of cubic perovskite crystal structure .....	2
1-2	Record efficiency and numbers of publications with the topic on perovskite solar cells from 2009 to 2016 .....	4
1-3	Schematics of perovskite solar cell architectures .....	5
1-4	(a) Schematic diagram and (b) working mechanism of the conventional DSSC ....	6
1-5	(a) Schematic diagram of perovskite sensitizers. (b) IPCE of DSSCs using MAPbI <sub>3</sub> and MAPbBr <sub>3</sub> . (c) Energy level diagram of a liquid-electrolyte DSSC with perovskite sensitizers .....	7
1-6	(a) Schematic of a DSSC with the perovskite QDs. (b) J-V and EQE curves of the device .....	8
1-7	(a) Cross-sectional SEM image, (b) J-V characteristic, (c) energy level diagram, and (d) stability of a perovskite solar cell in solid-state mesoscopic structure.....	10
1-8	Schematic diagram of (a) mesoporous and (b) meso-superstructured PSCs. (c) Measured binding energy of perovskite, Al <sub>2</sub> O <sub>3</sub> /perovskite, and mp-TiO <sub>2</sub> /perovskite.....	12
1-9	(a) Schematic illustration, (b) IPCE curves, and (c) J-V characteristics of the PSCs with different mp-TiO <sub>2</sub> thickness.....	14
1-10	(a-c) Cross-sectional SEM image and (d-f) corresponding J-V curves of PSCs with different perovskite capping layers.....	15

1-11	(a) Cross-sectional and (b) surface SEM images of a PSC in the planar n-i-p configuration prepared by solution-based deposition. (c) Cross-sectional SEM image of a PCS prepared by the vapor-based deposition. (d) J-V characteristics of the planar n-i-p type PSCs .....	17
1-12	(a) Structure and (b) energy level diagram of a PSC in the planar p-i-n heterojunction structure .....	18
1-13	(a) Structure of a PSC in the planar p-i-n structure. (b) Cross-sectional and (c) surface SEM images of the perovskite film deposited on a ITO substrate. (d) J-V characteristic, (e) EQE, and (f) stability measurement of a PSC in the planar p-i-n structure.....	20
1-14	Preparation methods for perovskite absorber (a) single-step solution process, (b) two-step solution process, (c) vapor assisted solution process, and (d) thermal vapor process .....	21
1-15	Proposed phase diagram for MAPbI <sub>3</sub> .....	24
1-16	MAPbI <sub>3</sub> perovskite films prepared by the single-step solution deposition using (a), (b) GBL and (c), (d) DMF solvents.....	25
1-17	(a) Schematic illustration, (b) cross-sectional, and (c) surface SEM images of perovskite film prepared by vapor assisted solution process.....	27
1-18	Schematic images of (a) dual source evaporation, (b) chemical vapor deposition, and (c) flash evaporation.....	28
1-19	(a) Mechanism illustration of solvent engineering using DMSO. (b) J-V characteristics and (c) IPCE curve of PSCs prepared with DMSO additive .....	30

1-20	Schematics of (a) anti-solvent drop casting, (b) solvent annealing process, (c) hot-casting deposition method, and (d) vacuum-flash assisted solution process .....	32
1-21	Energy levels of commonly used cathode, n-type (ETM), absorber, p-type (HTM), and anode materials in perovskite solar cells.....	34
1-22	The versatility of hybrid perovskite materials $Cs_pFA_qMA_{1-p-q}PbBr_yI_{3-y}$ and their absorption tunability .....	37
1-23	(a) UV-vis absorbance and band gap values of $MASnI_3$ , $FASnI_3$ , $MAPbI_3$ , $FAPbI_3$ , $CsSnI_3$ , and $CsPbI_3$ . (b) Crystal structure and photos of $CsPbI_3$ , $Cs_xFA_{1-x}PbI_3$ , and $FAPbI_3$ .....	38
1-24	(a) Photographs and UV-vis absorption spectra of $MAPb(I_{1-x}Br_x)_3$ . (b) UV-vis spectra of $MAPb(I_{1-x}Cl_x)_3$ .....	39
1-25	Three main configurations of tandem solar cells: (a) 2-terminal monolithic, (b) 4-terminal stacked, and (c) 4-terminal optical coupling structures .....	42
2-1	Preparation of (a) the compact $TiO_2$ (b) meso-porous $TiO_2$ (c) $PbI_2$ , and (d & e) $MAPbI_3$ perovskite layers .....	51
2-2	(a) X-ray diffraction patterns of $PbI_2$ , and $MAPbI_3$ perovskite formed using different MAI concentrations (b) The peak areas of the $PbI_2$ (001) and summation of the (110), (202), and (220) of the $MAPbI_3$ perovskite as a function of the MAI concentration.....	55
2-3	SEM images of (a) $PbI_2$ seed layer and $MAPbI_3$ films prepared by using the MAI solutions of (b) 5 mg/ml, (c) 8 mg/ml, (d) 9 mg/ml, (e) 10 mg/ml, (f) 15 mg/ml, (g) 20 mg/ml, (h) 25 mg/ml, (i) 30 mg/ml, (j) 35 mg/ml, (k) 40 mg/ml, and (l) 100 mg/ml, respectively. (m) As deposited $MAPbI_3$ film from a 40 mg/ml solution...	57

2-4	Average grain size variation with the MAI concentration.....	58
2-5	Nucleation and growth process for MAPbI <sub>3</sub> perovskite with low (a) and High (b) concentration of MAI solution.....	61
2-6	Schematics of the MAPbI <sub>3</sub> perovskite growth under different conditions .....	62
2-7	XRD spectrum for an as-deposited MAPbI <sub>3</sub> perovskite from a 50mg/ml MAI solution.....	63
2-8	MAPbI <sub>3</sub> perovskite structure and its LDPs.....	64
2-9	X-ray diffraction patterns for the perovskite film prepared by sequentially spins of the 35 and 15 mg/ml MAI solutions and those prepared by a single spin of 35 mg/ml and 15 mg/ml solutions .....	65
2-10	Effect of the MAI concentration and the post annealing condition on critical parameters of (a) PCE, (b) J <sub>SC</sub> , (c) FF and (d) V <sub>OC</sub> .....	67
2-11	J-V characteristics for the best devices with spiro-MeOTAD.....	69
3-1	Surface SEM images of MAPbI <sub>3</sub> films prepared on a TiO <sub>2</sub> layer and a CdS layer using the two-step sequential deposition method .....	74
3-2	SEM images of the surface of as-spun MAPbI <sub>3</sub> thin films prepared (a) without and (b) with 10 mM CdCl <sub>2</sub> addition to the MAI solution. (c and d) Cross-sectional view of the as-spun MAPbI <sub>3</sub> perovskite films that display in the panels of (a) and (b), respectively. Panels (e) and (f) show the data corresponding to (a) and (b), respectively, after heating to 150 °C. (g and h) Cross-sectional view of the MAPbI <sub>3</sub> perovskite films that display in the panels of (e) and (f), respectively.....	79
3-3	UV-vis absorbance spectra of standard (MAPbI <sub>3</sub> ) and Cd-modified perovskite (Cd_ MAPbI <sub>3</sub> ) thin films .....	80

3-4	X-ray diffraction spectra of PbI <sub>2</sub> seed layer and MAPbI <sub>3</sub> perovskite films prepared with the standard and Cd-modified two-step deposition methods after the post-deposition heating .....	81
3-5	The SEM images of MAPbI <sub>3</sub> thin films prepared with (a) cadmium acetate and (b) methylammonium chloride additives, respectively .....	83
3-6	Steady state PL spectra and (b) intensity-normalized time resolved PL decay measured from MAPbI <sub>3</sub> and Cd_MAPbI <sub>3</sub> samples .....	84
3-7	Simulated crystal structure of PbI <sub>2</sub> projected in [001] direction and MAPbI <sub>3</sub> perovskite projected in [202] direction. (c) Low and (d) high magnification SEM images of surface of the PbI <sub>2</sub> seed layer .....	88
3-8	UV-vis absorbance spectra of 250 mM MAI in IPA, with and without 10 mM CdCl <sub>2</sub> .....	89
3-9	XRD spectra of MAI, MA <sub>2</sub> CdI <sub>4</sub> , and Cd-modified MAPbI <sub>3</sub> films with and without post-deposition heating .....	90
3-10	Thermogravimetric (TGA) analysis of MA <sub>2</sub> CdI <sub>4</sub> in N <sub>2</sub> .....	91
3-11	Histogram of efficiencies for devices prepared from MAPbI <sub>3</sub> and Cd_MAPbI <sub>3</sub> thin films .....	94
3-12	J-V measurements (b) EQE, IQE spectra, and integrated current densities of CH <sub>3</sub> NH <sub>3</sub> PbI <sub>3</sub> perovskite solar cells with and without CdCl <sub>2</sub> additives.....	96
3-13	Comparison of J-V characteristics (forward and reverse scans) from the champion cells .....	97
4-1	Surface (a, b, c, g, h, i, m, n, & o) and cross sectional (d, e, f, j, k, l, p, q, & r) SEM images from the MAPbI <sub>3</sub> films without (a & d) and with Mg <sup>2+</sup> (b & e), Ca <sup>2+</sup>	

	(c & f), Fe <sup>2+</sup> (g & j), Co <sup>2+</sup> (h & k), Cu <sup>2+</sup> (i & l), Zn <sup>2+</sup> (m & p), Cd <sup>2+</sup> (n & q), or Hg <sup>2+</sup> (o & r) addition.....	103
4-2	(a) XRD spectra of the MAPbI <sub>3</sub> perovskite control film and the films prepared with Mg <sup>2+</sup> , Ca <sup>2+</sup> , Fe <sup>2+</sup> , Co <sup>2+</sup> , Cu <sup>2+</sup> , Zn <sup>2+</sup> , Cd <sup>2+</sup> , and Hg <sup>2+</sup> additions in the two-step deposition. Zoom-in XRD spectra for the (b) perovskite (110) peak, and (c) LDP peaks .....	106
4-3	UV-vis absorbance spectra of control without any additive and Mg-, Ca-, Fe-, Co-, Cu-, Zn-, Cd-, and Hg-modified films .....	107
4-4	(a) Normalized PL spectra and (b) intensity normalized TRPL decay of control (MAPbI <sub>3</sub> ), Mg-, Ca-, Fe-, Co-, Cu-, Zn-, Cd-, and Hg-modified of perovskite films .....	111
5-1	Energy band diagram of CdTe/metal back junction for an undoped CdTe and a Cu-doped CdTe with and without a Te buffer .....	114
5-2	(a) Schematic of a regular CdS/CdTe solar cell. (b) Cross sectional SEM image of a CdS/CdTe solar cell with a Cu/Au back contact.....	117
5-3	Preparation of the MAI thin film on the CdTe surface.....	118
5-4	X-ray diffraction patterns from MAI treated and untreated CdTe samples.....	120
5-5	Surface morphology of MAI, MABr, and MAcl treated CdTe samples.....	122
5-6	Raman spectra from MAI, MABr, and MAcl treated samples, a cleaned sample, and a standard .....	124
5-7	CdCl <sub>2</sub> participation in an IPA solution and complete dissolution with the addition of MAI due to the formation of MA <sub>2</sub> CdI <sub>4</sub> perovskite.....	125

5-8	(a) Extracting Cd from the CdTe surface by forming MA <sub>2</sub> CdI <sub>4</sub> . (b) Removing MA <sub>2</sub> CdI <sub>4</sub> and excess MAI.....	126
5-9	Cross-sectional SEM images of (a) & (b) MAI treated and (c) & (d) untreated CdTe devices.....	126
5-10	Surface SEM images of MAI treated CdTe samples with (a) 125 mM, (b) 250 mM, (c) 375 mM, and (d) 500 mM MAI solutions .....	127
5-11	Photovoltaic performances of (a) V <sub>OC</sub> , (b) J <sub>SC</sub> , (c) FF, and (d) PCE of MAI treated and untreated CdS/CdTe devices .....	129
5-12	XRD of Cu-doped CdTe from MAI treated and untreated samples, and MAI treated CdTe without Cu doping.....	132
5-13	Energy-band diagrams for a CdS/CdTe device at 0.8-V bias under illumination (a) without and with (b) a Te buffer layer .....	132
5-14	Transmittance, absorbance, and reflectance of the MAI treated and untreated CdS/CdTe devices completed with the ITO back electrode .....	137
5-15	Temperature dependence J-V characteristics and corresponding ln(J/T <sup>2</sup> ) vs. 1/k <sub>B</sub> T plots for CdS/CdTe solar cells with (a) CdTe:Cu/Au, (b) CdTe/Te/Au (c) CdTe:Cu/Te/Au, (d) CdTe:Cu/ITO, and (e) CdTe:Cu/Te/ITO back junctions ...	139
5-16	J-V characteristics of champion devices from the MAI treated and untreated CdS/CdTe samples with Au or ITO back electrodes .....	140
6-1	EQE curve of the champion device, which is in the structure of CdS/CdTe:Cu/Te/Au.....	147
A-1	(a) J-V measurements (b) EQE spectra of CH <sub>3</sub> NH <sub>3</sub> PbI <sub>3</sub> perovskite solar cells prepared with different CdCl <sub>2</sub> concentrations.....	174

## List of Abbreviations

BCP	Bathocuproine
CdTe	Cadmium Telluride
DMF	Dimethyl Formamide
DMSO	Dimethyl Sulfoxide
DSSCs	Dye-Sensitized Solar Cells
EQE	External Quantum Efficiency
ETA	Extremely Thin Absorber
ETM	Electron Transport Material
GBL	$\gamma$ -Butyrolactone
HOIPs	Hybrid Organic-Inorganic Perovskites
HOMO	Highest Occupied Molecular Orbital
HTM	Hole Transport Material
IPA	Isopropanol
IPCE	Incident Photon to Electron Conversion Efficiency
IQE	Internal Quantum Efficiency
ITO	Indium Tin Oxide
LUMO	Lowest Unoccupied Molecular Orbital
MA <sub>2</sub> CdI <sub>4</sub>	Methylammonium Cadmium Iodide
MACl	Methylammonium Chloride
MAI	Methylammonium Iodide
MAPbBr <sub>3</sub>	Methylammonium Lead Bromide
MAPbI <sub>3</sub>	Methylammonium Lead Iodide
NIR	Near Infrared
NMP	N-2-Methyl Pyrrolidone
P3HT	Poly(3-hexylthiophene-2,5-diyl)
PC <sub>61</sub> BM	Phenyl-C <sub>61</sub> -Butyric acid Methyl ester
PCE	Power Conversion Efficiency

PEDOT:PSS.....Poly Polystyrene Sulfonate  
PL.....Photoluminescence  
PSC.....Perovskite Solar Cells  
PTAA.....Poly Triarylamine  
PV.....Photovoltaic

QDs.....Quantum Dots

SEM.....Scanning Electron Microscope  
SPS.....Stacked Perovskite Sheet

TCO.....Transparent Conducting Oxide  
TRPL.....Time Resolved Photoluminescence

## List of Symbols

$\gamma$	.....	Sum of surface tensions
$\eta$	.....	Device efficiency
$\theta$	.....	Angle
$\tau_1$	.....	Surface charge carrier life time
$\tau_2$	.....	Bulk charge carrier life time
$\phi_b$	.....	Back barrier height
$e$	.....	Charge of an electron
FF	.....	Fill Factor
$\Delta G^0$	.....	Standard state free energy change
$\Delta G_{\text{Total}}$	.....	Gibbs free energy change
$\Delta G_v$	.....	Bulk free energy per unit volume
$J_{\text{sc}}$	.....	Short Circuit Current Density
J-V	.....	Current Density–Voltage
K	.....	Boltzmann constant
$N_t$	.....	Charge trap density
R	.....	Universal gas constant
T	.....	Temperature
$V_{\text{oc}}$	.....	Open Circuit Voltage

# Chapter 1

## Evolution of Perovskite Solar Cells

### 1.1 Introduction

Perovskite is a naturally occurring mineral of calcium titanate with a chemical formula of  $\text{CaTiO}_3$ . This mineral was first discovered by German mineralogist Gustav Rose in 1839 and was named in honor of the Russian mineralogist Lev Perovski (1792–1856).[1] Generally, materials which have the same crystal structure of  $\text{CaTiO}_3$  are referred to as perovskite materials. These perovskite materials typically have a cubic or tetragonal crystal structure with the stoichiometry of  $\text{AMX}_3$ , where both A and M are metal cations and X is an anion (Figure 1-1). Each cation M is octahedrally coordinated with the anions X to form the basic building block of the perovskite structure. These  $\text{MX}_6$  octahedra are connected in a three-dimensional corner-sharing configuration, with the cation A embedded in the space formed between adjacent  $\text{MX}_6$  octahedron to neutralize the charge of the structure.[1]

Over the past few decades, the inorganic perovskite oxides (e.g.,  $\text{CaTiO}_3$ ,  $\text{BaTiO}_3$ ,  $\text{LaMnO}_3$  etc. ) and halides ( $\text{CsSnI}_3$ ,  $\text{CsPbI}_3$  etc.) have been extensively studied due to their versatile applications in optics,[2] magnetics,[3] electronics,[4] and superconductors.[5]

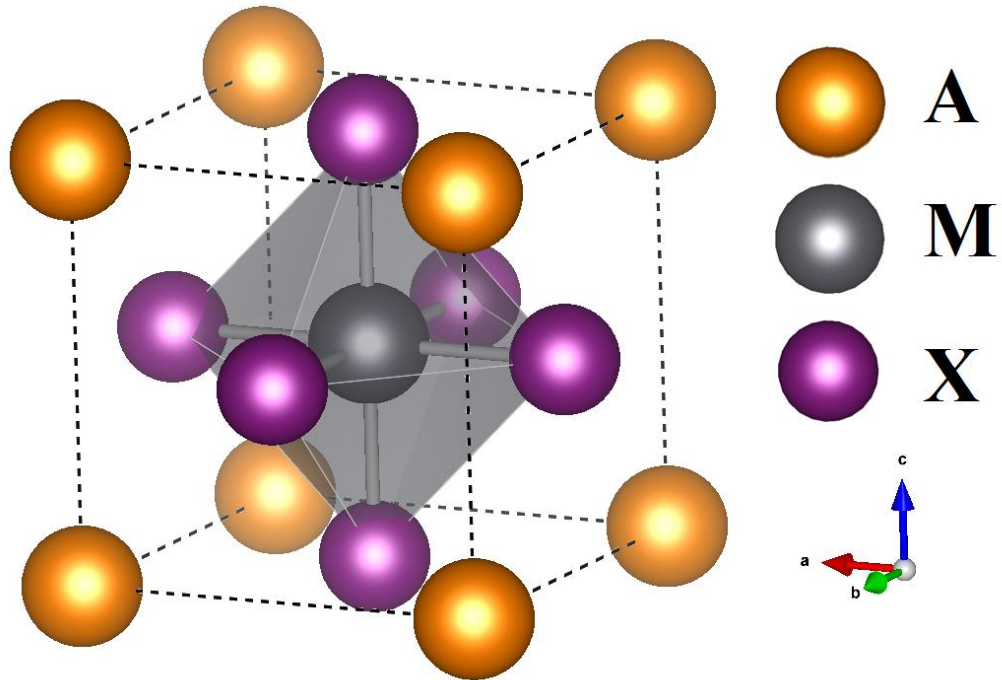


Figure 1-1. Diagram of cubic perovskite crystal structure.

In recent years, another group of perovskite materials called the hybrid organic-inorganic perovskites (HOIPs), which are comprised of an organic ammonium cation A ( $\text{CH}_3\text{NH}_3^+$ ,  $\text{NH}=\text{CHNH}_3^+$  etc.), a divalent metal cation M ( $\text{Pb}^{2+}$ ,  $\text{Sn}^{2+}$ ,  $\text{Cd}^{2+}$ ,  $\text{Fe}^{2+}$ ,  $\text{Co}^{2+}$ ,  $\text{Cu}^{2+}$  etc.), and halide ions X ( $\text{Cl}^-$ ,  $\text{Br}^-$ , or  $\text{I}^-$ ), have attracted substantial research interests. Since the 1970s, significant research has conducted on this family of materials to better understand their structural versatility and diversity in optical, magnetic, and electronic properties.[6-8] In the early 1990s, Sn- and Pb-based HOIPs were of great interest to materials scientists for fabricating field-effect transistors[9] and light-emitting diodes[10] due to their high charge carrier mobilities and strong excitonic transitions. These excellent optoelectronic properties also make the HOIP materials ideal for thin-film photovoltaic (PV) devices, however, their application as solar cells were not considered.

The first HOIP-based PV device was reported by Kojim et al. in 2009,[11] who used methylammonium lead iodide ( $\text{CH}_3\text{NH}_3\text{PbI}_3$ ,  $\text{MAPbI}_3$ ) and methylammonium lead bromide ( $\text{CH}_3\text{NH}_3\text{PbBr}_3$ ,  $\text{MAPbBr}_3$ ) as the sensitizers to fabricate dye-sensitized solar cells (DSSCs) with a liquid electrolyte.[11] Because of a low power conversion efficiencies (PCEs) of ~3% and poor device stability, HOIPs as light absorbing materials received little attention. In 2012, the liquid electrolyte was replaced with a solid-state hole transport material (HTM), and the PCE of  $\text{MAPbI}_3$ -based solar cells increased to ~10%.[12, 13] These revolutionary findings opened a new era of the emerging perovskite solar cells (PSCs) and spread the so-called “perovskite fever” all around the world.[14-16] Thanks to the tremendous efforts in the past few years, PSCs have rapidly progressed and reached 22.1% PCE.[17] Figure 1-2 shows some major milestones in the progress of PSCs, including the device evolution from dye-sensitized to planar structure and the advancements in the solvent and compositional engineering techniques. This successful progress also stimulated a great interest in this emerging PV technology, as the annual number of articles published with the topic of PSCs has increased from a single digit number in 2012 to ~2300 in 2016. This chapter traces this remarkable evolution mainly from the perspectives of device architecture and material deposition method by focusing on the early developments of the materials, notable devices with excellent performance, technical advances in preparation methods, and the future directions of the field.

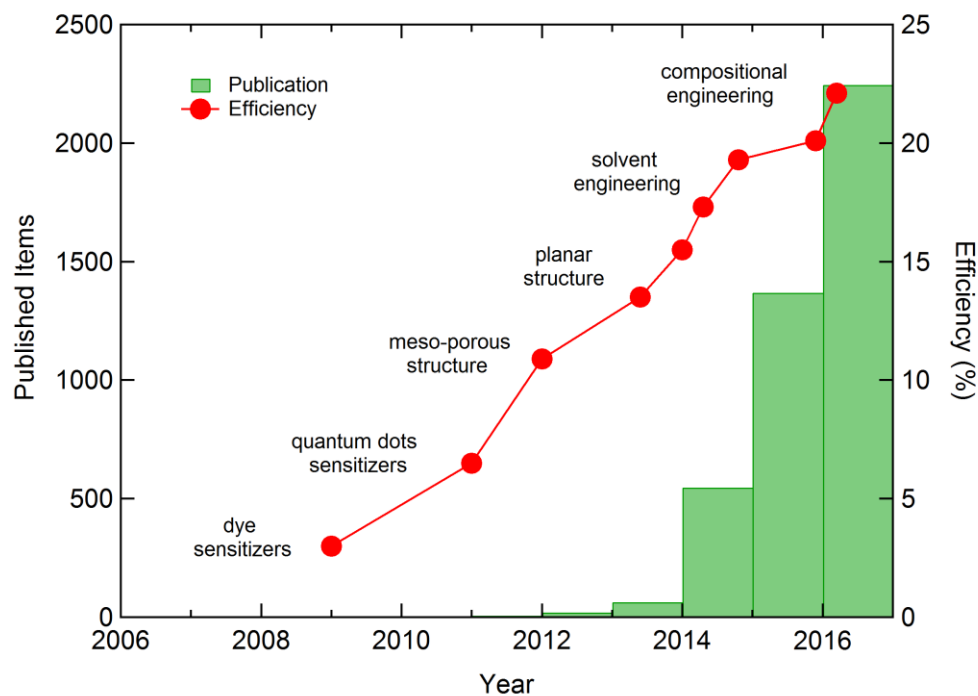


Figure 1-2. Record efficiency and numbers of publications with the topic on perovskite solar cells from 2009 to 2016. The publication data is adapted from ISI web of science.

## 1.2 Evolution of the Device Architecture

Advances in the design of device architecture is one of the most important factors that drove the evolution of PSCs, especially in the early stage of the technical development. In 2009, PSCs were first demonstrated based on the design of the liquid electrolyte DSSC configuration (Figure 1-3a). This device structure, inherited from the conventional DSSCs, has intrinsic material compatibility issues associated with the use of liquid electrolyte that limit the stability of the devices. Advances in solid-state HTM as a replacement for the liquid electrolyte led to the development of the mesoscopic (Figure 1-3b) and meso-superstructured (Figure 1-3c) architectures used in 2012. Based on these two preliminary structures, the so-called the “regular” or “mesoporous” structure (Figure 1-3d) constructed

with the HOIP materials penetrating into a thin mesoporous metal oxide layer and forming a capping layer on the top was developed during 2013 – 2014. Since then, the regular structure has been widely used to fabricate high efficiency PSCs. This success has attracted the experts of inorganic thin-films and organic PV materials to the field of PSC research, resulting in the development of the planar heterojunction structures in the n-i-p (Figure 1-3e) and p-i-n (Figure 1-3f) configurations. The planar p-i-n structure, with the film stack deposited in the opposite sequence of the regular structure, is often referred as the inverted structure.

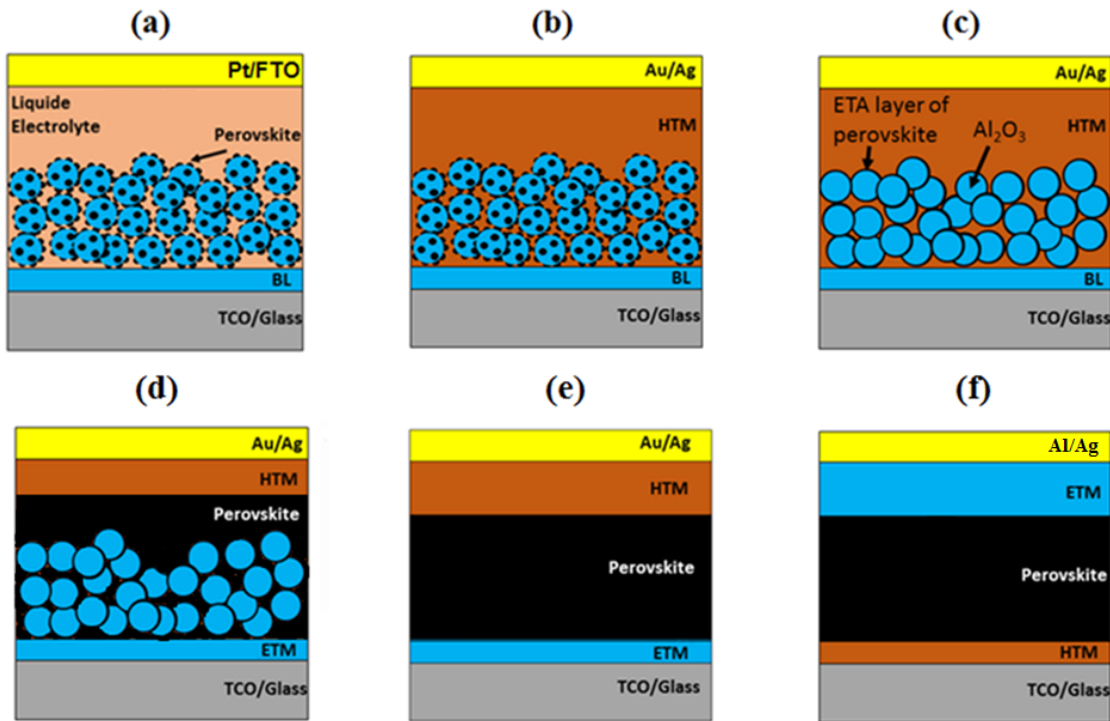


Figure 1-3. Schematics of perovskite solar cell architectures: (a) liquid electrolyte DSSC structure, (b) solid-state mesoscopic structure, (c) meso-superstructured structure, (d) the regular structure, (e) planar n-i-p heterojunction structure, and (f) planar p-i-n heterojunction structure (inverted planar structure).

### 1.2.1 Liquid Electrolyte Dye-Sensitized Solar Cells (DSSC) Structure

PSCs were initially fabricated in the conventional DSSC structure (Figure 1-4a) which is comprised of a glass substrate/transparent conducting oxide (TCO), a thin compact  $\text{TiO}_2$  (c- $\text{TiO}_2$ ) hole blocking layer (BL), a several micron thick mesoporous  $\text{TiO}_2$  (mp- $\text{TiO}_2$ ) layer sensitized with molecular dyes, a liquid electrolyte, and a counter electrode (Pt/TCO/glass).[18] Figure 1-4b shows the working principle of DSSC, which is based on photoexcitation of the sensitizer dye.

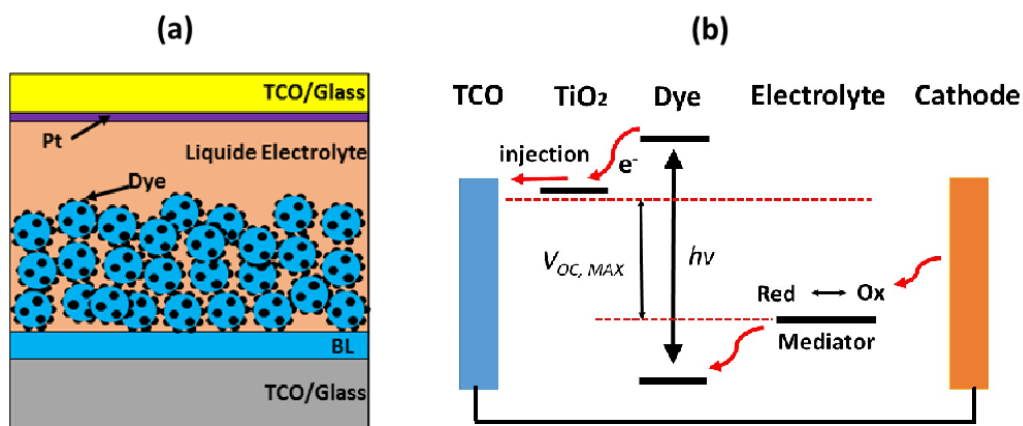


Figure 1-4. (a) Schematic diagram and (b) working mechanism of the conventional DSSC.

When the incident photons are absorbed by the photosensitizers coating the surface of  $\text{TiO}_2$ , electrons are excited from the ground state to the excited state. The photoexcitation results in the injection of electrons into the conduction band of mp- $\text{TiO}_2$ , and then to the front electrode (anode). This process leaves the photosensitizers in an oxidized state, which is subsequently reduced back to the ground state by an injected electron from the reductants (e.g.,  $\text{I}^-$ ) in the liquid electrolyte. After the electron donation, the deactivated reductants, i.e. the oxidants (e.g.,  $\text{I}_3^-$ ), diffuse to the metal counter electrode and are regenerated by

electrons from the cathode. This complete electron flow creates a photogenerated current in a DSSC. The energy difference between the Fermi level of  $\text{TiO}_2$  and the redox potential of the mediator in the electrolyte determines the maximum value of open circuit voltage ( $V_{\text{OC}}$ ).[18, 19]

In 2009, Kojima et al. replaced the organic dye in the DSSC structure with  $\text{MAPbI}_3$  or  $\text{MAPbBr}_3$  perovskite (Figure 1-5a) by spin-coating a precursor solution containing equimolar  $\text{MAX}$  and  $\text{PbX}_2$  ( $X = \text{I}$  or  $\text{Br}$ ) onto the mp- $\text{TiO}_2/\text{c-TiO}_2/\text{FTO}$  substrate.[11] The best  $\text{MAPbI}_3$  device demonstrated a PCE of 3.8%, with a  $V_{\text{OC}}$  of 0.61 V, a short circuit current density ( $J_{\text{SC}}$ ) of  $11.0 \text{ mA/cm}^2$ , and a fill factor (FF) of 57%. In comparison, the champion  $\text{MAPbBr}_3$  device had a PCE of 3.2%, with  $V_{\text{OC}} = 0.96 \text{ V}$ ,  $J_{\text{SC}} = 5.57 \text{ mA/cm}^2$ , and  $\text{FF} = 59\%$ .

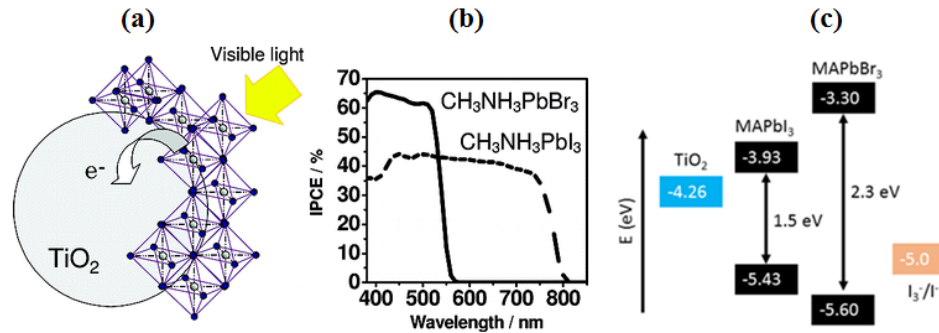


Figure 1-5. (a) Schematic diagram of perovskite sensitizers. (b) Incident photon to electron conversion efficiency (IPCE) of DSSCs using  $\text{MAPbI}_3$  and  $\text{MAPbBr}_3$ . (c) Energy level diagram of a liquid-electrolyte DSSC with perovskite sensitizers. Panels (a) and (b) are reprinted with permission from Ref.[11]. Copyright 2009 American Chemical Society

The higher  $J_{\text{SC}}$  of the  $\text{MAPbI}_3$  device is a result of photo conversion of longer wavelengths light (550 – 800 nm) (Figure 1-5b) due to a lower bandgap (1.5 eV) relative

to MAPbBr<sub>3</sub> (2.3 eV), but the  $V_{OC}$  of the MAPbI<sub>3</sub> devices is lower due to a smaller energy level difference between the conduction band of the perovskite absorber and the redox potential of the X<sup>3-</sup>/X<sup>-</sup> (X = I or Br) mediator (Figure 1-5c). Although this work demonstrated the potential of using the HOIP materials in PV applications, it did not receive much attention due to the relatively low efficiency and instability of the devices.

Two years later, Im et al. fabricated perovskite-sensitized DSSCs using 2-3 nm MAPbI<sub>3</sub> quantum dots (QDs) to coat the 3.6 μm thick mp-TiO<sub>2</sub> layer (Figure 1-6a).[19] Their champion device shows an improved PCE of 6.54%, with  $V_{OC}$  = 0.706 V,  $J_{SC}$  = 15.82 mA/cm<sup>2</sup>, and FF = 58.6% (Figure 1-6b).

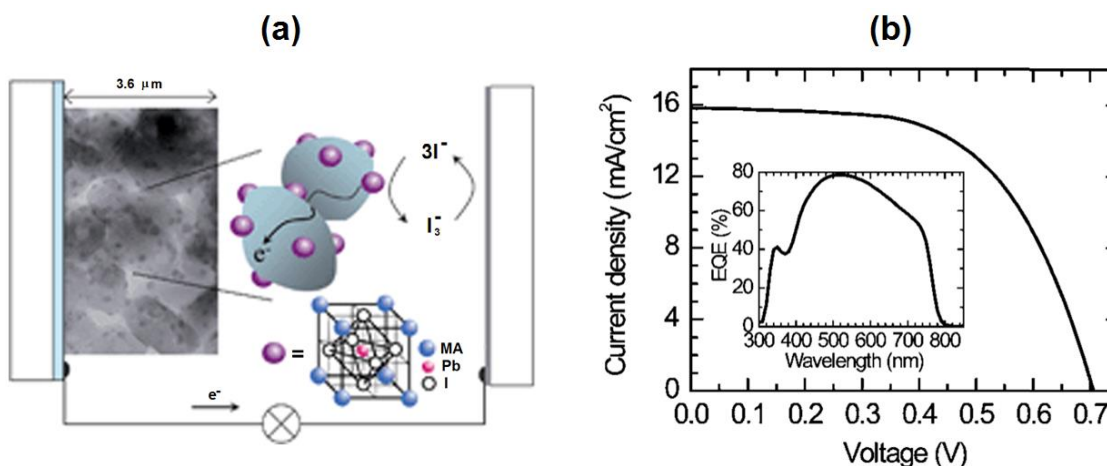


Figure 1-6. (a) Schematic of a DSSC with the perovskite QDs. (b) Current density–voltage (J-V) and EQE curves of the device. Reprinted with permission from Ref.[19]. Copyright 2011, Royal Society of Chemistry

The  $J_{SC}$  enhancement is due to the improved light conversion in the MAPbI<sub>3</sub> QDs, which shows the maximum external quantum efficiency (EQE) of ~80% at 530 nm. The increased  $V_{OC}$  is likely due to the thicker mp-TiO<sub>2</sub> which prevents recombination at the

perovskite/FTO interface. This work revealed the high light absorption coefficient of the HOIP materials, which is one of the key factors for fabricating high efficiency solar cells. Still, instability of these devices limits their practical application – the device performance degraded ~80% in 10 min due to the dissolution of the perovskite QDs in the liquid electrolyte.

### 1.2.2 Solid-State Mesoscopic Structure

To overcome the instability issue associated with the liquid electrolyte, Kim et al. in 2012, developed the first solid-state PSC by replacing the liquid electrolyte with the solid hole transport material HTM 2,2',7,7'-tetrakis-(*N,N*-di-*p*-methoxyphenyl-amine)-9,9'-spirobifluorene (Spiro-MeOTAD) that was successfully used in solid-state DSSC.[13] This device configuration (Figures 1-3b) was named the mesoscopic structure because it consists of a thin mp-TiO<sub>2</sub> layer similar to that used in the liquid electrolyte perovskite-sensitized solar cells, although the thickness of the mp-TiO<sub>2</sub> layer was reduced from ~3 μm to ~0.6 μm. In this device configuration, part of the Spiro-MeOTAD HTM penetrates into the pores of the mp-TiO<sub>2</sub> layer, making direct contact with the perovskite sensitizers. The remaining HTM material forms a dense capping layer that covers the mp-TiO<sub>2</sub>, preventing shunts between the electron transport materials (ETM) and the back contact (Figure 1-7a).

The working principle of this device configuration differs from the conventional DSSCs. In contrast to the electrolyte that suffered from low charge carrier mobility, the solid-state Spiro-OMeTAD allows holes to move more efficiently. The champion device

demonstrated a PCE of 9.7%, with  $V_{OC} = 0.89$  V,  $J_{SC} = 17.6$  mA/cm<sup>2</sup>, and FF = 62% (Figure 1-7b).

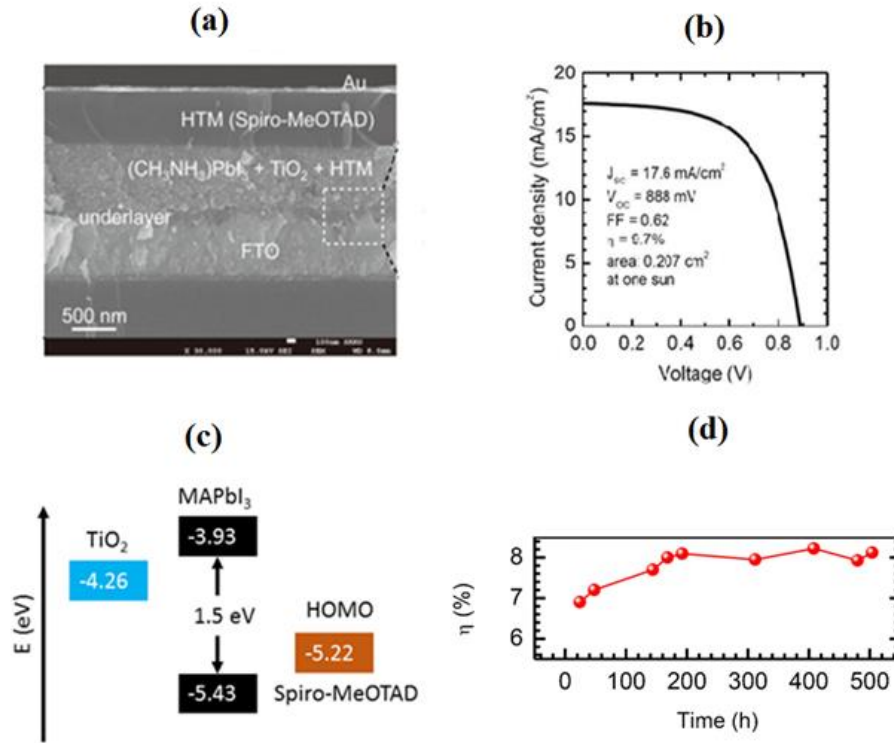


Figure 1-7. (a) Cross-sectional scanning electron microscope (SEM) image, (b) J-V characteristic, (c) energy level diagram, and (d) stability of a perovskite solar cell in solid-state mesoscopic structure. Panels (a), (b), and (d) are reprinted with permission from Ref.[13]. Copyright 2012, Nature Publishing Group.

Replacing the liquid electrolyte with the solid HTM significantly improved  $V_{OC}$  from 0.71 to 0.89 V due to the better alignment of the highest occupied molecular orbital (HOMO) level of the Spiro-MeOTAD (-5.22 eV) with the valence band of MAPbI<sub>3</sub> (-5.43 eV), enabling more efficient hole extraction from the perovskite absorber and widening the hole Fermi energy splitting under illumination (Figure 1-7c). In addition to the PCE

improvement, the device stability was also dramatically enhanced. Some devices even exhibited the enhanced PCEs after 500 h of operation (Figure 1-7d).

### 1.2.3 Meso-Superstructured Structure

Analogous to the mesoscopic configuration, Snaith et al. invented the meso-superstructured structure by replacing the mp-TiO<sub>2</sub> layer with the insulating Al<sub>2</sub>O<sub>3</sub>.<sup>[12]</sup> This device configuration has almost the same structure as in the mesoscopic structure (Figure 1-8a), but the perovskite materials formed a continuous extremely thin absorber (ETA) layer on the surface of the porous metal oxide (Figure 1-8b). Snaith et al. investigated a mixed halide CH<sub>3</sub>NH<sub>3</sub>PbI<sub>3-x</sub>Cl<sub>x</sub>, instead of the pure MAPbI<sub>3</sub> perovskite as the absorber material and studied the electronic properties of the meso-superstructured perovskite films.<sup>[20]</sup> The champion device with the porous Al<sub>2</sub>O<sub>3</sub> layer achieved a PCE of 10.9%, with V<sub>OC</sub> = 0.98 V, J<sub>SC</sub> = 17.8 mA/cm<sup>2</sup>, and FF = 63%, while the best control device made with mp-TiO<sub>2</sub> demonstrated a PCE of 7.6% with V<sub>OC</sub> = 0.80 V, J<sub>SC</sub> = 17.8 mA/cm<sup>2</sup>, and FF = 53%. Interestingly, a significantly higher V<sub>OC</sub> value of ~1.1 V was achieved in some devices with the Al<sub>2</sub>O<sub>3</sub> layer. This low V<sub>OC</sub> deficiency, i.e. the difference between E<sub>g</sub>/e of the absorber material and V<sub>OC</sub> of the corresponding devices, indicates low non-radiative recombination and long carrier diffusion lengths of the mixed halide perovskites. These excellent optoelectronic properties that favor the PV application were confirmed by optical and charge transport measurements.<sup>[21, 22]</sup>

The charge transport mechanism of the meso-superstructured cells differs from that of the mesoscopic devices in one critical way. Unlike the case of mp-TiO<sub>2</sub>, injection of photoexcited electrons from the perovskite absorber into Al<sub>2</sub>O<sub>3</sub> is energetically unfavorable due to the higher conduction band of Al<sub>2</sub>O<sub>3</sub> relative to MAPbI<sub>3-x</sub>Cl<sub>x</sub> (Figure 1-8c).

Moreover,  $\text{Al}_2\text{O}_3$  is electrically insulating as indicated by the poor performance of the DSSC with the N719 dye and mesoporous  $\text{Al}_2\text{O}_3$ . [12] Therefore, in this device, the porous  $\text{Al}_2\text{O}_3$  layer merely serves as a meso-scale scaffold for the perovskite absorber.

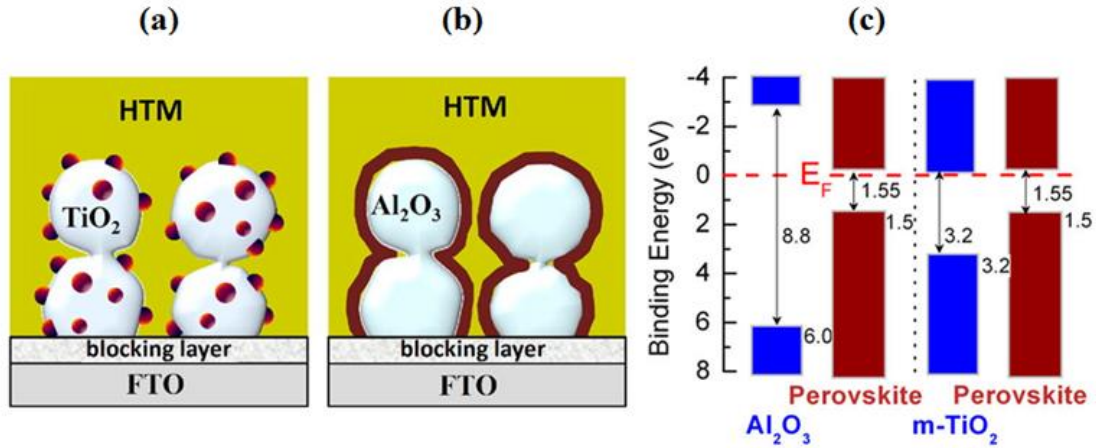


Figure 1-8. Schematic diagram of (a) mesoporous and (b) meso-structured PSCs. (c) Measured binding energy of perovskite,  $\text{Al}_2\text{O}_3$ /perovskite, and mp- $\text{TiO}_2$ /perovskite. Panels (a) and (b) are reprinted with permission from Ref.[23] Copyright 2014 American Chemical Society. Panel (c) is reprinted with permission from Ref.[20] Copyright 2014 American Chemical Society.

Electrons have to transport to the c- $\text{TiO}_2$  layer through the ETA layer of perovskites, which is enabled by the long diffusion lengths of both electrons and holes in the perovskite materials.[21, 22] These good electric properties suggested PSCs could be fabricated without the mesoporous layer. While Snaith et al. only achieved a PCE of 1.8% for their preliminary planar junction device,[12] high PCE devices were realized in the following years after the advances in deposition techniques, interface passivation,

compositional control, and the understanding of the perovskite materials (See Section 1.4 for the details).

#### 1.2.4 The Regular (Mesoporous) Structure

The success of meso-superstructured cells motivated many researchers in the related field to study these exciting materials. The breakthrough was enabled when researcher discovered the low trap state density and long carrier diffusion length in HOIPs,[21, 22] indicating thicker perovskite films instead of ETA could be used in the PSCs. Increasing the absorber thickness can improve the absorption of long wavelength photons and prevent the direct shunts between the electrodes. Consequently, the device structure was developed based on the meso-superstructure configuration but with a thicker and dense perovskite layer (Figure 1-3d). This structure was widely adopted by researchers all around the world for fabricating high efficiency PSCs, and thus is called the “regular” structure due to its popularity.

The regular device structure was originated from the PSCs with “pillared structures”. In 2013, Heo et al. reported this structure with MAPbI<sub>3</sub> completely filled the pores of the mp-TiO<sub>2</sub> and formed individual MAPbI<sub>3</sub> pillars (Figure 1-9a).[24] These perovskite pillars were covered by a thin poly triarylamine (PTAA) HTM and Au electrode to complete the device. The PCE of the best cell was 12%, with  $V_{OC} = 0.997$  V,  $J_{SC} = 16.5$  mA/cm<sup>2</sup>, and  $FF = 72.7\%$ . Heo et al. found that devices that had a mp-TiO<sub>2</sub> layer of ~600 nm exhibited the best incident photon-to-electron conversion efficiency (Figure 1-9b) and device performance (Figure 1-9c) due to the formation of a perovskite overlayer. However, this overlayer suffered from a rough and discontinuous morphology, limiting the improvement of device performance.

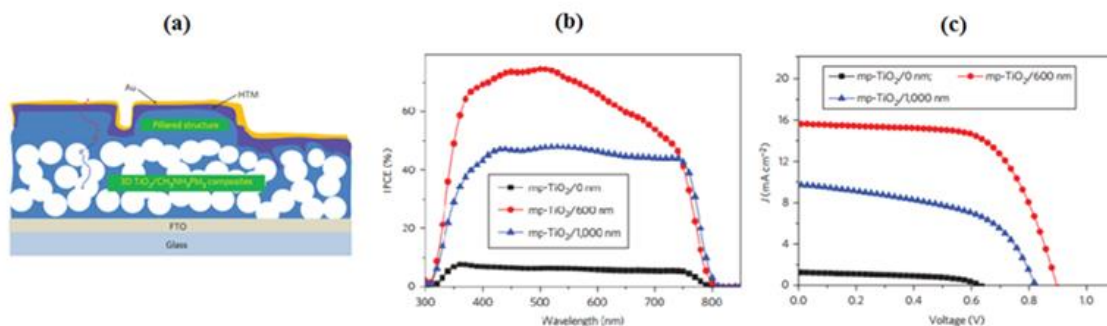


Figure 1-9. (a) Schematic illustration, (b) Incident photon-to-electron conversion efficiency (IPCE) curves, and (c) J-V characteristics of the PSCs with different mp-TiO<sub>2</sub> thickness. Reprinted with permission from Ref.[24]. Copyright 2013, Nature Publishing Group.

The further progress of the regular structure was propelled by the advances in the perovskite film deposition techniques,[1] allowing thicker perovskite films to be deposited on a thinner mp-TiO<sub>2</sub> layer. Bruska et al. reported PSCs with the best PCE of 15% in the regular configuration by fabricating a smooth and thin perovskite capping layer (~ 50 nm) on the top of a ~300 nm mp-TiO<sub>2</sub> layer (Figure 1-10a) using the two-step sequential deposition method (see the section 1.3.2).[25] The efficiency enhancement, especially the improved J<sub>SC</sub> (20.0 mA/cm<sup>2</sup>) (Figure 1-10d), was mainly due to the formation of a dense and uniform perovskite layer. The same deposition technique was then used by Im et al. to prepare PSCs on a thinner mp-TiO<sub>2</sub> layer (~100 nm), resulting in the increased thickness of the perovskite capping layer (~150 nm) (Figure 1-10b),[26] and improved the J<sub>SC</sub> (21.64 mA/cm<sup>2</sup>), V<sub>OC</sub> (1.056 V), and efficiency (17%) of the devices (Figure 1-10e). By employing the Li-doped TiO<sub>2</sub> and a thicker perovskite capping layer (~300 nm) (Figure 1-10c), Giordano et al. achieved a PCE of 19.3%, with V<sub>OC</sub> = 1.114 V, J<sub>SC</sub> = 23.0 mA/cm<sup>2</sup>,

and FF = 74% (Figure 1-10f).[27] To date, the state-of-the-art PSCs with PCEs >20% were predominantly fabricated in the regular configuration.[1]

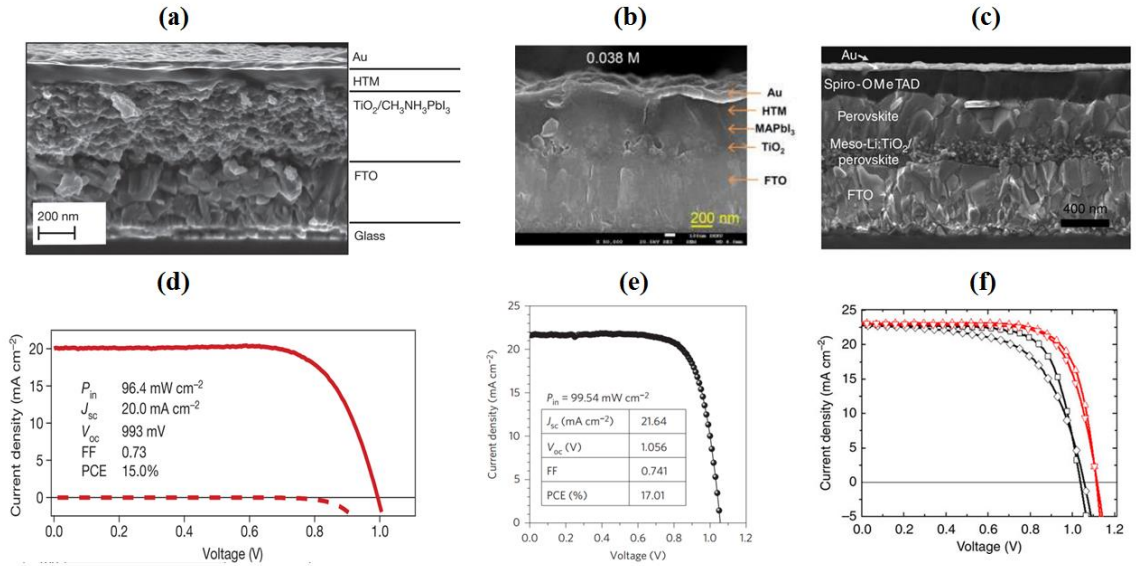


Figure 1-10. (a-c) Cross-sectional SEM image and (d-f) corresponding J-V curves of PSCs with different perovskite capping layers. Panels (a) and (d) are reprinted with permission from Ref.[25]. Copyright 2013, Nature Publishing Group. Panels (b) and (e) are reprinted with permission from Ref. [26]. Copyright 2014, Nature Publishing Group. Panels (c) and (f) are reprinted with permission from Ref.[27]. Copyright 2015 Nature Publishing Group.

### 1.2.5 Planar n-i-p Heterojunction Structure

The planar n-i-p heterojunction structure (Figure 1-3e) was developed as the mesoporous oxide layer of the regular structure getting thinner that they eventually were removed. Analogous to inorganic thin-film solar cells, the structure is comprised of a TCO cathode, an n-type ETM, an intrinsic perovskite layer, a p-type HTM, and a metal anode. Due to the low exciton bounding energy and long diffusion lengths of charge carriers, photoexcited electrons and holes have sufficiently long lifetimes to transport to the

interfaces with the charge selective layers (HTM and ETM). In 2012, Snaith et al. made the first attempt on planar heterojunction PSCs using  $\text{MAPbI}_{3-x}\text{Cl}_x$  but only achieved a PCE of 1.8%, [12] likely due to the incomplete film coverage that led to shunts in the devices. Efforts to increase the PCE by optimizing the processing conditions, including annealing temperature and film thicknesses, resulted in values of 4.5% [28] in 2013 and 11.4% [29] in 2014. Although the preliminary n-i-p type planar devices seemed to be comprised of smooth and uniform films in the devices (Figure 1-11a), the perovskite films were porous and had a high surface defect density (Figure 1-11b). To improve the smoothness of the perovskite film, Snaith et al. developed a dual-source coevaporation of  $\text{PbCl}_2$  and MAI technique (see Section 1.3.4) to prepare a uniform  $\text{MAPbI}_{3-x}\text{Cl}_x$  layer on the c- $\text{TiO}_2$  layer in 2013 (Figure 1-11c). [30] The champion device achieved a PCE of 15%, with  $V_{\text{OC}} = 1.07$  V,  $J_{\text{SC}} = 21.5$   $\text{mA}/\text{cm}^2$ , and  $\text{FF} = 0.67$  (Figure 1-11d). Thanks to the advances in the film deposition techniques (see Section 1.4), the present state-of-the-art planar PSCs prepared by solution-based deposition methods yields PCEs of ~20%, [31-33] with a  $V_{\text{OC}}$  of up to 1.214 V. [33] Additionally, these devices exhibited stable performance under operating conditions over hundreds of hours. [34] These advancements in efficiency and stability have made the planar device structure a promising candidate for the commercialized manufacturing of PSCs.

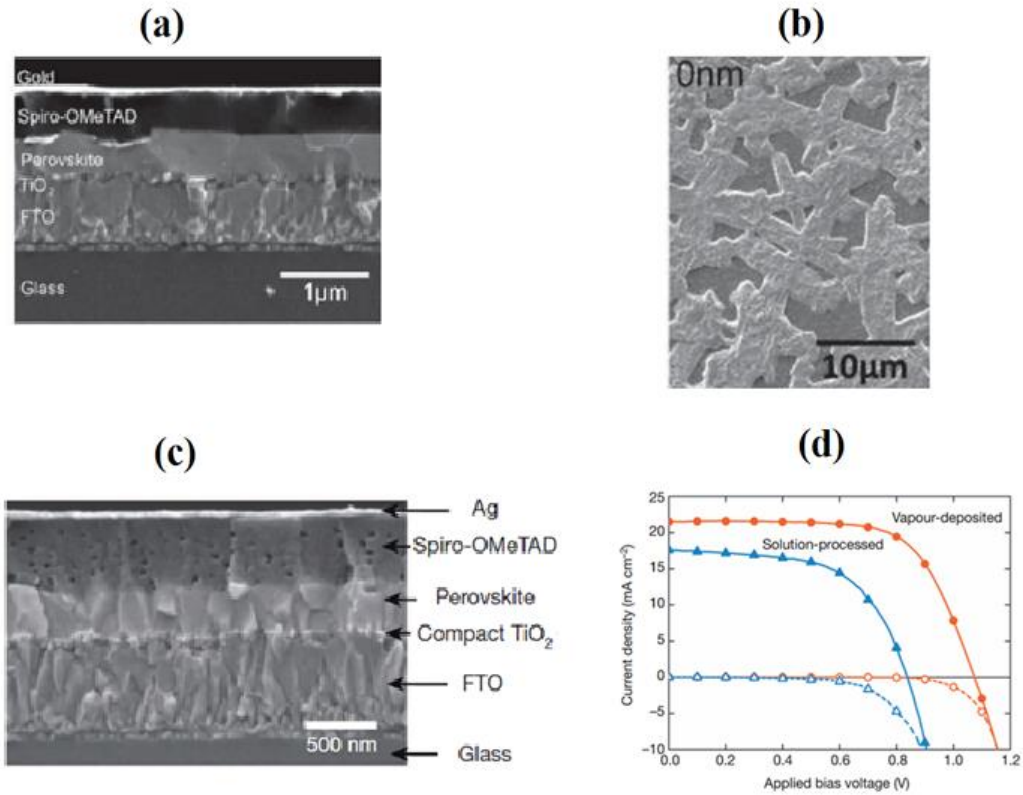


Figure 1-11. (a) Cross-sectional and (b) surface SEM images of a PSC in the planar n-i-p configuration prepared by solution-based deposition. (c) Cross-sectional SEM image of a PCS prepared by the vapor-based deposition. (d) J-V characteristics of the planar n-i-p type PSCs. Panels (a) and (b) are reprinted with permission from Refs.[29]. Copyright 2013 WILEY-VCH Verlag GmbH & Co. KGaA, Weinheim. Panels (c) and (d) are reprinted with permission from Ref. [30]. Copyright 2013, Nature Publishing Group.

### 1.2.6 Inverted Planar p-i-n Heterojunction Structure

While the regular and planar n-i-p structures progressed, the planar p-i-n heterojunction structure originally used in the organic PV devices was adopted by the PSC community as an alternative. Because the planar p-i-n heterojunction structure has an opposite sequence of HTM and ETM than the regular configuration, it is often referred as

the “inverted” structure (Figure 1-3f). The p-i-n structure is comprised of a TCO anode, a p-type HTM, an intrinsic perovskite layer, an n-type ETM, and a metal cathode. In 2013, Jeng et al. reported the prototype of planar p-i-n PSC with the structure ITO/PEDOT:PSS/MAPbI<sub>3</sub>/C<sub>60</sub>/BCP/Al,[35] where they categorized the MAPbI<sub>3</sub>/C<sub>60</sub> as a planar heterojunction and bathocuproine (BCP) and poly polystyrene sulfonate (PEDOT:PSS) as the ETM and HTM (Figure 1-12a). The preliminary device yielded a PCE of 1.6%, which improved to 3.9% when phenyl-C<sub>61</sub>-butyric acid methyl ester (PC<sub>61</sub>BM) was used instead of C<sub>60</sub>. The increased efficiency was attributed to the larger energy offset between the HOMO of MAPbI<sub>3</sub> (donor) and the lowest unoccupied molecular orbital (LUMO) of PC<sub>61</sub>BM (acceptor) and more efficient electron injection into the Al cathode (Figure 1-12b).

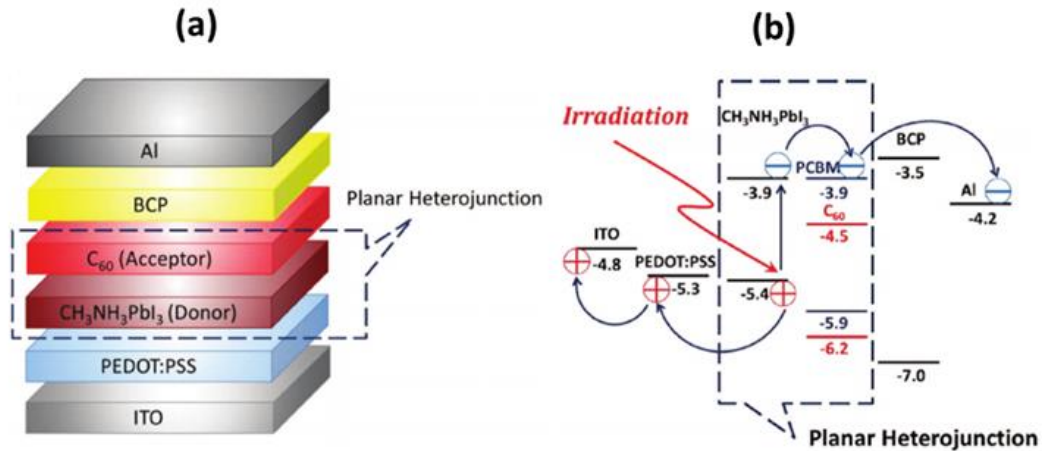


Figure 1-12. (a) Structure and (b) energy level diagram of a PSC in the planar p-i-n heterojunction structure. Reprinted with permission from Refs. [35]. Copyright 2013 WILEY-VCH Verlag GmbH & Co. KGaA, Weinheim.

The efficiency of PSCs in the planar p-i-n structure has rapidly progressed. Sun et al. applied the solution-processed PC<sub>61</sub>BM to the p-i-n type PSC and improved the PCE to 7.4%. [36] Snaith et al. prepared the planar PSC in the structure FTO/PEDOT:PSS/MAPbI<sub>3-x</sub>Cl<sub>x</sub>/PC<sub>61</sub>BM/TiO<sub>x</sub>/Al and obtained a PCE of 9.8%. [37] You et al. further improved the device efficiency to 11.5 % by optimizing the perovskite deposition. [38] Malinkiewicz et al. employed the co-evaporation technique for preparing MAPbI<sub>3</sub> and achieved a 12.0% PCE champion cell. [39] Wang et al. introduced a double fullerene layer consisting of C<sub>60</sub> and PC<sub>61</sub>BM to passivate the perovskite film, [40] and demonstrated a 12.2% PCE device with a record high FF of 80.1%.

While the early work established the standard configuration of the p-i-n planar structure (Figure 1-13a), the further progress of the p-i-n planar PSCs was due to advances in perovskite fabrication techniques (see Section 1.4). [41, 42] Nie et al. fabricated mm-sized perovskite grains using the hot casting deposition technique and achieved a PCE of 17.7%. [43] Meanwhile, Huang et al. used non-wetting HTM and ETM to assist the preparation of large-size perovskite grains (Figure 1-13b, c), [44, 45] achieving the champion PCE of 19.5%, with  $J_{SC} = 22.6 \text{ mA/cm}^2$ ,  $V_{OC} = 1.07 \text{ V}$ ,  $FF = 80.6\%$  (Figure 1-13d). [45] These state-of-the-art planar p-i-n devices not only exhibited excellent photon-to-electron conversion rate (Figure 1-13e), but also demonstrated enhanced device stability maintaining ~90% PCE after 30 days of exposure to the ambient condition (Figure 1-13f).

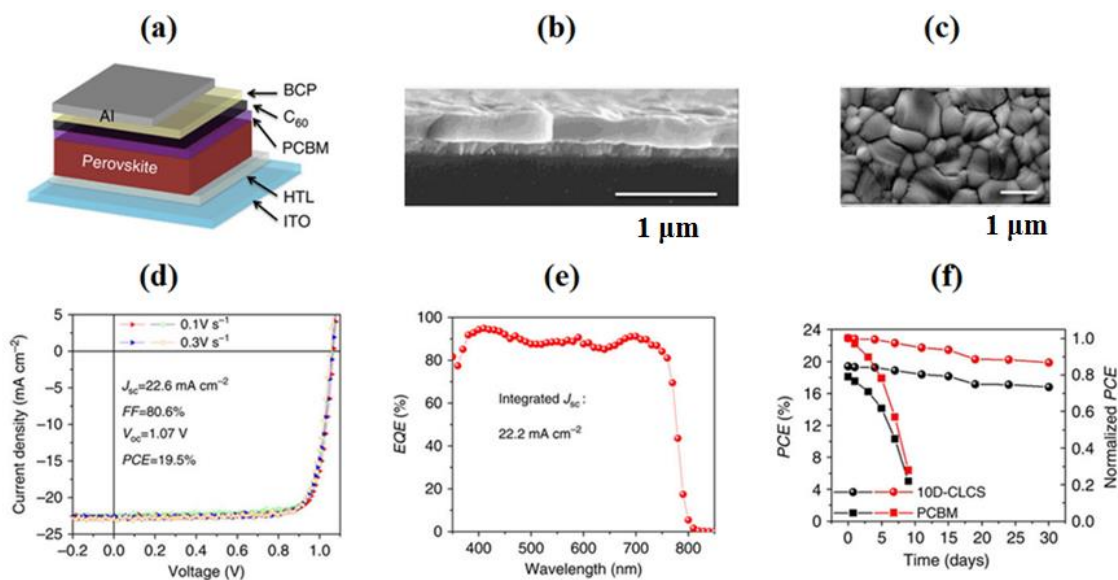


Figure 1-13. (a) Structure of a PSC in the planar p-i-n structure. (b) Cross-sectional and (c) surface SEM images of the perovskite film deposited on a ITO substrate. (d) J-V characteristic, (e) EQE, and (f) stability measurement of a PSC in the planar p-i-n structure. Panels (a) - (c) are reprinted with permission from Refs.[44] Copyright 2015, Nature Publishing Group. Panels (d) - (f) are reprinted with permission from Refs.[45] Copyright 2016, Nature Publishing Group.

### 1.3 Evolution of the Film Deposition Methods

Advances in the design of device architecture drove the evolution of PSCs, especially in the early stage (2009 - 2013) of the technical evolution. As the technology progressed, preparation of the perovskite layer became essential for fabricating high efficiency devices. Generally, delicate control of the stoichiometry, crystallographic phase, and grain structure of the HOIP material is required to fabricate high efficiency PSCs. Because these properties can be controlled by the preparation methods, substantial research into the development of film deposition techniques has occurred.

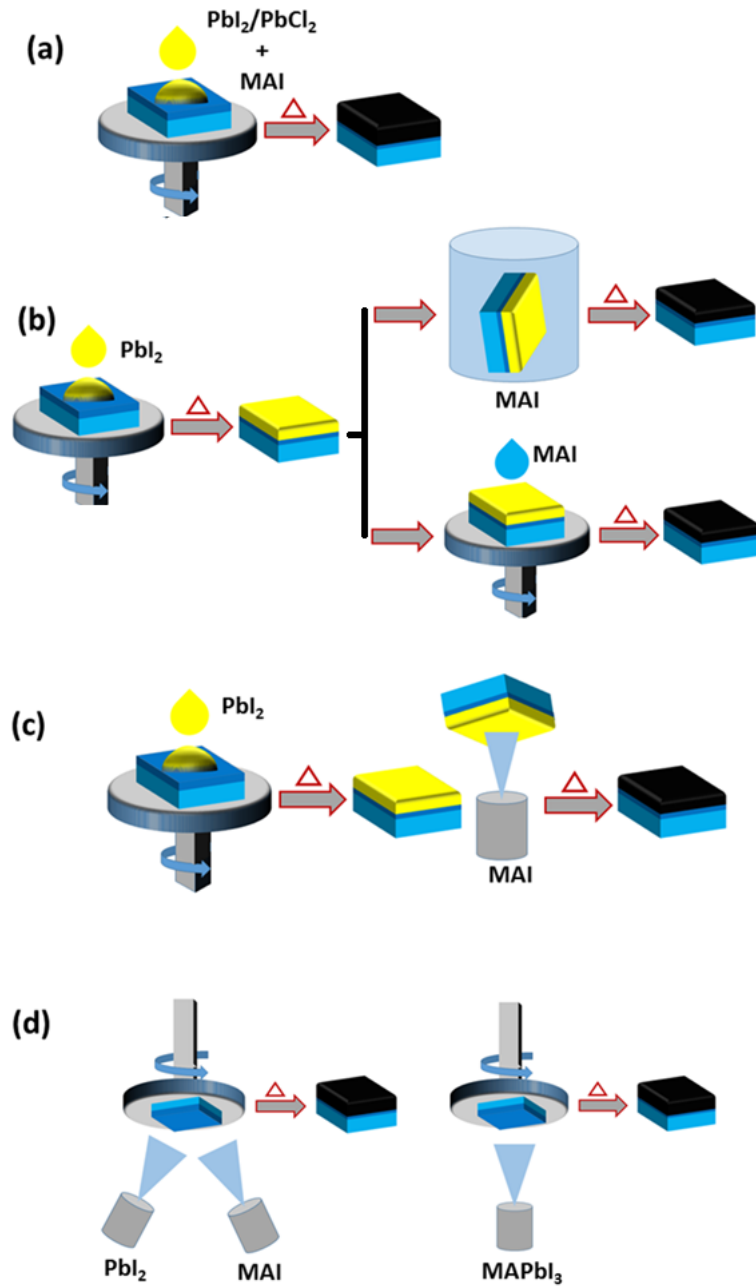


Figure 1-14. Preparation methods for perovskite absorber (a) single-step solution process, (b) two-step solution process, (c) vapor assisted solution process, and (d) thermal vapor process.

During the evolution of PSCs, 4 primary deposition approaches, single-step solution process (Figure 1-14a),[12] two-step solution process (Figure 1-14b),[25] vapor assisted solution process (Figure 1-14c),[46] and thermal evaporation process (Figure 1-14d),[30] were developed to fabricate the perovskite films.

### 1.3.1 Single-Step Solution Process

The single-step solution deposition was first used to fabricate PSCs due to the ease of processing[11-13] and is now the most widely adopted processing technique for preparing the perovskite films. In this process, the precursor solution is prepared by dissolving organic halide MAX and metal halide  $PbX_2$  in an aprotic polar solvent, such as  $\gamma$ -butyrolactone (GBL), dimethyl formamide (DMF), dimethyl sulfoxide (DMSO), N-2-methyl pyrrolidone (NMP), or a mixture of them. A wide range of precursor MAX to  $PbX_2$  ratios have been used to fabricate high efficiency PV devices.[47] For example, high PCE MAPbI<sub>3</sub> devices were prepared using a MAI to PbI<sub>2</sub> ratio of 0.8:1 (MAI-poor)[48] and 3:1 (MAI-rich).[49] To deposit a perovskite film using the single-step solution process, the precursor solution is spin-coated on a substrate followed by a post-deposition annealing at temperatures ranging from 80 to 150 °C (Figure 1-14a).[1, 50] The appropriate selection of post-deposition temperature and time based on the precursor composition is crucial for fabricating high quality perovskite films.[29, 47, 51] Additionally, the environmental conditions (e.g., oxygen and humidity), morphology of the substrates, and other processing parameters (rotational speed and time) can also influence the uniformity, crystallinity, phase purity, surface morphology and interface properties of the perovskite films.

Advancements of the single-step solution deposition method started with understanding the effect of substrate morphology and annealing temperature on the surface morphology of the perovskite films. Snaith et al. showed that the perovskite capping layer coverage increased with decreasing the mesoporous Al<sub>2</sub>O<sub>3</sub> thickness.[29] However, poor surface coverage was observed with absence of the mesoporous Al<sub>2</sub>O<sub>3</sub> layer, indicating that the mesoporous scaffold was important to form a conformal perovskite coating. They further investigated the morphology of perovskite films on a c-TiO<sub>2</sub> layer annealed at different temperatures and found that increasing the annealing temperature led to less surface coverage of the perovskite films.[29] Therefore, temperature that is sufficiently high to crystallize the perovskite film while preserve a good surface coverage is recommended for the film preparation. Dualeh et al. investigated the effects of post-deposition annealing on the surface morphology of MAPbI<sub>3</sub> films deposited on a mp-TiO<sub>2</sub> layer.[52] The best devices were achieved using temperatures in the range of 80 - 100 °C, due to a smooth surface morphology and good phase purity.

Clearly, the empirical optimization of various deposition parameters can lead to high efficiency PSCs. However, without the development of rational synthetic guidelines, further advances would be difficult to achieve. To address this need, a recent work systematically studied the impact of the precursor composition and reaction temperature on the MAPbI<sub>3</sub> formation using the single-step deposition method and proposed a near-equilibrium phase diagram for the perovskite formation (Figure 1-15).[47] Although the pure tetragonal MAPbI<sub>3</sub> perovskite phase ( $\alpha$ ) occurs in a narrow compositional space where the composition is close to the stoichiometric value [MAI/(MAI+PbI<sub>2</sub>) = 0.5], the benign nature of the stacked perovskite sheet (SPS) phase that formed in the MAI-rich region

enables a wider composition range for high efficiency device fabrication. The result is consistent with early work, in which the off-stoichiometry MAI to  $\text{PbI}_2$  ratio (3:1,  $X_{\text{MAI}} = 75\%$ ) was used in the precursor solution and the films were subjected to a high temperature ( $\sim 150^\circ\text{C}$ ) annealing.[21] This off-stoichiometry precursor composition led to smoother morphology than using a stoichiometric precursor solution at that time.

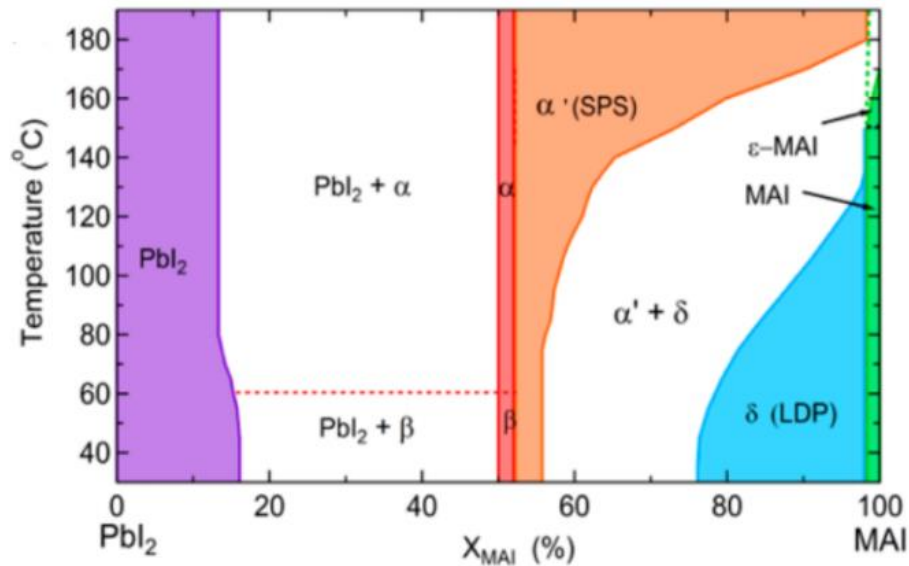


Figure 1-15. Proposed phase diagram for  $\text{MAPbI}_3$ . Reprinted with permission from Refs.[47]. Copyright 2015 American Chemical Society.

### 1.3.2 Two-Step Solution Deposition

In the early stage of PSC evolution, the devices prepared by the single-step solution deposition was inhibited by the poor surface coverage of the perovskite film (Figure 1-16a-d). To overcome this, Burschka et al. developed the two-step solution deposition method, based on the pioneering work by Mitzi et al.,[8] to prepare uniform  $\text{MAPbI}_3$  films on the mp- $\text{TiO}_2$  layer.[25] In the two-step method, a  $\text{PbI}_2$  seed layer is first deposited and

subsequently reacted with MAI in isopropanol (IPA) solution introduced by dipping or spin-coating (Figure 1-14b) to form MAPbI<sub>3</sub>. The films prepared by the two-step method formed a dense conformal layer (Figure 1-16e & f), while contemporary films prepared using the single-step solution method formed of spherical-shaped individual islands (with GBL) (Figure 1-16a & b) or highly porous needle-shaped crystals (with DMF) (Figure 1-16c, d).

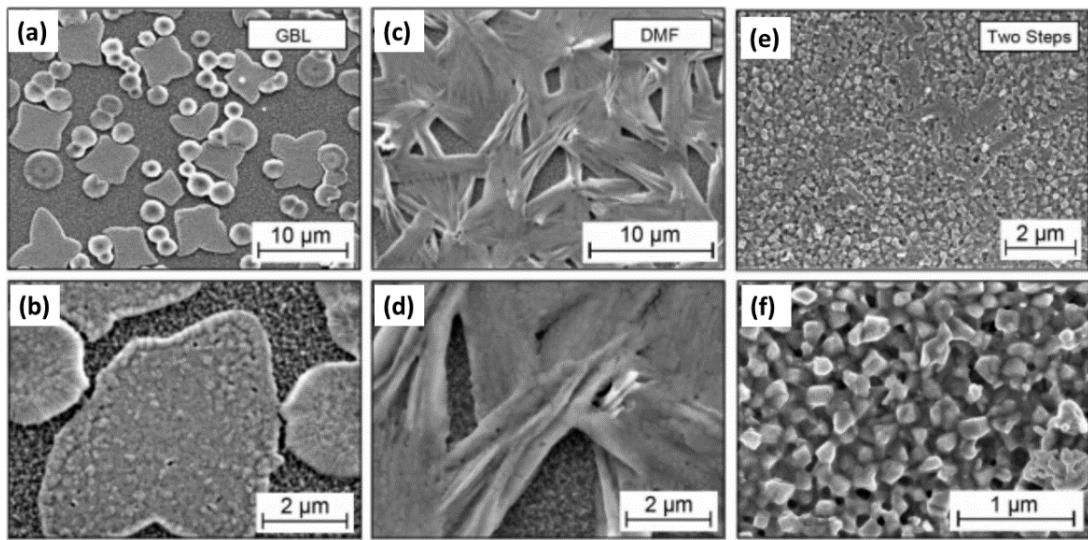


Figure 1-16. MAPbI<sub>3</sub> perovskite films prepared by the single-step solution deposition using (a), (b) GBL and (c), (d) DMF solvents. Panels (e), (f) show the fabricated MAPbI<sub>3</sub> films using the two-step sequential deposition. Reprinted with permission from Ref.[25].

Copyright 2013, Nature Publishing Group.

Im et al. continued the work on the two-step deposition by investigating the relationship between grain size of perovskite and the MAI concentration.[26] They found that grain size decreased with increasing MAI concentration, with the best PCE of 17.01%

achieved at the MAI concentration of 0.038 M. Due to the success in fabrication high efficiency PSCs in the normal device structure, the two-step solution method was subsequently applied to the planar n-i-p and p-i-n architectures.[41, 53, 54] However, there were several drawbacks to this method. The major one is the trade-off between perovskite grain size and surface smoothness. Surface roughness increases with increasing the size of perovskite grains, leading to a higher surface recombination and leakage current. In contrast, smooth films with small grains suffer from low carrier lifetime and short diffusion length. Another drawback is the incomplete conversion of  $\text{PbI}_2$ , especially in the planar structures.[55, 56] The remaining  $\text{PbI}_2$  not only decreases the total light absorption, but also blocks the efficient charge carrier transport to the selective contacts, resulting in reduced  $V_{OC}$  and  $J_{SC}$ . In the past few years, these hurdles were overcome using advanced film deposition techniques (see Section 1.4) and devices with PCEs of >20% were fabricated using the two-step methods.[57]

### 1.3.3 Vapor Assisted Solution Process

The vapor assisted solution process was developed as a modified two-step solution deposition where the MAI is introduced by a vapor deposition process. Yang et al. introduced this method to fabricate uniform and conformal  $\text{MAPbI}_3$  films with high phase purity (Figure 1-17a).[46] They deposited the  $\text{PbI}_2$  seed layer by spin-coating, followed by exposing to the MAI vapor generated by heating the MAI powder at 150 °C in an inert environment. This method effectively avoids delamination issues during the two-step solution process when the sample is removed from the MAI solution or washed by the IPA solution.[41, 46] Perovskite films formed by this method showed a full conversion of  $\text{PbI}_2$

and a conformal, uniform, and smooth film with large sized grains up to the micrometer scale (Figure 1-17b, c). However, the process of MAI incorporation into the  $\text{PbI}_2$  framework is much slower than the solution deposition, needing several hours for complete conversion. This long processing time limits the practical application of this method.

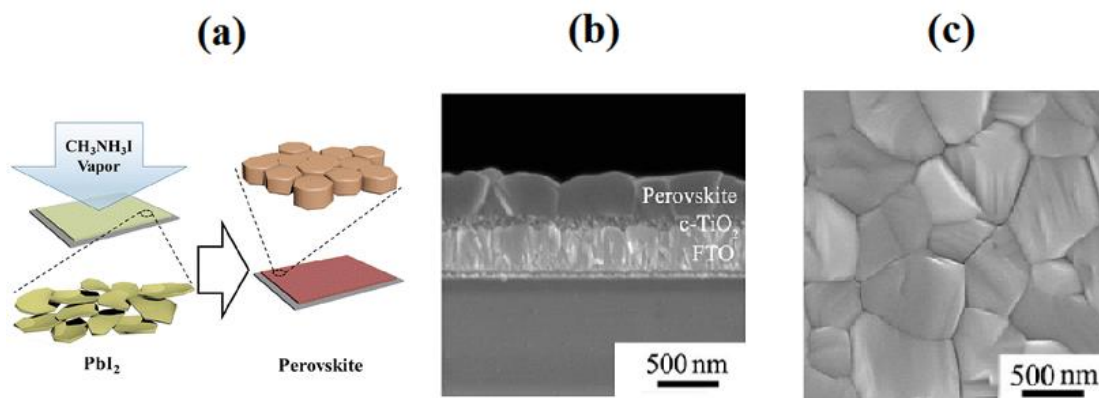


Figure 1-17. (a) Schematic illustration, (b) cross-sectional, and (c) surface SEM images of perovskite film prepared by vapor assisted solution process. Reprinted with permission from Ref.[46]. Copyright 2014 American Chemical Society.

#### 1.3.4 Thermal Vapor Deposition

Thermal evaporation was used to fabricate HOIP films in 1990s because it was widely used in the semiconductor industry.[58, 59] In 2013, Snaith et al. rejuvenated this method by using the dual coevaporation to prepare the first planar heterojunction PSCs.[30]  $\text{MAPbI}_{3-x}\text{Cl}_x$  films were prepared by coevaporation of  $\text{PbCl}_2$  and MAI followed by annealing (Figure 1-18a). Smooth, conformal, and uniform perovskite films were the result, and a then record PCE of 15.4% was achieved. This success stimulated development of alternative vapor deposition methods, such as the layer-by-layer vacuum evaporation, [60] chemical vapor deposition (Figure 1-18b),[61] and flash evaporation (Figure 1-18c).[62]

Perovskite films deposited using vapor deposition are more uniform and pinhole-free compared to solution processed films.[63] This can lead to high efficiency devices, however, due to the low thermal stability of both the precursor sources and the products, control over temperature during deposition is difficult and often results in off-stoichiometric films. Therefore, only few research groups have fabricated high efficiency devices using this method.[30, 39, 60, 64, 65]

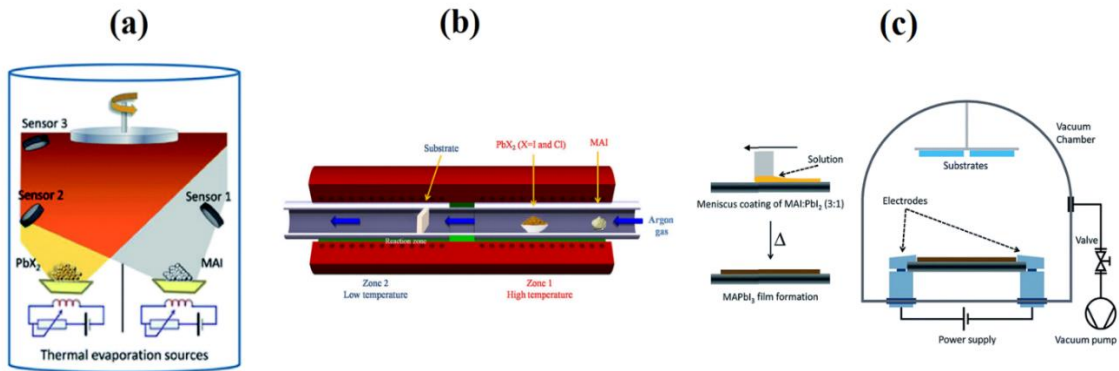


Figure 1-18. Schematic images of (a) dual source evaporation, (b) chemical vapor deposition, and (c) flash evaporation. Panel (a) is reprinted with permission from Ref.[63]. Copyright 2015 Materials Research Society. Panel (b) is reprinted with permission from Ref.[61]. Copyright 2015 Nature Publishing Group. Panel (c) is reprinted with permission from Ref.[62]. Copyright 2015 Royal Society of Chemistry.

#### 1.4 Advanced Device Engineering Techniques

The rapid progress of PSCs in the early stage (2012 - 2014) relied mainly on the innovation on the device architecture and film preparation method. During this period, the champion PCE was rapidly increased to 15%. The further advances in fabricating high efficiency PSCs with PCEs of ~20% were enabled by some advanced device engineering

techniques developed in 2014 - 2016 to address problems associated with the primary deposition methods and improve the quality of the perovskite films.[1] These strategies, solvent engineering, deposition process engineering, contact material engineering, band gap engineering, yield uniform and dense perovskite films with improved optoelectronic properties and interface passivation. Consequently, the present state-of-the-art PSCs typically employed combined engineering strategies to achieve high performance and stability. In addition to single junction PSCs, research on perovskite-based tandem devices has been progressed as a promising future direction.

#### 1.4.1 Solvent Engineering

After common device structures and film deposition methods were established, the most challenging aspect of processing PSCs became achieving a homogeneous composition and uniform thickness over large area. In the early 2014, two-step solution process was mostly used to prepare uniform and pinhole-free perovskite films because of easy process and high reproducibility. In contrast, single-step method often resulted in inconsistent film morphology with high porosity (Figure 1-16). To address this, many researchers investigated solvent engineering techniques to improve the surface morphology of single-step solution processed perovskite films.

Jeon et al. first used DMSO as an additive to the precursor solution, improving the crystallinity and morphology of perovskite films.[66] During the single-step deposition, the intermediate phase of MAI-PbI<sub>2</sub>-DMSO was formed via an intercalation process, retarding the crystallization kinetics of perovskite formation. The intermediate phase was then converted into MAPbI<sub>3</sub> via a heat treatment which removes the DMSO molecules

(Figure 1-19a). This process allowed a uniform grain growth rate of perovskite crystals, leading to the formation of uniform and dense perovskite layers. By incorporating the DMSO additive, Jeon et al. demonstrated PSCs with an improved PCE of 16.5% (Figure 1-19b) and high photon-to-electron conversion efficiencies over the visible light spectrum (Figure 1-19c).[66]

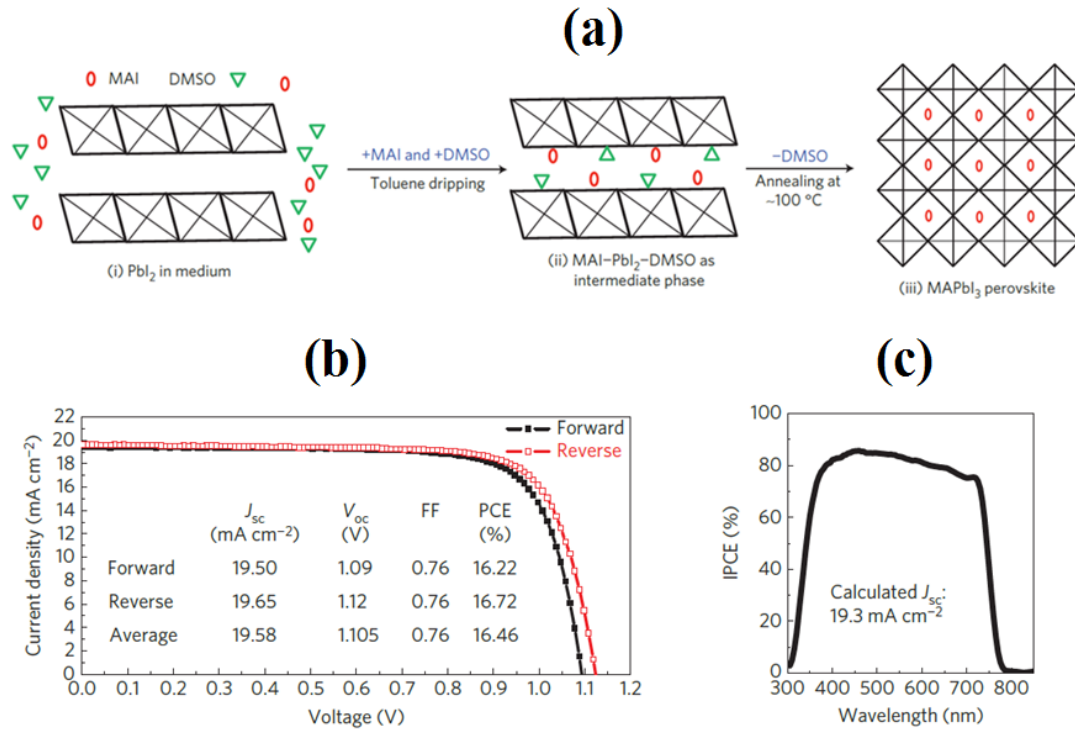


Figure 1-19. (a) Mechanism illustration of solvent engineering using DMSO. (b) J-V characteristics and (c) IPCE curve of PSCs prepared with DMSO additive. Reprinted with permission from Ref.[66]. Copyright 2014, Nature Publishing Group.

Besides DMSO that was added to the precursor solution for decoupling the nucleation and grain growth processes during the deposition, several other additives such as  $\text{CH}_3\text{NH}_3\text{Cl}$ , [67]  $\text{HI}$ , [68]  $\text{MAI/I}_2$ , [69]  $\text{NH}_4\text{Cl}$ , [70]  $\text{H}_2\text{O/HBr}$ , [71] 1,8-diiodooctane, [72]

5-ammoniumvaleric acid,[73] and phosphonic acid ammonium[74] have also been used in the single-step solution deposition to fabricate perovskite films with higher crystallinity and better surface coverage. The solvent engineering technique was also applied to the two-step solution deposition. The conventional two-step solution deposition is hampered by the incomplete conversion that leaves a dense  $\text{PbI}_2$  layer on the ETM or HTM.[75, 76] When MAI is introduced on to a dense  $\text{PbI}_2$  seed layer, the top surface reacts with MAI and forms a dense perovskite capping layer, which hinders the MAI diffusion to the underlying  $\text{PbI}_2$  layer.[75] Fabricating a porous  $\text{PbI}_2$  film is an effective way to avoid the formation of dense perovskite capping layer and increase the perovskite conversion. Adding additives such as n-butanol,[77] MAI,[53]  $\text{H}_2\text{O}$ ,[78] or 4-tert-butylpyridine[54] in the  $\text{PbI}_2$ /DMF precursor solution, or by employing DMSO as a solvent,[55] researchers can control the porosity in the  $\text{PbI}_2$  layer. Additionally, modifying the MAI solution by incorporating small concentrations of metal ions (e.g.,  $\text{Zn}^{2+}$ ,  $\text{Cd}^{2+}$ ,  $\text{Hg}^{2+}$  etc.) was also used to prepare perovskite films with uniform morphology and large grains.[79, 80] Despite these advancements, two-step has become less popular after the recent progress of deposition process engineering techniques.

#### 1.4.2 Deposition Process Engineering

Jeon et al. introduced the anti-solvent drop casting technique to complement the solvent engineering in the single-step solution deposition.[66] A precursor solution consisting of the equimolar MAX and  $\text{PbX}_2$  in DMF/DMSO is spin onto a substrate. During the last tens of seconds of spinning, an anti-solvent to DMF, such as toluene, chloroform, chlorobenzene, diethyl ether is dripped on the substrate (Figure 1-20a).[66, 81,

82] The anti-solvent addition rapidly extracts DMSO from the precursor solution, leading to the increased solute concentration in the precursor solution. Consequently, the intermediate MAI-PbI<sub>2</sub>-DMSO phase is rapidly formed, which avoids the needle- and spherical-shaped perovskite crystals that usually occurs with DMF and GBL solvents, respectively. After annealing, smooth and dense perovskite films with high phase purity which are essential for fabricating high efficiency PCSs are formed. Many research groups have further improved PCEs to > 20% by optimizing the precursor composition and preparation recipe of this advanced processing technique.[81-84]

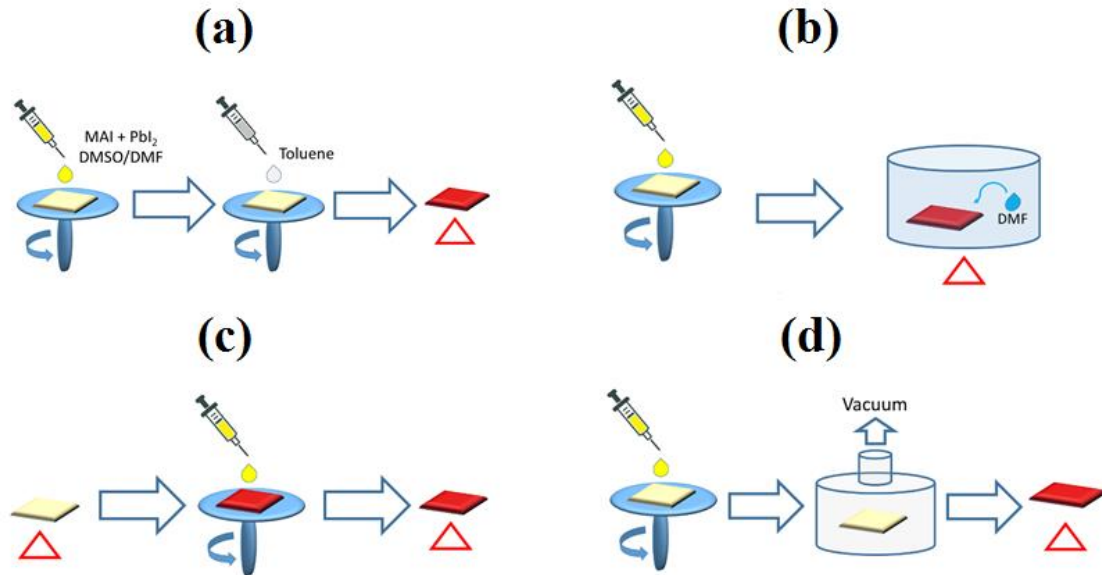


Figure 1-20. Schematics of (a) anti-solvent drop casting, (b) solvent annealing process, (c) hot-casting deposition method, and (d) vacuum-flash assisted solution process.

Other modifications on the perovskite deposition and/or post-deposition processes have also been successfully applied for fabricating high efficiency PSCs. Xiao et al. developed a solvent annealing technique for the two-step solution deposition (Figure 1-

20b) to enhance the grain size.[42] Annealing the as-deposited perovskite films with a small amount of DMF vapor enhanced the perovskite grain size from 300 nm to  $\sim 1 \mu\text{m}$  and increased PCE from 9.9% to 15.6%. Perovskite films annealed with pyridine[85] or MAI[86] vapor also demonstrated the improved photoluminescence and carrier lifetimes, indicating the formation of high-quality perovskites films that could be used to fabricate high efficiency solar cells.

While the anti-solvent technique promotes the formation of intermediate phase by delaying the crystal growth kinetics, the same results can be achieved by speeding the nucleation kinetics. Nie et al. demonstrated that the hot-casting method (Figure 1-20c), in which crystallization of the perovskite film occurs immediately after a hot precursor solution is loaded onto the substrate held at an elevated temperature, can be used to prepare high-quality perovskite films with millimeter-scale grains.[43] Li et al. developed another approach called the vacuum-flash assisted solution process to replace the addition of anti-solvent, (Figure 1-20d).[87] In this process, the spin-coated perovskite precursor film is placed in a vacuum chamber for a few seconds to remove the residual solvents more quickly. This rapid solvent extraction due to different vapor pressures of the solvents accelerates the crystallization of the perovskite intermediate phase, and the subsequent thermal annealing produces a high-quality perovskite film. The advantage of this technique over the anti-solvent method is the ability to fabricate a uniform perovskite film over a large area. The champion cell fabricated with this method with a  $> 1 \text{ cm}^2$  aperture area achieved a maximum PCE of 20.5%, with a  $V_{\text{OC}} = 1.14 \text{ V}$ ,  $J_{\text{SC}} = 23.24 \text{ mA/cm}^2$ , and  $\text{FF} = 75.9\%$ .

### 1.4.3 Contact Materials Engineering

In addition to the advances in the perovskite film preparation, the progress in ETM and HTM also played an essential role in the development of PSCs. Various materials possessing combined merits, including proper band alignment with the conduction or valence band of the perovskite absorber, efficient charge carrier transport, and low charge recombination defect densities at the interfaces, have been developed as the ETMs or HTMs. Figure 1-21 shows the band energy levels of these commonly used ETM and HTM in comparison with HOIPs and electrodes.

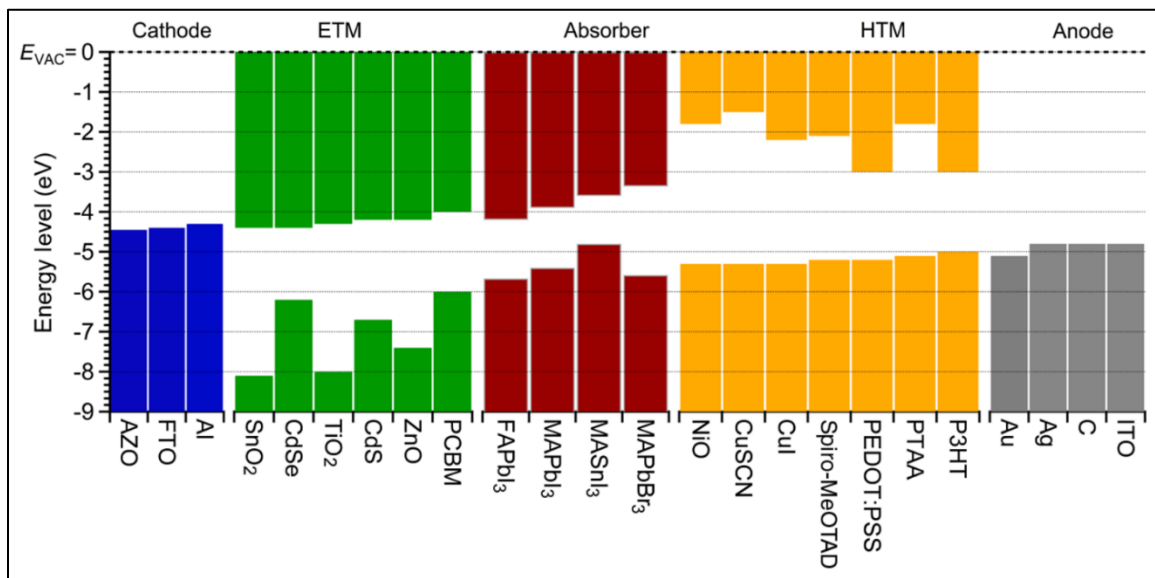


Figure 1-21. Energy levels of commonly used cathode, n-type (ETM), absorber, p-type (HTM), and anode materials in perovskite solar cells. Reprinted with permission from Ref.[1]. Copyright 2016 Society of Photo Optical Instrumentation Engineers.

Since the PSCs emerged, TiO<sub>2</sub> has been widely used as the compact and porous ETM in the n-i-p structure configuration.[11, 19] With the evolution of perovskite technology, the thickness of the mp-TiO<sub>2</sub> layer, conventionally used in DSSCs, gradually

decreased from  $\sim 4 \mu\text{m}$  to  $\sim 100 \text{ nm}$  in the regular structure and was omitted in the planar structure.[26, 29, 30] This progress was enabled by the high crystallinity and long carrier lifetime of the HOIP materials. Removing the mesoporous oxide layer made the compact ETM an essential component of the devices for efficient collection of photoexcited electrons. Therefore, some dedicated control technique (e.g., ALD) has become popular to fabricate high quality ETM. Besides c-TiO<sub>2</sub>, other ETMs such as ZnO,[88] SnO<sub>2</sub>,[31-33, 89, 90] CdSe,[91] CdS,[92] TiO<sub>2</sub>-graphene,[40] and yttrium-doped TiO<sub>2</sub>[49] have been developed as ETMs. The use of these alternative ETMs allows PSCs to be processed without high temperature ( $\sim 500 \text{ }^\circ\text{C}$ ) treatment that is required for the anatase TiO<sub>2</sub>. C<sub>60</sub> and its derivatives such PC<sub>61</sub>BM or PC<sub>71</sub>BM are among the commonly used organic ETM materials in the p-i-n device configuration.[36, 93] These materials can also be processed at low temperatures, enabling the potential for roll-to-roll manufacturing on flexible substrates and incorporating with another cell to fabricate tandem devices.

HTMs are also critical for a good PV performance, especially for a high Voc.[94] Both organic and inorganic HTMs have been investigated in recent years. The organic HTMs can be categorized into two groups: small molecules and conducting polymers. Spiro-MeOTAD is the most used small molecules HTM due to high device performance ( $> 20\%$  PCEs).[87] However, the devices using spiro-OMeTAD typically exhibit poor stability, especially after exposure to humidity.[95-97] Conducting polymers of PTAA, P3HT (Poly(3-hexylthiophene-2,5-diyl)), and triazatruxene derivatives have also been applied as the HTMs.[98] Among them, PTAA (20.2%)[57] and triazatruxene derivatives (18.3%)[99] showed competitive PCEs to the Spiro-MeOTAD but improved stability. P3HT, on the other hand, is not good as the Spiro-MeOTAD, demonstrating only 12-15%

efficiencies.[98, 100] Nonetheless, higher material cost and lack of stability of the organic HTMs are still the main hurdles for the commercialization of PSCs. One possible solution is employing cost-effective and more stable inorganic HTMs, such as NiO<sub>x</sub>,[101-104] CuO,[105] Cu<sub>2</sub>O,[105] and CuSCN.[106] Among these, the devices using NiO<sub>x</sub> showed > 17% PCE,[103, 104] which is promising for utilization in commercial manufacturing.

#### 1.4.4 Band Gap Engineering of Perovskites

In the early stage of PSC progress (2009 - 2013), MAPbI<sub>3</sub> was used as the prototype due to its band gap of 1.55 eV that is suitable for high efficiency solar conversion.[11, 13] As the field advanced, the composition of the perovskite AMX<sub>3</sub> has been altered by incorporating other monovalent cations A (formamidinium (FA<sup>+</sup>) and Cs<sup>+</sup>), divalent cation M (Sn<sup>2+</sup>), and halide ions X (Br<sup>-</sup> and Cl<sup>-</sup>), which results in optical absorption tunability (Figure 1-22).[107, 108] This versatility in optical band gap enables various PV applications of PSCs, including single-junction devices as well as both the top and bottom cells in tandem structures.[109]

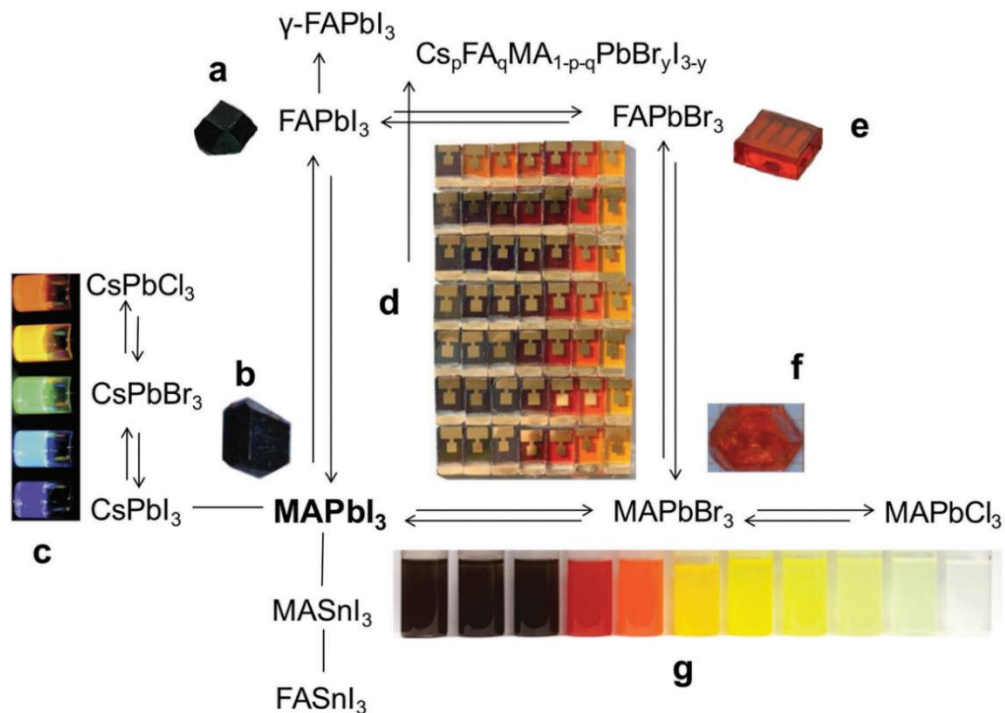


Figure 1-22. The versatility of hybrid perovskite materials  $Cs_pFA_qMA_{1-p-q}PbBr_yI_{3-y}$  and their absorption tunability. Reprinted with permission from Ref.[107]. Copyright 2017, Royal Society of Chemistry.

The substitution of the monovalent A cation does not directly affect the electronic band structure in halide perovskites because the valence band maximum and conduction band minimum are mainly contributed from the strong Pb-s and I-p antibonding state and Pb-p state, respectively.[110] However, the size of the A cation affects to the tolerance factor  $t$ , and thus changes to the spacing of  $[MX_6]^{4-}$  octahedra, altering the band gap.[15] The A cations of  $FA^+$ ,  $MA^+$ , and  $Cs^+$  have the decreasing ionic sizes of 253 pm, 217 pm, and 181 pm, respectively, and thus the increasing band gaps 1.48 eV ( $FAPbI_3$ ), 1.52 eV ( $MAPbI_3$ ) and 1.67 eV ( $CsPbI_3$ ) (Figure 1-23a).[108, 111] The  $MA_xFA_{1-x}PbI_3$  mixed

perovskite fabricated by engineering a mixture of  $\text{FA}^+$  and  $\text{MA}^+$  in the A site showed a red shifted optical absorption with respect to  $\text{MAPbI}_3$ , extending solar energy absorption to the longer wavelengths thereby increasing the  $J_{\text{SC}}$ . [112] This mixed cation perovskite  $\text{MA}_x\text{FA}_{1-x}\text{PbI}_3$  was used to fabricate PSCs with  $\text{PCE} > 20\%$ . [57] Additionally, the mixed cation perovskite  $\text{Cs}_x\text{FA}_{1-x}\text{PbI}_3$  (Figure 1-23b) has improved moisture stability and photoexcited carrier lifetime over  $\text{MAPbI}_3$  or  $\text{FAPbI}_3$ . [34, 113, 114] The enhanced interaction between  $\text{FA}^+$  and  $\text{I}^-$  due to reduction of the octahedral volume increases the chemical inertness of the perovskite. [113] Moreover, incorporation of the inorganic  $\text{Cs}^+$  stabilizes the perovskite phase of  $\text{FAPbI}_3$  and reduces the defect density. [114]

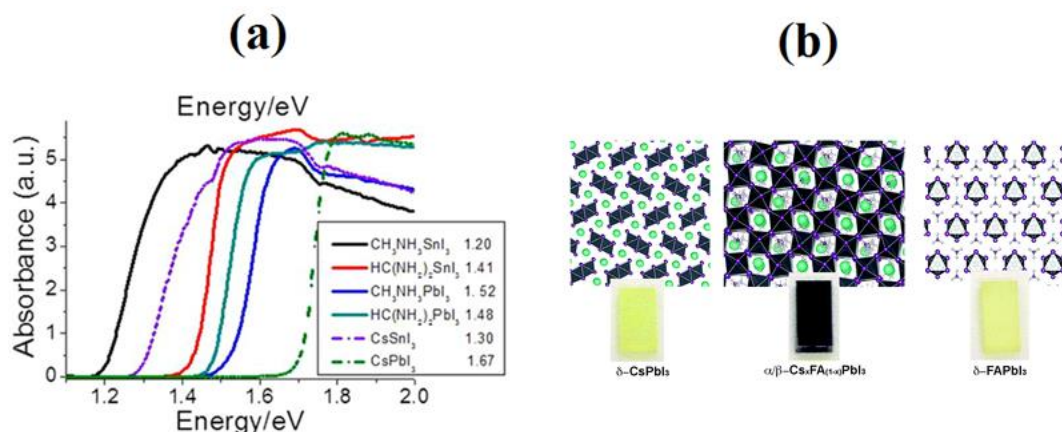


Figure 1-23. (a) UV-vis absorbance and band gap values of  $\text{MASnI}_3$ ,  $\text{FASnI}_3$ ,  $\text{MAPbI}_3$ ,  $\text{FAPbI}_3$ ,  $\text{CsSnI}_3$ , and  $\text{CsPbI}_3$ . (b) Crystal structure and photos of  $\text{CsPbI}_3$ ,  $\text{Cs}_x\text{FA}_{1-x}\text{PbI}_3$ , and  $\text{FAPbI}_3$ . Panel (a) is reprinted with permission from Ref. [108]. Copyright 2013 American Chemical Society. Panel (b) is reprinted with permission from Ref. [114]. Copyright 2016 Royal Society of Chemistry.

The substitution of different halide anions X can be used to tune the optical band gap of the metal halide perovskites (Figure 1-22).  $\text{MAPb}(\text{I}_{1-x}\text{Br}_x)_3$  is commonly used to

fabricate high bandgap perovskite absorber layer.[111, 115, 116] Increasing Br content ( $x$  value) results in a continuous blue shift of the absorption band edge from 1.5 eV (830 nm) at  $x = 0$  to 2.3 eV (540 nm) at  $x = 1$  (Figure 1-24a).[115-117] In contrast to Br incorporation, which is used to alter the band gap, the Cl mixed phase  $\text{MAPb}(\text{I}_{1-x}\text{Cl}_x)_3$  shows negligible band gap alternation to the pristine  $\text{MAPbI}_3$  (Figure 1-24b) due to the relatively low Cl concentrations (< 4%) in the final product.[12]

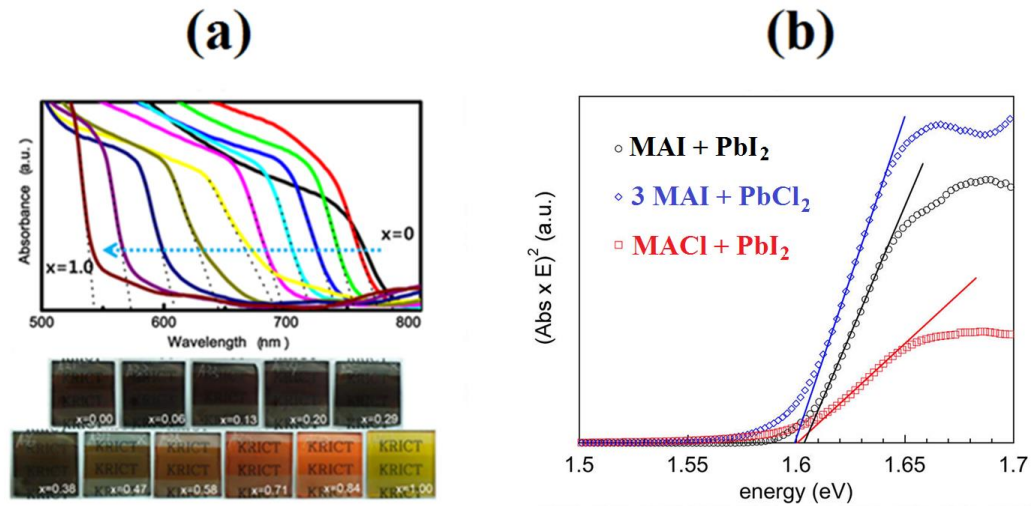


Figure 1-24. (a) Photographs and UV-vis absorption spectra of  $\text{MAPb}(\text{I}_{1-x}\text{Br}_x)_3$ . (b) UV-vis spectra of  $\text{MAPb}(\text{I}_{1-x}\text{Cl}_x)_3$ . Panel (a) is reprinted with permission from Ref.[116] Copyright 2013 American Chemical Society. Panel (b) is reprinted with permission from Ref.[118]. Copyright 2013 American Chemical Society.

However, the charge carrier diffusion length in  $\text{MAPb}(\text{I}_{1-x}\text{Cl}_x)_3$  is greater than 1  $\mu\text{m}$ , which is one order of magnitude higher than the pure iodide perovskite,[21] leading to the improved PV performance. Therefore,  $\text{MAPb}(\text{I}_{1-x}\text{Cl}_x)_3$  was widely used to fabricate high performance devices in the early stage (2012 – 2014).[12, 117-119] To date,

perovskite absorbers combined mixed organic cations ( $\text{FA}^+$  and  $\text{MA}^+$ ) and halides ( $\text{I}^-$  and  $\text{Br}^-$ ) have been widely used to fabricate  $\text{FA}_{1-x}\text{MA}_x\text{Pb}(\text{I}_{1-y}\text{Br}_y)_3$  based solar cells,[120] which has achieved  $>20\%$  PCE with a high degree of reproducibility.[81, 87] The present champion PSC with the  $\text{FA}_{1-x}\text{MA}_x\text{Pb}(\text{I}_{1-y}\text{Br}_y)_3$  absorber demonstrated a PCE of 22.1%, with  $V_{\text{OC}} = 1.105$ ,  $J_{\text{SC}} = 24.97 \text{ mA/cm}^2$ , and  $\text{FF} = 80.3\%$ .[57]

The substitution of divalent cation M can also alter the band gap of the perovskite absorber. Due to the environmental concerns with water soluble lead based perovskites,[121, 122] many research efforts have been devoted to replacing Pb by nontoxic Sn.[123, 124] The  $\text{MASnI}_3$  perovskite has a lower band gap ( $\sim 1.2 \text{ eV}$ ) compared to its Pb counterpart ( $1.55 \text{ eV}$ ), and thus exhibits light absorption at the longer wavelengths, which is beneficial for a higher  $J_{\text{SC}}$ .[108] However, due to the high  $V_{\text{OC}}$  deficit the pure Sn-based PSCs typically exhibited poor PV performance.[123, 125] More recently, mixed tin-lead perovskite low-bandgap perovskite solar cells have been developed for bottom-cell tandem solar cells.[126, 127] Recently, Zhao et al. achieved a 17.6% PCE, with  $V_{\text{OC}} = 0.853 \text{ V}$ ,  $J_{\text{SC}} = 28.5 \text{ mA/cm}^2$ , and  $\text{FF} = 72.5\%$  in a single junction PSC based on  $(\text{FASnI}_3)_{0.6}(\text{MAPbI}_3)_{0.4}$  perovskite film.[127] Further, by connecting this with a  $\sim 1.58 \text{ eV}$  band gap perovskite top cell, they were able to achieve a steady-state efficiency of 21.0% in the four-terminal tandem cell. However, stability of the Sn-based perovskite solar cells is not comparable to their Pb-based counterparts[108, 128] and needs to be addressed in the future research.

#### 1.4.5 Perovskite Tandem Solar Cells

Due to their tunable band gap that ranges of 1.2 to 2.3 eV and versatility in the device configurations, HOIPs are ideal candidates for tandem solar cells (Figure 1-25).[109, 111, 115, 129] The  $\text{MAPb}(\text{I}_x\text{Br}_{1-x})_3$  perovskites with relatively high band gaps (1.5 to 2.3 eV) and high PCEs (~20%) are commonly used as the top cell for a variety of combinations of tandems, including perovskite-Si,[130-132] perovskite-CuInGaSe<sub>2</sub>, [133, 134] and perovskite-Cu<sub>2</sub>ZnSnS<sub>4</sub>. [135] The low band (1.2 to 1.5 eV) perovskites  $(\text{FASnI}_3)_x(\text{MAPbI}_3)_{1-x}$  were developed recently as the bottom cells for the perovskite-perovskite tandems.[127, 136]

The perovskite tandem solar cells were first demonstrated in the 4-terminal configuration (Figure 1-25b) due to the simplicity of implementation. In this configuration, a high bandgap cell is mechanically mounted on top of a low bandgap cell. The subcells are fabricated independently, often by incompatible processes. Individual operation of the subcells is possible as well, which allows for a high combined PCE since the two cells can be independently maintained at differing maximum power points. Bailie et al. fabricated the first 4-terminal perovskite tandems using the  $\text{MAPbI}_3$  top cell coupled with CuInGaSe<sub>2</sub> and Si bottom cells, achieving 18.6% and 17.0% PCEs, respectively.[134] More recently, McMeekin et al. reported a high PCE of 25.2% by combining a top cell with  $\text{FA}_{0.83}\text{Cs}_{0.17}\text{Pb}(\text{I}_{0.6}\text{Br}_{0.4})_3$  perovskite ( $E_g = \sim 1.74$  eV) with a Silicon-heterojunction bottom cell.[137] Fu et al. demonstrated perovskite-CuInGaSe<sub>2</sub> tandems with a efficiency of 22.1%. [138]

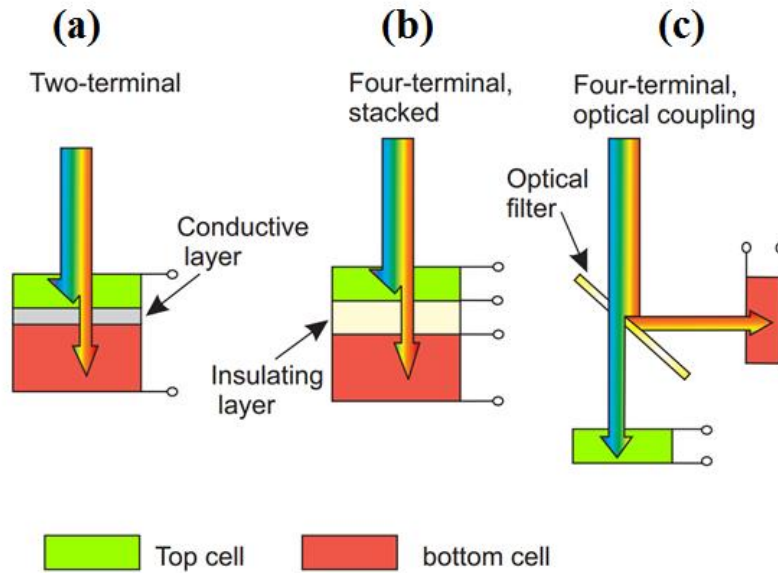


Figure 1-25. Three main configurations of tandem solar cells: (a) 2-terminal monolithic, (b) 4-terminal stacked, and (c) 4-terminal optical coupling structures. Reprinted with permission from Ref.[139]. Copyright 2016, Nature Publishing Group.

The 4-terminal optical coupling tandem structure was developed as an alternative 4-terminal configuration (Figure 1-25c). Instead of stacking the subcells, an optical splitter was used to split photons with short and long wavelengths to the high and low band gap cells, respectively. Uzu et al. fabricated such tandems by coupling a MAPbI<sub>3</sub> perovskite cell and a silicon heterojunction bottom cell with a 550 nm cutoff splitter and achieved a PCE of 28%.[140] The high PCE is due to the optical splitter which allows more efficient utilization of long wavelength photons, however, the additional cost for the optical components may make it infeasible for practical application.

After the demonstration of 4-terminal tandem devices and the advances in the processing techniques for HOIP materials, 2-terminal monolithic perovskite-based

tandems were developed. The low temperature processing allows the perovskite top cell being processed directly on the bottom cell (e.g., Si and CuInGaSe<sub>2</sub>) and connected via a recombination layer. Due to the 2-terminal configuration, only a single transparent conductive electrode is needed, lowering parasitic absorption in the electrode and manufacturing cost. However, it is challenging to fabricate high efficiency devices due to the complexity of processing the PSC on a completed bottom cell and electrical and optical design of the whole tandem. At present, perovskite-Si and perovskite-CuInGaSe<sub>2</sub> tandems in this configuration have demonstrated PCEs up to 23.6% [131, 132, 141] and 10.9%, [133] respectively.

More recently, perovskite-perovskite tandem solar cells proposed by many researchers due to a tunable band gap were demonstrated. [111, 115, 129] Both 2-terminal monolithically integrated and 4-terminal mechanically stacked perovskite-perovskite tandems have been developed in recent years. [127, 136, 142] Eperon et al. fabricated both types using a FA<sub>0.83</sub>CS<sub>0.17</sub>Pb(I<sub>0.5</sub>Br<sub>0.5</sub>)<sub>3</sub> top cell (1.8 eV) and a FA<sub>0.75</sub>CS<sub>0.25</sub>Sn<sub>0.5</sub>Pb<sub>0.5</sub>I<sub>3</sub> bottom cell (1.2 eV), demonstrating 17% and 20% PCEs, respectively. [136] This perovskite-perovskite tandem is very promising due to the potential of high PCE and low costs, which could be the future direction of PSCs.

## 1.5 Outlook and Summary

Despite the rapid progress of PSCs, the obvious challenges limiting the commercialization of PSCs is lack of long-term and operational stability. In recent years, significant effort has been directed to understanding the operative decay mechanisms and developing appropriate solutions to improve device stability, [34, 143] but there is much

to learn and control if PSCs are to be widely deployed. Although the underlying degradation mechanisms are far from completely understood, degradation has been attributed to humidity,[144] oxygen,[145] light,[146] heat,[147] and intrinsic instability.[148] In nearly all studies, humidity has been demonstrated as the most aggressive cause of instability in materials and devices due to the strong interaction between water molecules and perovskite materials.[97] However, isolating the device from the external environment via encapsulation procedures[149, 150] can significantly slow the degradation. Additionally, PSCs employing hydrophobic back contact materials (e.g., carbon fiber) have also demonstrated enhanced performance stability in outdoor tests.[151, 152]

Hysteresis in the J-V characteristics of devices is another important effect that must be controlled. Without a complete understanding of the origins of hysteresis, as well as methods to circumvent or control it, it will be impossible to manage the operation of PSCs. Hysteresis has received elevated attention recently but its origin and mitigation are still under investigation.[153-157] Although there is evidence that hysteresis could be attributed to the formation and migration of ionic defects and the interfaces between the perovskite absorber and the selective contacts, a detailed understanding of the degradation and hysteresis mechanisms in perovskite solar cells is needed. If the advances in this emerging PV technology continue and the stability problem can be solved, perovskite PV would be a viable option in the PV market. Such an economic advantage without subsidies would stimulate a wider degree of PV deployment.

In summary, the solution-processed PSCs have made remarkable progress, becoming one of the most promising PV technologies of the future. High efficiency PSCs

with a diverse set of device architectures and material combinations have been successfully developed. In this chapter, we discussed the evolution of device structures, film deposition methods, and advanced device engineering techniques that has led to the unprecedented rate of device advancement. Additional research is needed to provide a better understanding of the material and device properties and address challenges such as long term stability and hysteresis in J-V characteristics. Moving forward, it is expected that more encouraging results will be reported, and PSCs will continue to be an area the interest of the PV community.

## **1.6 Dissertation Overview**

This dissertation has focused on the solution based fabrication of methylammonium lead iodide perovskite ( $\text{CH}_3\text{NH}_3\text{PbI}_3$ ,  $\text{MAPbI}_3$ ) thin films and the back interface engineering of the cadmium telluride (CdTe) solar cells.

In this chapter, Chapter 1, the evolution of the perovskite solar cells was presented. Brief description of the history of perovskite materials and the early studies of Sn- and Pb-based perovskites were discussed. Evolution of the device architecture, film deposition methods, advanced device engineering techniques, challenges, and future directions of perovskite photovoltaic (PV) devices were explained.

Chapter 2 investigates the nucleation and growth mechanisms of  $\text{MAPbI}_3$  in the two-step solution deposition process. Three distinct perovskite formation behaviors; Ostwald ripening, the blocking layer formation, and low-dimensional perovskites (LDPs) assisted diffusion were observed at various MAI concentrations, and a tentative model was proposed to explain the reaction mechanisms.

Chapter 3 focuses on improving the grain size, crystallinity, and charge carrier lifetime of MAPbI<sub>3</sub> perovskite thin films, and therefore the improved device performance by introducing small concentrations of the divalent metal cation Cd<sup>2+</sup> during the two-step growth process.

Chapter 4 discuss other possible divalent metal cations that can be used in the perovskite fabrication process to improve the grain size, crystallinity, morphology, and charge carrier life times of MAPbI<sub>3</sub> perovskite thin films.

Chapter 5 starts with a short introduction to the CdTe solar cell technology, explaining the formation of back contact barrier, and unfavorable band bending at the back junction. A new wet-chemical process is introduced to form a Te layer on the CdTe surface using MAI solutions that would reduce the back barrier height and the downward valance-band bending from the low work function electrode to the p-type CdTe. Optimization of the MAI treatment on the CdS/CdTe devices with Au back electrode is presented and the experimental results from the CdS/CdTe devices, which are subjected to the optimized MAI treatment, with an indium tin oxide (ITO) back electrode is discussed. Further, back contact barrier height for CdS/CdTe devices with both Au and ITO back electrodes are compared and related to their device performances.

Chapter 6 concludes this dissertation with a summary of all studies, which are discussed from Chapter 2 to Chapter 5, and future considerations.

## Chapter 2

# Understanding the Nucleation and Growth Behaviors of Methylammonium Lead Iodide Perovskites in the Two-Step Solution Process

Understanding the nucleation and growth mechanisms involved in the solution-processing of semiconductor thin films is of importance to fabricate low-cost, high-quality materials for optoelectronic and photovoltaic applications. Among the emerging materials of interest for solar cells, organic-inorganic hybrid lead halide perovskites have attracted considerable attention in recent years due to rapid improvements in device performance. However, a comprehensive understanding of the mechanisms for the formation of perovskites is still needed to be improved to control of the crystal growth and to further boost device performance.

In this Chapter, we investigate nucleation and growth mechanisms of methylammonium lead iodide perovskite ( $\text{MAPbI}_3$ ) formed in a two-step solution process when the pre-deposited lead iodide ( $\text{PbI}_2$ ) films were reacted with methylammonium iodide (MAI) in iso-propanol solution at various concentrations. Three different perovskite formation behaviors were observed as varying the MAI concentrations. From the observation, we propose a tentative model to explain the reaction mechanisms at different

MAI concentrations. We show that Ostwald ripening, the blocking layer formation, and the low-dimensional perovskite assisted diffusion are likely to be the primary mechanisms for the reaction as the MAI concentration increases. By controlling the MAI concentration, perovskite PV devices with different grain sizes and morphologies were fabricated and the highest device efficiency of 10.8% was achieved.

## **2.1 Introduction and Motivation**

Solar cells based on organic-inorganic hybrid perovskites, especially methylammonium lead iodide ( $\text{MAPbI}_3$ ), have recently emerged as promising alternative to compete the market-dominant silicon technology in photovoltaics (PV). Starting with a power conversion efficiency (PCE) of 3.8 % in 2009,[11] perovskite PV devices have achieved the first breakthrough (9.7 %)[158] in 2012 and improved the champion cell efficiency to more than 22% now.[57] Such unprecedentedly rapid progress is mainly due to a unique combination of intrinsic optical and electronic properties of the perovskites, such as high absorption coefficients, appropriate band gaps, fast charge separation, long electron/hole diffusion lengths, and low-cost, facile preparation methods.[25, 26, 66, 159]

High performance perovskite PV devices have been prepared by using a variety of deposition approaches.[25, 26, 41, 52, 160] Among them, two-step solution-based deposition provides an easy and low-cost route to prepare uniform and full-coverage perovskite thin films.[25, 26, 41, 93] In the two-step method, a  $\text{PbI}_2$  seed layer is first deposited and subsequently reacted with methylammonium iodide (MAI) in iso-propanol (IPA) solution that introduced by dipping or spin-coating.[25, 26] The two-step method was first developed for the meso-structured perovskite devices,[25, 26] and is now widely

used in the planar n-i-p and p-i-n architectures.[41, 56, 93] Although it has been used for fabricating high-efficiency devices, critical issues are still remain. One of the issues is the incomplete conversion of  $\text{PbI}_2$ , especially in the planar structures.[56, 161] The formation of a compact perovskite capping layer significantly hinder the MAI diffusion to the underlying  $\text{PbI}_2$ , and thus result in a mixture of  $\text{PbI}_2$  and  $\text{MAPbI}_3$ . [75] A common approach to reduce the  $\text{PbI}_2$  residue is to have a long MAI interaction time. However, a longer interaction time often causes significant delamination of the film and non-uniform surface.[8, 41, 162] The other issue is the difficulty of reproducibly controlling the grain size and morphology.[55] Adding additives, such as DMSO,[55]  $\text{H}_2\text{O}$ , [78] and MAI [53] into the  $\text{PbI}_2$  precursor solution helps to achieve more uniform morphology and better device performance, but these advanced procedures only focus on the optimization of the  $\text{PbI}_2$  seed layer and overlook the importance of the understanding of formation mechanisms.

When the two-step deposition is applied for fabricating high performance devices, two empirical extremes of MAI concentrations, low (8 to 10 mg/ml) and high (40 to 50 mg/ml) are found to be optimal for the n-i-p and p-i-n structures, respectively.[26, 41, 93] The effect of MAI concentration on the perovskite film properties and device performance has been investigated previously near the ranges of these two extremes.[26, 41, 93] These studies demonstrate that controlling MAI concentration is crucial to optimize high performance devices, but the comprehensive understanding of the crystallization process in the two-step method is still not clear. While growth mechanisms have been previously proposed in other investigations,[75, 163] less attentions have been given to intermediate region of the MAI concentration between these two extremes. Besides, these theories[75,

163] were proposed for a relatively long reaction time (several hours), but may not be applicable for a short reaction time (~20 s) that generally used for PV devices. Comprehensive understating the nucleation and growth behavior of perovskites during the MAI intercalation process would provide insights to improve the control of the two-step process.

To address this need, we investigate the effect of MAI concentration on the formation of MAPbI<sub>3</sub> perovskite in the two-step method. A wide range of MAI concentration varying from 5 to 50 mg/ml was used to grow MAPbI<sub>3</sub> perovskite films on meso-porous TiO<sub>2</sub> substrates and to fabricate perovskite PV devices. Here, we show that the nucleation and growth of the perovskites at the solid-liquid interface changes with the MAI concentration and verify the formation of a dense perovskite capping layer in the intermediate range (10 to 20 mg/ml) of MAI concentration. We propose a tentative model to explain the MAI diffusion through the perovskite capping layer at high MAI concentrations and provide a route toward fully conversion of thick perovskite films.

## 2.2 Experimental Details

### 2.2.1 Perovskite Films and Device Fabrication

*Materials:* All chemicals were purchased from Sigma-Aldrich unless otherwise stated and used without any further modifications. Methylammonium iodide (CH<sub>3</sub>NH<sub>3</sub>PbI, MAI) was synthesized according to the literature.[46] In brief, hydroiodic acid (HI, 57 wt% in water) was reacted with methylamine solution (CH<sub>3</sub>NH<sub>2</sub>, 33 wt% in ethanol) under a nitrogen atmosphere in an ice bath with continuous stirring for 2 hours. Then the resulting solution was evaporated at 80 °C and the precipitate was washed three times using diethyl ether and

the white color product was obtained. Finally, the product was dried in vacuum to obtain the MAI powder.

*Films and Device fabrication:* A 6 in. X 6 in. fluorine-doped tin-oxide (FTO) coated glass substrate (TEC 15 Pilkington) was wiped using soap, acetone, and methanol. After that, it was cut in to 1.25 in. X 1.25 in. pieces and further cleaned in an ultrasonic bath with Micro-90 detergent for 1 h and then 30 m with de-ionized water. Finally, nitrogen gas was used to dry the samples thoroughly. All the depositions were conducted in a nitrogen filled glove box with  $\sim 0.1$  ppm  $\text{H}_2\text{O}$  and  $\text{O}_2$ .

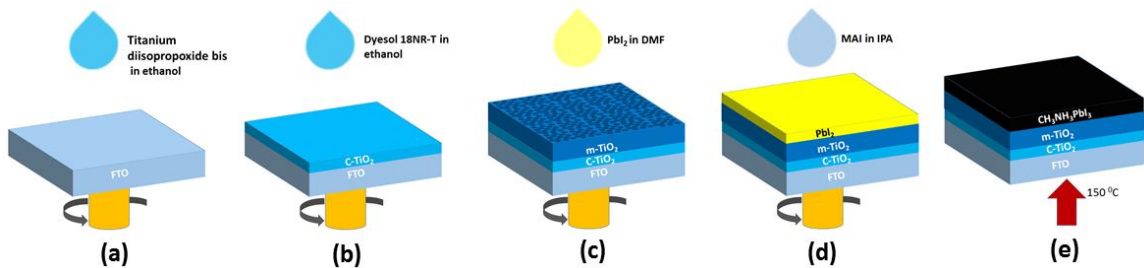


Figure 2-1. Preparation of (a) the compact  $\text{TiO}_2$  (b) meso-porous  $\text{TiO}_2$  (c)  $\text{PbI}_2$ , and (d & e)  $\text{MAPbI}_3$  perovskite layers.

The hole blocking compact titanium dioxide ( $\text{TiO}_2$ ) layer was deposited on FTO by spin-coating of 0.3 M titanium diisopropoxide bis (acetylacetonate) in ethanol at 3,000 rpm for 30 s and dried at  $125^\circ\text{C}$  for 5 min, followed by annealing at  $500^\circ\text{C}$  for 30 min in air (Figure 2-1a).[164]  $\text{TiO}_2$  paste (Dyesol 18NR-T) diluted in 2:7 (w/w) ethanol was spun at 3,000 rpm for 30 s to deposit the meso-porous  $\text{TiO}_2$  layer and annealed in air at  $500^\circ\text{C}$  for 30 min (Figure 2-1b).[25] Two-step sequential spin deposition of  $\text{PbI}_2$  and MAI was conducted to form  $\text{CH}_3\text{NH}_3\text{PbI}_3$  perovskite absorber.[26, 41, 93] The 1 M  $\text{PbI}_2$  solution

was prepared by dissolving 462 mg of  $\text{PbI}_2$  (99.999%) in 1 ml anhydrous N,N-Dimethylformamide (DMF) with overnight stirring at  $70^\circ\text{C}$ . 230  $\mu\text{L}$   $\text{PbI}_2$  was spun on the meso layer at 3,000 rpm for 30 s and dried at  $100^\circ\text{C}$  for 15 min on a hot plate (Figure 2-1c). Various concentrations of MAI solutions (5 to 100 mg/ml) were prepared by dissolving synthesized MAI in anhydrous Iso-propanol (IPA). 500  $\mu\text{L}$  MAI solution with different concentrations were spin-coated at 4,000 rpm with a 20 s waiting time (for the 5 mg/ml sample, 60 s waiting time was used) (Figure 2-1d). The samples were then annealed at  $150^\circ\text{C}$  for 5 min or  $100^\circ\text{C}$  for 15 min to complete  $\text{CH}_3\text{NH}_3\text{PbI}_3$  perovskite formation (Figure 2-1e). The HTM solution consisted of P3HT dissolved in dichlorobenzene (15 mg/mL) with two additives of tert-butylpyridine (tBP) (3.4  $\mu\text{L}/\text{mL}$ ) and lithium bis(trifluoromethanesulfonyl)imide (Li-TFSI) (6.8  $\mu\text{L}/\text{mL}$ ) from a solution of 28.3 mg/mL Li-TFSI in acetonitrile was spin-coated at 3,000 rpm for 30 s on the perovskite [165]. For the best performing devices, a solution of spiro-MeOTAD in chlorobenzene (90 mg/mL) was prepared containing 45  $\mu\text{L}$  solution of Li-TFSI/acetonitrile (from a solution of 170 mg/mL), and 75  $\mu\text{L}$  of tBP. [49] The spiro-MeOTAD solution was spin-coated on to the perovskite thin film for 30 s at 1,500 rpm. Devices were completed by thermal evaporation of 80 nm of gold (Au) back electrode with a  $0.08\text{ cm}^2$  active area.

### 2.2.2 Thin Film Characterization

A field emission scanning electron microscope (SEM) (Hitachi S-4800) was used to capture SEM images of perovskite thin films which were deposited on meso-porous  $\text{TiO}_2$ . X-ray diffraction patterns for the prepared thin films were recorded (Rigaku Ultima III) from  $10^\circ$  to  $35^\circ$  of  $2\theta$  with 0.02 step size with the scanning speed of  $0.5^\circ$  per second.

### 2.2.3 Device Characterization

J-V characteristics were measured using a Keithley 2440 digital source meter and a solar simulator (Newport model 91195A-1000) which is configured to simulate AM1.5 illumination. A standard Si solar cell was used as a reference to calibrate the exact light intensity.

## 2.3 Exploring the Degree of Conversion

To understand the phase properties of MAPbI<sub>3</sub> perovskite formed in the two-step method, we measured XRD spectra of a spin-coated PbI<sub>2</sub> seed layer on a meso-porous TiO<sub>2</sub> coated substrate and perovskite films synthesized by reacting the seed layer with MAI solution in IPA at different concentrations. The reaction process follows the procedure reported in the literature[26] and detailed description is provided in the Section 2.1. As shown in the Figure 2-2a, the PbI<sub>2</sub> seed layer exhibits a strong preferred orientation along the c-axis of a hexagonal 2H polytype, with the predominant (001) peak at  $2\theta = 12.7^\circ$  and the minor (002) peak at  $25.5^\circ$ . [25] After the reaction, the characteristic features of the tetragonal perovskite phase (space group I4/mcm) appear at  $2\theta$  angles of  $14.1^\circ$ ,  $23.5^\circ$ ,  $24.5^\circ$ , and  $28.5^\circ$ , corresponding to the (110), (211), (202), and (220), planes respectively. [11, 19, 52, 166, 167] However, the reactions are incomplete for most of samples as indicated by the existence of the PbI<sub>2</sub> characteristic peaks.

The resultant film phase composition can be characterized by comparing the peak areas of all the MAPbI<sub>3</sub> and the PbI<sub>2</sub> peaks as a function of the MAI concentration (Figure 2-2b). In the low MAI concentration region ( $< 10$  mg/ml), while the MAPbI<sub>3</sub> perovskite is the primary phase ( $\sim 65\%$ ), the conversion is not complete. With the increasing MAI

concentration, the  $\text{PbI}_2$  residue decreases first and reaches a minimum at 9 mg/ml, but then gradually becomes the primary phase in the intermediate MAI concentration region (10 to 20 mg/ml). Further increasing the MAI concentration ( $> 20$  mg/ml) reverses the trend and results in the perovskite-dominant films. Nearly full conversion of  $\text{MAPbI}_3$  perovskite ( $> 99\%$ ) with negligible  $\text{PbI}_2$  residues ( $< 1\%$ ) outcomes for MAI concentrations above 40 mg/ml. However, the perovskite peak area decreases at 50 mg/ml MAI, which is likely due to the enhanced solubility of perovskite in a solution with high  $\text{I}^-$  concentration.[75] From the observation, it is obvious that the two extremes of the MAI concentrations (8 to 10 mg/ml and 40 to 50 mg/ml) are chosen to fabricate high performance solar cells because the  $\text{PbI}_2$  to  $\text{MAPbI}_3$  perovskite conversion rate is high in those ranges while the intermediate concentrations are not selected because the films are dominated by the  $\text{PbI}_2$  phase.

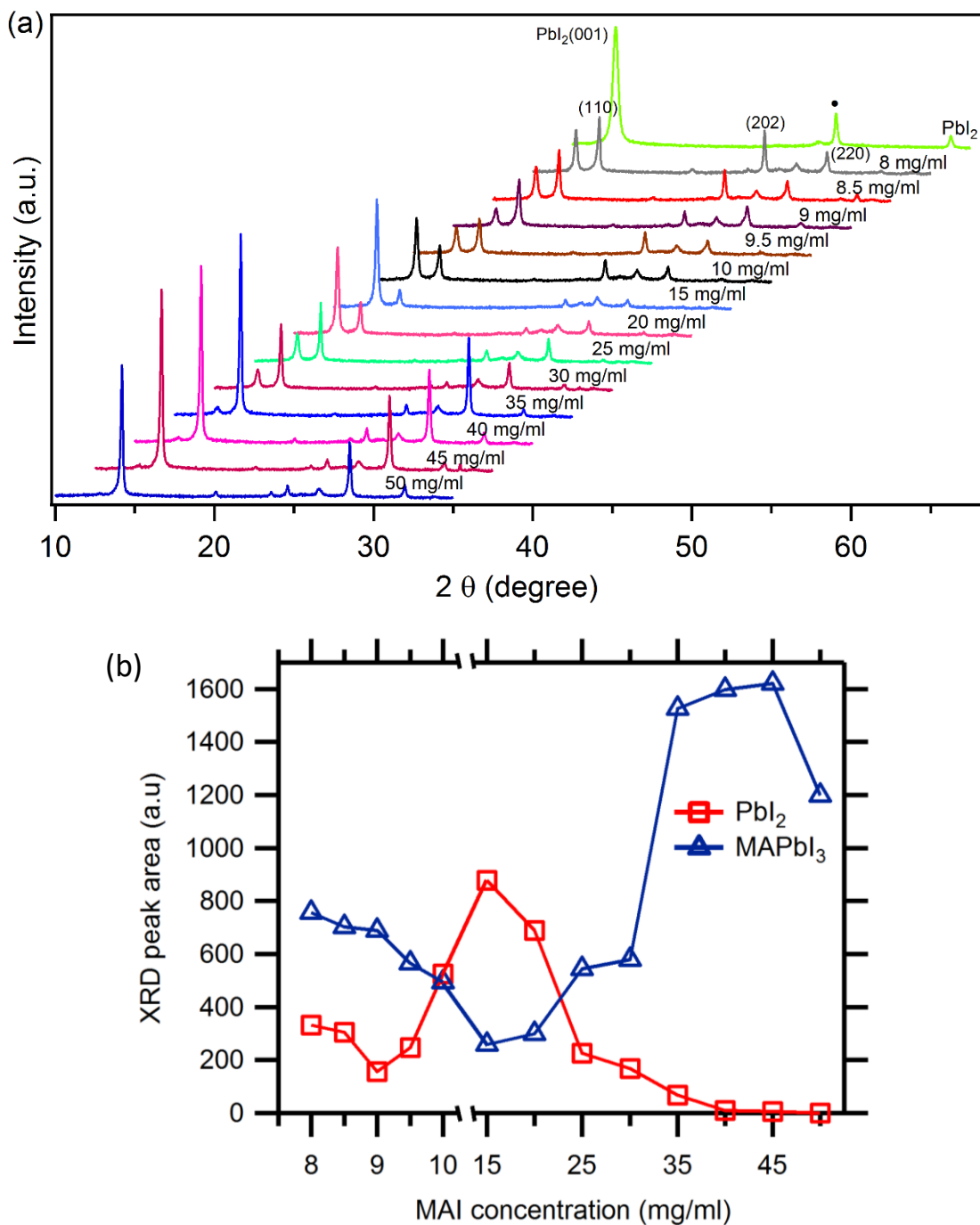


Figure 2-2. (a) X-ray diffraction patterns of  $PbI_2$ , and  $MAPbI_3$  perovskite formed using different MAI concentrations. The solid dot indicates the  $SnO_2(110)$  peak from the FTO substrate.[168] (b) The peak areas of the  $PbI_2(001)$  and summation of the (110), (202), and (220) of the  $MAPbI_3$  perovskite as a function of the MAI concentration.

## 2.4 Grain Size Variation

The variation of the morphology is confirmed by the SEM images (Figure 2-3) of perovskite films prepared with different MAI concentrations. All the perovskite films were converted from a smooth and dense  $\text{PbI}_2$  seed layer (Figure 2-3a). The low MAI concentrations ( $< 10$  mg/ml) result in loosely connected, large-sized, cuboid-shaped perovskite grains (Figures 2-3b-d), while the slightly higher concentrations (10 to 15 mg/ml) lead to dense and small grains (Figures 2-3e & f). In stark contrast to the rough surface with protruding grains formed with the lower MAI concentrations, MAI concentrations above 20 mg/ml show smooth perovskite surfaces (Figures 2-3g-k). Interestingly, the perovskite films prepared from the reaction with the high concentration MAI solutions (e.g. 40 mg/ml) without any thermal treatment contain high contrast, circular shaped structures on the films (Figure 2-3m). These structures, likely corresponding to the low-dimensional perovskite (LDP) phases (vide infra), dismissed after the post annealing at high temperature ( $150$  °C) for a short period of time (5 min), resulting in a smooth surface (Figure 2-3k). The LDP features also appears in the samples resultant from an extremely high MAI concentration (100 mg/ml) (Figure 2-3l), leading to irreversible damages to the film morphology.

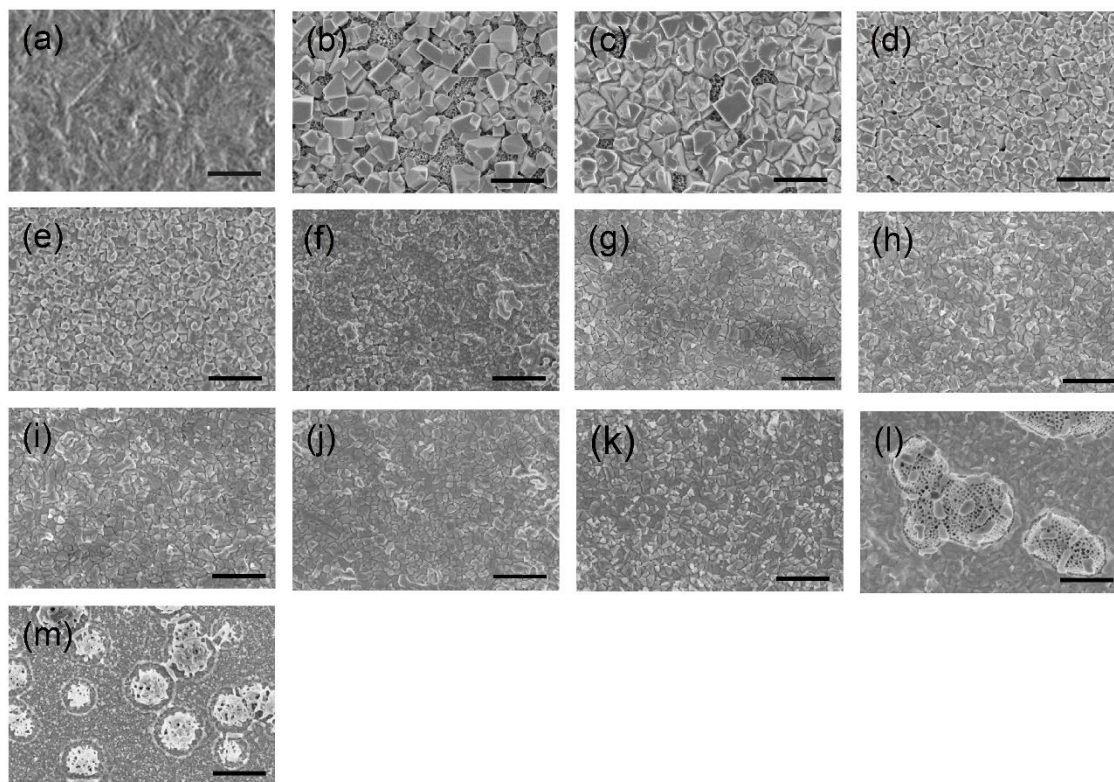


Figure 1-3. SEM images of (a) PbI<sub>2</sub> seed layer and MAPbI<sub>3</sub> films prepared by using the MAI solutions of (b) 5 mg/ml, (c) 8 mg/ml, (d) 9 mg/ml, (e) 10 mg/ml, (f) 15 mg/ml, (g) 20 mg/ml, (h) 25 mg/ml, (i) 30 mg/ml, (j) 35 mg/ml, (k) 40 mg/ml, and (l) 100 mg/ml, respectively. (m) As deposited MAPbI<sub>3</sub> film from a 40 mg/ml solution. Note that the scale bars correspond to 1 μm.

Figure 2-4 plots the average grain sizes extracted from the SEM images using a graphical analysis software (ImageJ). As the MAI concentration increases from 5 to 10 mg/ml, the average grain size decreases from ~400 to ~200 nm. With further increase of the MAI concentration to 15 mg/ml, the grain size decreases to the minimum of ~100 nm. However, at the MAI concentration of 20 mg/ml, a significant increase in the grain size

(~250 nm) is observed and the average grain size remains constant with further increase of the MAI concentration.

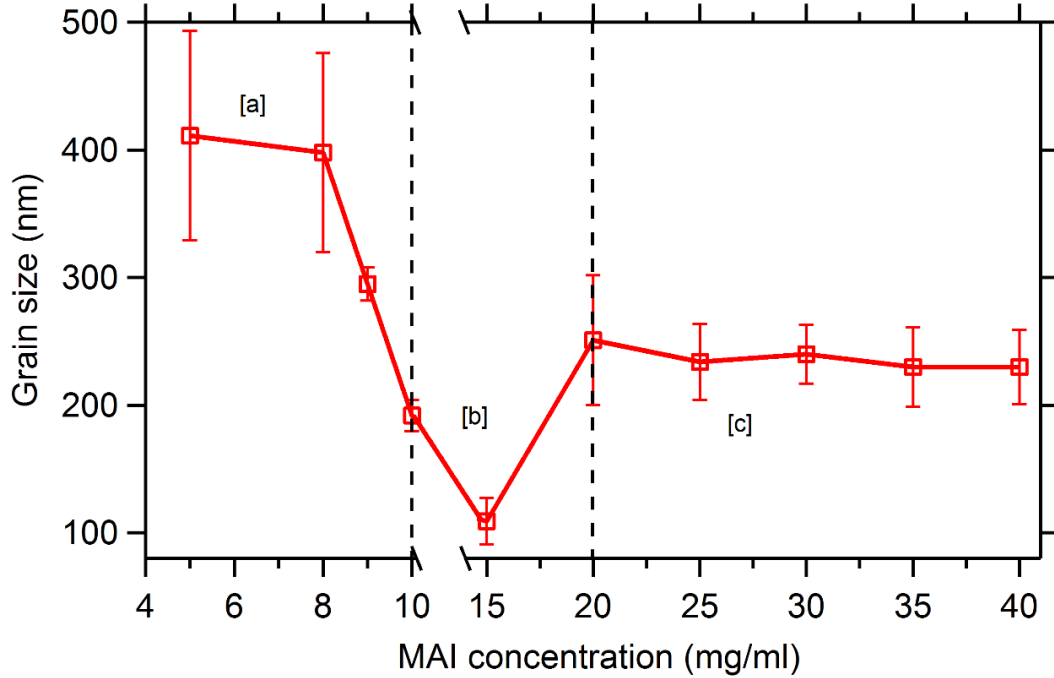
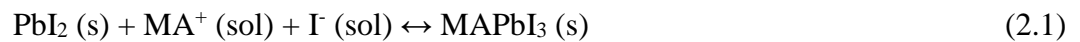


Figure 2-4. Average grain size variation with the MAI concentration. Labels form a to c represent the schematics in figure 2-6.

## 2.5 Change of Gibbs Free Energy

The change of grain size as a function of the MAI concentration can be understood by considering the change of Gibbs free energy of the system. In the MAI intercalation process, the formation of MAPbI<sub>3</sub> on the PbI<sub>2</sub> surface occurs immediately after the introduction of the MAI solution. The reaction between the PbI<sub>2</sub> seed layer and the MAI solution can be described by the formation reaction as below.[56, 75]



Considering the nucleation of perovskite, the total Gibbs free energy change is a superposition of the bulk free energy and the surface free energy of the perovskite nucleus. In general, the free energy change for the formation of a perovskite nucleus with a size of  $r$  can be represented as [169, 170]

$$\Delta G_{Total} = ar^3\Delta G_v + br^2\gamma \quad (2.2)$$

where  $\Delta G_v$  is the bulk free energy per unit volume,  $a$  and  $b$  are structural coefficients determined by the shape of the nucleus (e.g.  $a = 4\pi/3$  and  $1$  for spherical and cubic shapes, respectively), and  $\gamma$  is the sum of surface tensions. Since the formation of perovskite is not from the condensation of its liquid phase but from a reversible reaction in the solution (Eq. 1), the reaction quotient (as expressed by the concentration ratio) has to be considered in the bulk free energy change  $\Delta G_v$ , as described in the equation [171]

$$\Delta G_v = \Delta G^0 + RT \ln \frac{[MAPbI_3]}{[PbI_2][MAI]} \quad (2.3)$$

where  $R$  is the universal gas constant, and  $T$  is the reaction temperature. The critical size  $r^*$ , which is inversely proportional to  $\Delta G_v$ , thus can be deduced by setting the first derivative of total free energy (Eq. 2) to zero.

$$(r^*) = -\frac{2b\gamma}{3a} \frac{1}{\Delta G_v} \quad (2.4)$$

### 2.5.1 $CH_3NH_3^+$ cation concentration in solid $CH_3NH_3PbI_3$ perovskite and MAI solution

- Consider the tetragonal unit cell for  $CH_3NH_3PbI_3$  perovskite with  $a = 8.844 \text{ \AA}$  and  $c = 12.588 \text{ \AA}$ .
- The unit volume =  $4.06 \times 10^{-27} \text{ m}^3$
- Total number of  $CH_3NH_3^+$  cations per unit volume = 4

- So,  $\text{CH}_3\text{NH}_3^+$  cation concentration (per volume) in the  $\text{CH}_3\text{NH}_3\text{PbI}_3$  perovskite ( $C_0$ )  
 $= 9.85 \times 10^{26}$  molecules/ $\text{m}^3$

The  $\text{CH}_3\text{NH}_3^+$  cation concentrations ( $C$ ) in MAI solution for different MAI concentrations are shown in the table 2.1.

Table 2.1:  $\text{CH}_3\text{NH}_3^+$  cation concentrations ( $C$ ) in MAI solution for different MAI concentrations.

MAI concentration (mg/ml)	$\text{CH}_3\text{NH}_3^+$ cation concentration (molecules/ $\text{m}^3$ )
8	$8.39 \times 10^{23}$
8.5	$8.91 \times 10^{23}$
9	$9.43 \times 10^{23}$
9.5	$9.96 \times 10^{23}$
10	$1.05 \times 10^{24}$
15	$1.57 \times 10^{24}$
20	$2.10 \times 10^{24}$
25	$2.62 \times 10^{24}$
30	$3.14 \times 10^{24}$
35	$3.67 \times 10^{24}$
40	$4.19 \times 10^{24}$
45	$4.72 \times 10^{24}$
50	$5.24 \times 10^{24}$

## 2.6 Nucleation and Growth Mechanism

In the low MAI concentration region, Ostwald ripening[172] becomes the dominant reaction mechanism for the formation of perovskites. The newly formed perovskite nuclei with a size smaller than  $r^*$  will dissolve into the solution and redeposit onto large crystals

(Figure 2-5a). As the MAI concentration increases,  $\Delta G_v$  becomes more negative, indicating a stronger driving force for the perovskite formation and a reduced critical size. Therefore, a large population of perovskite nuclei are likely to form and grow up. This leads to perovskite films with an increased nucleation density and smaller grain size (Figure 2-5b).

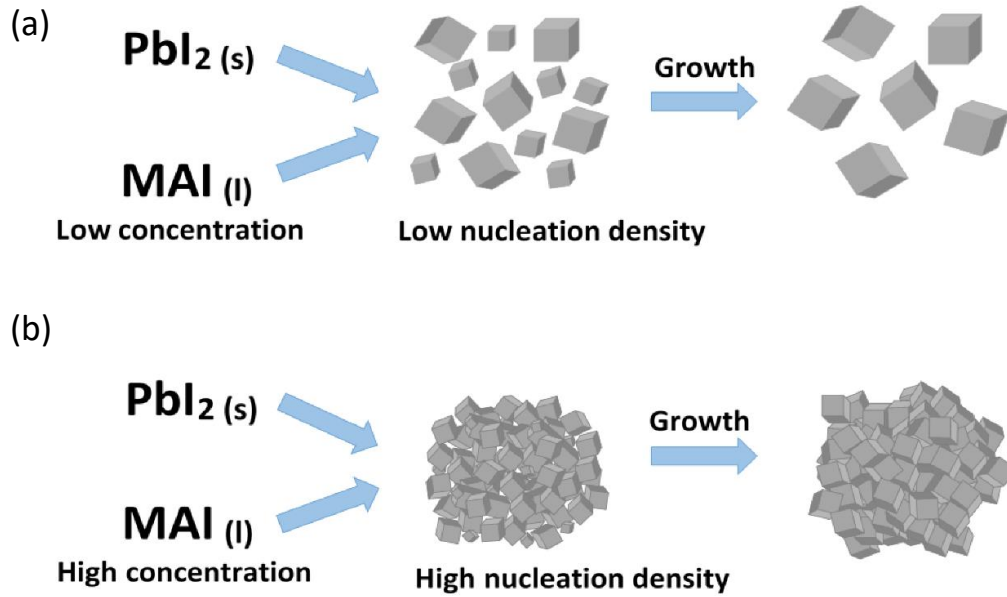


Figure 2-5. Nucleation and growth process for MAPbI<sub>3</sub> perovskite with low (a) and High (b) concentration of MAI solution.

The high driving force at the relatively higher MAI concentration may lead to a rapid formation of a large number of perovskites grains on the PbI<sub>2</sub> surface. In the perovskite crystal structure, the MA<sup>+</sup> cations are rigidly bounded to PbI<sub>3</sub><sup>-</sup> octahedra due to the Coulomb interaction, leaving no free space for mobile ions to diffuse. Additionally, perovskite, if regarded as a MAI intercalated PbI<sub>2</sub> network, contains higher CH<sub>3</sub>NH<sub>3</sub><sup>+</sup> and I<sup>-</sup> concentrations than that in the MAI solution, which would generate a blocking barrier for MAI diffusion at the liquid-solid interface (Figure 2-6b and Table 2.1 in the section

2.5.1). Thus, the  $\text{MA}^+$  and  $\text{I}^-$  ions in the solution are isolated from the underlying  $\text{PbI}_2$  and perovskite conversion halts at an early stage.

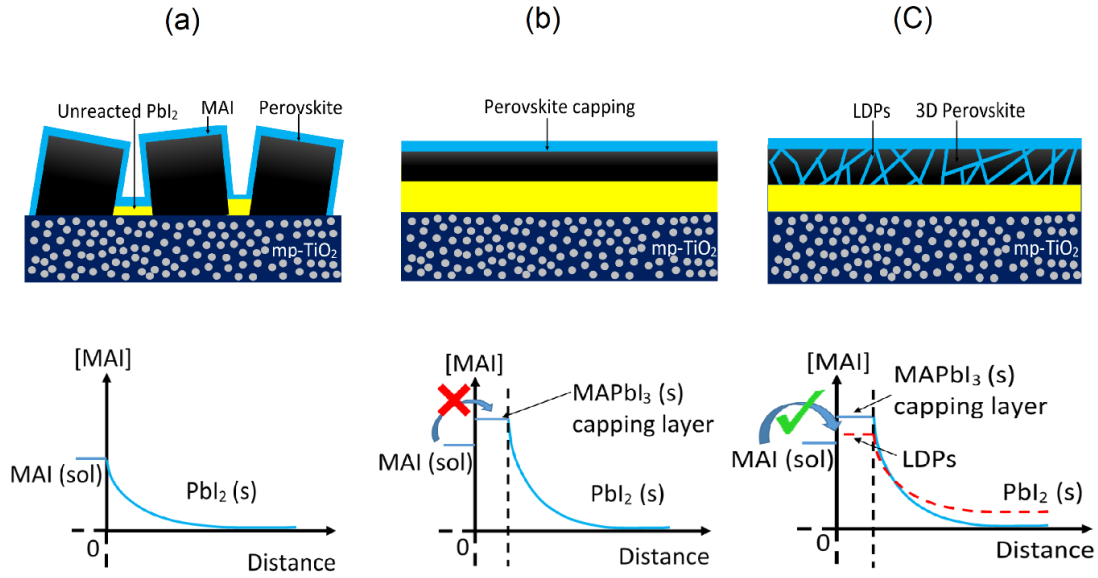


Figure 2-6. Schematics of the  $\text{MAPbI}_3$  perovskite growth under different conditions. (a) In the low MAI concentration region ( $<10$  mg/ml), the formation of large and loosely connected grains allows MAI diffusion through the voids between grains. (b) In the intermediate concentration region (10 to 20 mg/ml), the formation of  $\text{MAPbI}_3$  capping layer on the  $\text{PbI}_2$  seed layer and block the MAI diffusion. (c) In the high MAI concentration region ( $> 20$  mg/ml), the formation of a LDPs opens the pathway for the MAI diffusion. The figures in the bottom row depict the qualitative change of MAI concentration as a function of distance from the top of the film.

Interestingly, perovskite nucleation and growth behavior seems quite different with further increase of MAI concentrations ( $> 20$  mg/ml). The significant increase of grain size after the 15 mg/ml (Figure 2-4) does not follow the free energy explanation. Furthermore, the fraction of  $\text{PbI}_2$  decreases and the perovskite phase becomes the predominant phase

(Figure 2-2b). These results show that the increase of the MAI concentration overcomes the blocking layer and facilitates the perovskite crystallization and growth. The mechanism of such nucleation and growth behavior may attribute to the formation of LDPs with excess MAI.[7, 47] Our previous study on the MAPbI<sub>3</sub> perovskite phase and processing diagram reveals that the LDP phases are formed in a MAI-rich perovskite composition.[47] Here, when the polycrystalline perovskite grains are exposed to the solution with a high MAI concentration, LDPs are likely formed on the surface of the grains (or grain boundaries) of the perovskite where the local MAI concentration is higher than that in the bulk perovskite (Figure 2-6c).

The formation of LDPs was confirmed in both XRD and SEM analysis when the high MAI concentration was applied (Figures 2-7 and 2-3i & m).

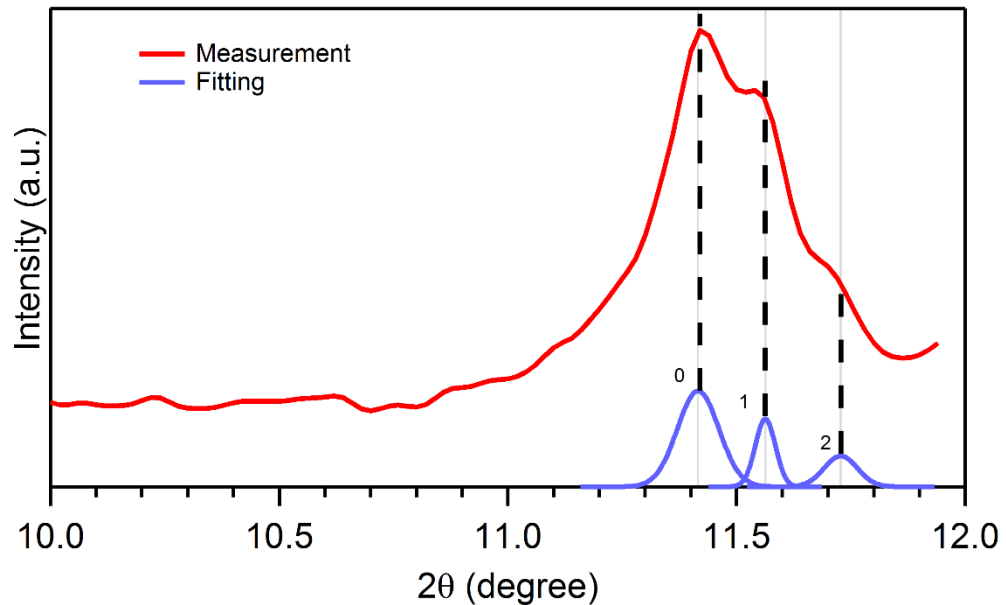


Figure 2-7. XRD spectrum for an as-deposited MAPbI<sub>3</sub> perovskite from a 50mg/ml MAI solution. Peaks at 11.41<sup>o</sup>, 11.56<sup>o</sup>, and 11.72<sup>o</sup> were matched with the LDP peaks that we observed in our pervious study.[47]

The crystal structure of LDP phases consists of lead iodide nanostructures (e.g. dots, wires, and sheets) wrapped by an organic MA<sup>+</sup> matrix, where the MA<sup>+</sup> are loosely bounded (Figure 2-8).

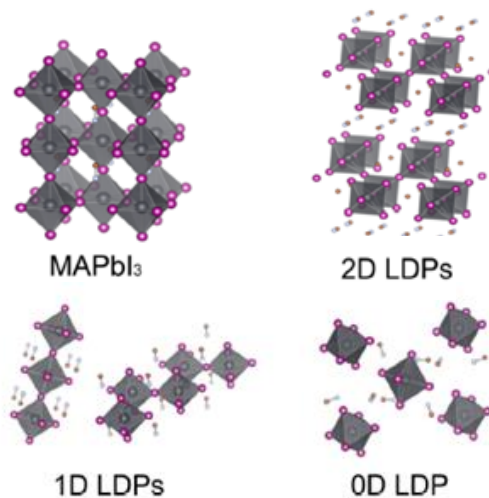


Figure 2-8. MAPbI<sub>3</sub> perovskite structure and its LDPs. Reprinted with permission from Ref.[47]. Copyright 2015 American Chemical Society.

The MA<sup>+</sup> in the LDPs are mobile and may vary with the change of the composition. Therefore, these LDPs grain boundaries enable the diffusion of MA<sup>+</sup> and I<sup>-</sup> ions. As previously shown, the number of LDPs increases with increasing MAI concentration. Thus, the conversion of perovskite can be completed within a short time when the MAI concentration is sufficiently high. In our experiment, we verified that 20 s reaction time, which is commonly used by others,[26] is enough for the complete perovskite conversion. A longer reaction time may result in the delamination of the films due to the dissolving of the perovskite[75]. This diffusion mechanism of MAI molecules is similar to incorporating additives, such as H<sub>2</sub>O and DMSO into the PbI<sub>2</sub> seed layer to improve the conversion,[55,

78] while could be potentially better since no external impurities are introduced to the films. Furthermore, this is also consistent with the diffusion of water molecules in hydrated MAPbI<sub>3</sub> perovskite thin films.[173]

Understanding the perovskite formation mechanism with a high MAI concentration may potentially provide an easy route to prepare a uniform thick perovskite film. To verify the idea, we prepared a thick perovskite film with the help of LDPs. Here, a thick PbI<sub>2</sub> film (~350 nm) was first reacted with a 35 mg/ml MAI solution to form a stack of LDP-MAPbI<sub>3</sub>/PbI<sub>2</sub> (Figure 2-6c). Then a 15 mg/ml MAI solution, which showed the lowest PbI<sub>2</sub> conversion itself, was used to react with the composite film. The XRD spectra (Figure 2-9) showed an almost complete perovskite conversion, indicating that a controllable conversion of perovskite films is potentially achievable by multiple-time spin coating of MAI solution.[56]

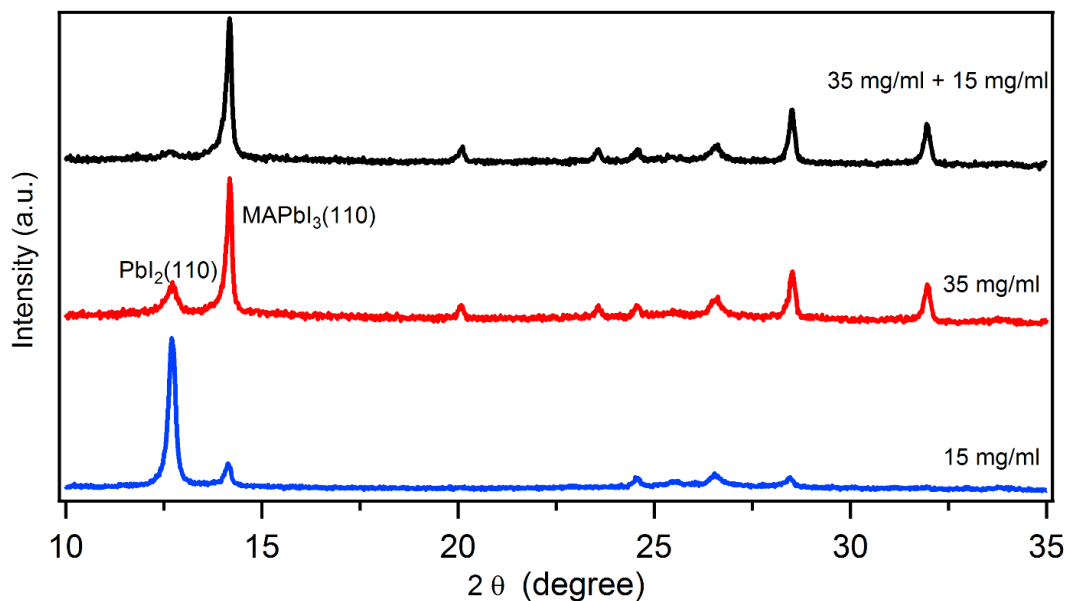


Figure 2-9. X-ray diffraction patterns for the perovskite film prepared by sequentially spins of the 35 and 15 mg/ml MAI solutions and those prepared by a single spin of 35 mg/ml and 15 mg/ml solutions.

For the perovskite films prepared using solutions with high MAI concentrations, the annealing process is critical to convert all the LDPs into perovskite structure and to achieve desired electronic properties.[47] The LDPs formed at MAI concentrations higher than 15 mg/ml (Figure 2-6c) are converted to MAPbI<sub>3</sub> perovskite with the post deposition annealing (Figures 2-2k&m). This is likely to be the reason for the grain size enhancement for MAI concentrations above 20 mg/ml. Since the post annealing treatment is similar for all of the concentrations, the average size of grains does not change significantly in high MAI concentrations (> 20 mg/ml) (Figures 2-3 and 2-4).

## **2.7 Impact on Device Performances**

To study the effect of the phase and morphology of perovskite films on the photovoltaic device performance, we fabricated perovskite solar cells using the two-step method. In these devices, Poly(3-hexylthiophene) (P<sub>3</sub>HT) was used as the hole-transporting material (HTM) because it is sensitive to the morphology, porosity, and grain size of the perovskite films.[174] Figure 2-10 shows the MAI concentration dependent variations of the critical parameters of PV devices, including power conversion efficiency (PCE), short-circuit current density (J<sub>SC</sub>), fill factor (FF) and open-circuit voltage (V<sub>OC</sub>) for devices prepared under two different annealing conditions (150 °C for 5 min and 100 °C for 15 min). The highest device efficiency of around 9% was achieved at both low (9 mg/ml) and high (40 mg/ml) concentrations, while the intermediate concentration (15 mg/ml) result in the lowest efficiency of less than 2%. The low efficiency is likely due to the incomplete perovskite conversion which significantly affect the total light absorption and the series

resistance, resulting in a reduction of  $J_{SC}$  and FF. Moreover, the differences in size of the grains and the film morphology cause performance discrepancy.

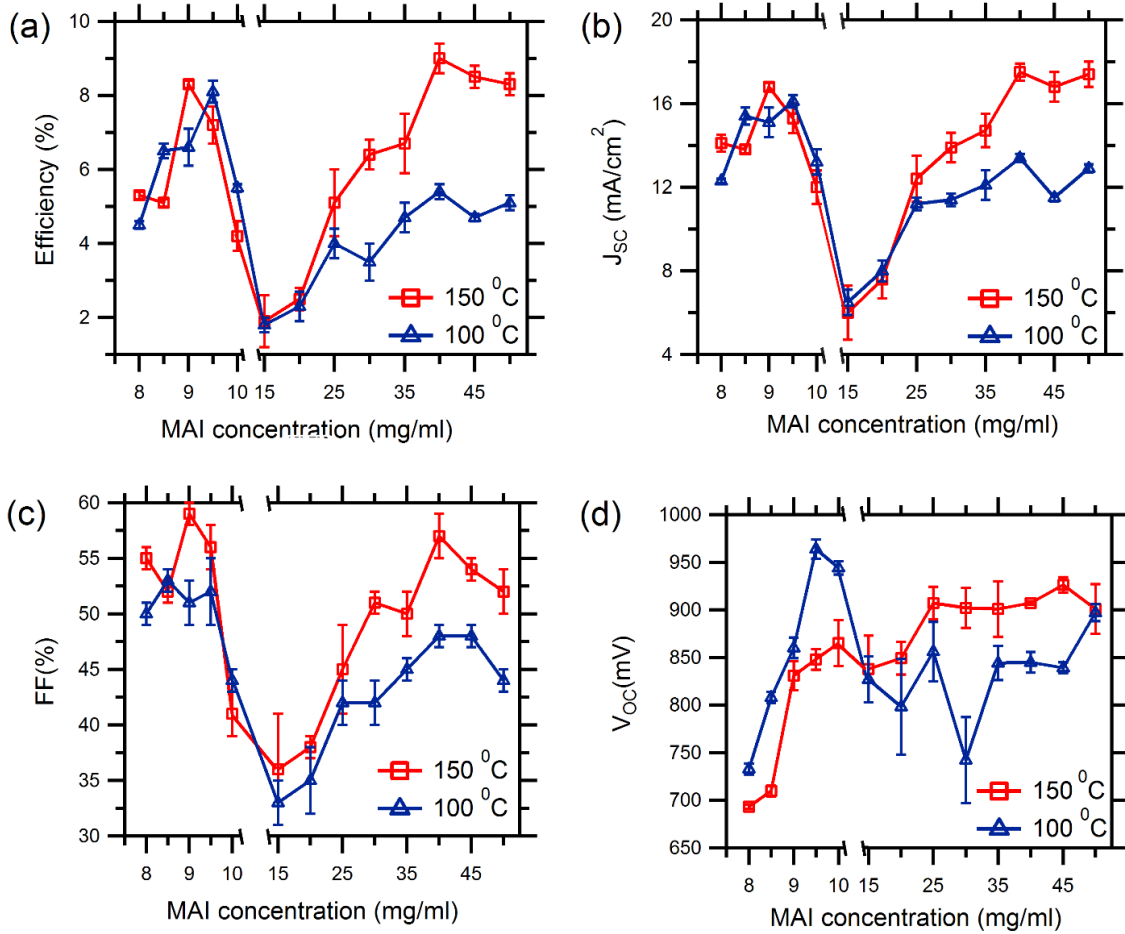


Figure 2-10 Effect of the MAI concentration and the post annealing condition on critical parameters of (a) PCE, (b)  $J_{SC}$ , (c) FF and (d)  $V_{OC}$  under a standard AM 1.5G illumination (100 mW/cm<sup>2</sup>). Note that the average values were derived from measurements on more than 20 devices.

The devices with large sized cuboids formed in a low MAI concentration solution (e.g. 9 mg/ml) show higher values of  $J_{SC}$  and FF than that with a similar phase composition

but prepared in a higher MAI concentration (30 mg/ml), which is likely due to the increased light scattering[175] and a lower grain boundary density[26].

Post deposition annealing temperature also influences on the device performance. The perovskite devices annealed at 100 °C show similar variation of the device performance parameters as a function of the MAI concentration. However, in the high MAI concentration region, the devices annealed at 100 °C performed more poorly than those annealed at 150 °C due to the residual LDP structures which are stable at a temperature below 150 °C.[47]

Our best performing devices were prepared using 2,2',7,7'-tetrakis(N,N-di-p-methoxy-phenylamine)-9,9'-spirobifluorene (spiro-MeOTAD) as the HTM. The best efficiency of 10.8%, with 1020 mV  $V_{OC}$ , 17.0 mA/cm<sup>2</sup>  $J_{SC}$ , and 62.5% FF was achieved with the MAPbI<sub>3</sub> films prepared using the 9.5 mg/ml MAI solution (Figure 2-11). Comparably, a competitive efficiency of 10.7%, with 1022 mV  $V_{OC}$ , 16.1 mA/cm<sup>2</sup>  $J_{SC}$ , and 65.4% FF was achieved at the MAI concentration of 40 mg/ml. This demonstrates that both low and high MAI concentrations can be used for fabricating high performance perovskite devices in the n-i-p structure.

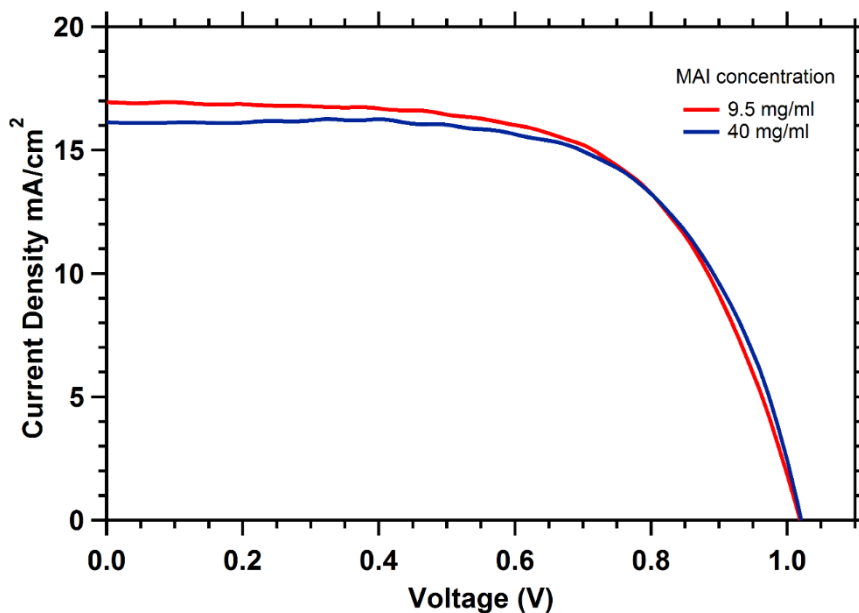


Figure 2-11 Current voltage (J-V) characteristics for the best devices (with spiro-MeOTAD) under a standard AM 1.5G illumination ( $100 \text{ mW/cm}^2$ ).

## 2.8 Conclusion

In conclusion, we have demonstrated the conversion rate, grain size, and morphology of  $\text{MAPbI}_3$  perovskites formed in the two-step methods depend on the concentration of the MAI solution. We showed that in the two-step solution process, the perovskite formation behaviors are dominated by Ostwald ripening, the blocking layer formation, and the LDPs formation when reacting with the MAI solution with various concentrations. The formation of the LDPs grain boundaries which facilitates the MAI diffusion and improves the perovskite conversion may be used to prepare thick and uniform perovskite films. With the assistance of LDPs, we were able to prepare conformal and dense films of phase pure perovskite. High efficiency devices were achieved by using both low concentration and high concentration MAI solutions. This indicates the two-step

method can be used to prepare high performance perovskite devices by manipulating the MAI concentration.

## Chapter 3

### **Enhanced Grain Size, Photoluminescence, and Photoconversion Efficiency with Cadmium Addition During the Two-Step Growth of Methylammonium Lead Iodide**

Control over grain size and crystallinity is important for preparation of methylammonium lead iodide (MAPbI<sub>3</sub>) solar cells. In this chapter, we explore the effects of using small concentrations of Cd<sup>2+</sup> and unusually high concentrations of methylammonium iodide (MAI) during the growth of MAPbI<sub>3</sub> in the two-step solution process. In addition to improved crystallinity and an enhancement in the size of the grains, time resolved photoluminescence measurements indicated a dramatic increase in the carrier lifetime. As a result, devices constructed with the Cd-modified perovskites showed nearly a factor of two improvement in the power conversion efficiency (PCE) relative to similar devices prepared without Cd addition. The grains also showed a very higher degree of orientation in the <110> direction, indicating a change in the growth mechanism, and the films were compact and smooth. We propose a Cd-modified film growth mechanism that invokes a critical role for low dimensional Cd perovskites to explain the experimental observations.

### 3.1 Introduction and Motivation

Thin film solar cells based on organic-inorganic metal halide perovskites have become highly attractive over the past several years with solar to electric power conversion efficiencies (PCEs) reaching 22.1%. [17] Methylammonium lead iodide ( $\text{CH}_3\text{NH}_3\text{PbI}_3$ ,  $\text{MAPbI}_3$ ), and related perovskite materials possess high absorption coefficients, long minority carrier lifetimes and diffusion lengths, desirable optical band gaps, and carrier collection can be highly efficient when these materials are paired with appropriate electron and hole transport materials (ETMs and HTMs, respectively). [1, 25, 26, 30, 66, 159] Moreover,  $\text{MAPbI}_3$  solar cells can be fabricated via solution-based routes, with the potential for low-cost scale-up to large area manufacturing. This combination of attributes may give perovskite solar cells (PSCs) an advantage over currently available commercial photovoltaic (PV) technologies. Importantly, recent life cycle assessment studies show that the toxicity impact of the lead used in the formation of the absorber layer is negligible [122] and that perovskite solar modules possess the shortest energy payback time. [121]

Several challenges must be overcome before the full potential of PSCs can be realized. Composition control is important to avoid the presence of undesirable phases, [47, 69] and morphology control is desired to achieve smooth, continuous, and compact perovskite films to avoid shunts and reduce surface recombination rates. [175, 176] Control over grain size and crystallinity is extremely important for reducing the density of charge traps which can control the recombination rates of photoexcited carriers. [43, 177]

The development of the two-step deposition method by Burschka et al. was a major advance in perovskite film formation. [25] In their pioneering work, a  $\text{PbI}_2$  layer was spin-coated from a dimethylformamide (DMF) solution onto a mesoporous  $\text{TiO}_2$  film and then

converted to MAPbI<sub>3</sub> by exposure to methylammonium iodide (MAI). With this approach the PCE of MAPbI<sub>3</sub> perovskite solar cells was immediately improved from 12 to 15%. [25] The approach relied upon the formation of a thin (150 – 300 nm) mesoporous TiO<sub>2</sub> layer with high transparency and electron mobility. Such films are a by-product of tremendous research in the dye sensitized solar cell community and have been achieved in only a few labs. [25] [40] [26] [57] PCEs have been pushed to 17% with this approach in the basic MAPbI<sub>3</sub> device. [26] An optimized mesoporous TiO<sub>2</sub> scaffold allows the PbI<sub>2</sub> solution to partially penetrate so that a high surface area PbI<sub>2</sub> film can be formed. Such a film can be converted into the perovskite phase upon exposure to MAI, although the resultant grains are still relatively small (c.a. 100 – 300 nm). In an effort to produce high efficiency devices in the so-called planer structure, i.e. without fabrication of the mesoporous TiO<sub>2</sub> layer, investigators have engineered porosity into the PbI<sub>2</sub> layer by adding n-butanol, [77] MAI, [53] or 4-tert-butylpyridine [54] to the PbI<sub>2</sub>/DMF precursor solution, or by employing DMSO as a solvent. [55] The resulting high surface area porous PbI<sub>2</sub> layers can also be readily converted to MAPbI<sub>3</sub> but, once again, the resultant grains are not as large as desired. Even with porous layers there is a need to balance the degree of PbI<sub>2</sub> conversion while seeking to avoid the formation of MAI-rich precipitates that lead to poor device behavior. Consequently, researchers typically use MAI concentrations of 50–70 mM to optimize the PCE. [53, 54, 77] Without porosity in the PbI<sub>2</sub> layer, MAI diffusion is hindered and the conversion to MAPbI<sub>3</sub> is incomplete. [54, 75] Interestingly, Zhang et al. produced devices with PCEs of 1.5% or 10.7% depending on whether the PbI<sub>2</sub> seed layer was compact or porous. [54]

In an effort to decouple the perovskite conversion process from the need to prepare  $\text{PbI}_2$  in a porous configuration, we explored the effects of including small concentrations of  $\text{Cd}^{2+}$  into unusually high concentration MAI (250 mM) solutions.

This idea was originally begun with the observation of impressive grain size enhancement when we prepared perovskite films on a cadmium sulfide (CdS) layer. We had been trying to replace the  $\text{TiO}_2$  ETL layer using CdS, and these perovskite devices were fabricated in the structure of  $\text{SnO}_2\text{:F}/\text{CdS}/\text{MAPbI}_3/\text{spiro-MeOTAD}/\text{Au}$ . Once we characterized the surface morphology of the perovskite films that fabricated on the CdS layer, a tremendous improvement in the grain sized was observed (Figure 3-1). Since all the processing are similar, we speculated that the grain size improvement may be due to the incorporation of  $\text{Cd}^{2+}$  in the nucleation and growth process of the perovskite formation. We then tested perovskite film formation on a  $\text{TiO}_2$  layer with the addition of  $\text{Cd}^{2+}$ , which was introduced by adding a small amount of  $\text{CdCl}_2$  in to the MAI solution.

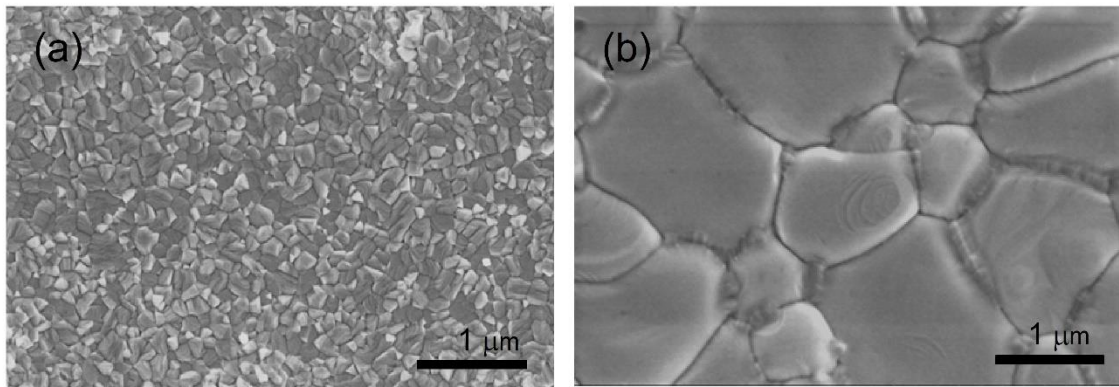


Figure 3-1. Surface SEM images of  $\text{MAPbI}_3$  films prepared on a  $\text{TiO}_2$  layer and a CdS layer using the two-step sequential deposition method.

We found that the large grains could be retained by including small concentrations of  $\text{CdCl}_2$  into the MAI solutions, and that a high degree of  $\text{PbI}_2$  conversion could be achieved without the formation of deleterious MAI-rich precipitates. In addition, the solution-phase Cd incorporation route also led to a dramatic enhancement in the carrier lifetime as determined by time resolved photoluminescence (TRPL) measurements. As a result, the PCE of finished devices was enhanced by nearly a factor of two relative to devices constructed without Cd addition. The grains also showed a very high degree of orientation in the  $\langle 110 \rangle$  direction, and the films were more compact and smooth. To explain the experimental results, we propose a film growth mechanism that invokes a critical role for low dimensional Cd perovskites.

## **3.2 Experimental Details**

### **3.2.1 Perovskite Films Preparation**

1 in. X 1 in. FTO coated glass substrates (TEC 15, Pilkington) were cleaned in an ultrasonic bath with Micro-90 detergent for 1 h and then rinsed for 1 h in de-ionized water. The samples were thoroughly dried using nitrogen gas and transferred to a nitrogen filled glove box with ( $\sim 0.1$  ppm  $\text{H}_2\text{O}$  and  $\text{O}_2$ ). An  $\sim 50$  nm thick compact  $\text{TiO}_2$  film was prepared by spinning a 0.3 M titanium diisopropoxide bis (acetylacetonate) in ethanol onto the FTO substrates. The deposited layer was dried at  $125^\circ\text{C}$  for 5 min and then annealing at  $500^\circ\text{C}$  for 30 min in air.[164] The  $\text{MAPbI}_3$  perovskite layer was formed by reacting a  $\text{PbI}_2$  seed layer with a 250 mM solution of MAI in IPA. A mixture of MAI (250 mM) and  $\text{CdCl}_2$  (7.5 mM, 10 mM, and 15 mM) in IPA was used in the Cd-assisted deposition. The  $\text{PbI}_2$  layer was deposited by spin-coating a hot ( $\sim 70^\circ\text{C}$ ) solution of 1 M  $\text{PbI}_2$  in anhydrous DMF at

5000 rpm for 30 s, followed by drying at 100 °C for 15 min. After cooling to room temperature, the MAI-IPA solution (with and without CdCl<sub>2</sub>) was preheated to 70 °C and spin-coated onto the PbI<sub>2</sub> layer. The reaction was completed by heating to 150 °C for 5 min on a hot plate.

### 3.2.2 Thin Film Characterization

SEM (Hitachi S-4800) images and XRD (Rigaku Ultima III) spectra were gathered from films prepared on FTO/glass substrates that were coated with a compact TiO<sub>2</sub> layer. Films were directly deposited onto soda-lime glass substrates to obtain UV-vis absorption (PerkinElmer Lambda 1050), PL, TRPL data of MAPbI<sub>3</sub> films and XRD of (MA)<sub>2</sub>CdI<sub>4</sub> LDPs.

Steady state photoluminescence measurements were obtained at several locations on the MAPbI<sub>3</sub> samples with 532 nm CW excitation from the film side (laser spot size of ~140 μm, integration time of 0.5 s, laser intensity of 140 mW/cm<sup>2</sup>) at room temperature. The PL signal was detected with a Symphony II CCD detector (Horiba) after a 300 g/mm grating monochromator. Time resolved photoluminescence measurement at different locations of the samples were performed with a time correlated single photon counting module (Becker & Hickel Simple Tau SPCM 130-E/M module). A 532 nm pulsed laser (beam diameter of ~100 μm micron) was used as a source of excitation. Samples were excited with ~10<sup>10</sup> photons/pulse/cm<sup>2</sup> at the peak emission wavelength, as determined from the steady-state PL measurement. The PL signal was detected by PMT hybrid detector after a Horiba IHR 320 monochromator (900 g/mm, 850 nm blaze) grating. Decay curves were fitted to a bi-exponential decay function.

### 3.2.3 Device Preparation

After deposition of the compact TiO<sub>2</sub>, an ~150 nm thick mesoporous TiO<sub>2</sub> layer was deposited by spin-coating a diluted TiO<sub>2</sub> paste (Dyesol 18NR-T) in ethanol (1:7 w/w) at 5,000 rpm for 30 s. The deposit was dried at 125 °C for 5 min prior to annealing in air at 550 °C for 30 min. Then MAPbI<sub>3</sub> absorber was formed using the two-step solution method as described above. The hole transport layer was made by dissolving 73.3 mg of 2,2',7,7'-tetrakis(N,N-di-p-methoxy-phenylamine)-9,9'-spirobifluorene (Spiro-MeOTAD) in 1 ml of chlorobenzene with two additives; a 28.8 μL aliquot of tert-butylpyridine and a 17.6 μL aliquot of a lithium bis(trifluoromethanesulfonyl)imide (Li-TFSI) solution in acetonitrile. The latter was obtained from a stock solution (520 mg Li-TFSI /mL). The film was formed by spinning 80 μL of the mixture at 3,000 rpm for 30 s on the perovskite layer. Finally, devices were completed by depositing 40 nm of gold as a back electrode with a 0.08 cm<sup>2</sup> active area using thermal evaporation.

### 3.2.4 Device Characterization

J-V characteristics were measured under simulated AM1.5G illumination using a Keithley 2440 digital source meter and a solar simulator (Newport model 91195A-1000). The light intensity of the simulator was calibrated using a standard Si solar cell. The external quantum efficiency (EQE) measurements were acquired from wavelength range of 300-800 nm using a PV measurements Inc., model IVQE8-C QE system without bias voltage.

### 3.3 Grain Size Enhancement with the Addition of CdCl<sub>2</sub>

Figure 3-2 compares the SEM images of the films formed with and without 10 mM CdCl<sub>2</sub> in the MAI solution that was used to convert the PbI<sub>2</sub> seed layer. Note that other concentrations were also examined, but 10 mM CdCl<sub>2</sub> was found to produce the best results (see the Appendix B). The effect of the CdCl<sub>2</sub> addition is evident in that well defined, large grains are present in the Cd incorporated samples (Cd\_MAPbI<sub>3</sub>) immediately after spinning, while samples prepared without CdCl<sub>2</sub> show poorly defined and poorly crystalline films with obvious gaps between grains. The inclusion of 10 mM CdCl<sub>2</sub> increased the grain sizes fivefold, from ~200 nm to ~1 μm. After the 150 °C step that is conventionally used to complete the perovskite formation in the two-step process, SEM showed that the crystallinity in the samples formed without CdCl<sub>2</sub> (Figure 3-2e) had improved dramatically even though the grain size was not substantially increased. Similarly, the grain size of the as-deposited film produced with CdCl<sub>2</sub> was also not substantially increased with the 150 °C reaction step (Figure 3-2f). However, there is evidence for smaller grains having merged into larger ones, and the spaces between grains have been more completely filled and the film is more dense and compact. An additional significant change is the improved electrical conductivity at the grain boundary edges. Before heating, Cd\_MAPbI<sub>3</sub> films showed high contrast at the grain edges, consistent with charging during SEM imaging.

Cross-sectional SEM images revealed that single, flat-topped grains extended through the entire film thickness when CdCl<sub>2</sub> was employed (Figure 3-2d & h), while the grains were jumbled and less well organized for the conventional MAPbI<sub>3</sub> synthesis (Figure 3-2c & g). The cross-sectional images also revealed that the film thickness had also

increased by ~100 nm when Cd was used. Evidently, Cd incorporation improves grain growth in both lateral and vertical directions, resulting in the formation of a larger volume of perovskite material. This result is consistent with the UV-vis absorbance spectra (Figure 3-3), in which the Cd-modified film shows the strongest absorption at the perovskite band edge (~750 nm).

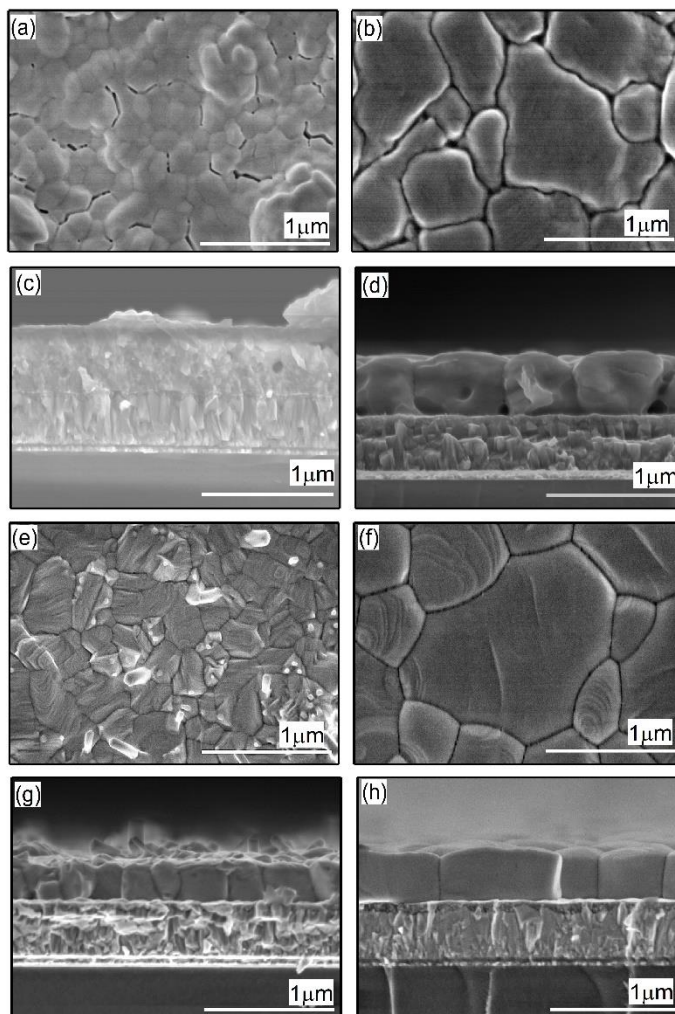


Figure 3-2. SEM images of the surface of as-spun  $\text{MAPbI}_3$  thin films prepared (a) without and (b) with 10 mM  $\text{CdCl}_2$  addition to the MAI solution. (c and d) Cross-sectional view of the as-spun  $\text{MAPbI}_3$  perovskite films that display in the panels of (a) and (b), respectively. Panels (e) and (f) show the data corresponding to (a) and (b), respectively, after heating to

150 °C. (g and h) Cross-sectional view of the MAPbI<sub>3</sub> perovskite films that display in the panels of (e) and (f), respectively.

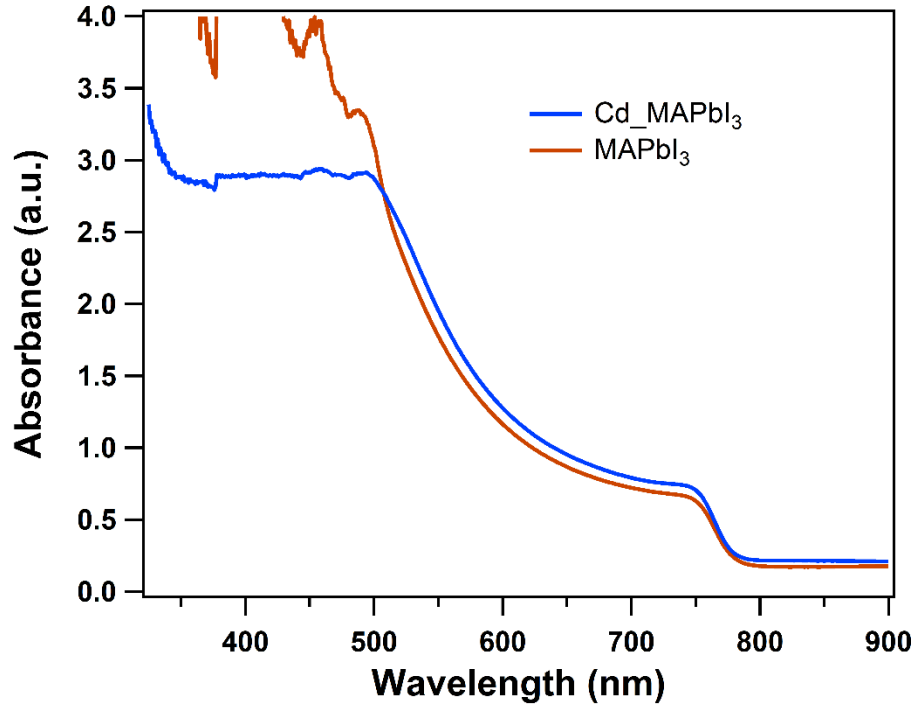


Figure 3-3. UV-vis absorbance spectra of standard (MAPbI<sub>3</sub>) and Cd-modified perovskite (Cd\_MAPbI<sub>3</sub>) thin films.

### 3.4 Improved Degree of Crystallinity and Preferred Orientation

X-ray diffraction data (Figure 3-4) confirmed that the degree of crystallinity was dramatically improved when CdCl<sub>2</sub> was added to the MAI solution. Both Cd\_MAPbI<sub>3</sub> and MAPbI<sub>3</sub> films showed characteristic X-ray peaks for the tetragonal perovskite phase (space group I4/mcm), [47, 52] but the intensity of the (110) peak at  $2\theta = 14.1^\circ$  was larger by a factor of ~6.5 for the Cd\_MAPbI<sub>3</sub> film, and its full-width-half-maximum value was reduced by a factor of 1.6.

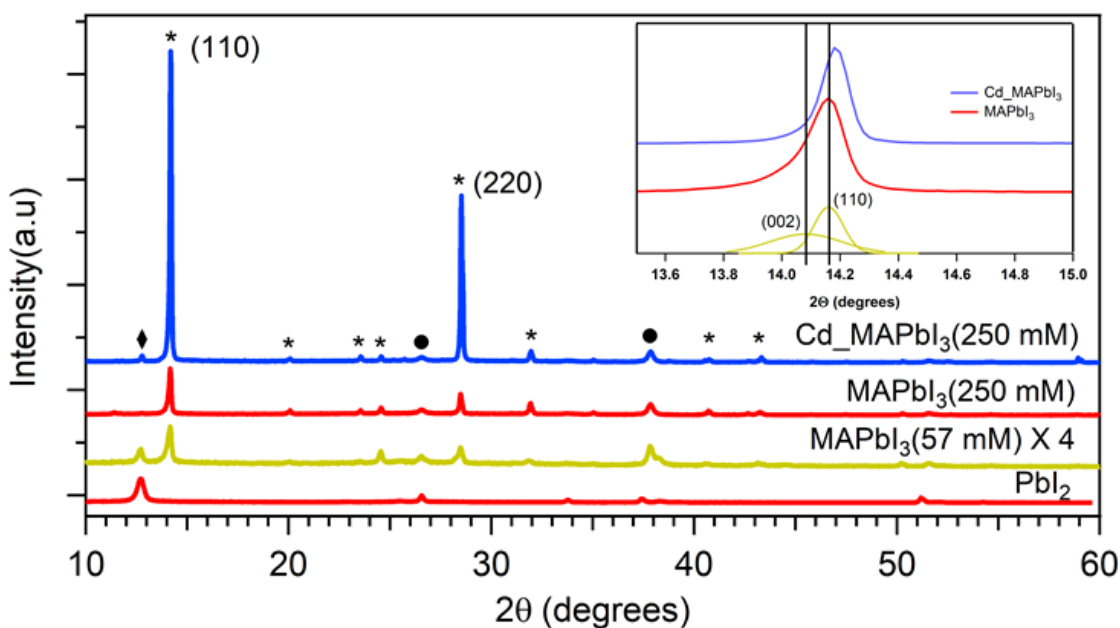


Figure 3-4. X-ray diffraction spectra of  $\text{PbI}_2$  seed layer and  $\text{MAPbI}_3$  perovskite films prepared with the standard and Cd-modified two-step deposition methods after the post-deposition heating. The spectrum for the material prepared with 57 mM MAI was multiplied by a factor of 4 to allow the peaks to be clearly seen on the same scale. The characteristic XRD peaks belong to  $\text{MAPbI}_3$  perovskite (stars),  $\text{PbI}_2$  (diamonds) and FTO/c- $\text{TiO}_2$  substrate (circles).

Similar changes were observed for the (220) diffraction peak. In addition to a much higher degree of crystallinity, the data indicates that the crystallites comprising the  $\text{Cd\_MAPbI}_3$  film are nearly completely oriented along the  $\langle 110 \rangle$  direction. In contrast, the crystallites produced without Cd exhibited more random orientations (Table 3.1).

Table 3.1: Calculated orientation index values for the XRD peaks of MAPbI<sub>3</sub> and Cd\_  
MAPbI<sub>3</sub> perovskite films.

Peak (hkl)	MAPbI <sub>3</sub>	Cd_ MAPbI <sub>3</sub>
110	2.49	3.02
200	1.52	0.35
211	1.69	0.48
202	2.39	0.33
220	1.31	2.23
310	0.85	0.22
224	0.27	0.09
330	0.20	0.13

The orientation index was calculated using XRD peak areas as follows.

$$\text{Orientation index} = \frac{M_{hkl} / \sum hkl M_i}{I_{hkl} / \sum hkl I_i} \quad (3.1)$$

Where, M is the XRD peak area from the thin film and I is the XRD peak area from a MAPbI<sub>3</sub> powder sample. The MAPbI<sub>3</sub> powder was prepared by mixing PbI<sub>2</sub> and MAI (in DMF) in a 1 to 1 molar ratio, followed by drying.

For comparison, Figure 3-4 also shows the XRD pattern that resulted when the PbI<sub>2</sub> films were processed with 57 mM MAI. In this case, the poor crystallinity and the remaining PbI<sub>2</sub> are clearly evident. The highest intensity peak at  $2\theta = 14.1^\circ$  can be deconvoluted into two components from (002) and (110) planes (Figure 3-4), which is a characteristic feature of the tetragonal structure.[47] With the addition of Cd<sup>2+</sup> the (110) peak shifted to higher values of  $2\theta$ . This is likely due to a change in the lattice parameter associated with substitution of the smaller Cd<sup>2+</sup> species onto Pb<sup>2+</sup> sites.

### 3.5 Verifying the Cd<sup>2+</sup> Involvement in the Improvement in Grain Size and Crystallinity

To determine that Cd, rather than Cl,[178, 179] was responsible for the observed changes in film growth we prepared additional films using Cd(CH<sub>3</sub>CO<sub>2</sub>)<sub>2</sub> (cadmium acetate) and CH<sub>3</sub>NH<sub>3</sub>Cl as additives to the MAI solution. Concentrations were chosen to produce the same Cd and Cl concentrations as was experienced with CdCl<sub>2</sub>. The perovskite films prepared with Cd(CH<sub>3</sub>CO<sub>2</sub>)<sub>2</sub> showed a similar enhancement in the grain size and crystallinity as was found with CdCl<sub>2</sub>, while no change in the films characteristics relative to the control preparation were observed when CH<sub>3</sub>NH<sub>3</sub>Cl was employed (Figure 3-5). Consequently, we can be confident that Cd species, rather than Cl, are responsible for these observations.

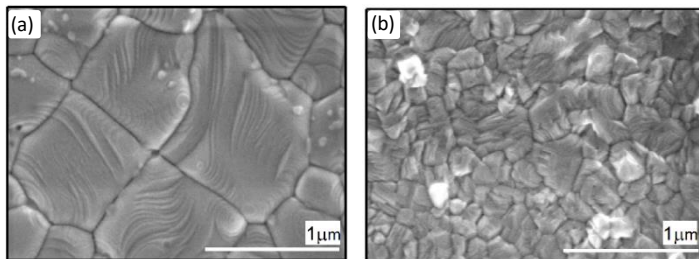


Figure 3-5. The SEM images of MAPbI<sub>3</sub> thin films prepared with (a) cadmium acetate (10 mM/250 mM MAI) and (b) methylammonium chloride (20 mM/230 mM MAI) additives, respectively.

### 3.6 Effect of Cd Incorporation on the Optoelectronic Properties of the Perovskite Films

Steady-state and time-resolved photoluminescence measurements were performed to determine the effect of Cd incorporation on the optoelectronic properties of the

perovskite films. For these measurements, the films were deposited on soda-lime glass without electron and hole transport layers in an effort to minimize carrier collection at the surfaces and allow the intrinsic characteristics of the perovskite film to govern the recombination kinetics (see the Section 3.2). The PL emission (Figure 3-6a) from the MAPbI<sub>3</sub> films made without Cd was relatively weak and centered at 753 nm, while the PL emission from Cd\_MAPbI<sub>3</sub> samples was red-shifted to 768 nm, narrower, and more intense by a factor of ~9. The increase in PL intensity and the reduction in the linewidth indicates a significant reduction in trap-mediated, non-radiative recombination.

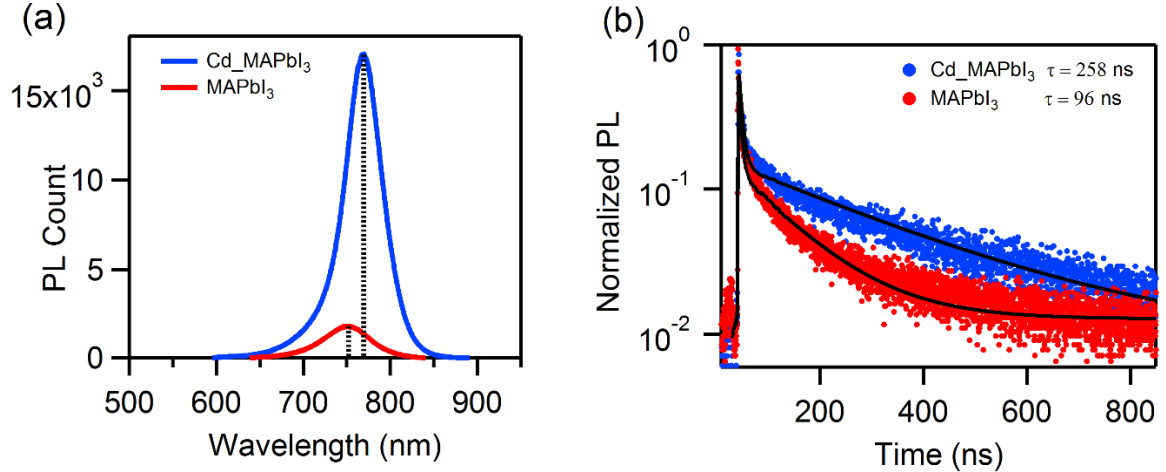


Figure 3-6. (a) Steady state PL spectra from sample excited with 140 mW/cm<sup>2</sup> of 532 nm laser light and (b) intensity-normalized time resolved PL decay measured from the longest mean lifetime MAPbI<sub>3</sub> and Cd\_MAPbI<sub>3</sub> samples excited with  $\sim 10^{10}$  photons/pulse/cm<sup>2</sup> at the peak emission wavelength, as determined from the steady-state PL measurement shown in part (a) (see Experimental Details in the see the Section 3.2).

Consistent with the steady state PL data, TRPL measurements (Figure 3-6b) showed that the PL decay was significantly slowed in Cd\_MAPbI<sub>3</sub> samples. The TRPL

decays for both Cd\_MAPbI<sub>3</sub> and MAPbI<sub>3</sub> samples were well-fit with a bi-exponential function having two decay constants (Table 3.2). The initial PL decay for both types of samples is associated with an initial relatively fast process with a time constant,  $\tau_1$ , of ~5-6 ns. After the initial fast decay, there is a slow decay component with a time constant,  $\tau_2$  that is very different in the two kinds of films. The excitation wavelength that we used in this study (532 nm) is more sensitive to the surface. Previous reports demonstrated that the excitation light of 532 nm has a penetration depth ~80 nm in perovskite.[180, 181] Therefore,  $\tau_1$  and  $\tau_2$  can be assigned to the surface charge recombination and deeper sub-surface or bulk charge recombination, respectively. While the MAPbI<sub>3</sub> films formed by the standard two-step deposition process showed a slow decay time constant of 103 ns,  $\tau_2$  for the sample prepared with Cd had a value of 266 ns. Furthermore, the yield of the long-lifetime component was also improved for the Cd\_MAPbI<sub>3</sub> samples, from 82 to 88%. Overall, Cd inclusion increased the mean lifetime (Table 3.2) from 86 to 237 ns, an increase of nearly a factor of 3. The increase in PL intensity and lifetime indicates that the non-radiative recombination rates have been slowed in the Cd\_MAPbI<sub>3</sub> samples. Unfortunately, there is no data in the literature which allows us to compare our findings to theoretical expectations for defect levels that might be introduced during Cd substitution for Pb, although Shi et al.[182] did comment that substitution could occur. Our observation of longer PL lifetimes with Cd substitution suggests that no new defects are introduced. Furthermore, the red-shift in the PL emission that is observed can be favorably compared to the band gap reduction that has been calculated by Navas et al.[183] for Cd substitution in Pb-based perovskites. In addition, a red-shift in the PL emission peak with the grain size enhancement for polycrystalline films, and a red-shift in the bulk emission compared to the

surface emission for single crystals has also been reported. [181, 184] Further, charge carrier life times are also improved with these red-shifts. Therefore, the reduction in the band gap with the Cd-modified films may also be due to the reduced recombination with the formation of highly-crystalized large grains (grain size and crystallinity improvements shifted the optoelectronic properties of the film toward the single crystal).

Table 3.2: Bi-exponential fitting time constants and mean lifetime of the carriers (average over three different sample spots).

Sample	$\tau_1$ (ns)	Yield 1 %	$\tau_2$ (ns)	Yield 2 %	Mean lifetime (ns)
Standard Perovskite	5.2	18	103	82	86
Cd-modified Perovskite	6.3	12	266	88	237

### 3.7 Perovskite Formation Mechanism with Cd<sup>2+</sup>

To develop an understanding of the mechanism that leads to the enhancement in grain size and crystallinity we first consider the basic nucleation and growth mechanisms of MAPbI<sub>3</sub> perovskite in the two-step process without Cd. Once MAI is introduced to the PbI<sub>2</sub> seed layer, MAI interacts with the PbI<sub>2</sub> framework to form the perovskite phase. As described in Chapter 2, the density of MAPbI<sub>3</sub> nuclei is determined by the concentration of MAI in the IPA solution. [26] At high MAI concentrations the PbI<sub>2</sub> can be partially dissolved and the nucleation of the MAPbI<sub>3</sub> can be viewed as occurring in a nearly homogeneous manner. [75] In this case a relatively large number of nuclei are created, there

is little preferred orientation, and the grain growth is diffusion limited. Under these conditions, the perovskite film is comprised of relatively small, randomly oriented grains. Additional consideration of the phase diagram[47] indicates that LDPs are present when the MAI concentration is high. Consequently, the as-deposited film is highly defective and poorly ordered (Figure 3-2a & c). The LDPs and small crystallites can be converted into material with improved crystallinity and higher electronic quality by the simple post-deposition heat treatment (Figure 3-2e & g).

The dramatic improvement in grain size observed when Cd is included is clearly connected to a change in the growth process. Heterogeneous nucleation is suggested by the fact that the addition of Cd to the MAI solution leads to MAPbI<sub>3</sub> films that are highly oriented. However, note that the PbI<sub>2</sub> film is oriented in the <001> direction, which would be consistent with templating of (202) perovskite planes (Figure 3-7 & 3-4), but the Cd\_MAPbI<sub>3</sub> films are oriented in the <110> direction. Note also that the grain sizes and shapes are very different in the PbI<sub>2</sub> and Cd\_MAPbI<sub>3</sub> films. While the Cd\_MAPbI<sub>3</sub> films are compact with 1–2 micron grains, the PbI<sub>2</sub> seed layer is terraced and slightly porous (~6%)[185] with grain sizes on the order of a few hundred nanometers (Figure 3-7 c & d).

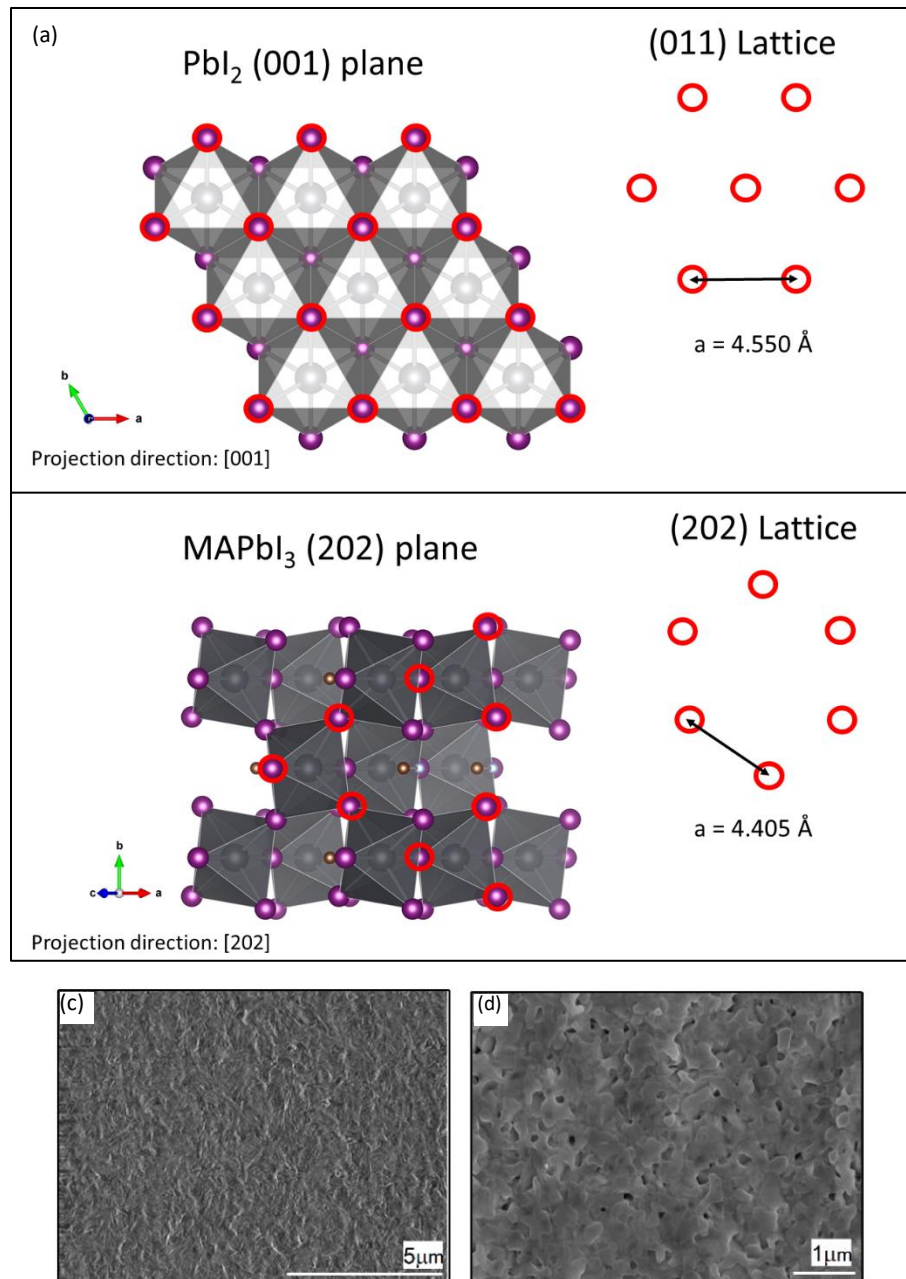


Figure 3-7. (a) Simulated crystal structure of PbI<sub>2</sub> projected in [001] direction and MAPbI<sub>3</sub> perovskite projected in [202] direction. Both the PbI<sub>2</sub> (001) and MAPbI<sub>3</sub> (202) planes possess a hexagonal lattice. The center lattice site in the MAPbI<sub>3</sub> (202) plane is not occupied. Lattice mismatch between these two structures is  $\sim 3\%$ . (c) Low and (d) high magnification SEM images of surface of the PbI<sub>2</sub> seed layer.

To develop more insight, optical absorption spectroscopy was performed on the Cd-containing MAI solutions. Absorption in the range of 300 – 325 nm was ascribed to the formation of molecular complexes (Figure 3-8). The solutions were optically clear for at least a week, indicating that the Cd-based MAI complexes do not interact or coalesce. In contrast, addition of 10 mM Pb ions to MAI solutions lead to turbid solutions and precipitation, indicating the growth of larger particles. Evidently, the surfaces of the Cd complexes are terminated in such a way that they are less reactive than their Pb counterparts such that they do not readily agglomerate.

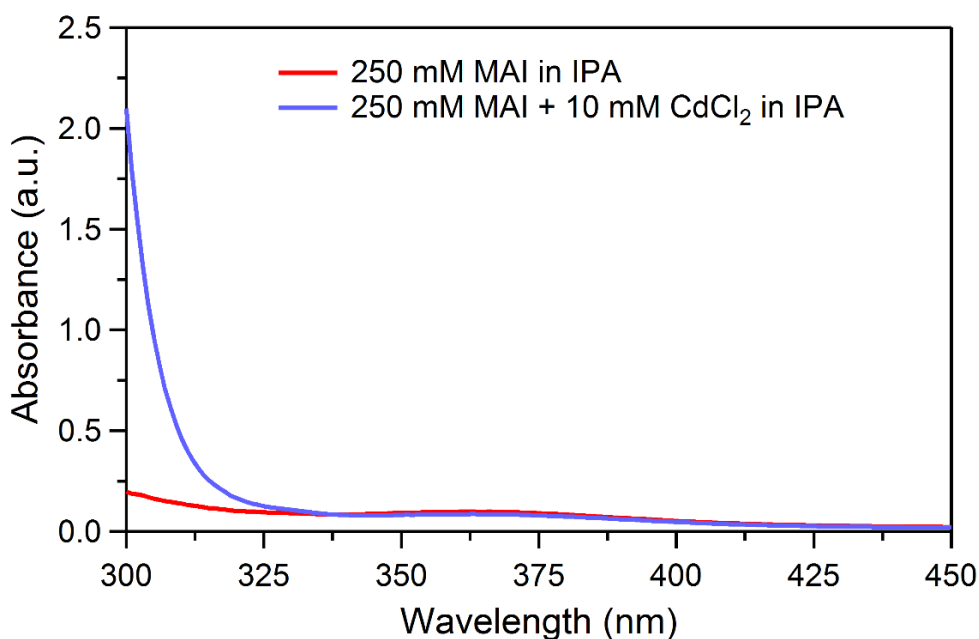


Figure 3-8. UV-vis absorbance spectra of 250 mM MAI in IPA, with and without 10 mM CdCl<sub>2</sub>.

X-ray studies of films formed by deposition of the Cd-MAI complexes onto glass substrates (Figure 3-9) revealed diffraction peaks at  $2\theta$  of  $9.1^\circ$ ,  $16.7^\circ$ , and  $25.2^\circ$ . The XRD pattern indicates that the solution phase complexes are most likely Cd-based LDPs such as

( $\text{CH}_3\text{NH}_3$ ) $_2\text{CdI}_4$ . [6, 186] Note that similar X-ray signals were also observed in the as-deposited  $\text{Cd\_MAPbI}_3$  films, but they disappeared after the films were subjected to the mild post-deposition heating (Figure 3-9). Thermal gravimetric analysis (TGA) showed that the decomposition of the ( $\text{CH}_3\text{NH}_3$ ) $_2\text{CdI}_4$  material initiated at  $\sim 200$  °C, in strong similarity to TGA data for  $\text{MAPbI}_3$  [47] (Figure 3-10).

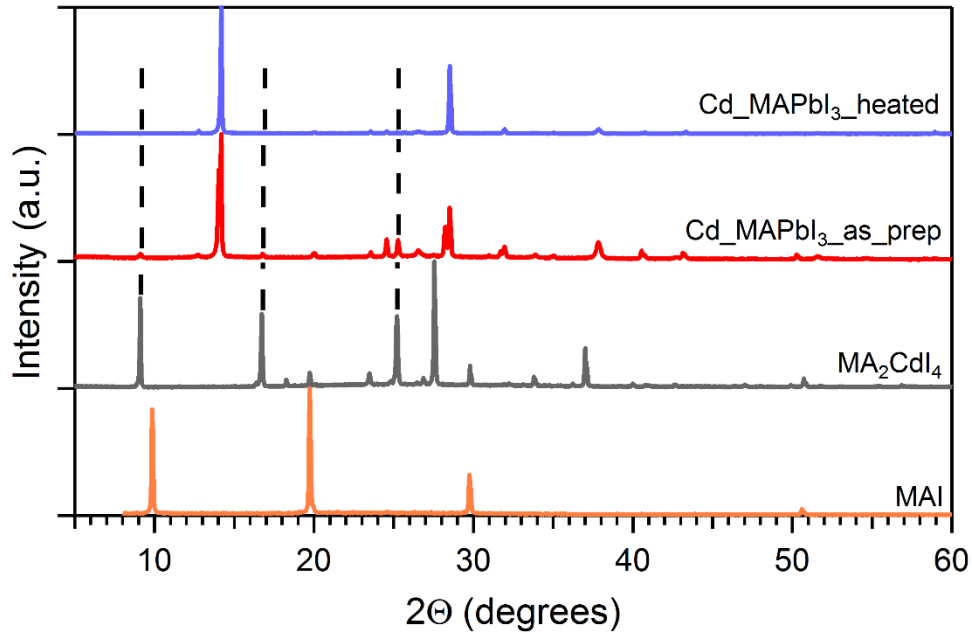


Figure 3-9. X-ray diffraction (XRD) spectra of MAI,  $\text{MA}_2\text{CdI}_4$ , and Cd-modified  $\text{MAPbI}_3$  films with and without post-deposition heating. XRD spectra of  $\text{MA}_2\text{CdI}_4$  was acquired using a thin film that was deposited on a glass substrate by spin coating a solution that was prepared by mixing MAI and  $\text{CdCl}_2$  (3 to 1 molar ratio) in IPA. Prior to XRD measurement the  $\text{MA}_2\text{CdI}_4$  sample was heated to 150 °C for 15 min.

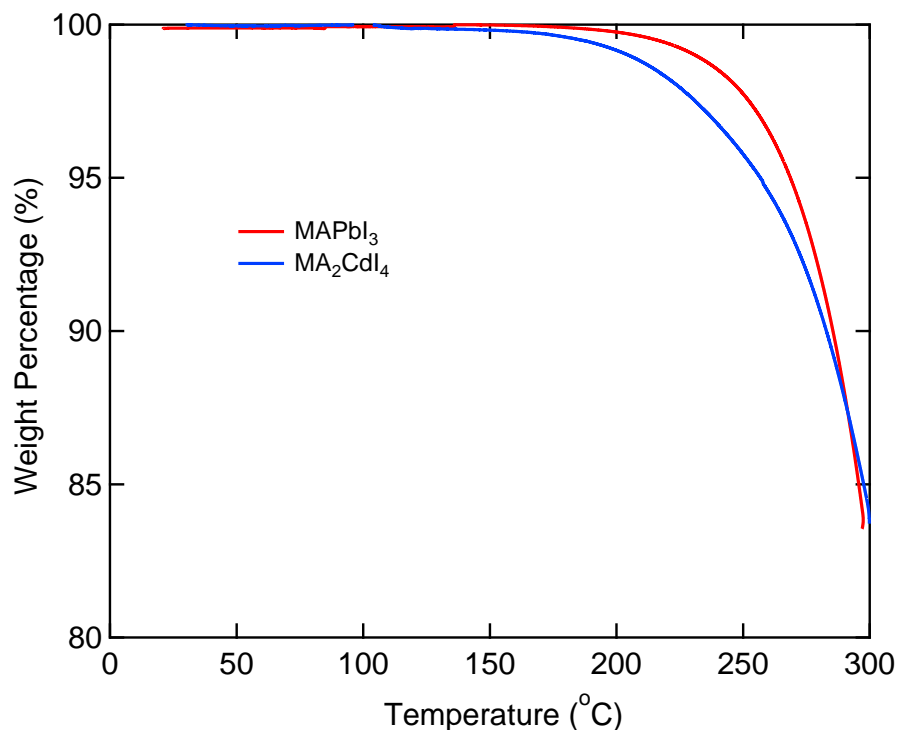


Figure 3-10. Thermogravimetric (TGA) analysis of MA<sub>2</sub>CdI<sub>4</sub> in N<sub>2</sub>. The heating ramp was 2°C/min.

With all of the data in hand we can speculate on a possible mechanism by which the small grain <001> oriented PbI<sub>2</sub> seed layer can be transformed into the large, compact grains of MAPbI<sub>3</sub> with nearly complete <110> orientation. First, because the growth of the large oriented grains occurs immediately upon introduction of the Cd-containing MAI solution, without the need for any annealing process, it is very likely that the PbI<sub>2</sub> film is not dissolved, reacted, and re-precipitated as MAPbI<sub>3</sub>. This so-called dissolution/precipitation reaction has been evoked to describe the growth of the smaller, randomly oriented crystallites that typically result from the two-step process[75] (Figure 3-2e & g). As an alternative, we can consider a process in which the PbI<sub>6</sub> octahedra that

comprise the  $\text{PbI}_2$  are not moved significantly from their initial positions but, instead, are rotated and transition from edge sharing to corner sharing coordination with incorporation of MAI. In this view, the large grain sizes are a consequence of the conversion of the  $\langle 001 \rangle$   $\text{PbI}_2$  seed layer proceeding in an organized fashion as might be expected for a topotactic process. Apparently, the Cd-LDPs serve as a type of flux or catalyst for enabling the transformation. The concept is similar to the solution-liquid-solid growth mechanism that has been developed for understanding the growth of III-V crystals.[187] In the present case, the fluxing species is the Cd-LDPs which are formed in the MAI solution. When the MAI solution is introduced to the  $\text{PbI}_2$  seed layer the Cd-LDPs will have a high affinity for the  $\text{PbI}_2$  terrace edges. At the interface, mixed-metal LDPs may form with some degree of interdiffusion. Since the  $(\text{CH}_3\text{NH}_3)_2\text{CdI}_4$  structure consists of cadmium iodide octahedra nanostructures (sheets) encased in an organic  $\text{MA}^+$  matrix in an open configuration,[6] Cd-LDPs interfaced to  $\text{PbI}_2$  grains should provide low energy pathways for incorporation and transport of  $\text{MA}^+$  and I species. In this way, the phase transformation of the parent  $\text{PbI}_2$  film to  $\text{MAPbI}_3$  would be facilitated. The difference in grain size of the initial  $\text{PbI}_2$  and final  $\text{MAPbI}_3$  films can be rationalized by two-dimensional annealing that could be additionally facilitated by the presence of the Cd-LDP flux. This recrystallization process fills the pin-holes and voids between grains, resulting in the observed large grains with a reduced grain boundary area. Returning to the SEM image of Figure 3-1b, the high contrast edges of the grains in the as-deposited Cd- $\text{MAPbI}_3$  film can now be understood as being due to the presence of electrically insulating Cd-LDPs that are left decorating the edges of the grains. Interestingly, EDS scans of both surface and cross-sectional views did not detect any Cd, indicating that the Cd concentration is below 1%. The subsequent heat treatment

decomposes the LDP structure and integrates the Cd more fully into the MAPbI<sub>3</sub> structure (Figure 3-1f). With respect to the photoexcited carrier lifetimes (*vide supra*), the benefits of the grain growth apparently outweigh any detrimental effects associated with Cd doping.[182, 183]

### **3.8 Impact of the Increased Grain Size and Carrier Lifetime on the Photovoltaic Device Performance**

To determine the impact of the increased grain size and carrier lifetime on the photovoltaic device performance, solar cells were fabricated based on Cd\_MAPbI<sub>3</sub> and MAPbI<sub>3</sub> thin films in the FTO/c-TiO<sub>2</sub>/m-TiO<sub>2</sub>/MAPbI<sub>3</sub>/spiro-MeOTAD/Au configuration. Current-voltage (J-V) were collected under simulated AM 1.5G solar spectrum at light intensity of 100 mW/cm<sup>2</sup>. We note that this non-optimized cell configuration with a relatively thin mesoporous layer was adopted to allow relatively high throughput experimentation and investigation of the impacts of the Cd-induced grain growth. Figure 3-11 shows that the PCEs for the 30 films that were turned into full devices fell into two narrow and distinct ranges. Note that the low PCE for the devices formed without Cd (~7%) using 250 mM MAI should be compared to a value of 10.8% which is typical for cells made on TiO<sub>2</sub> layers produced in our labs using an MAI concentration that optimizes efficiency without Cd (57 mM, see Figure 3-4). This latter value can then be compared to a state-of-the-art device formed with similar processing but with a more fully optimized TiO<sub>2</sub> electron transfer bilayer (15-17%).[25, 26] Devices made from Cd\_MAPbI<sub>3</sub> with 10 mM CdCl<sub>2</sub> and 250 mM MAI yielded efficiencies that were approximately twice the

average efficiency of the 250 mM MAI MAPbI<sub>3</sub> devices using a similarly unoptimized TiO<sub>2</sub> bilayer.

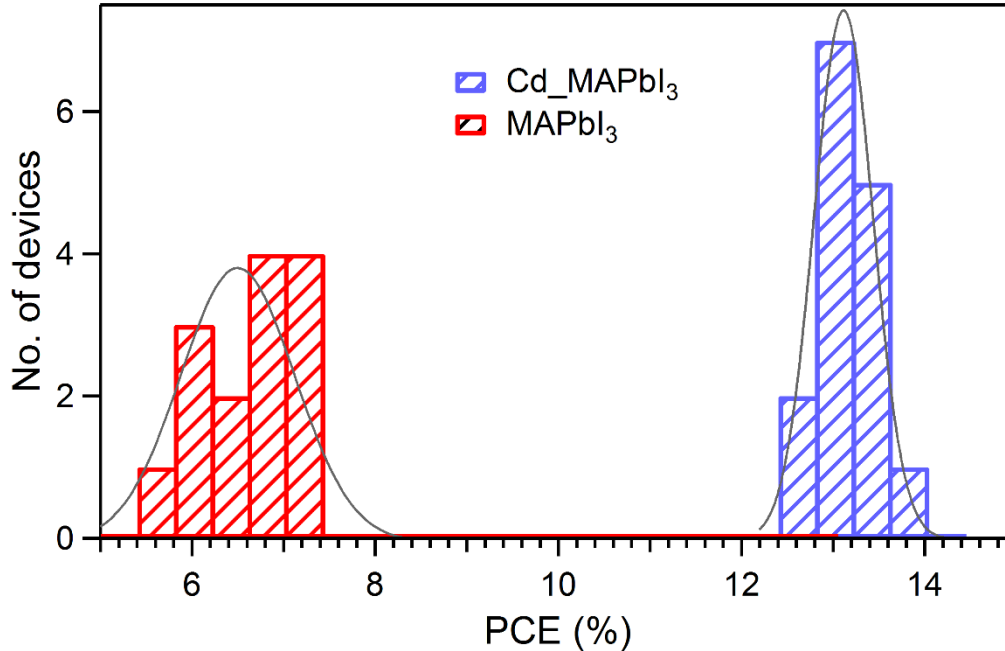


Figure 3-11. Histogram of efficiencies for devices prepared from MAPbI<sub>3</sub> and Cd\_MAPbI<sub>3</sub> thin films.

Table 3.3 shows that the improved PCE for the devices made with Cd\_MAPbI<sub>3</sub> comes from increases in the open circuit voltage ( $V_{OC}$ ), short circuit current density ( $J_{SC}$ ), and fill factor (FF). Note that a  $V_{OC}$  value of 1.06 V for the champion Cd\_MAPbI<sub>3</sub> device is very close to the highest value of 1.15 V at the time that this experiment conducted,[188] consistent with the reduction in the associated trap density ( $N_t$ ) and the associated non-radiative recombination rates. J-V Hysteresis appeared in both devices of standard and Cd-modified perovskite films (Figure 3-13) and the hysteresis factor[189], H slightly improved with the addition of Cd from 42 % to 39 %. With an average value of 17.8 mA/ cm<sup>2</sup>, which

is substantially lower than the highest record value of 23.5 mA/cm<sup>2</sup> at the time that the experiment conducted,[188] it is clear that the J<sub>SC</sub> is the primary factor that limits the performance of the devices.

Table 3.3: Solar cell performance metric for devices made with Cd\_MAPbI<sub>3</sub> and MAPbI<sub>3</sub> films.

Sample	V <sub>oc</sub> (V)	J <sub>sc</sub> (mA/cm <sup>2</sup> )	FF (%)	PCE (%)
Control				
Average	0.91 ± 0.03	12.3 ± 1.4	58.65 ± 8.66	6.5 ± 0.7
Champion	0.92	12.5	62.06	7.1
With CdCl <sub>2</sub>				
Average	1.04 ± 0.01	17.8 ± 0.3	70.42 ± 0.99	13.1 ± 0.3
Champion	1.06	17.9	72.59	13.8

To explore the origin of the low J<sub>SC</sub> values the external quantum efficiency (EQE) was measured. Consistent with the J-V measurements, the champion Cd\_MAPbI<sub>3</sub> device showed an EQE response that was higher than the response of the champion MAPbI<sub>3</sub> device across the entire wavelength range (Figure 3-12). Of particular note is the long wavelength response which was reduced for both devices. Poor long wavelength response is generally associated with poor collection of the photocarriers that are generated deep within the device. To gain more insight, the EQE data was corrected by the transmission spectral data for the glass/FTO/c-TiO<sub>2</sub>/m-TiO<sub>2</sub> portion of the device that reduces the amount of light admitted into the perovskite absorber. Thus, the internal quantum efficiency (IQE) could be evaluated (Figure 3-12).

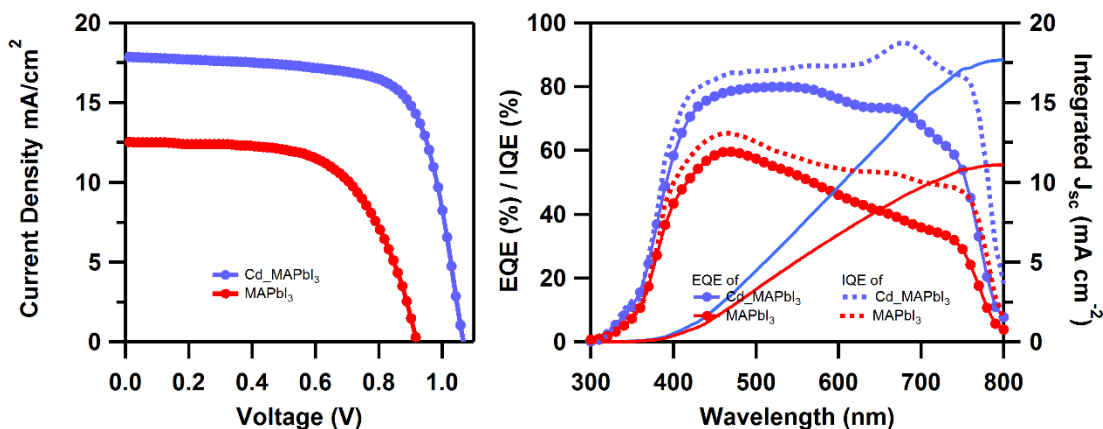


Figure 3-12. (a) J-V measurements (See the Figure 3-13 for characteristics variation of champion cells from groups of control and Cd-modified deposition with forward and reverse scan) (b) EQE, IQE spectra, and integrated current densities of CH<sub>3</sub>NH<sub>3</sub>PbI<sub>3</sub> perovskite solar cells with (blue) and without (red) CdCl<sub>2</sub> additives. The integrated photocurrent density values were 11.22 and 17.7 mA/cm<sup>2</sup> for devices prepared with standard and Cd-assisted MAPbI<sub>3</sub>, respectively. These values were in good agreement with the experimentally measured J<sub>SC</sub> values (Table 3.3).

IQE data shows that the current collection for the Cd<sub>0.1</sub>MAPbI<sub>3</sub> sample is fairly high across the full spectrum (average of 83 % from 460 to 750 nm), while the IQE for the MAPbI<sub>3</sub> control device is still poor at wavelengths longer than ~450 nm. The poor long wavelength response from the control MAPbI<sub>3</sub> film indicates that the dominant recombination mechanism is associated with traps that reduce the probability of harvesting photoexcited electrons in the HTM at the back of the device. Evidently, the inclusion of Cd during synthesis improves the collection of photoexcited electrons by reducing the effective value of charge trap density. On the other hand, the relatively high but flat IQE for the Cd<sub>0.1</sub>MAPbI<sub>3</sub> film suggests that the film's thickness should be increased to more

thoroughly absorb the incident light. Because the transparent conductor/ETL portion of our devices has not been optimized for transmission, it is interesting to estimate the theoretical maximum for  $J_{SC}$  of the device by integrating the IQE data. In this case, we would expect a  $J_{SC}$  of  $21.4 \text{ mA/cm}^2$ , which would give rise to a 16.4% device with all other parameters held constant.

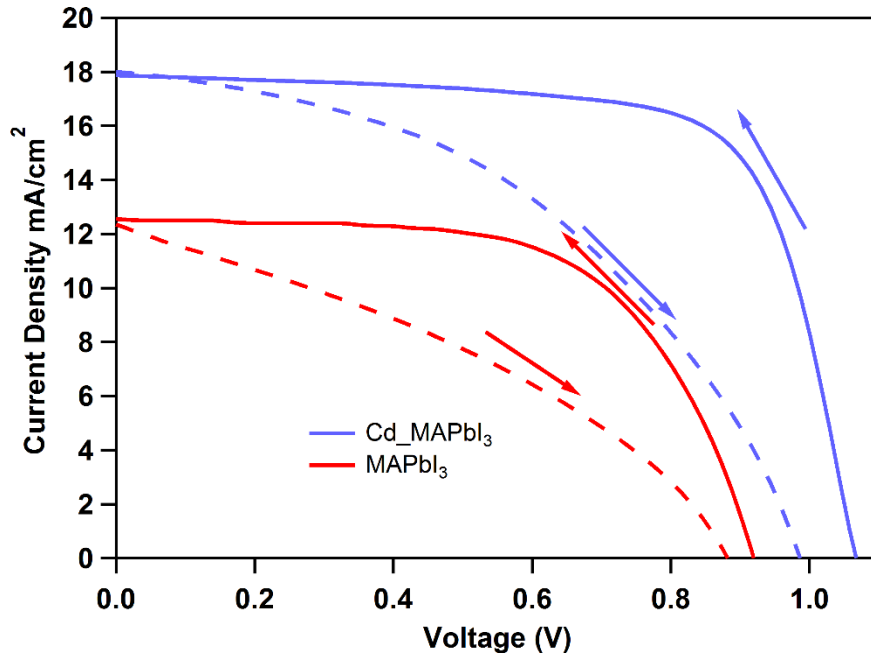


Figure 3-13. Comparison of J-V characteristics (forward and reverse scans) from the champion cells. The hysteresis index,  $H$ , was calculated using the following

equation.[189] 
$$H = \frac{\int_0^{V_{oc}} J_R(V)dV - \int_0^{V_{oc}} J_F(V)dV}{\int_0^{V_{oc}} J_F(V)dV}$$
 ; Without Cd = 42 % and With Cd = 39 %

### 3.9 Conclusion

We have shown that Cd salts introduced into the MAI precursor solution can allow the use of higher MAI concentrations and significantly improve the quality of MAPbI<sub>3</sub> perovskite films prepared by the two-step method. The grain size and crystallinity were strongly enhanced, and the <110> oriented Cd\_MAPbI<sub>3</sub> films exhibited increased carrier lifetimes and solar cell device efficiency with improved reproducibility. The growth mechanism clearly changes, and the resultant films demonstrate improved carrier lifetimes. Using an unoptimized TiO<sub>2</sub> bilayer, we showed that the PCE of perovskite solar cells can be improved with Cd<sup>+2</sup> incorporation during the film preparation. The Cd-assisted deposition method may provide way to improve the quality of films grown by high rate deposition processes.

## Chapter 4

### **Impact of Divalent Metal Additives on the Structural and Optoelectronic Properties of Methylammonium Lead Iodide Perovskite Prepared by the Two-Step Solution Process**

In this chapter, we investigate the effect of inclusion of small concentrations of divalent metal cations of  $\text{Mg}^{2+}$ ,  $\text{Ca}^{2+}$ ,  $\text{Fe}^{2+}$ ,  $\text{Co}^{2+}$ ,  $\text{Cu}^{2+}$ ,  $\text{Zn}^{2+}$ , and  $\text{Hg}^{2+}$  on the structural and optoelectronic properties of  $\text{MAPbI}_3$  perovskite materials prepared by the two-step deposition process, and compared with the inclusion of  $\text{Cd}^{2+}$  that discussed in Chapter 3. We found that the incorporation of small concentrations of  $\text{Fe}^{2+}$ ,  $\text{Co}^{2+}$ ,  $\text{Cu}^{2+}$ ,  $\text{Zn}^{2+}$ , or  $\text{Hg}^{2+}$  can also enhance the grain size dramatically. The maximum grain size increased from  $\sim 500$  nm to  $\sim 2$   $\mu\text{m}$  and  $\sim 5$   $\mu\text{m}$  with the addition of  $\text{Zn}^{2+}$ , and  $\text{Fe}^{2+}$ ,  $\text{Co}^{2+}$ ,  $\text{Cu}^{2+}$  or  $\text{Hg}^{2+}$ , respectively. However, only the  $\text{Zn}^{2+}$ , and  $\text{Fe}^{2+}$  addition showed an improved charge carrier lifetimes than the control without any additives, indicating that  $\text{Zn}^{2+}$ , and  $\text{Fe}^{2+}$  can substitute the role of  $\text{Cd}^{2+}$  in the nucleation and growth process of  $\text{MAPbI}_3$  perovskite. In addition,  $\text{Zn}^{2+}$ , and  $\text{Fe}^{2+}$  were identified as potential candidates for  $\text{Pb}^{2+}$  substitution in the lead halide perovskites.

## 4.1 Introduction and Motivation

Typically, the crystallinity, grain size, and morphology of the perovskite film in PSCs are crucial to the optoelectronic properties of the films and the performance of the devices.[26] These factors determine the density of trap states ( $N_t$ ), which causes non-radiative recombination of charge carriers and energy loss in the devices.[43, 44] To enhance solar cell performance,  $N_t$  has to be reduced. One effective way is to enhance the grain size of the perovskite films, which can greatly reduce the grain boundary and decrease  $N_t$  at boundaries. Furthermore, the diffusion length and mobility of carriers can be improved significantly in large grains.[43] In addition to the grain size and crystallinity, surface morphology of the methylammonium lead iodide (MAPbI<sub>3</sub>) perovskite film is also crucial to achieve better performance in the PV devices. Poor surface coverage and rough surfaces cause high surface charge recombination and significantly affect the charge carrier collection.[175, 176] In Chapter 3, we have demonstrated that Cd<sup>2+</sup> addition during the two-step growth of MAPbI<sub>3</sub> enhances grain size and photoluminescence, and thus the photoconversion efficiency. However, due to the toxicity of the Cd, we wanted to find any other possible metal cation/s that can substitute the role of the Cd<sup>2+</sup>. In this chapter, we compare the effects of including small concentrations of other possible divalent metal cations of Mg<sup>2+</sup>, Ca<sup>2+</sup>, Fe<sup>2+</sup>, Co<sup>2+</sup>, Cu<sup>2+</sup>, Zn<sup>2+</sup>, and Hg<sup>2+</sup> during the two-step fabrication process, and compared with the Cd<sup>2+</sup>.

## 4.2 Experimental Details

Thin film fabrication and characterization are similar to the Cd-modified MAPbI<sub>3</sub> and explained details in the section 3.2. In brief, MAPbI<sub>3</sub> perovskite films were prepared on the compact TiO<sub>2</sub> (c-TiO<sub>2</sub>) coated F-doped SnO<sub>2</sub> (FTO) glass (TEC 15; Pilkington NA) substrates. A PbI<sub>2</sub> seed layer (~350 nm) was first deposited on the c-TiO<sub>2</sub> layer (~ 50 nm) by spin-coating a hot solution of 1 M PbI<sub>2</sub> in N,N-Dimethylformamide (DMF), followed by annealing at 100 °C for 15 min to evaporate the solvent and crystallize PbI<sub>2</sub>. Then solutions of 250 mM methylammonium iodide (MAI) in isopropanol (IPA) with 10 mM MCl<sub>2</sub> (where; M is Mg, Ca, Fe, Co, Cu, Zn, or Hg) were spin coated on the PbI<sub>2</sub> seed layer to form metal-modified (Mg-, Ca-, Fe-, Co-, Cu-, Zn-, or Hg-modified) MAPbI<sub>3</sub> films. A solution of 250 mM MAI in IPA was used to prepare the control sample. After the MAI was spin coated, samples were annealed at 150 °C for 5 minutes to complete the MAPbI<sub>3</sub> perovskite formation reaction. The films were characterized using scanning electron microscopy (SEM), X-ray diffraction (XRD), UV-vis spectroscopy, and steady-state and time-resolved photoluminescence (PL and TRPL). PL measurements were obtained at several locations on the MAPbI<sub>3</sub> samples with 532 nm CW excitation from the film side (laser spot size of ~140 μm and intensity of 140 mW/cm<sup>2</sup>) at room temperature. TRPL measurements were performed with a time correlated single photon counting module (Becker & Hickel Simple Tau SPCM 130-E/M module) using a 532 nm pulsed laser (beam diameter of ~100 μm) as a source of excitation. Samples were excited with ~10<sup>10</sup> photons/pulse/cm<sup>2</sup> at the peak emission wavelength, as determined from the steady-state PL measurement.

### 4.3 Grain Size Enhancement

For all the metals, except for  $\text{Fe}^{2+}$ , a formation of pin-hole free surfaces with a full coverage on the substrate (Figure 4-1b, c, h, i, m, & o) was observed. Films with the addition of  $\text{Fe}^{2+}$  contained voids between grains, forming pin-holes. Addition of  $\text{Fe}^{2+}$ ,  $\text{Co}^{2+}$ ,  $\text{Cu}^{2+}$ ,  $\text{Zn}^{2+}$ , and  $\text{Hg}^{2+}$  improved the grain size dramatically (more than the  $\text{Cd}^{2+}$ ), but the grain size for  $\text{Mg}^{2+}$ ,  $\text{Ca}^{2+}$  remained similar to the control.

Smooth  $\text{MAPbI}_3$  thin films were formed with the addition of these metal salts, while films prepared by the standard method were rough and contained impurities (high contrast spots) on the surface (Figure 4-1a & d). The maximum grain size increased from  $\sim 200$  nm to  $5 \mu\text{m}$  with the addition of  $\text{Fe}^{2+}$ ,  $\text{Co}^{2+}$ ,  $\text{Cu}^{2+}$ , or  $\text{Hg}^{2+}$ , and to  $\sim 2 \mu\text{m}$  with the  $\text{Zn}^{2+}$ .

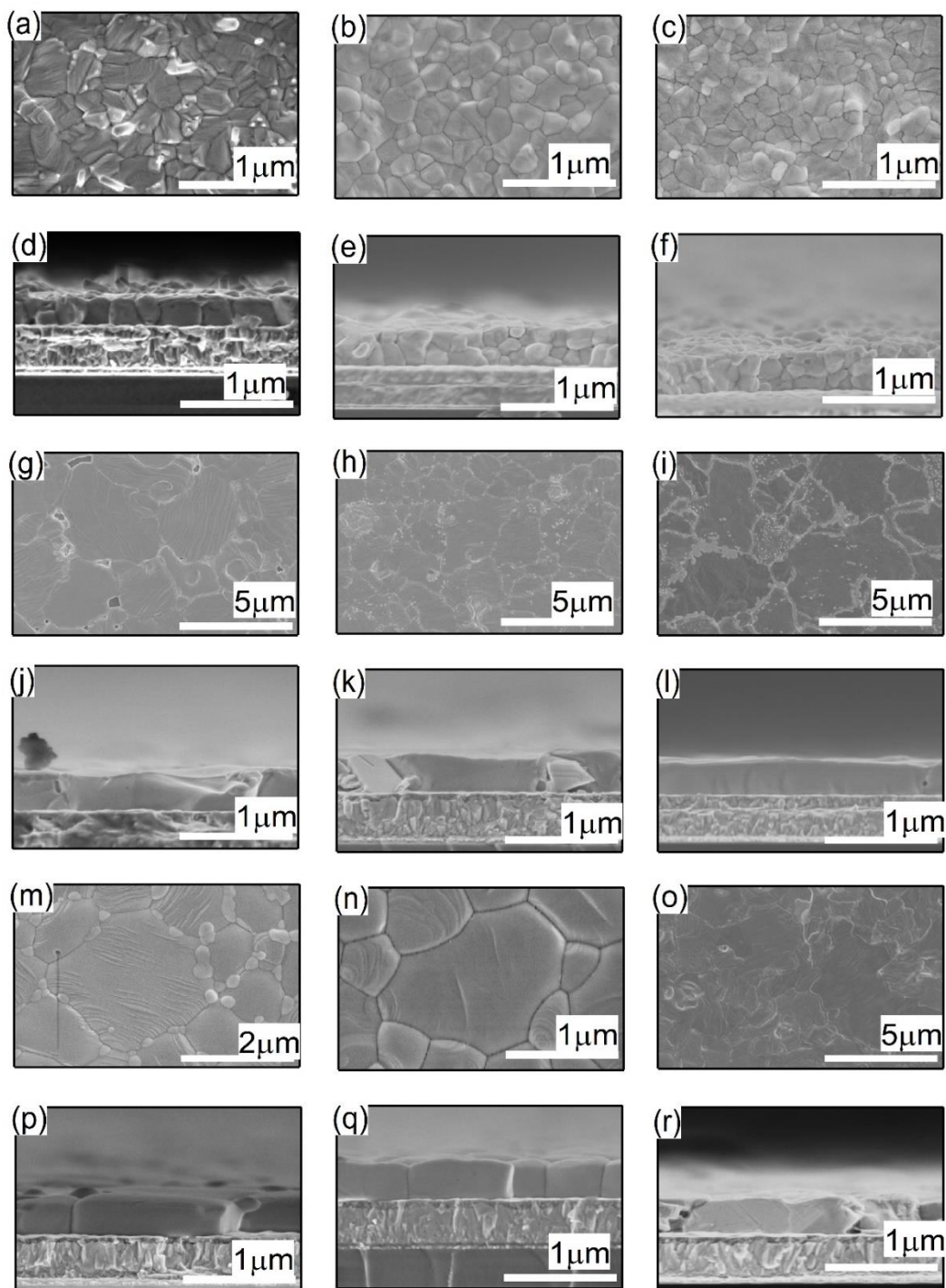


Figure 4-1. Surface (a, b, c, g, h, i, m, n, & o) and cross sectional (d, e, f, j, k, l, p, q, & r) SEM images from the MAPbI<sub>3</sub> films without (a & d) and with Mg<sup>2+</sup> (b & e), Ca<sup>2+</sup> (c & f), Fe<sup>2+</sup> (g & j), Co<sup>2+</sup> (h & k), Cu<sup>2+</sup> (i & l), Zn<sup>2+</sup> (m & p), Cd<sup>2+</sup> (n & q), or Hg<sup>2+</sup> (o & r) addition.

The cross sectional images (Figure 4-1j, k, i, p, & r) revealed the formation of a single grain throughout the entire film thickness for  $\text{Fe}^{2+}$ ,  $\text{Co}^{2+}$ ,  $\text{Cu}^{2+}$ ,  $\text{Zn}^{2+}$ , and  $\text{Hg}^{2+}$ . Films modified with  $\text{Mg}^{2+}$  and  $\text{Ca}^{2+}$  consisted of stacked formation of small grains (Figure 4-1e & f). Some small grains were found on the edges of the large perovskite grain in the films when  $\text{Fe}^{2+}$ ,  $\text{Co}^{2+}$ ,  $\text{Cu}^{2+}$ ,  $\text{Zn}^{2+}$ , and  $\text{Hg}^{2+}$  were used (Figures 4-1g, h, i, m, & o), which is likely due to the phase segregation of metal chlorides and/or Fe-, Co-, Cu-, Zn-, and Hg-based low dimensional perovskites (LDPs).

#### 4.4 Impact on Crystallinity

Figure 4-2a compares the XRD spectra of  $\text{MAPbI}_3$  films prepared with and without metal additives. All  $\text{MAPbI}_3$  films showed characteristic peak positions belonging to the tetragonal perovskite phase (space group  $I4/mcm$ ). [47, 52] With the addition of  $\text{Mg}^{2+}$ ,  $\text{Ca}^{2+}$ ,  $\text{Cu}^{2+}$ ,  $\text{Cd}^{2+}$  or  $\text{Zn}^{2+}$  peak position of the (110) (at  $2\theta$  angle of  $14.1^\circ$ ) shifted to higher values of  $2\theta$  (Figure 4-2b). The peak shift increased in the order  $\text{Ca}^{2+} < \text{Cd}^{2+} < \text{Zn}^{2+} < \text{Cu}^{2+} < \text{Mg}^{2+}$ . This is likely due to crystal lattice distortion that occurs with substitution of  $\text{Pb}^{2+}$  by a smaller cation, and the peak shift is consistent with the order of reducing ionic radii (the ionic radii reduces in the order  $\text{Ca}^{2+}$  (100 pm)  $>$   $\text{Cd}^{2+}$  (95 pm)  $>$   $\text{Zn}^{2+}$  (74 pm)  $>$   $\text{Cu}^{2+}$  (73 pm)  $>$   $\text{Mg}^{2+}$  (72 pm)), [190] which causes the perovskite unit cell to shrink, leading to the increases in  $2\theta$ . Interestingly, the addition of  $\text{Fe}^{2+}$ ,  $\text{Co}^{2+}$  or  $\text{Hg}^{2+}$  resulted in a splitting of the peaks, which can be attributed to the formation of Fe-, Co-, or Hg-based organic-inorganic halides such as  $\text{MABX}_3$  and  $(\text{MA})_2\text{BX}_4$  (Where; B = Fe, Co, or Hg, and X = I or Cl). [191-194] Furthermore, XRD peaks at  $2\theta$  angle of  $\sim 11.5^\circ$  were observed from the films made with  $\text{Ca}^{2+}$ ,  $\text{Mg}^{2+}$ ,  $\text{Fe}^{2+}$ , and  $\text{Hg}^{2+}$  additives, which can be attributed to the Ca- Mg-,

Fe-, or Hg-based LDPs (Figure 4-2c).[47, 191, 194] These LDPs lead to the excitonic absorption at ~360 nm that is seen in the absorbance spectrum (Figure 4-3a).

The intensity of the (110) XRD peak for the Mg-, Ca-, Fe-, Co-, Cu-, Zn-, and Hg-modified films was much lower than that for the Cd-modified film, and decreased in the order of Cd > Cu > control > Fe > Zn > Mg > Co > Ca > Hg. The reduced XRD intensity indicates a lower degree of crystallinity in the Mg-, Ca-, Fe-, Co-, Cu-, Zn-, and Hg-incorporated films (Figure 4-2a). This result is consistent with the UV-vis absorbance spectra (Figure 4-3), in which the Cd-modified film with the highest degree of crystallinity shows the strongest absorption at the perovskite band edge (~750 nm). In contrast, though the addition of Fe<sup>2+</sup>, Cu<sup>2+</sup>, Co<sup>2+</sup>, Zn<sup>2+</sup>, and Hg<sup>2+</sup> enhanced the grain size, the lower degree of crystallinity of MAPbI<sub>3</sub> grains led to reduced optical absorption.

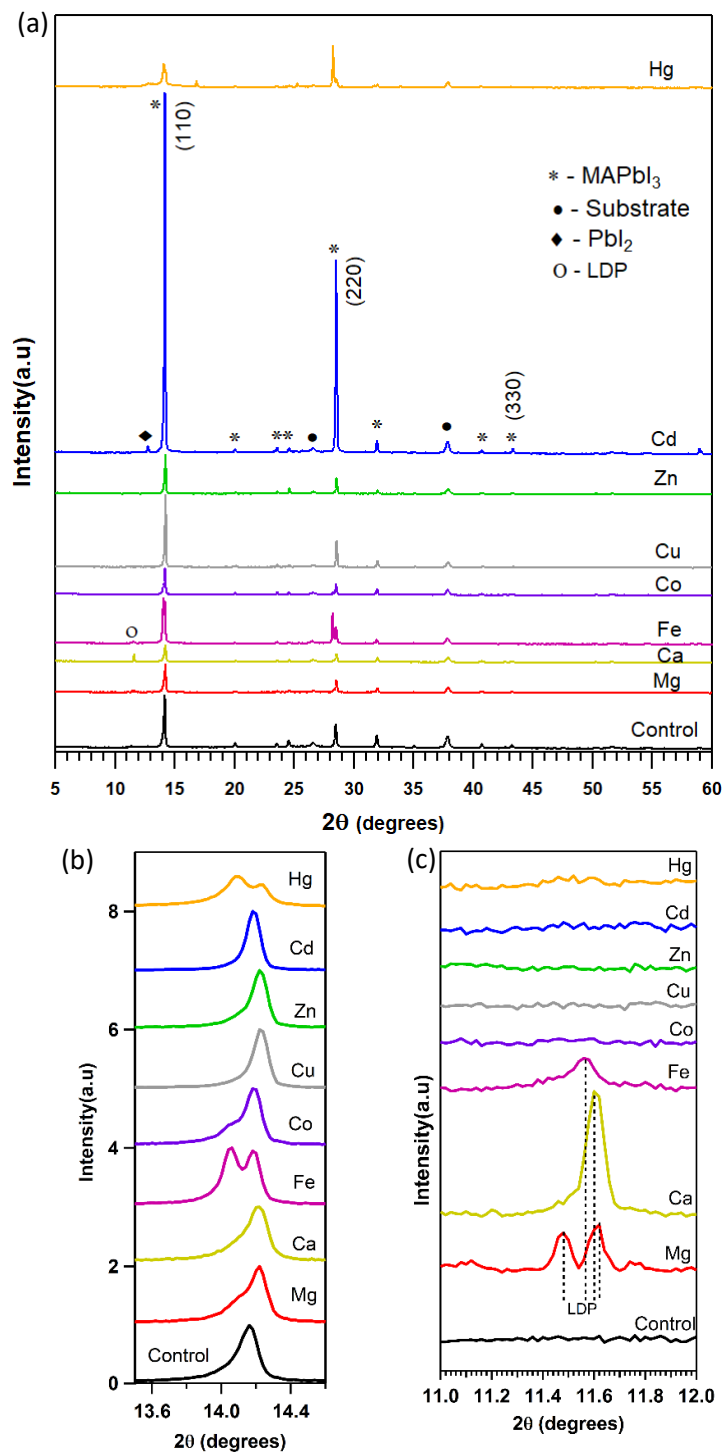


Figure 4-2. (a) XRD spectra of the MAPbI<sub>3</sub> perovskite control film and the films prepared with Mg<sup>2+</sup>, Ca<sup>2+</sup>, Fe<sup>2+</sup>, Co<sup>2+</sup>, Cu<sup>2+</sup>, Zn<sup>2+</sup>, Cd<sup>2+</sup>, and Hg<sup>2+</sup> additions in the two-step deposition. Zoom-in XRD spectra for the (b) perovskite (110) peak, and (c) LDP peaks.

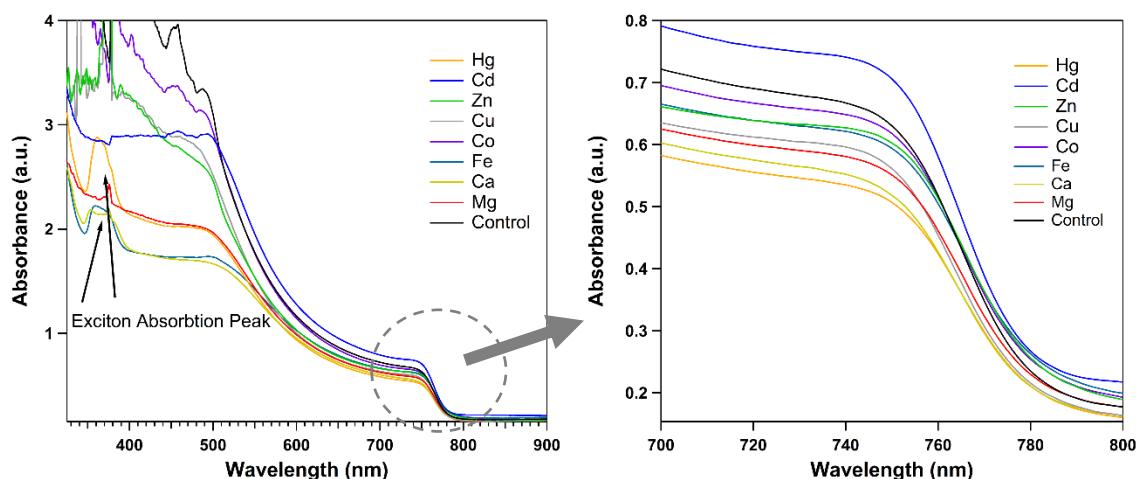


Figure 4-3. UV-vis absorbance spectra of control without any additive and Mg-, Ca-, Fe-, Co-, Cu-, Zn-, Cd-, and Hg-modified films.

#### 4.5 Impact on Optoelectronic Properties

Addition of the  $\text{Fe}^{2+}$ ,  $\text{Co}^{2+}$ ,  $\text{Cu}^{2+}$ ,  $\text{Zn}^{2+}$ , and  $\text{Hg}^{2+}$  divalent metal cations assists the formation of large grains; however, these metals may introduce deep-level charge trap states. To examine this possibility, PL and TRPL measurements were performed to determine the effect of these metal cation inclusion on the optoelectronic properties of the perovskite films ( $\text{Mg}^{2+}$  and  $\text{Ca}^{2+}$  were also measured for comparison). The PL emission (Figure 4-4a) from the  $\text{MAPbI}_3$  film was centered at 753 nm, consistent with the reported value for the  $\text{MAPbI}_3$  thin films.[195] For all the metals, the perovskite emission peak exhibited a red shift ( $\sim 10\text{-}20$  nm) with respect to the control sample (753 nm), indicating a decrease in the band gap between the valence-band-maximum (VBM) and the conduction-band-minimum (CBM) of the perovskite. Further, all the metals other than the  $\text{Co}^{2+}$  showed a narrowed PL emission peak. PL emission peak from the Co-modified  $\text{MAPbI}_3$  film was

broad and had a shoulder peak (Figure 4-4a), indicating an increased defect density and a formation of mid gap defects in the film.

There could be several reasons for the band gap reduction in the MAPbI<sub>3</sub> films with the metal incorporation. One reason could be that the substitution of the Pb<sup>2+</sup> sites by these metal cations in the MAPbI<sub>3</sub> system alters the interaction with the ions in the network and leads to the changes in the band gap.[183, 196, 197] Formation of shallow defects could also be a potential reason.[85, 180] In the case of Co<sup>2+</sup>, the peak at ~ 880 nm is likely belonged to transition due to mid gap defects. The emission peak ~763 nm could be due to the transition associated with either shallow defects or band to band transition from a reduced band gap that changed by the Co<sup>2+</sup> substitution. Another possible reason for the red-shifted PL emission peak in the Mg-, Ca-, Fe-, Cu-, Zn-, Cd- and Hg-modified films is an improved surface passivation. As described in Chapter 3, the excitation wavelength of 532 nm is more sensitive to the surface (penetration depth ~80 nm). Therefore, if there is an improved surface passivation, then we should observe an improved  $\tau_1$  for these perovskite films compared to the control.

The TRPL decays (Figure 4-4b) for all the films were well-fit with a bi-exponential function having two decay constants (Table 4.1). As predicted based on the PL data, for all the metals, except for Co<sup>2+</sup>, an improved  $\tau_1$  was observed, indicating improved surface passivation of the perovskite grains. Therefore, the red-shift in the PL emission peak with the Mg<sup>2+</sup>, Ca<sup>2+</sup>, Fe<sup>2+</sup>, Cu<sup>2+</sup>, Zn<sup>2+</sup>, Cd<sup>2+</sup> and Hg<sup>2+</sup> inclusion is likely due to the reduced surface charge trap density due to the surface passivation, and/or Pb<sup>2+</sup> substitution by these metal cations, and/or formation of shallow defects.

Only Fe- and Zn-modified perovskite films showed increased  $\tau_1$  and  $\tau_2$  compared to the control sample. It is likely due to the result of combining grain boundary passivation and grain size enhancement. However, the high yield of  $\tau_1$  indicates that a possible charge extraction to the small Fe- or Zn-based impurities on the surface of perovskite grain (Figure 4-1g & m) which would limit the PV device performance. The  $\tau_2$  of the Fe\_MAPbI<sub>3</sub> film (255 ns) was approximately similar to that of the Cd\_MAPbI<sub>3</sub> (266 ns), but lower in the Zn\_MAPbI<sub>3</sub> (155 ns), indicating that the deep level trap states density in the bulk of the Zn-modified MAPbI<sub>3</sub> is higher than that of the Fe- and Cd-modified films.

Table 4.1: Bi-exponential fitting time constants and mean lifetime of the carriers for the Mg-, Ca-, Fe-, Co-, Cu-, Zn-, Cd- and Hg-modified, and control films (average over three different sample spots).

Metal additive	$\tau_1$ (ns)	Yield 1 %	$\tau_2$ (ns)	Yield 2 %	Mean lifetime (ns)
Standard	5.2	18	103	82	86
Mg	16	39	61	72	50
Ca	19	39	69	61	49
Fe	34	25	255	75	200
Co	3.4	42	58	36	23
Cu	9.5	30	104	70	76
Zn	30.8	51	155	49	91
Cd	6.3	12	266	88	237
Hg	8.9	22	78	74	60

Both  $\tau_1$  and  $\tau_2$  for the Co-modified film were lower than the control, indicating higher surface and bulk recombination. This is consistent with the steady-state PL measurements (Figure 4-4a). This could be due to the formation of Co-based perovskite and/or  $\text{CoCl}_2$  segregation. The  $\text{Cu}^{2+}$  incorporation slightly improved the surface-lifetime component  $\tau_1$ . However, the high yield of  $\tau_1$  compared to the control indicates an existence of surface defects. The bulk-lifetime component  $\tau_2$  was similar to the control sample, indicating an approximately equal density of non-radiative recombination centers in the control and Cu-modified films. This is consistent with the crystallinity of the control and Cu-modified films (Figure 4-2a). Since the  $\text{Cu}^{2+}$  incorporation forms large grains (Figure 4-1i), the density of grain boundary decreases, reducing the non-radiative recombination centers. Therefore,  $\text{Cu}^{2+}$  inclusion may have formed deep level charge trap states in the  $\text{MAPbI}_3$  film.

The  $\text{Mg}^{2+}$ ,  $\text{Ca}^{2+}$ , or  $\text{Hg}^{2+}$  incorporation improved the surface passivation of the perovskite grains, resulting in an improvement in surface-lifetime component  $\tau_1$ . However, the high yield of  $\tau_1$  compared to the control indicates an existence of surface defects. The reduced  $\tau_2$  explains that the Mg-, Ca- Hg-based impurities (LDPs or metal chlorides) can introduce non-radiative recombination centers which reduce the possibility to separate photoexcited charge carriers.

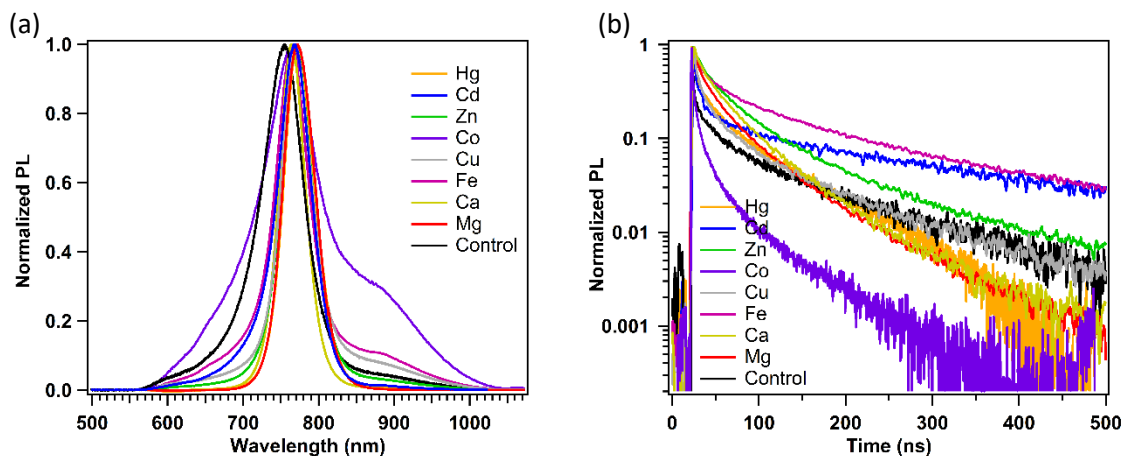


Figure 4-4. (a) Normalized PL spectra and (b) intensity normalized TRPL decay of control (MAPbI<sub>3</sub>), Mg-, Ca-, Fe-, Co-, Cu-, Zn-, Cd-, and Hg-modified of perovskite films.

#### 4.6 Conclusion

Inclusion of the divalent metal cations of Fe<sup>2+</sup>, Co<sup>2+</sup>, Cu<sup>2+</sup>, Zn<sup>2+</sup>, or Hg<sup>2+</sup> also enhanced the grain size dramatically, but only the Fe-, and Zn- modified films showed an improved charge carrier lifetimes than the control without any additives, indicating that the addition of Zn<sup>2+</sup>, and Fe<sup>2+</sup> can also change the nucleation and growth process of MAPbI<sub>3</sub> perovskite, and improve the material quality. In addition, Zn<sup>2+</sup>, and Fe<sup>2+</sup> were identified as potential candidates for Pb<sup>2+</sup> substitution in the lead halide perovskites.

Since the concentration was not varied during the experiment, further research is needed to develop a precise control of Mg<sup>2+</sup>, Ca<sup>2+</sup>, Fe<sup>2+</sup>, Co<sup>2+</sup>, Cu<sup>2+</sup>, Zn<sup>2+</sup>, and Hg<sup>2+</sup> concentrations in the MAPbI<sub>3</sub> film that could lead to the improvement of the structural and optoelectronic properties of the film.

## Chapter 5

### **Selective Cd Removal from CdTe Surface for High Efficiency Te Back Contact Formation in CdTe Solar Cells**

Formation of a Te-rich surface or a Te layer on the CdTe absorber is beneficial to the formation of a low barrier contact at the back junction in CdTe solar cells. Regardless of the CdTe fabrication method, surface etching or direct deposition processes are widely used to form Te-rich CdTe surfaces or Te layers. In this chapter, we show that methylammonium iodide ( $\text{CH}_3\text{NH}_3\text{I}$ , MAI) can simply and controllably react with the CdTe surface to produce elemental tellurium. Both X-ray diffraction and Raman spectroscopy confirmed formation of a Te layer. P-type doping on the CdTe surface was conducted by diffusing a small amount of Cu through the Te layer. The Te layer, which is located between the p-type doped CdTe surface and the back electrode, reduces the Schottky barrier height and band bending at the back contact, improving the open circuit voltage ( $V_{\text{OC}}$ ) and fill factor (FF) in CdTe solar cells. MAI concentration, MAI reaction time and temperature, and the amount of Cu used for the doping of the treated devices were optimized with an Au back electrode. CdS/CdTe samples that were treated with 125 mM MAI solution and heated to 125 °C for 10 minutes showed the best power conversion

efficiency (PCE) of 14.1%, while the best efficiency of a standard device without treating was 13.0%. Further, this improved efficiency was achieved with less Cu than the standard. PCE for the devices with the indium tin oxide (ITO) back electrode was also improved from 11.0% to 12.2% with the MAI treatment, indicating the formation of a Te layer adjacent to the p-type doped CdTe surface is a potential technique for the fabrication of high efficiency transparent or bifacial CdTe solar cells.

## 5.1 Introduction and Motivation

CdTe solar cell technology is one of the most well-established approaches for preparing high efficiency, low cost, and stable thin films photovoltaics (PV). [198] With a direct band gap of 1.45 eV, CdTe is an ideal absorber material for single junction solar cells, and a power conversion efficiency (PCE) as high as 22.1% has recently been achieved. [17] Creating an efficient and stable back contact is necessary to achieve high efficiency CdTe solar cells that exhibit long-term stability. [199] Since CdTe has a high electron affinity, a high work function metal is required to form a low resistance ohmic contact; however, no metals have a work function high enough to form an ohmic contact with p-type CdTe (Figure 5-1a). Therefore, CdTe/metal junctions typically result in a Schottky barrier (Figure 5-1d). This increases the back junction recombination and causes lower device performance.[199-203] A typical method to reduce this barrier height is to add Cu to the back contact with (Figure 5-1h & i) or without (Figure 5-1e-f) a Te layer, and, more recently, a Te layer without the Cu (Figure 5-1g).[204, 205] The added Cu diffuses to the CdTe, doping the CdTe surface as a  $p^+$  region, or/and forms a  $Cu_xTe$  degenerate semiconductor layer.[203, 206-209] The layer that consists of this  $p^+$  region



interface increases with increasing the carrier density of the buffer layer ((e) < (f)), which formed by diffusing Cu to the CdTe, to dope the CdTe surface as a p<sup>+</sup> region, or/and form a Cu<sub>x</sub>Te layer. Energy band diagram of CdTe, Te buffer layer, and metal back electrode after being connected (g) without and (h) & (i) with Cu addition. Note that the panels (h) & (i) represent the change in energy band diagrams, which are shown in the panels (e) and (f), respectively, after the Cu incorporation.

Doping of the CdTe surface is often conducted by deposition of a thin Cu layer on the CdTe surface, followed by annealing. [209, 211] For the Cu<sub>x</sub>Te fabrication, the Cu deposition is conducted on a Te-rich CdTe surface or separately deposited Te layer on the CdTe surface. [205-207] Depending on the reaction temperature, Cu diffuses to the bulk CdTe, doping the surface as a p<sup>+</sup> region, or reacts with the Te, forming a Cu<sub>x</sub>Te layer. [205-207] To fabricate a Te-rich surface or a Te layer on the CdTe layer, wet-chemical surface etching processes, such as bromine-methanol (BrMeOH), which uses a diluted solution of bromine in methanol [199], nitric-phosphoric etch (NP etch), which uses a mixture of nitric and phosphoric acid in water [212], and dry etching in Ar plasma [213] are commonly used. Alternatively, either physical vapor deposition (close space sublimation (CSS) [214] or evaporation [204]) or chemical bath deposition (CBD) [215] have also been used to form a Te layer on the CdTe absorber.

In Chapter 3 we explained that MAI, which is one of the main precursors used in the fabrication of lead halide perovskite solar cells, readily forms (CH<sub>3</sub>NH<sub>3</sub>)<sub>2</sub>CdI<sub>4</sub> (MA<sub>2</sub>CdI<sub>4</sub>) perovskite with Cd<sup>2+</sup> ions. So, a question raised whether MAI can extract Cd from CdTe surface leaving Te. To answer this question, MAI thin films, which were

fabricated on the CdTe surface by spin-coating MAI/isopropanol (IPA) solutions, were reacted with the CdTe surface, and characterized the surface using XRD and Raman spectroscopic analysis, and SEM imaging. After reacting the MAI on the CdTe surface, formation of a layer of elemental Te was noticed, indicating that MAI can extract Cd from CdTe surface leaving Te. With this finding, we introduced a new wet-chemical process to form a Te layer on the CdTe surface using, MAI solutions. Facile preparation, reduced toxicity, and high controllability are the main advantages of this process.

Current density-voltage (J-V) characteristics showed significant improvements in open circuit voltage ( $V_{OC}$ ) and fill factor (FF) with the MAI treatment. Improved  $V_{OC}$  and FF, resulted a higher PCE (14.1%) in the MAI treated devices relative to standard devices prepared without any surface treatment (13.0%). We investigated the effect of MAI concentration, and MAI reaction time and temperature on the surface morphology, structure, and device performance. Furthermore, the amount of diffused Cu for MAI treated devices was also optimized. The optimized MAI treatment was applied to improve the PCE of CdS/CdTe solar cells with a transparent indium tin oxide (ITO) back electrode from 11.0% to 12.2%. Temperature dependent J-V measurements were conducted to investigate the effect of the MAI treatment on the back contact barrier height ( $\phi_b$ ). The Schottky barrier height at the back contact for both Au and ITO electrodes dramatically reduced with the MAI treatment, consistent with the improved  $V_{OC}$  and FF.

## 5.2 Experimental Details

### 5.2.1 MAI Surface Treatment

CdS and CdTe were deposited onto glass substrates, which are consisted of a pre-deposited stack of a transparent conductive oxide (TCO) and a high-resistance transparent (HRT) layer (Figure 5-2) using a commercial vapor transport deposition process. The TCO and HRT layers are made of fluorine-doped SnO<sub>2</sub> (FTO or F:SnO<sub>2</sub>) and intrinsic SnO<sub>2</sub> (i-SnO<sub>2</sub>), respectively. CdCl<sub>2</sub> was deposited on the CdTe film by dropper using a saturated methanolic solution. Samples were heated at 387 °C in dry air for 30 min to activate the device. [216] Excess CdCl<sub>2</sub> was removed by thorough rinsing with methanol.

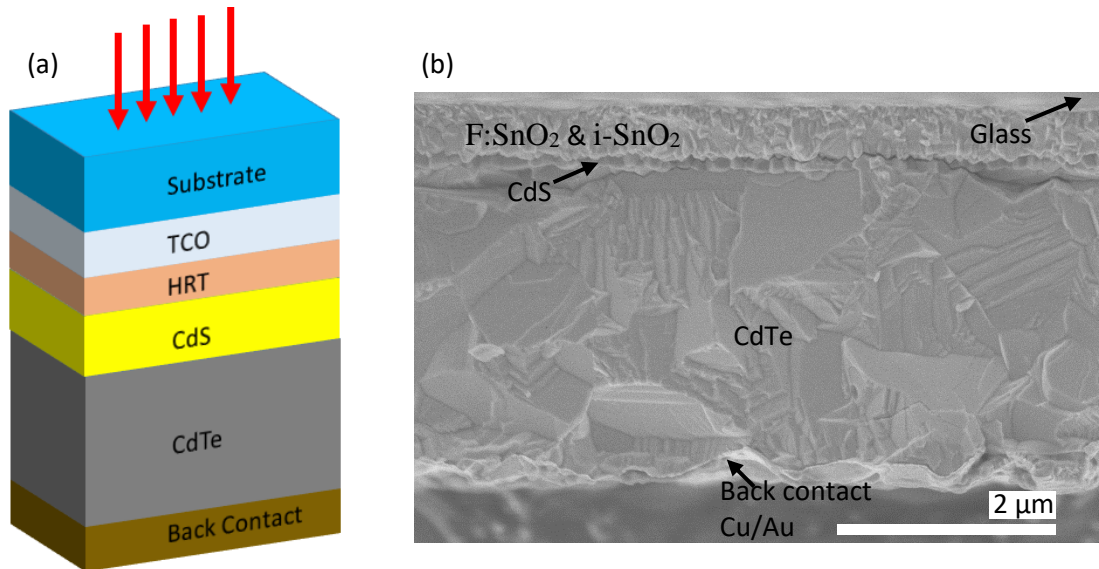


Figure 5-2. (a) Schematic of a regular CdS/CdTe solar cell. (b) Cross sectional SEM image of a CdS/CdTe solar cell with a Cu/Au back contact that used in the study.

The CdTe surface was then covered with 500 μL of MAI in anhydrous IPA at different concentrations ranging from 67.5 mM to 500 mM. After letting the solution sit

on the CdTe layer for 40 s, the sample was spun at 4000 rpm for 20 s to form a thin MAI film on the CdTe surface (Figure 5-3a). The samples were then heated at 110 °C, 125 °C, 150 °C or 175 °C for 10 min (For the 150 °C, different annealing times ranging from 5 min to 20 min were used) (Figure 5-3b), followed by thorough rinsing using anhydrous IPA (Figure 5-3c).

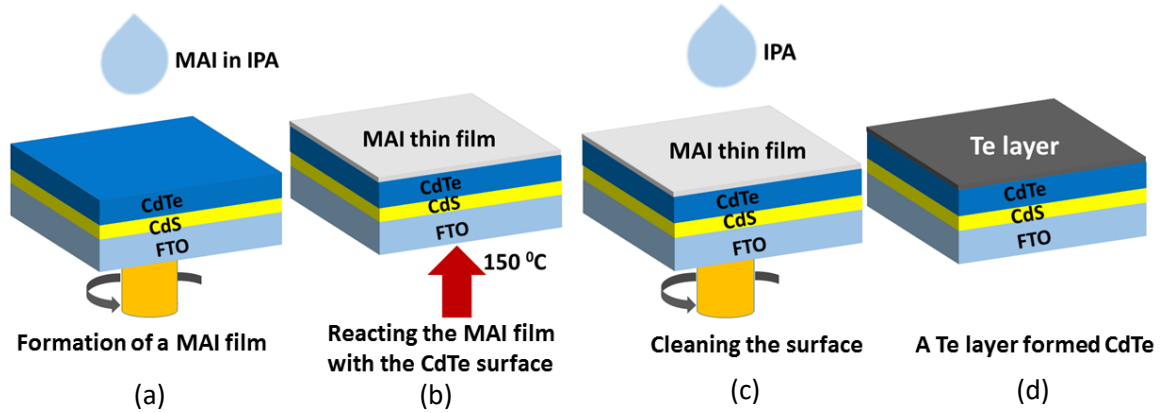


Figure 5-3. (a) Preparation of the MAI thin film on the CdTe surface. (b) Reacting the MAI thin film with the CdTe surface. (c) Removing the access MAI and MA<sub>2</sub>CdI<sub>4</sub> perovskite by IPA, (d) leaving Te on the CdTe surface.

### 5.2.2 Film Characterization

X-ray diffraction (XRD) patterns of the films were recorded from  $2\theta = 20^\circ$  to  $50^\circ$  with a  $0.02^\circ$  step size and a scanning speed of  $0.5^\circ/\text{s}$  using a Rigaku Ultima III X-ray diffractometer. Surface scanning electron microscope (SEM) images of the films were obtained using a field emission scanning electron microscope (Hitachi S-4800). Raman spectra of the films were obtained at room temperature from  $50$  to  $500\text{ cm}^{-1}$  using a LabRam confocal scanning microspectrometer (Horiba-Jobin Yvon) equipped with a He-Ne laser with line excitation at  $632\text{ nm}$ .

### 5.2.3 Solar Cell Preparation

After reacting the MAI thin films with the CdTe surface and cleaning the surface, different thickness (from 0.5 to 5 nm) of Cu and 40 nm of Au were deposited by thermal evaporation without breaking the vacuum. The samples were then annealed at 150 °C for 45 min. Individual cells were scribed on a 3 mm x 3 mm grid. [217] The active area of the fabricated solar cells is 0.08 cm<sup>2</sup>. For the devices with a transparent back electrode, the Cu diffusion was completed prior to the deposition of 125 nm of ITO layer by sputtered from a 3" ITO target (Lesker) onto a room temperature CdTe in an Ar atmosphere with a pressure of 3 mTorr at a 100 W power.

### 5.2.4 Solar Cell Characterization

J-V characteristics were measured using a Keithley 2440 digital source meter and a solar simulator (Newport model 91195A-1000) configured to simulate AM1.5 illumination. A NIST-traceable Si reference solar cell was used to calibrate the light intensity.

### 5.2.5 Low Temperature J-V Measurements

For low temperature J-V measurements the devices were placed in a closed-cycle helium cryostat, and the temperature was varied from 180 to 300 K. A LabVIEW program interfaced to the temperature controller and a Keithley 2400 source-meter allowed for automatic data acquisition. Dark J-V curves were collected while scanning from -0.5 to +1.5 V at 0.01V/s.

### 5.3 Results and Discussion

#### 5.3.1 XRD spectroscopy analysis

XRD was used to investigate the effect of MAI treatment on the CdTe structure. The XRD spectra (Figure 5-4) of the CdTe samples treated with varying concentration of MAI all show three main diffraction peaks at  $2\theta$  of  $23.8^\circ$ ,  $39.3^\circ$ , and  $46.4^\circ$ , corresponding to diffractions from the (111), (220), and (311) crystalline planes of cubic CdTe, respectively. [218] After the MAI treatment, a new XRD peak at  $27.5^\circ$  appeared. This peak is likely due to hexagonal Te (PDF: 97-009-6502) structure, suggesting that MAI treatment selectively removes Cd from the surface.

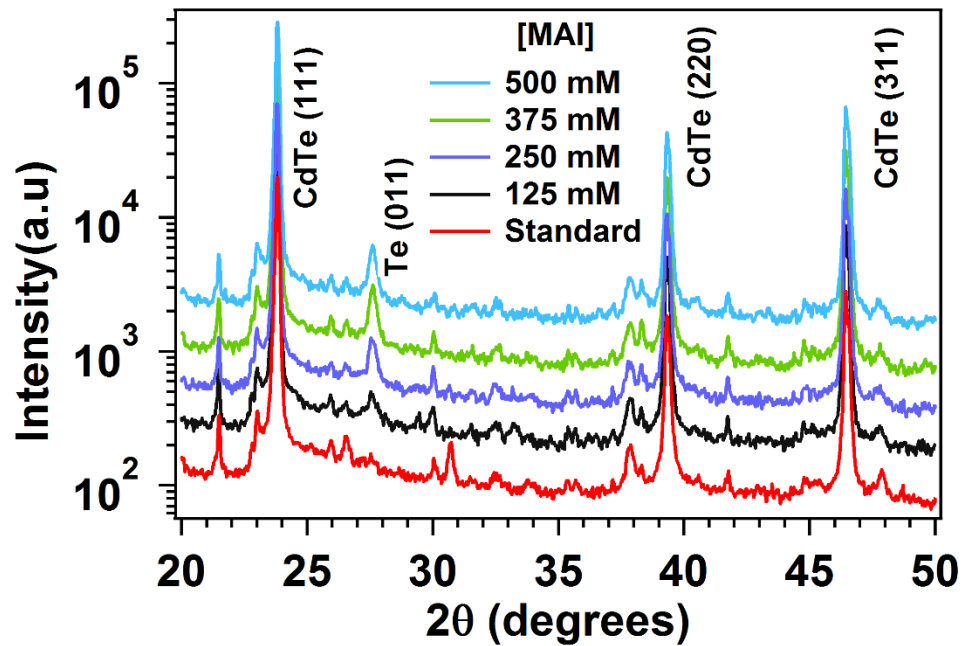


Figure 5-4. X-ray diffraction patterns from MAI treated (using 125 mM, 250 mM, 375 mM, and 500 mM MAI solutions) and untreated CdS/CdTe (standard) samples.

### 5.3.2 Variation of the Surface Morphology

To examine the impact of MAI treatment on the morphology of the CdTe surface, we obtained SEM images (Figure 5-5) of the samples. Figure 5-5a shows the surface morphology of a CdCl<sub>2</sub> treated CdTe sample. The morphology of the CdTe surface dramatically changed after MAI treatment. Figures 5-5b and 5-5c show the surface morphology of a CdTe sample after reacting with a MAI thin film formed by spin coating a 125 mM MAI solution on the CdTe surface. Here, small islands less than 100 nm in diameter were found on the CdTe surface. These islands evidently consist of Te. Reacting the CdTe surface with methylammonium bromide (MABr) (Figure 5-5d) or methylammonium chloride (MACl) (Figure 5-5e) thin films also showed the formation of these small islands. However, the size of the islands decreases in the order MAI > MABr > MACl. To determine at which step these Te islands were formed, MAI was deposited as above, but the sample was rinsed with IPA prior to heating (henceforth referred to as the cleaned sample). Te islands were not observed on these cleaned samples (Figure 5-5f), indicating heating is a necessary step for Cd removal.

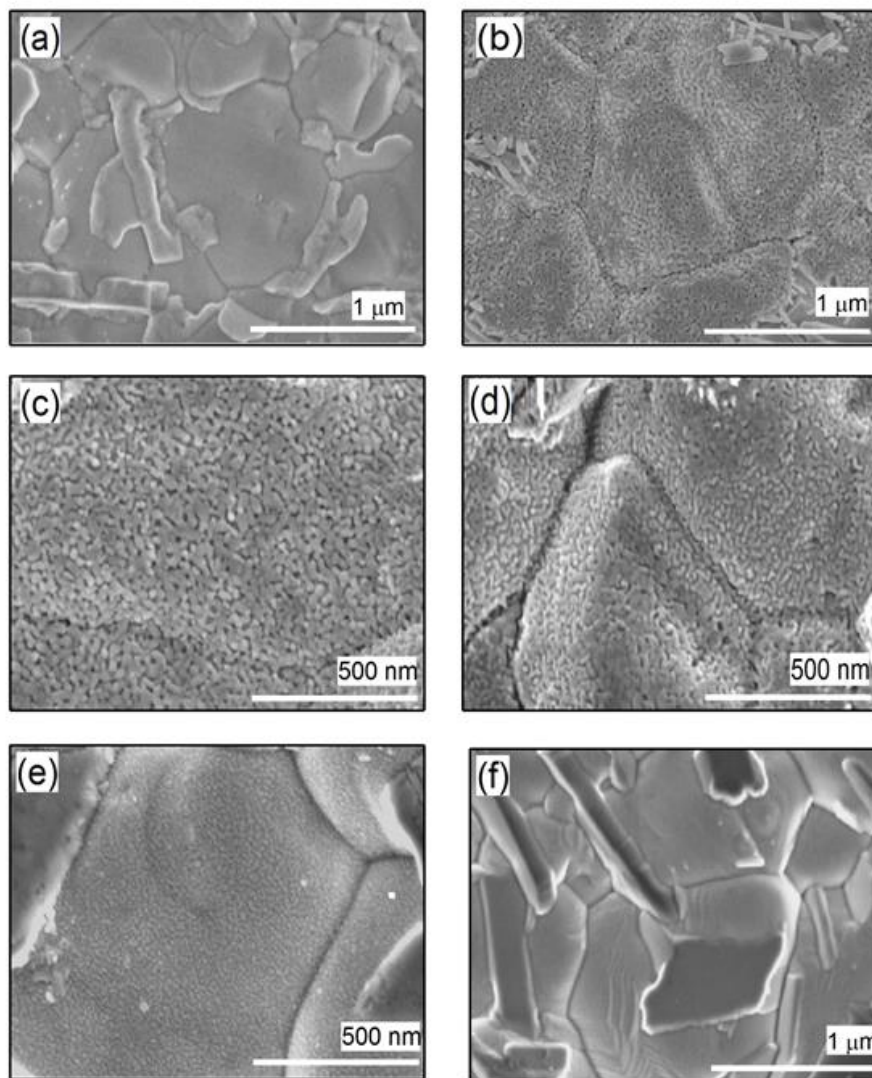


Figure 5-5. SEM images of (a) CdCl<sub>2</sub> treated CdTe sample. Panels (b) and (c) show the surface morphology of a MAI treated sample using a 125 mM MAI solution and heated for 10 min, in low (b) and high (c) magnifications. Panels (d) and (e) show the surface morphology of (d) MABr and (e) MACl treated CdTe samples using 125 mM MABr and MACl solutions, respectively, and heated for 10 min. (f) Surface morphology of a CdTe sample, with the MAI rinsed prior to heating.

### 5.3.3 Raman Spectroscopy Analysis

To better understand the surface of the films, Raman spectroscopy analysis (Figure 5-6) was performed on MAI, MABr, and MACl treated samples using 125 mM MAI, MABr and MACl solutions, respectively and heated for 10 min at 150 °C, a cleaned sample, and a standard. Raman spectra of all the samples showed the presence of LO phonons of CdTe (LO(CdTe)) peak at 165  $\text{cm}^{-1}$  and the E(Te) mode peak at 108  $\text{cm}^{-1}$  [219, 220]. After the MAI, MABr, and MACl treatment, two new distinct peaks appeared at 123  $\text{cm}^{-1}$  and 143  $\text{cm}^{-1}$ . These peaks are likely due to the A(Te) and E(Te) modes [219, 220]. The calculated integrated peak intensity of the highest intense peak at 123  $\text{cm}^{-1}$  was reduced in the order MAI (3245 a.u.) > MABr (746 a.u.) > MACl (666 a.u.), indicating a reduction of the Te volume in the order MAI, MABr, and MACl, respectively. This is consistent with the SEM observation of size reduction of the Te islands in the order MAI > MABr > MACl. Once again, no evidence of the Te islands were observed for the cleaned samples.

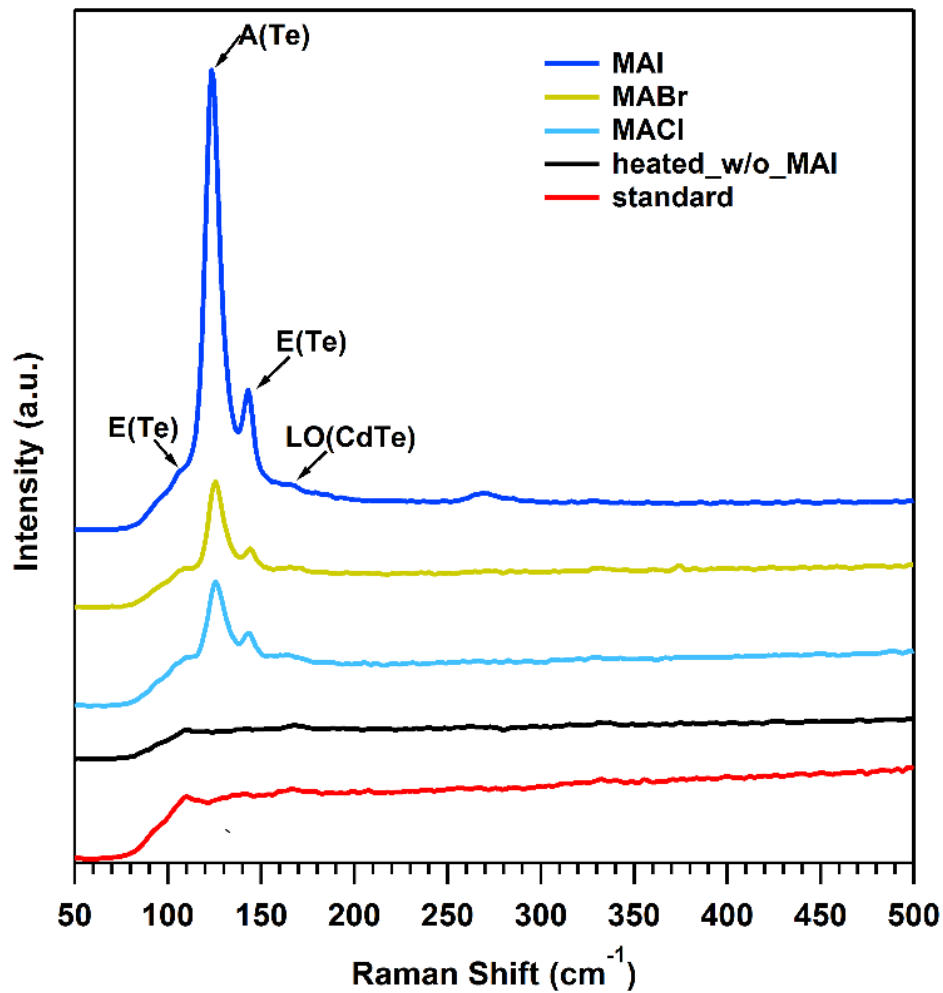


Figure 5-6. Raman spectra from MAI, MABr, and MACl treated samples using 125 mM MAI, MABr and MACl solutions, respectively, and heated for 10 min at 150 °C, a cleaned sample, and a standard.

#### 5.3.4 Formation of a Te Layer

As explained in Chapter 3, MAI, which is one of the main precursors used in the fabrication of lead halide perovskite solar cells, readily forms  $(\text{CH}_3\text{NH}_3)_2\text{CdI}_4$  ( $\text{MA}_2\text{CdI}_4$ ) perovskite with  $\text{Cd}^{2+}$  ions. [79, 80] In those studies, MAI was mixed with  $\text{CdCl}_2$  in an IPA

solution, and  $\text{MA}_2\text{CdI}_4$  perovskite spontaneously formed in solution at room temperature (Figure 5-7).

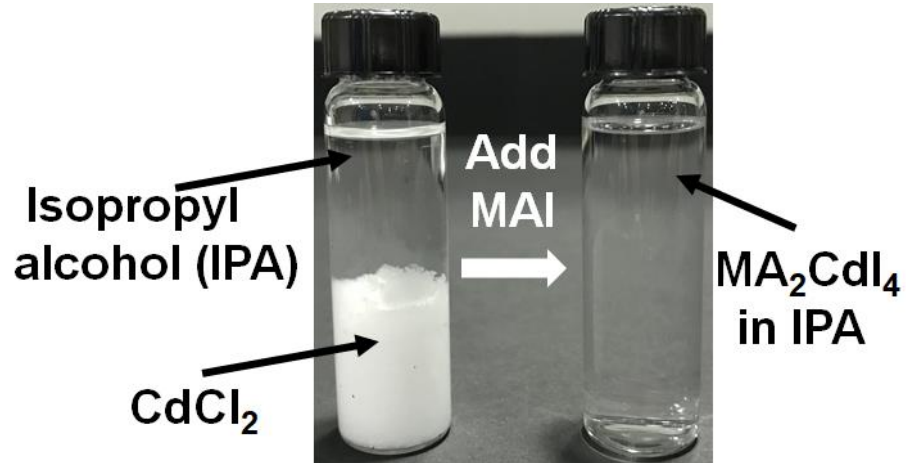
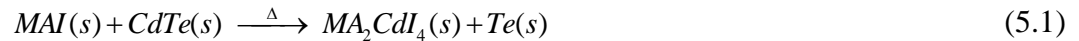


Figure 5-7.  $\text{CdCl}_2$  participation in an IPA solution and complete dissolution with the addition of MAI due to the formation of  $\text{MA}_2\text{CdI}_4$  perovskite.

Here, the data from the cleaned samples indicate that the perovskites do not spontaneously form in solution. The Te island formation only occurs after the sample was heated. Therefore, the formation of a Te layer can be explained by the following reaction (Figure 5-8a).



Because,  $\text{MA}_2\text{CdI}_4$  perovskite is soluble in IPA[79, 80], the  $\text{MA}_2\text{CdI}_4$  can be rinsed, leaving a Te layer behind on the CdTe film (Figures 5-8b, 5-3d & 5-5b,c ). The formed Te layer is ~80 nm thick, as determined from the cross-sectional SEM images (Figure 5-9).

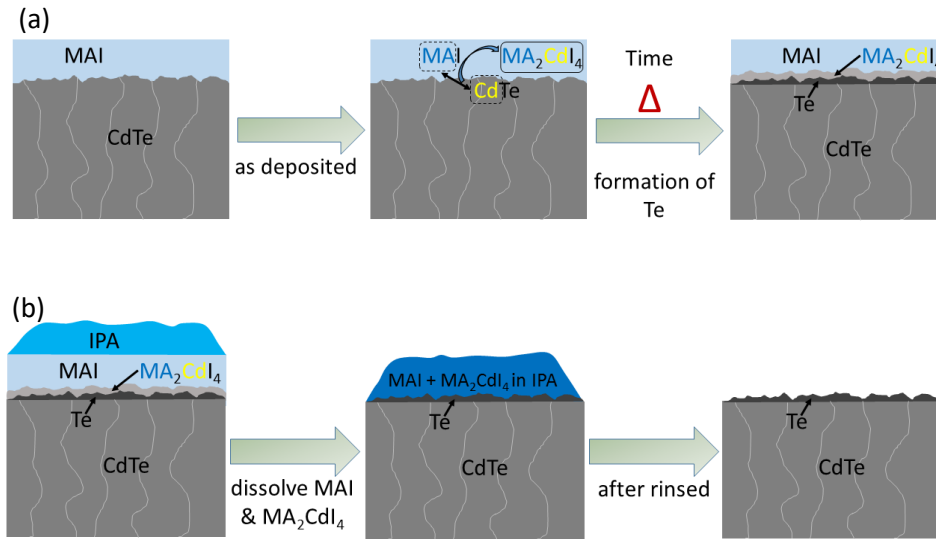


Figure 5-8. (a) Extracting Cd from the CdTe surface by forming  $MA_2CdI_4$ . (b) Removing  $MA_2CdI_4$  and excess MAI.

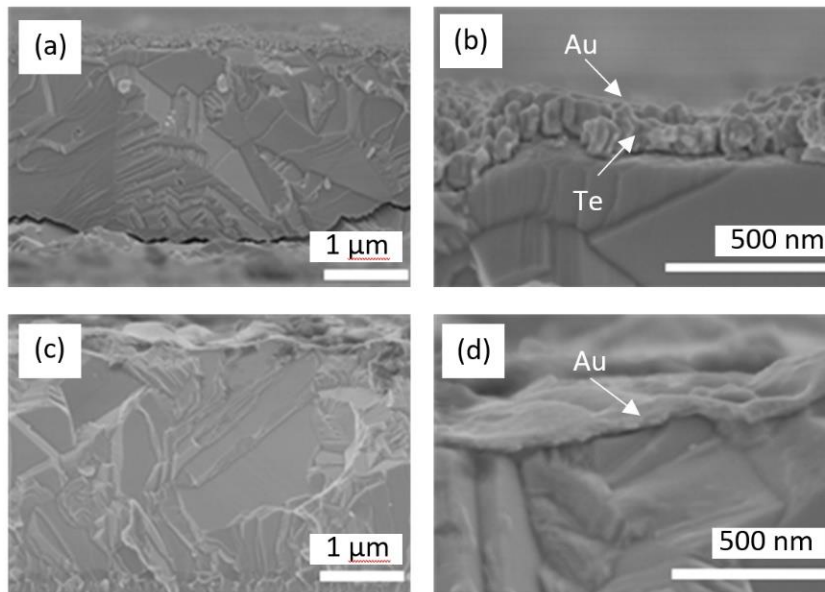


Figure 5-9. Cross-sectional SEM images of (a) & (b) MAI treated and (c) & (d) untreated CdTe devices. Note that the Au layer is clearly visible in the untreated sample, but in the treated sample, Au is decorated the Te layer.

The MAI treatment appears to be self-limiting as significant changes in the surface morphology images were not observed with changes in the MAI concentration (Figure 5-10). One reason could be that as the Te layer grows, it may form a capping layer for the CdTe, blocking the contact between the CdTe and the MAI film, hindering the formation of additional Te. Another reason could be that the MAI source was exhausted during the reaction and that sufficiently high quantities were not tested here to show significant differences in Te thickness.

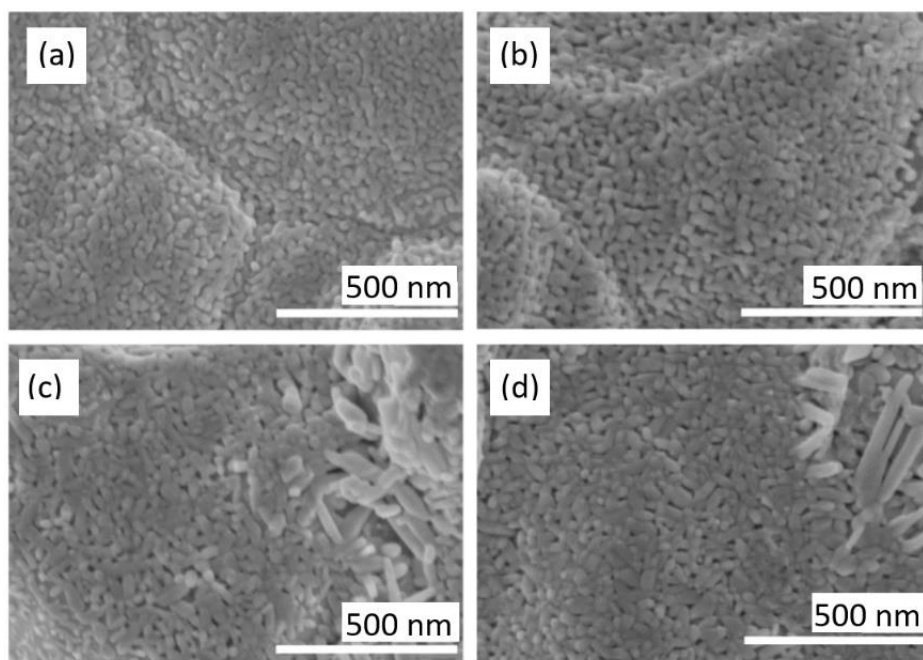


Figure 5-10. Surface SEM images of MAI treated CdTe samples with (a) 125 mM, (b) 250 mM, (c) 375 mM, and (d) 500 mM MAI solutions.

Similar to MAI, MABr and MACl also form Te-rich surface by forming  $\text{MA}_2\text{CdBr}_4$  and  $\text{MA}_2\text{CdCl}_4$  perovskites, respectively. However, SEM and Raman spectroscopy analysis showed that the yield of the Te is reduced in the order  $\text{MAI} > \text{MABr} > \text{MACl}$ .

Since all the processing was similar for these reactions, the data indicates that the formation energy of  $\text{MA}_2\text{CdX}_4$  (where X is I, Br, or Cl) perovskites reduces in the order  $\text{Cl} > \text{Br} > \text{I}$ .

It is clear that the MAI treatment selectively removes the Cd from the CdTe surface through an interaction with the methyl ammonium. It is likely that any defects at this surface would exist in a higher energy state and be most susceptible to treatment and removed first. This would suggest that Te layers created through the MAI treatment process should not only be in better electrical contact with the CdTe underneath due to selective removal of Cd, but also have fewer interface defects than a Te layer deposited onto the CdTe surface. As a result, better electrical properties at the back junction can be expected in the devices with a Te layer formed using this method than devices with an evaporated or sputtered Te layer.

### 5.3.5 Device Performances

Complete devices were fabricated to study the effect of MAI treatment on the device performances. Figure 5-11 shows the open circuit voltage ( $V_{\text{OC}}$ ), short circuit current density ( $J_{\text{SC}}$ ), Fill Factor (FF), and PCE data for devices reacted with MAI thin films fabricated with various MAI concentrations and reaction times with the 150 °C reaction temperature. Samples treated with 125 mM MAI solution and heated for 10 min achieved the highest average  $V_{\text{OC}}$ , FF, and PCE of  $824 \pm 3$  mV,  $77.1 \pm 0.6\%$ , and  $13.0 \pm 0.2\%$ , respectively. The average  $V_{\text{OC}}$ , FF, and PCE for devices made without MAI treatment were  $771 \pm 12$  mV,  $74.2 \pm 1.8\%$ , and  $11.8 \pm 0.4\%$ , respectively. The highest efficiency of 13.5% with  $V_{\text{OC}}$  of 829 mV,  $J_{\text{SC}}$  of  $20.8 \text{ mA/cm}^2$ , and a FF of 78.1% was also achieved using a 125 mM MAI solution with the 10 min reaction time. The best standard

device prepared without treating the CdTe surface had a PCE of 12.7% with a  $V_{OC}$  of 799 mV, a  $J_{SC}$  of 21.0 mA/cm<sup>2</sup>, and a FF of 75.9%.

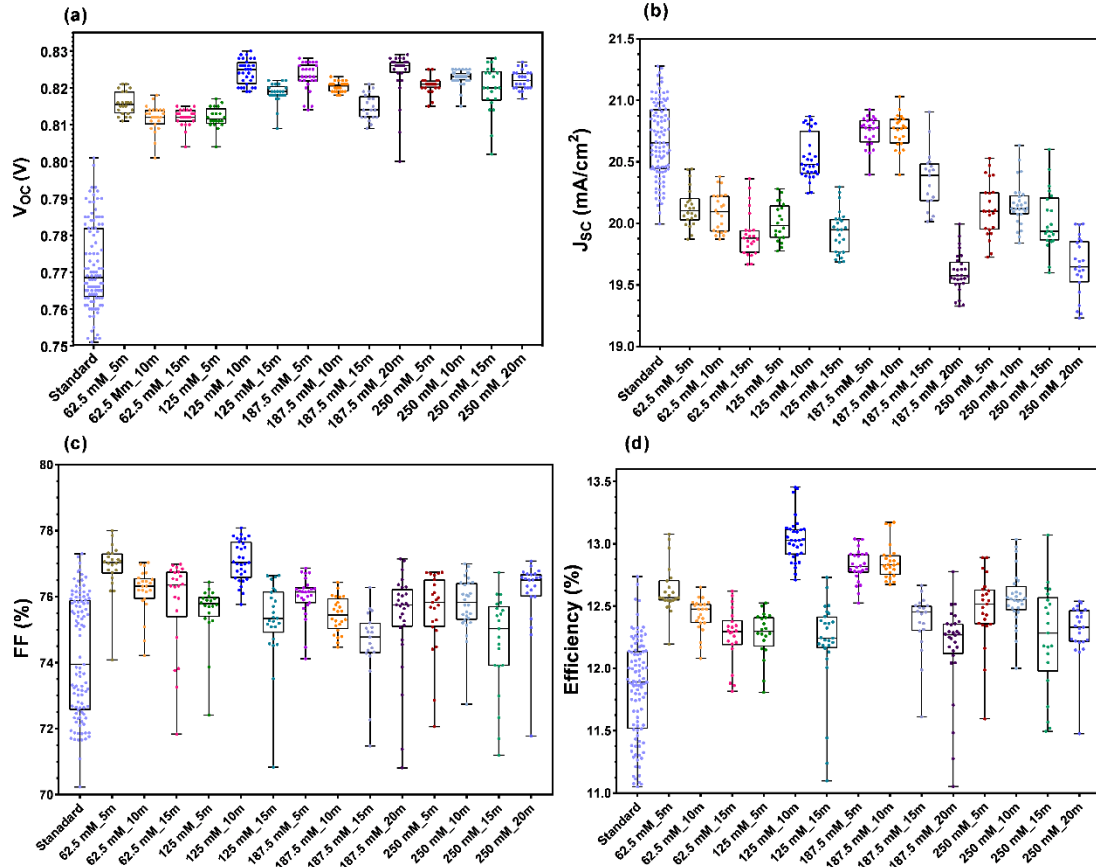


Figure 5-11. Photovoltaic performances of (a)  $V_{OC}$ , (b)  $J_{SC}$ , (c) FF, and (d) PCE of MAI treated (with various concentrations and reaction times) and untreated CdS/CdTe devices. Note that the average values presented in the figure were derived from measurements on more than 20 devices.

We then used these parameters to optimize the reaction temperature. Table 5.1 summarize the photovoltaic parameters and device efficiencies for different reaction temperatures. The 3 nm of Cu, which is the optimum thickness for our device standard,

was used in these devices and to determine the optimum concentration and reaction time (Note that the average and champion device performance of the standard changed in this study due to a change in the commercial vapor transport deposition process, which used to deposit the CdS and CdTe layers.)

Table 5.1: Device parameters for different reaction temperatures (At least 20 devices were measured for the average).

<b>Temp</b>	<b>Voc (mV)</b>	<b>Jsc (mA/cm<sup>2</sup>)</b>	<b>FF (%)</b>	<b>Eff (%)</b>
<b>Standard</b>	796 ± 14	21.1 ± 0.2	74.6 ± 2.0	12.5 ± 0.4
Best	811	21.3	75.6	13.0
MAI treated at				
<b>110 °C</b>	818 ± 5	21.2 ± 0.2	76.2 ± 0.8	13.2 ± 0.2
Best	821	21.7	76.7	13.7
<b>125 °C</b>	828 ± 3	21.2 ± 0.2	76.6 ± 1.3	13.5 ± 0.3
Best	830	21.5	77.5	13.8
<b>150 °C</b>	827 ± 3	21.2 ± 0.4	75.6 ± 1.2	13.3 ± 0.3
Best	826	21.7	75.7	13.5
<b>175 °C</b>	826 ± 4	21.1 ± 0.6	74.9 ± 1.2	13.0 ± 0.4
Best	833	21.4	75.8	13.5

For all treatment temperatures, the treated samples showed higher average  $V_{oc}$  than the standard samples. FF improved with the treatment up to 125 °C, above which it began to decrease. The  $J_{sc}$  was not affected by the MAI treatment, indicating that the photocurrent generation in the CdS/CdTe devices is independent of the nature of the back junction of the device. Treatment at 125 °C resulted in the best performing devices with highest

average  $V_{OC}$ , FF, and PCE of  $828 \pm 3$  mV,  $76.6 \pm 1.3\%$ , and  $13.5 \pm 0.3\%$ , respectively. The highest efficiency of 13.8% with a  $V_{OC}$  of 830 mV, a  $J_{SC}$  of  $21.5 \text{ mA/cm}^2$ , and a FF of 77.5% was also obtained with the  $125 \text{ }^\circ\text{C}$  reaction temperature. Interestingly, a significant change in the  $V_{OC}$  was not observed for devices treated above  $125 \text{ }^\circ\text{C}$ , indicating nearly identical back contact formation.

The back contact of the devices is completed by depositing 3 nm of Cu and 40 nm of Au followed by a diffusion step at  $150 \text{ }^\circ\text{C}$ . This temperature is insufficient to form  $\text{Cu}_x\text{Te}$  [205-207] (Figure 5-12), so Cu is directly diffused through the Te layer into the CdTe absorber.[205] Therefore, the back junction of our devices is likely to consist of a Cu-doped CdTe (CdTe:Cu) surface with a Te layer. Doping the CdTe surface by Cu as a  $p^+$  region reduces the band bending at the back of the device and narrows the back barrier (Figure 5-1e,f).[203] By conducting the numerical simulation using the SCAPS-1D software, Sites et al. demonstrated a reduction in downward valance-band bending from the low work function metal to the p-type CdTe with the formation of Te layer (Figure 5-13).[204, 221] Since the amount of Cu in each of these devices is nominally the same and the Cu does not react with the Te, the interface between the CdTe and Te are expected to be equal. Improvements in  $V_{OC}$  and FF for the treated devices can, therefore, be attributed to the reduced downward valance-band bending from the Au to the p-type CdTe with the formation of Te layer.[204, 221]

For treatment temperatures above  $125 \text{ }^\circ\text{C}$ , the FF, unlike the  $V_{OC}$ , begins to decrease. It is possible that the rapid reaction at high temperature may result in additional etching at the grain boundaries, which decreases the shunt resistance.

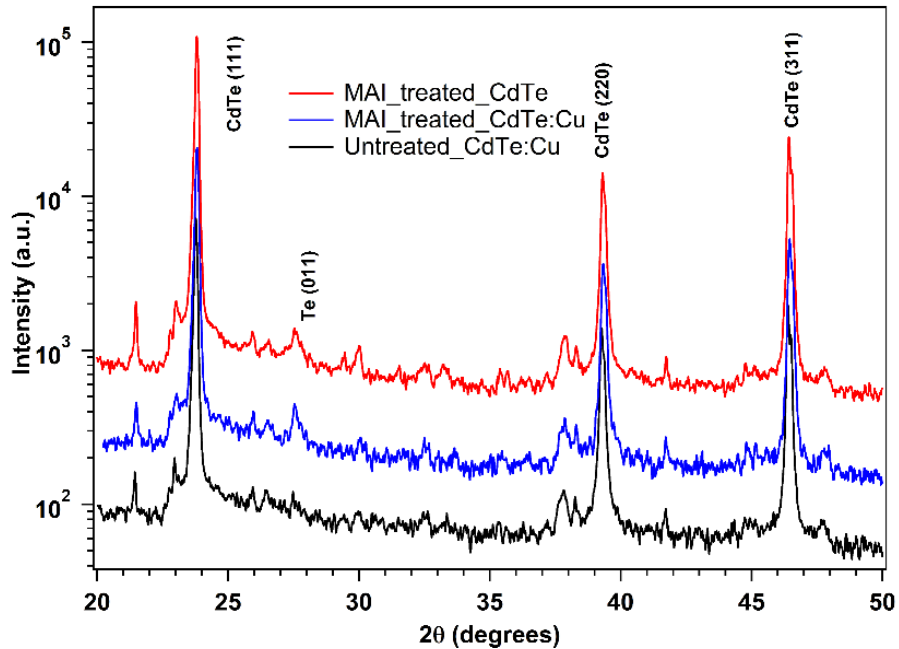


Figure 5-12. XRD of Cu-doped CdTe from MAI treated (using 125 Mm MAI solution) and untreated samples, and MAI treated CdTe without Cu doping. Note that the Cu<sub>x</sub>Te peaks were not observed.[205-207]

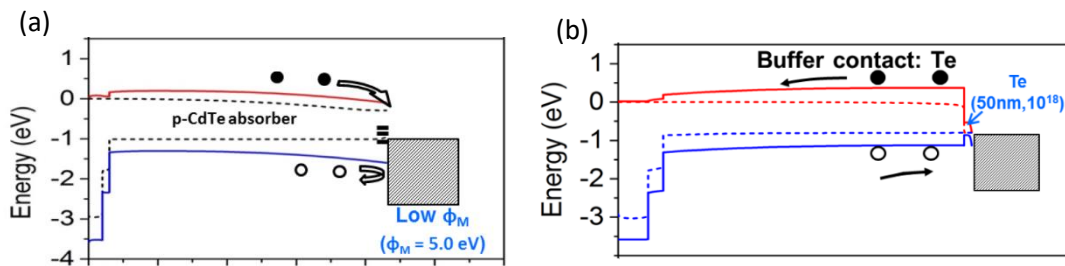


Figure 5-13. Energy-band diagrams for a CdS/CdTe device at 0.8-V bias under illumination (a) without and with (b) a Te buffer layer. © 2017 IEEE. Reprinted, with permission, from Tao Song and James R. Sites, Role of Tellurium Buffer Layer on CdTe Solar Cells' Absorber/Back-Contact Interface, in IEEE 44<sup>th</sup> Photovoltaic Specialists Conference (PVSC), 2017 June 25-30.[221].

The Cu thickness for the devices treated with 125 mM MAI solution and heated for 10 min at 125 °C was also optimized. The results are shown in the Table 5.2.

Table 5.2: Device performances for different amount of Cu. Note that the average values presented in the table were derived from measurements on more than 20 devices.

<b>Cu thickness</b>	<b>Voc (mV)</b>	<b>Jsc (mA/cm<sup>2</sup>)</b>	<b>FF (%)</b>	<b>Eff (%)</b>
Without MAI treated				
<b>0 nm</b>	649 ± 14	20.4 ± 0.3	68.4 ± 0.9	9.0 ± 0.3
Best	668	20.7	69.5	9.6
<b>3 nm</b>	796 ± 14	21.1 ± 0.2	74.6 ± 2.0	12.5 ± 0.4
Best	811	21.3	75.6	13.0
With MAI treated				
<b>0 nm</b>	775 ± 3	20.0 ± 0.1	70.7 ± 0.6	11.0 ± 0.1
Best	774	20.3	71.0	11.2
<b>0.5 nm</b>	817 ± 5	21.8 ± 0.1	75.3 ± 0.8	13.4 ± 0.2
Best	820	21.9	76.3	13.7
<b>1 nm</b>	821 ± 5	21.7 ± 0.1	74.9 ± 0.9	13.3 ± 0.2
Best	828	21.8	76.1	13.7
<b>2 nm</b>	834 ± 2	21.4 ± 0.2	77.2 ± 0.9	13.8 ± 0.2
Best	831	21.8	77.9	14.1
<b>3 nm</b>	828 ± 3	21.2 ± 0.2	76.6 ± 1.3	13.5 ± 0.3
Best	830	21.5	77.5	13.8
<b>4 nm</b>	821 ± 2	21.5 ± 0.1	76.6 ± 0.7	13.5 ± 0.2
Best	821	21.6	77.5	13.7
<b>5 nm</b>	814 ± 4	21.5 ± 0.2	76.5 ± 1.1	13.4 ± 0.2
Best	821	21.9	76.4	13.7

The untreated devices without Cu showed low  $V_{OC}$  and FF values, resulting poor PCEs due to the high back contact barrier [199-203] and band bending (Figures 5-13a & 5-1d). However, dramatic improvements in the average  $V_{OC}$  (126 mV) and FF (2.3) were observed with MAI treatment even when Cu was not used at the back contact. This is consistent with the literature and attributed to an enhanced charge carrier collection due to the reduced downward valance-band bending from the low work function Au to p-type CdTe (Figure 5-13b & 5-1g).[204, 221] With the deposition of Cu,  $V_{OC}$  and FF further improved, and 2 nm of Cu showed the highest average  $V_{OC}$ , FF, and PCE of  $834 \pm 2$  mV,  $77.2 \pm 0.9\%$ , and  $13.8 \pm 0.2\%$ , respectively. The champion device efficiency of 14.1% with  $V_{oc}$  of 831 mV,  $J_{SC}$  of  $21.8 \text{ mA/cm}^2$ , and FF of 77.9% was also achieved with 2 nm of Cu. For devices with more than 2 nm of Cu, the average  $V_{OC}$  decreased gradually, though the FF appeared to saturate.

Since the Cu diffuses through the Te layer, it acts as a dopant in the CdTe. The primary mechanism for this is Cu substitution on Cd site as an acceptor.[208] However, p-type doping of the CdTe is highly compensated by the formation of various other defects and complexes.[204] The reduction in Cu for the devices with a Te layer compared to the standard is consistent with the literature and attributed to reduced compensation from Cu. [204] The p-type doping of the CdTe first decreases, then increases, and then again decreases with increasing amounts of diffused Cu.[222] The  $V_{OC}$  drop observed for more than 2 nm of Cu is likely due to reduced p-type doping of the CdTe, which increases the band bending and barrier height at the back contact (Figure 5-1e & f).

In addition to the improvements in the  $V_{OC}$ , FF, and PCE, the standard deviations of these photovoltaic parameters for the optimized devices were also reduced with the MAI treatment. This is due to the precise control of the Cd removal process.

#### 4.3.6 Devices with Transparent Back Contact

Since the Te layer reduces the downward valance-band bending from the back electrode to p-type CdTe, ITO was investigated as a back electrode for MAI treated CdTe devices. Previous attempt to use a Te layer between ITO and CdTe for transparent devices required the use of a  $Cu_xTe$  layer.[223] Here, we formed a Te layer at the back interface of the device using the MAI treatment, followed by Cu diffusion, and deposition of an ITO layer. Control samples without any surface treatment were also fabricated for comparison. Device performances with and without MAI treatment are summarized in the Table 5.3.

Without any surface treatment, the control devices without Cu showed poor performances  $\sim 5.0\%$  PCE with low  $V_{OC}$  and FF. With the Cu doping,  $V_{OC}$  and FF improved dramatically, resulting a  $\sim 11.0\%$  champion device efficiency, due to a reduced Schottky barrier at the back contact with the p-type doping of the CdTe. With MAI treatment, significant improvements in  $V_{OC}$  and FF, compared to the untreated devices, were observed and can be attributed to the reduced recombination due to the reduction in downward valance-band bending from the ITO to the p-type CdTe (Figures 5-13b & 5-1g).[221] Use of a CdTe:Cu surface with the Te layer further increased the  $V_{OC}$  and FF. The  $V_{OC}$  of these devices were compatible with the Au counterpart, but the FF values were lower due to the higher sheet resistance of the ITO ( $\sim 35 \Omega/sq.$ ). The best PCE for devices

made with ITO back electrode was 12.2% with  $V_{OC}$  of 823 mV,  $J_{SC}$  of 21.4 mA/cm<sup>2</sup>, and FF of 69.3%.

Table 5.3: The J-V Parameters for ITO back electrode. Note that the average was taken from the results of more than 20 cells for each back contact structure.

<b>ITO with:</b>	<b>Voc (mV)</b>	<b>Jsc (mA/cm<sup>2</sup>)</b>	<b>FF (%)</b>	<b>Eff (%)</b>
<b>Without MAI treated</b>				
<b>CdTe</b>	471 ± 23	20.4 ± 0.4	51.3 ± 2.3	4.9 ± 0.3
Best	483	21.2	52.6	5.4
<b>CdTe:Cu</b>	810 ± 4	21.1 ± 0.4	57.2 ± 4.3	9.8 ± 0.7
Best	807	21.2	64.4	11.0
<b>With MAI treated</b>				
<b>CdTe</b>	748 ± 13	21.0 ± 0.4	57.9 ± 4.2	9.1 ± 0.8
Best	757	21.2	61.8	10.0
<b>CdTe:Cu</b>	820 ± 3	21.3 ± 0.2	66.3 ± 2.5	11.6 ± 0.5
Best	823	21.4	69.3	12.2

Further, the transmittance reduction caused by the MAI treatment in the near infrared (NIR) region is only ~6%. (Figure 5-14). Therefore, MAI treatment is a potential technique for the fabrication of high performance transparent CdTe solar cells that use in tandem solar cell or window applications.

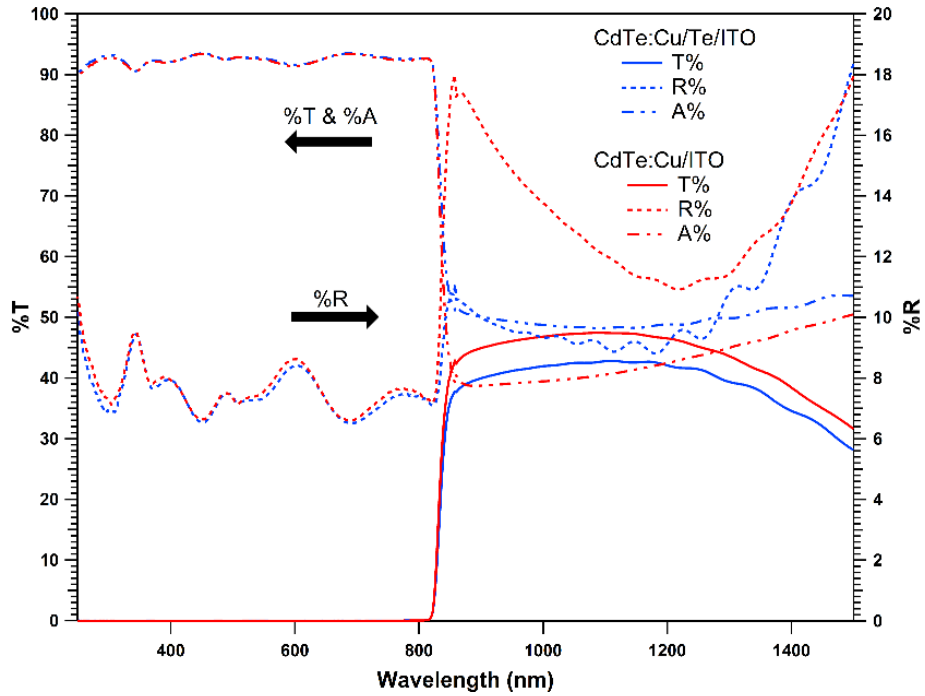


Figure 5-14. Transmittance, absorbance, and reflectance of the MAI treated and untreated CdS/CdTe devices completed with the ITO back electrode.

#### 4.3.7 Back Contacts Barrier Height

To understand the effect of MAI treatment on the back contact barrier height ( $\phi_b$ ), the temperature dependent J-V measurements (measured the temperature dependence of the current when the device placed in forward bias) were conducted, and the method that described by Niemegeers and Burgelman [224] was used to process the data. A quantitative assessment of  $\phi_b$  was determined by considering that the carrier transport is controlled by thermionic emission. In this case, the current through the interface is governed by the following equation.

$$J_c \propto T^2 \exp\left(\frac{-e\Phi_b}{k_B T}\right) \quad (5.2)$$

$\ln(J/T^2)$  vs.  $1/k_B T$  was plotted and the slope of the linear fit for the data was used to estimate the  $\phi_b$  (Figure 5-15). Table 5.4 shows the calculated  $\phi_b$  for the champion devices from the untreated-CdTe/Cu/Au (standard, CdTe:Cu/Au), MAI-treated-CdTe/Au (CdTe/Te/Au), MAI-treated-CdTe/Cu/Au (CdTe:Cu/Te/Au), untreated-CdTe/Cu/ITO (CdTe:Cu/ITO), and MAI-treated-CdTe/Cu/ITO (CdTe:Cu/Te/ITO). Figure 5-16 shows the J-V characteristics of these champion devices captured under a standard AM 1.5G illumination ( $100 \text{ mW/cm}^2$ ) at room temperature.

Table 5.4: Back contact barrier height for devices made with and without MAI treatment.

Device	$\phi_b$ (eV)
CdTe:Cu/Au	$0.344 \pm 0.010$
CdTe/Te/Au	$0.293 \pm 0.010$
CdTe:Cu/Te/Au	$0.198 \pm 0.007$
CdTe:Cu/ITO	$0.246 \pm 0.005$
CdTe:Cu/Te/ITO	$0.130 \pm 0.001$

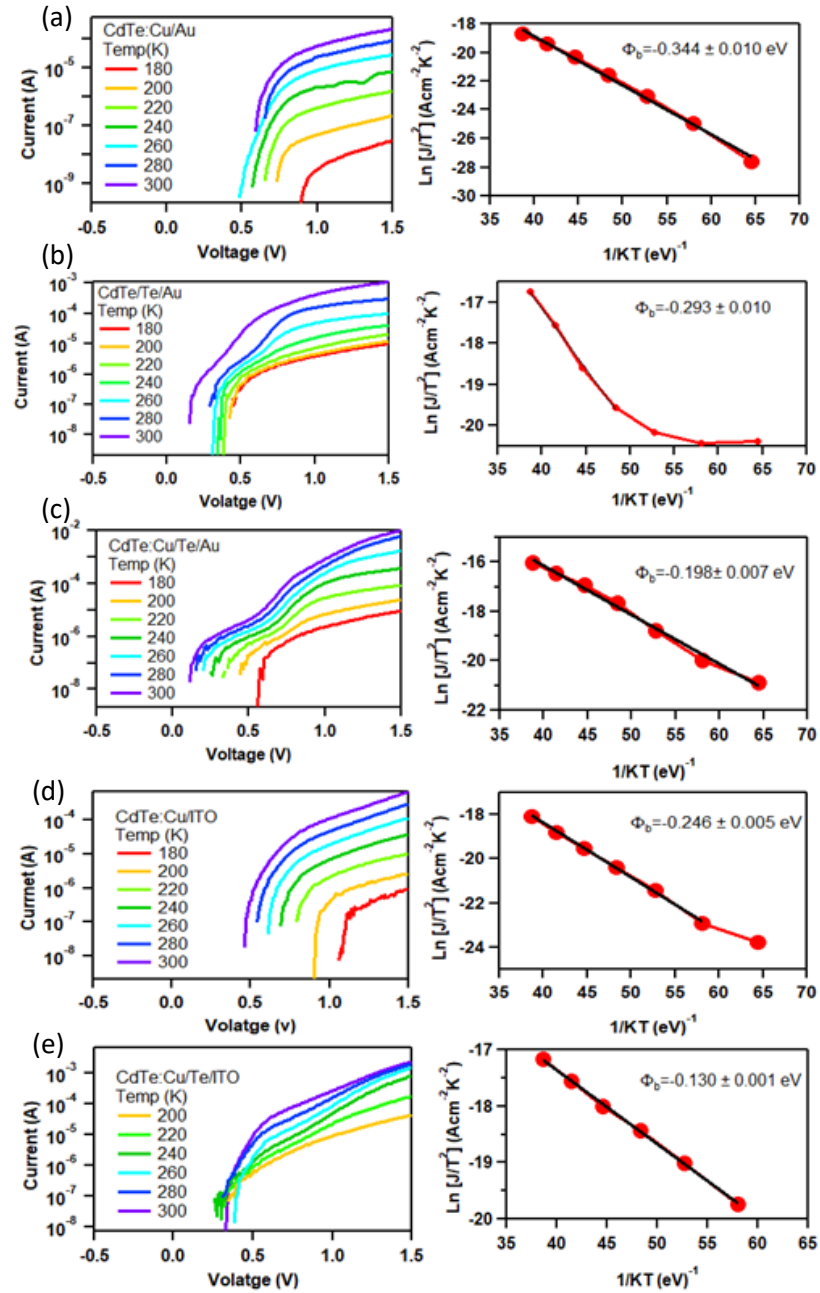


Figure 5-15. Temperature dependence dark current-voltage (J-V) characteristics and corresponding  $\ln(J/T^2)$  vs.  $1/k_B T$  plots (at 1V) for CdS/CdTe solar cells with (a) CdTe:Cu/Au, (b) CdTe:Te/Au (c) CdTe:Cu/Te/Au, (d) CdTe:Cu/ITO, and (e) CdTe:Cu/Te/ITO back junctions (The current is presented on a logarithmic scale). Note that the black line is the linear fit to the data.

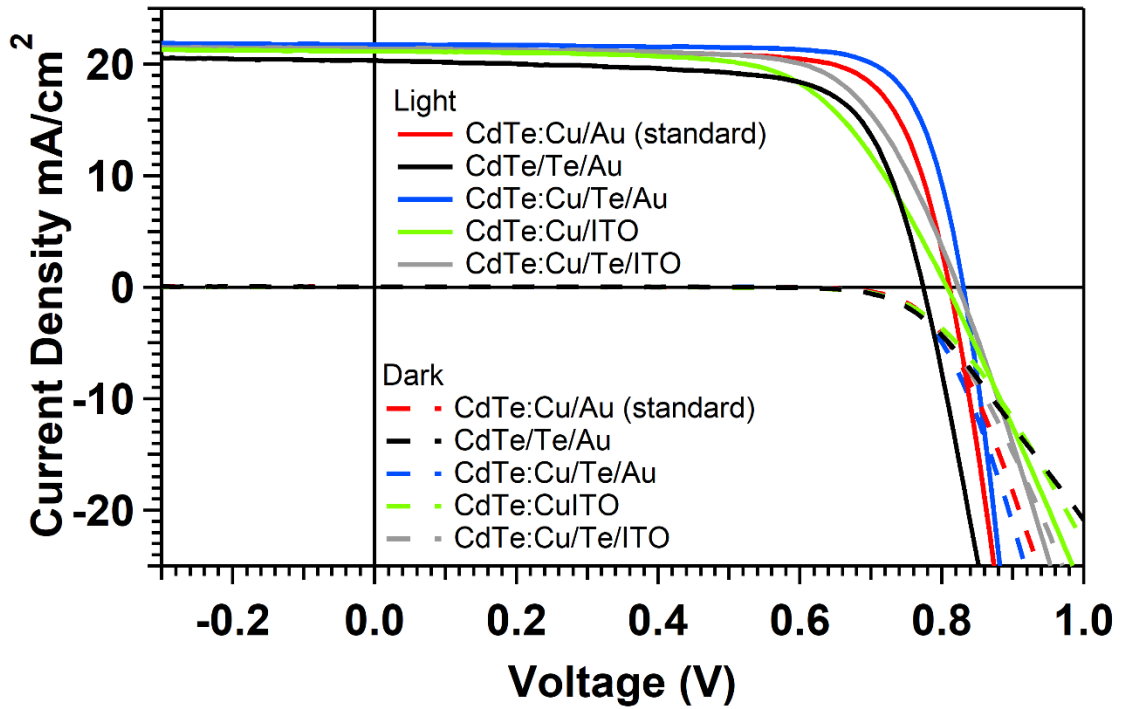


Figure 5-16. J-V characteristics of champion devices from the MAI treated and untreated CdS/CdTe samples with Au or ITO back electrodes.

The barrier height of 344 meV for the CdTe:Cu/Au is consistent with reported values. [201, 225, 226]. When Te layer is added between the CdTe and Au through the MAI treatment, the barrier was reduced by 51 meV without even Cu doping. This is consistent with the simulation of Sites et al. that the downward valence-band bending from the low work function metal to the p-type CdTe reduces with the addition of Te buffer (Figure 5-13)[204, 221], reducing the back contact barrier. However, the device performances from the CdTe/Te/Au were lower than the devices from CdTe:Cu/Au. The back interface recombination, depends not only on  $\phi_b$ , but also on  $w\phi_b$ . Although the  $\phi_b$  is lowered with the addition of a Te buffer, the  $w\phi_b$  may not be narrowed compared to the

Cu-doped devices without Te buffer (Figure 5-1e,f, & g), resulting a higher back interface recombination in the devices with CdTe/Te/Au back junction than the CdTe:Cu/Au standards. This is likely to be the reason for the low performances in the devices, which contained a Te buffer layer without Cu doping than the standard Cu-doped CdTe devices without a Te layer.

When the MAI treated CdTe absorber is doped by Cu, the barrier was further reduced by 95 meV. This barrier reduction should be accompanied by a further reduction in band bending of the valance band, which will reduce the amount of recombination at the back surface (Figure 5-1g-i). Interestingly, for the untreated CdTe samples,  $\phi_b$  for the ITO back contact device was  $\sim 100$  meV lower the standard Au electrode, indicating the band alignment of ITO is better than that of Au. The ITO  $\phi_b$  was further reduced with the MAI treatment, yielding the lowest barrier of the devices measured at 130 meV, over 60% below the standard device configuration. This result suggests that with further optimization, the MAI treated CdTe devices with a transparent back contact may perform as well or better than CdTe:Cu/Te/Au devices. Furthermore, this reduced barrier and band bending should become more important as the CdTe thickness is reduced for window applications.

#### **5.4 Conclusion**

We have shown that methylammonium iodide (MAI) can be simply and controllably reacted with CdTe surfaces to form a Te layer. MAI extracts Cd from the CdTe surface by forming the  $(\text{CH}_3\text{NH}_3)_2\text{CdI}_4$  perovskite. SEM and Raman spectra confirmed that thermal annealing is required for this reaction to occur. It was found that reacting a MAI thin film formed by spin-coating a 125 mM MAI solution with the CdTe surface at 125 °C

for 10 min was the optimum MAI treatment. The optimized Cu thickness that used to dope the CdTe surface for the treated devices was 2 nm.

The technique was successfully applied to increase the performance of CdS/CdTe devices with an ITO back electrode. The back barrier height reduced with the MAI treatment for the devices with both Au and ITO back electrodes. Higher  $V_{OC}$  and FF resulted in higher PCEs of 14.1% and 12.2% for the Au and ITO back contacts, respectively, in the MAI treated devices, compared to the champion standard devices prepared without any surface treatment of 13.0% and 11.0% for the Au and ITO electrodes, respectively. Further, only ~6% reduction in transmittance in the near infrared (NIR) region was observed with the MAI treatment for the CdS/CdTe devices with an ITO back electrode. Therefore, this technique can be applied to fabricate high performance transparent CdTe solar cells for tandem solar cell or window applications.

## Chapter 6

### Summary and Future Research

#### 6.1 Thesis Summary

This thesis has investigated the solution processing of methylammonium lead halide perovskite and back interface engineering for high efficiency cadmium telluride solar cells. The study started with the investigation of nucleation and growth mechanisms associated with the two-step deposition method, which was the widely used deposition technique at the time of the study, for preparing perovskite films, and several nucleation and growth mechanisms were proposed. We showed that the nucleation rate and the critical size of the perovskite nuclei are dependent on the concentration of the MAI solution. Large perovskite grains with random orientations are formed when a low concentration MAI solution is introduced. Once the MAI concentration is increased, the critical nucleus size decreases and a dense blocking layer of  $\text{MAPbI}_3$  is formed on the  $\text{PbI}_2$  layer. Consequently, the penetration of MAI molecules is hindered. Further increase in the MAI concentrations leads to the formation of the low-dimensional perovskites at grain boundaries which facilitates the diffusion of MAI molecules in to the  $\text{PbI}_2$  layer and improves the perovskite conversion.

However, polycrystalline perovskite thin films fabricated from this method are consisted of small grains that increases the grain boundaries, resulting a higher charge trap states. To reduce the density of trap states that controls non-radiative recombination, it is important to prepare perovskite films consisting of large-sized grains with a high degree of crystallinity. In the second study, we show that the addition of small concentrations of  $\text{Cd}^{2+}$  in the methylammonium iodide precursor solution during the two-step sequential deposition can significantly improve the grain size and crystallinity of methylammonium lead iodide perovskite thin films. The grains are highly oriented in the  $\langle 110 \rangle$  direction compare to films produced by the standard two-step deposition, indicating a change in the growth mechanism. Time resolved photoluminescence measurements indicated a dramatic increase in the carrier lifetime which can be attributed to a reduction in the active trap density. The effect of improved charge carrier lifetime on the device performances were tested using an unoptimized  $\text{TiO}_2$  bilayer. Highly reproducible photovoltaic devices were obtained from the Cd-modified perovskites with a 13.8% device efficiency, while only 7.1% PCE was obtained from the standard two-step process.

In addition to  $\text{Cd}^{2+}$ , inclusion of  $\text{Fe}^{2+}$ ,  $\text{Co}^{2+}$ ,  $\text{Cu}^{2+}$ ,  $\text{Zn}^{2+}$ , and  $\text{Hg}^{2+}$  also improved the grain size dramatically, but only the  $\text{Zn}^{2+}$ , and  $\text{Fe}^{2+}$  addition showed an improved charge carrier lifetime compared to the control. Therefore, Zn or Fe-based salts can be potential alternatives for highly toxic  $\text{CdCl}_2$ . Further,  $\text{Zn}^{2+}$ , and  $\text{Fe}^{2+}$  can also be better substitutes for  $\text{Pb}^{2+}$  to reduce the toxicity in Pb-based perovskites. On the other hand, the inclusion of  $\text{Co}^{2+}$ ,  $\text{Cu}^{2+}$ , and  $\text{Hg}^{2+}$ , though increased the grain size, negatively affected the optoelectronic properties of the films due to formation of impurities phases.

We then used the ability of MAI to form metal complexes during contacting metal cations, for back interface engineering of CdTe solar cells. In this study, we showed that Cd can be selectively removed from the CdTe absorber by reacting MAI thin films with the CdTe surface, leaving elemental Te on the surface. This Te layer reduced the back barrier height for the devices with both Au and ITO back electrodes, decreasing the back junction recombination, resulting higher  $V_{OC}$  and FF, and thus improved PCEs. In addition to the improved device performance in the CdS/CdTe devices with the ITO back electrode, the transmittance reduction due to the MAI treatment in the near infrared (NIR) region is only ~6%. Therefore, this can be a potential treatment for the fabrication of high performance transparent CdTe solar cells that use in tandem solar cell or window applications.

## **6.2 Future Research**

### **6.2.1 Optimizing the metal addition in MAPbI<sub>3</sub> perovskite**

Defects formation in MAPbI<sub>3</sub> films with the metal addition is depends on several factors, such as concentration of the metal salt, processing method, and reaction temperature and time. In our study, we used the two-step deposition technique to fabricate perovskite films, because that was the most successful and widely used method at the time of the study. However, currently the single-step deposition with anti-solvent drop casting technique is widely used due to the formation of a dense perovskite film, and thus improved device performance.[1] Since the base line PCE of the MAPbI<sub>3</sub> perovskite solar cells from this processing method is ~ 18-20% [82, 227] (current PCE in our group is ~16%), future research can be performed to observe the effects of metal addition for the single-step

deposition with anti-solvent drop casting method. In addition, future research is expected to focus on substitution of  $\text{Pb}^{2+}$  sites by  $\text{Fe}^{2+}$  or  $\text{Zn}^{2+}$ , which showed the improved charge carrier life times in  $\text{MAPbI}_3$  films.

### 6.2.2 Fabrication of high efficiency transparent CdTe devices

In our CdTe devices, performance is mainly limited by the  $J_{\text{SC}}$ . This is due to the higher absorption in the thick CdS (~180 nm) layer (Figure 6.1). This can be reduced by using a thin CdS layer or replacing the CdS layer by large band gap window materials. Oxygenated-CdS (O:CdS) and (Mg,Zn)O (MZO) are the widely used large band gap materials in high efficiency CdTe solar cell fabrication. Champion device efficiencies of ~14%, ~16%, and ~16% have been reported for CdTe solar cells with thin CdS, O:CdS, and MZO respectively.[228] The average  $J_{\text{SC}}$  for the devices with O:CdS or MZO window layers is ~25-26  $\text{mA}/\text{cm}^2$ . If we have a  $J_{\text{SC}}$  of 25  $\text{mA}/\text{cm}^2$ , that would give rise to a 16.1% and 14.2% efficient devices with all other parameters held constant for the Au and ITO back electrodes, respectively. In addition to the  $J_{\text{SC}}$ , FF of the CdTe/ITO devices is also low due to the higher sheet resistance of the ITO layer (~35  $\Omega/\text{sq}$ ). If we improved the conductivity of the ITO layer, and therefore the FF, the device efficiency can be further improved. A FF of 75% with a  $J_{\text{SC}}$  of 25  $\text{mA}/\text{cm}^2$  can improve the PCE to 15.4% with the  $V_{\text{OC}}$  that we achieved. Therefore, future research is expected to focus on developing a better window layer and an ITO back electrode for thin CdTe devices, which is beneficial to achieve higher transmittance in the NIR region.

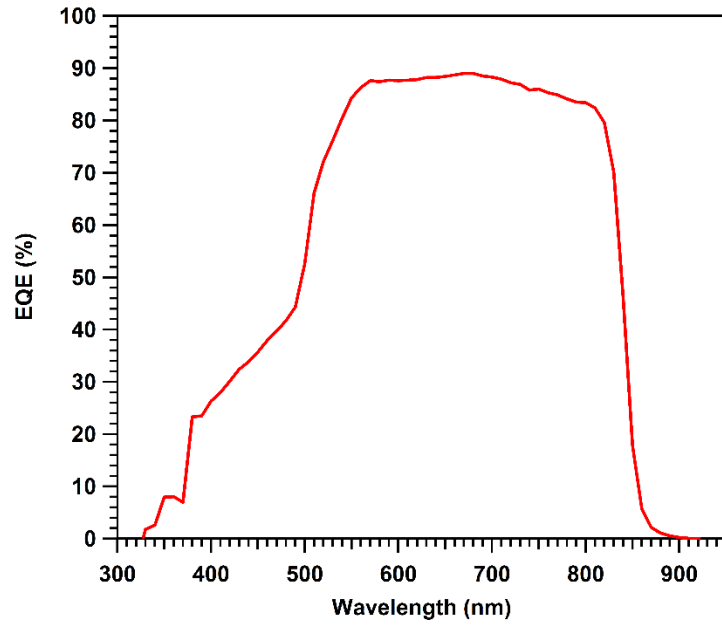


Figure 6-1. External quantum efficiency (EQE) curve of the champion device, which is in the structure of CdS/CdTe:Cu/Te/Au.

## References

- [1] Z. Song, S. C. Wathage, A. B. Phillips, and M. J. Heben, "Pathways toward high-performance perovskite solar cells: review of recent advances in organo-metal halide perovskites for photovoltaic applications," *Journal of Photonics for Energy*, vol. 6, p. 022001, 2016.
- [2] U. Schwarz, F. Wagner, K. Syassen, and H. Hillebrecht, "Effect of pressure on the optical-absorption edges of CsGeBr<sub>3</sub> and CsGeCl<sub>3</sub>," *Physical Review B*, vol. 53, pp. 12545-12548, 1996.
- [3] R. von Helmolt, J. Wecker, B. Holzapfel, L. Schultz, and K. Samwer, "Giant negative magnetoresistance in perovskitelike La<sub>2/3</sub>Ba<sub>1/3</sub>MnO<sub>x</sub> ferromagnetic films," *Physical Review Letters*, vol. 71, pp. 2331-2333, 1993.
- [4] J. H. Haeni, P. Irvin, W. Chang, R. Uecker, P. Reiche, Y. L. Li, S. Choudhury, W. Tian, M. E. Hawley, B. Craigo, A. K. Tagantsev, X. Q. Pan, S. K. Streiffer, L. Q. Chen, S. W. Kirchoefer, J. Levy, and D. G. Schlom, "Room-temperature ferroelectricity in strained SrTiO<sub>3</sub>," *Nature*, vol. 430, pp. 758-761, 2004.
- [5] J. G. Bednorz and K. A. Müller, "Perovskite-type oxides - The new approach to high-T<sub>c</sub> superconductivity," *Reviews of Modern Physics*, vol. 60, pp. 585-600, 1988.
- [6] H. Arend, W. Huber, F. H. Mischgofsky, and G. K. Richter-Van Leeuwen, "Layer perovskites of the (C<sub>n</sub>H<sub>2n+1</sub>NH<sub>3</sub>)<sub>2</sub>MX<sub>4</sub> and NH<sub>3</sub>(CH<sub>2</sub>)<sub>m</sub>NH<sub>3</sub>MX<sub>4</sub> families with M = Cd, Cu, Fe, Mn OR Pd and X = Cl OR Br: Importance, solubilities and simple growth techniques," *Journal of Crystal Growth*, vol. 43, pp. 213-223, 1978.
- [7] D. B. Mitzi, "Templating and structural engineering in organic-inorganic perovskites," *Journal of the Chemical Society, Dalton Transactions*, pp. 1-12, 2001.

- [8] K. Liang, D. B. Mitzi, and M. T. Prikas, "Synthesis and Characterization of Organic-Inorganic Perovskite Thin Films Prepared Using a Versatile Two-Step Dipping Technique," *Chemistry of Materials*, vol. 10, pp. 403-411, 1998.
- [9] C. R. Kagan, D. B. Mitzi, and C. D. Dimitrakopoulos, "Organic-Inorganic Hybrid Materials as Semiconducting Channels in Thin-Film Field-Effect Transistors," *Science*, vol. 286, pp. 945-947, 1999.
- [10] D. B. Mitzi, K. Chondroudis, and C. R. Kagan, "Organic-inorganic electronics," *IBM Journal of Research and Development*, vol. 45, pp. 29-45, 2001.
- [11] A. Kojima, K. Teshima, Y. Shirai, and T. Miyasaka, "Organometal Halide Perovskites as Visible-Light Sensitizers for Photovoltaic Cells," *Journal of the American Chemical Society*, vol. 131, pp. 6050-6051, 2009.
- [12] M. M. Lee, J. Teuscher, T. Miyasaka, T. N. Murakami, and H. J. Snaith, "Efficient Hybrid Solar Cells Based on Meso-Superstructured Organometal Halide Perovskites," *Science*, vol. 338, pp. 643-647, 2012.
- [13] H.-S. Kim, C.-R. Lee, J.-H. Im, K.-B. Lee, T. Moehl, A. Marchioro, S.-J. Moon, R. Humphry-Baker, J.-H. Yum, J. E. Moser, M. Graetzel, and N.-G. Park, "Lead Iodide Perovskite Sensitized All-Solid-State Submicron Thin Film Mesoscopic Solar Cell with Efficiency Exceeding 9%," *Scientific Reports*, vol. 2, p. 591, 2012.
- [14] H. J. Snaith, "Perovskites: The Emergence of a New Era for Low-Cost, High-Efficiency Solar Cells," *Journal of Physical Chemistry Letters*, vol. 4, pp. 3623-3630, 2013.
- [15] M. A. Green, A. Ho-Baillie, and H. J. Snaith, "The emergence of perovskite solar cells," *Nature Photonics*, vol. 8, pp. 506-514, 2014.
- [16] Editorial, "Perovskite fever," *Nat Mater*, vol. 13, pp. 837-837, 2014.
- [17] NREL, "Solar Cell Efficiency Chart". [[http://www.nrel.gov/ncpv/images/efficiency\\_chart.jpg](http://www.nrel.gov/ncpv/images/efficiency_chart.jpg)] accessed: September, 2017.
- [18] B. O'Regan and M. Gratzel, "A low-cost, high-efficiency solar cell based on dye-sensitized colloidal TiO<sub>2</sub> films," *Nature*, vol. 353, pp. 737-740, 1991.

- [19] J.-H. Im, C.-R. Lee, J.-W. Lee, S.-W. Park, and N.-G. Park, "6.5% efficient perovskite quantum-dot-sensitized solar cell," *Nanoscale*, vol. 3, pp. 4088-4093, 2011.
- [20] T. Leijtens, S. D. Stranks, G. E. Eperon, R. Lindblad, E. M. J. Johansson, I. J. McPherson, H. Rensmo, J. M. Ball, M. M. Lee, and H. J. Snaith, "Electronic Properties of Meso-Superstructured and Planar Organometal Halide Perovskite Films: Charge Trapping, Photodoping, and Carrier Mobility," *Acs Nano*, vol. 8, pp. 7147-7155, 2014.
- [21] S. D. Stranks, G. E. Eperon, G. Grancini, C. Menelaou, M. J. P. Alcocer, T. Leijtens, L. M. Herz, A. Petrozza, and H. J. Snaith, "Electron-Hole Diffusion Lengths Exceeding 1 Micrometer in an Organometal Trihalide Perovskite Absorber," *Science*, vol. 342, pp. 341-344, 2013.
- [22] G. Xing, N. Mathews, S. Sun, S. S. Lim, Y. M. Lam, M. Graetzel, S. Mhaisalkar, and T. C. Sum, "Long-Range Balanced Electron- and Hole-Transport Lengths in Organic-Inorganic  $\text{CH}_3\text{NH}_3\text{PbI}_3$ ," *Science*, vol. 342, pp. 344-347, 2013.
- [23] H. S. Kim, S. H. Im, and N. G. Park, "Organolead Halide Perovskite: New Horizons in Solar Cell Research," *Journal of Physical Chemistry C*, vol. 118, pp. 5615-5625, 2014.
- [24] J. H. Heo, S. H. Im, J. H. Noh, T. N. Mandal, C.-S. Lim, J. A. Chang, Y. H. Lee, H.-j. Kim, A. Sarkar, Md. K. Nazeeruddin, M. Gratzel, and S. I. Seok, "Efficient inorganic-organic hybrid heterojunction solar cells containing perovskite compound and polymeric hole conductors," *Nat Photon*, vol. 7, pp. 486-491, 2013.
- [25] J. Burschka, N. Pellet, S.-J. Moon, R. Humphry-Baker, P. Gao, M. K. Nazeeruddin, and M. Gratzel, "Sequential deposition as a route to high-performance perovskite-sensitized solar cells," *Nature*, vol. 499, pp. 316-319, 2013.
- [26] J.-H. Im, I.-H. Jang, N. Pellet, M. Grätzel, and N.-G. Park, "Growth of  $\text{CH}_3\text{NH}_3\text{PbI}_3$  cuboids with controlled size for high-efficiency perovskite solar cells," *Nat Nano*, vol. 9, pp. 927-932, 2014.
- [27] F. Giordano, A. Abate, J. P. Correa Baena, M. Saliba, T. Matsui, S. H. Im, S. M. Zakeeruddin, M. K. Nazeeruddin, A. Hagfeldt, and M. Graetzel, "Enhanced electronic properties in mesoporous  $\text{TiO}_2$  via lithium doping for high-efficiency perovskite solar cells," *Nature Communications*, vol. 7, p. 10379, 2016.

- [28] J. M. Ball, M. M. Lee, A. Hey, and H. J. Snaith, "Low-temperature processed meso-structured to thin-film perovskite solar cells," *Energy & Environmental Science*, vol. 6, pp. 1739-1743, 2013.
- [29] G. E. Eperon, V. M. Burlakov, P. Docampo, A. Goriely, and H. J. Snaith, "Morphological Control for High Performance, Solution-Processed Planar Heterojunction Perovskite Solar Cells," *Advanced Functional Materials*, vol. 24, pp. 151-157, 2014.
- [30] M. Liu, M. B. Johnston, and H. J. Snaith, "Efficient planar heterojunction perovskite solar cells by vapour deposition," *Nature*, vol. 501, pp. 395–398, 2013.
- [31] Q. Jiang, L. Zhang, H. Wang, X. Yang, J. Meng, H. Liu, Z. Yin, J. Wu, X. Zhang, and J. You, "Enhanced electron extraction using SnO<sub>2</sub> for high-efficiency planar-structure HC(NH<sub>2</sub>)<sub>2</sub>PbI<sub>3</sub>-based perovskite solar cells," *Nature Energy*, vol. 2, p. 16177, 2016.
- [32] J.-Y. Seo, T. Matsui, J. Luo, J.-P. Correa-Baena, F. Giordano, M. Saliba, K. Schenk, A. Ummadisingu, K. Domanski, M. Hadadian, A. Hagfeldt, S. M. Zakeeruddin, U. Steiner, M. Grätzel, and A. Abate, "Ionic Liquid Control Crystal Growth to Enhance Planar Perovskite Solar Cells Efficiency," *Advanced Energy Materials*, 6: 1600767. doi: 10.1002/aenm.201600767.
- [33] E. H. Anaraki, A. Kermanpur, L. Steier, K. Domanski, T. Matsui, W. Tress, M. Saliba, A. Abate, M. Gratzel, A. Hagfeldt, and J.-P. Correa-Baena, "Highly efficient and stable planar perovskite solar cells by solution-processed tin oxide," *Energy & Environmental Science*, vol. 9, pp. 3128-3134, 2016.
- [34] T. Leijtens, G. E. Eperon, N. K. Noel, S. N. Habisreutinger, A. Petrozza, and H. J. Snaith, "Stability of Metal Halide Perovskite Solar Cells," *Advanced Energy Materials*, vol. 5, p. 1500963, 2015.
- [35] J.-Y. Jeng, Y.-F. Chiang, M.-H. Lee, S.-R. Peng, T.-F. Guo, P. Chen, and T.-C. Wen, "CH<sub>3</sub>NH<sub>3</sub>PbI<sub>3</sub> Perovskite/Fullerene Planar-Heterojunction Hybrid Solar Cells," *Advanced Materials*, vol. 25, pp. 3727-3732, 2013.
- [36] S. Sun, T. Salim, N. Mathews, M. Duchamp, C. Boothroyd, G. Xing, T. C. Sum, and Y. M. Lam, "The origin of high efficiency in low-temperature solution-processable bilayer organometal halide hybrid solar cells," *Energy & Environmental Science*, vol. 7, pp. 399-407, 2014.

- [37] P. Docampo, J. M. Ball, M. Darwich, G. E. Eperon, and H. J. Snaith, "Efficient organometal trihalide perovskite planar-heterojunction solar cells on flexible polymer substrates," *Nature Communications*, vol. 4, p. 2761, 2013.
- [38] J. You, Z. Hong, Y. Yang, Q. Chen, M. Cai, T.-B. Song, C.-C. Chen, S. Lu, Y. Liu, H. Zhou, and Y. Yang, "Low-Temperature Solution-Processed Perovskite Solar Cells with High Efficiency and Flexibility," *ACS Nano*, vol. 8, pp. 1674-1680, 2014.
- [39] O. Malinkiewicz, A. Yella, Y. H. Lee, G. Minguez Espallargas, M. Graetzel, M. K. Nazeeruddin, and H. J. Bolink, "Perovskite solar cells employing organic charge-transport layers," *Nature Photonics*, vol. 8, pp. 128-132, 2014.
- [40] J. T.-W. Wang, J. M. Ball, E. M. Barea, A. Abate, J. A. Alexander-Webber, J. Huang, M. Saliba, I. Mora-Sero, J. Bisquert, H. J. Snaith, and R. J. Nicholas, "Low-Temperature Processed Electron Collection Layers of Graphene/TiO<sub>2</sub> Nanocomposites in Thin Film Perovskite Solar Cells," *Nano Letters*, vol. 14, pp. 724-730, 2014.
- [41] Z. Xiao, C. Bi, Y. Shao, Q. Dong, Q. Wang, Y. Yuan, C. Wang, Y. Gao, and J. Huang, "Efficient, high yield perovskite photovoltaic devices grown by interdiffusion of solution-processed precursor stacking layers," *Energy & Environmental Science*, vol. 7, pp. 2619-2623, 2014.
- [42] Z. Xiao, Q. Dong, C. Bi, Y. Shao, Y. Yuan, and J. Huang, "Solvent Annealing of Perovskite-Induced Crystal Growth for Photovoltaic-Device Efficiency Enhancement," *Advanced Materials*, vol. 26, pp. 6503-6509, 2014.
- [43] W. Nie, H. Tsai, R. Asadpour, J.-C. Blancon, A. J. Neukirch, G. Gupta, J. J. Crochet, M. Chhowalla, S. Tretiak, M. A. Alam, H.-L. Wang, and A. D. Mohite, "High-efficiency solution-processed perovskite solar cells with millimeter-scale grains," *Science*, vol. 347, pp. 522-525, 2015.
- [44] C. Bi, Q. Wang, Y. Shao, Y. Yuan, Z. Xiao, and J. Huang, "Non-wetting surface-driven high-aspect-ratio crystalline grain growth for efficient hybrid perovskite solar cells," *Nature Communications*, vol. 6, p. 7747, 2015.
- [45] Y. Bai, Q. Dong, Y. Shao, Y. Deng, Q. Wang, L. Shen, D. Wang, W. Wei, and J. Huang, "Enhancing stability and efficiency of perovskite solar cells with crosslinkable silane-functionalized and doped fullerene," *Nature Communications*, vol. 7, p. 12806, 2016.

- [46] Q. Chen, H. Zhou, Z. Hong, S. Luo, H.-S. Duan, H.-H. Wang, Y. Liu, G. Li, and Y. Yang, "Planar Heterojunction Perovskite Solar Cells via Vapor-Assisted Solution Process," *Journal of the American Chemical Society*, vol. 136, pp. 622-625, 2014.
- [47] Z. Song, S. C. Watthage, A. B. Phillips, B. L. Tompkins, R. J. Ellingson, and M. J. Heben, "Impact of Processing Temperature and Composition on the Formation of Methylammonium Lead Iodide Perovskites," *Chemistry of Materials*, vol. 27, pp. 4612-4619, 2015.
- [48] C. Roldan-Carmona, P. Gratia, I. Zimmermann, G. Grancini, P. Gao, M. Graetzel, and M. K. Nazeeruddin, "High efficiency methylammonium lead triiodide perovskite solar cells: the relevance of non-stoichiometric precursors," *Energy & Environmental Science*, vol. 8, pp. 3550-3556, 2015.
- [49] H. Zhou, Q. Chen, G. Li, S. Luo, T.-b. Song, H.-S. Duan, Z. Hong, J. You, Y. Liu, and Y. Yang, "Interface engineering of highly efficient perovskite solar cells," *Science*, vol. 345, pp. 542-546, 2014.
- [50] X. Liu, W. Zhao, H. Cui, Y. a. Xie, Y. Wang, T. Xu, and F. Huang, "Organic-inorganic halide perovskite based solar cells - revolutionary progress in photovoltaics," *Inorganic Chemistry Frontiers*, vol. 2, pp. 315-335, 2015.
- [51] Q. Wang, Y. Shao, Q. Dong, Z. Xiao, Y. Yuan, and J. Huang, "Large fill-factor bilayer iodine perovskite solar cells fabricated by a low-temperature solution-process," *Energy & Environmental Science*, vol. 7, pp. 2359-2365, 2014.
- [52] A. Dualeh, N. Tétreault, T. Moehl, P. Gao, M. K. Nazeeruddin, and M. Grätzel, "Effect of Annealing Temperature on Film Morphology of Organic-Inorganic Hybrid Perovskite Solid-State Solar Cells," *Advanced Functional Materials*, vol. 24, pp. 3250-3258, 2014.
- [53] T. Zhang, M. Yang, Y. Zhao, and K. Zhu, "Controllable Sequential Deposition of Planar  $\text{CH}_3\text{NH}_3\text{PbI}_3$  Perovskite Films via Adjustable Volume Expansion," *Nano Letters*, vol. 15, pp. 3959-3963, 2015.
- [54] H. Zhang, J. Mao, H. He, D. Zhang, H. L. Zhu, F. Xie, K. S. Wong, M. Grätzel, and W. C. H. Choy, "A Smooth  $\text{CH}_3\text{NH}_3\text{PbI}_3$  Film via a New Approach for Forming the  $\text{PbI}_2$  Nanostructure Together with Strategically High  $\text{CH}_3\text{NH}_3\text{I}$

Concentration for High Efficient Planar-Heterojunction Solar Cells," *Advanced Energy Materials*, 5: 1501354. doi: 10.1002/aenm.201501354.

- [55] Y. Wu, A. Islam, X. Yang, C. Qin, J. Liu, K. Zhang, W. Peng, and L. Han, "Retarding the crystallization of  $\text{PbI}_2$  for highly reproducible planar-structured perovskite solar cells via sequential deposition," *Energy & Environmental Science*, vol. 7, pp. 2934-2938, 2014.
- [56] Y. Zhou, M. Yang, A. L. Vasiliev, H. F. Garces, Y. Zhao, D. Wang, S. Pang, K. Zhu, and N. P. Padture, "Growth control of compact  $\text{CH}_3\text{NH}_3\text{PbI}_3$  thin films via enhanced solid-state precursor reaction for efficient planar perovskite solar cells," *Journal of Materials Chemistry A*, vol. 3, pp. 9249-9256, 2015.
- [57] W. S. Yang, J. H. Noh, N. J. Jeon, Y. C. Kim, S. Ryu, J. Seo, and S. I. Seok, "High-performance photovoltaic perovskite layers fabricated through intramolecular exchange," *Science*, vol. 348, pp. 1234-1237, 2015.
- [58] M. Era, T. Hattori, T. Taira, and T. Tsutsui, "Self-Organized Growth of PbI-Based Layered Perovskite Quantum Well by Dual-Source Vapor Deposition," *Chemistry of Materials*, vol. 9, pp. 8-10, 1997.
- [59] D. B. Mitzi, M. T. Prikas, and K. Chondroudis, "Thin Film Deposition of Organic-Inorganic Hybrid Materials Using a Single Source Thermal Ablation Technique," *Chemistry of Materials*, vol. 11, pp. 542-544, 1999.
- [60] C.-W. Chen, H.-W. Kang, S.-Y. Hsiao, P.-F. Yang, K.-M. Chiang, and H.-W. Lin, "Efficient and Uniform Planar-Type Perovskite Solar Cells by Simple Sequential Vacuum Deposition," *Advanced Materials*, vol. 26, pp. 6647-6652, 2014.
- [61] M. M. Tavakoli, L. Gu, Y. Gao, C. Reckmeier, J. He, A. L. Rogach, Y. Yao, and Z. Fan, "Fabrication of efficient planar perovskite solar cells using a one-step chemical vapor deposition method," *Scientific Reports*, 5, 14083; doi: 10.1038/srep14083 (2015).
- [62] G. Longo, L. Gil-Escrig, M. J. Degen, M. Sessolo, and H. J. Bolink, "Perovskite solar cells prepared by flash evaporation," *Chemical Communications*, vol. 51, pp. 7376-7378, 2015.
- [63] M. M. Sessolo, C.; Gil-Escrig, L.; Bolink, H. J., "Photovoltaic Devices Employing Vacuum-Deposited Perovskite Layers," *MRS Bulletin*, vol. 40, pp. 660-666, 2015.

- [64] D. Zhao, W. Ke, C. R. Grice, A. J. Cimaroli, X. Tan, M. Yang, R. W. Collins, H. Zhang, K. Zhu, and Y. Yan, "Annealing-free efficient vacuum-deposited planar perovskite solar cells with evaporated fullerenes as electron-selective layers," *Nano Energy*, vol. 19, pp. 88-97, 2016.
- [65] L. K. Ono, M. R. Leyden, S. Wang, and Y. Qi, "Organometal halide perovskite thin films and solar cells by vapor deposition," *Journal of Materials Chemistry A*, vol. 4, pp. 6693-6713, 2016.
- [66] N. J. Jeon, J. H. Noh, Y. C. Kim, W. S. Yang, S. Ryu, and S. I. Seok, "Solvent engineering for high-performance inorganic-organic hybrid perovskite solar cells," *Nat Mater*, vol. 13, pp. 897-903, 2014.
- [67] Y. Zhao and K. Zhu, "Efficient Planar Perovskite Solar Cells Based on 1.8 eV Band Gap  $\text{CH}_3\text{NH}_3\text{PbI}_2\text{Br}$  Nanosheets via Thermal Decomposition," *Journal of the American Chemical Society*, vol. 136, pp. 12241-12244, 2014.
- [68] J. H. Heo, D. H. Song, H. J. Han, S. Y. Kim, J. H. Kim, D. Kim, H. W. Shin, T. K. Ahn, C. Wolf, T.-W. Lee, and S. H. Im, "Planar  $\text{CH}_3\text{NH}_3\text{PbI}_3$  Perovskite Solar Cells with Constant 17.2% Average Power Conversion Efficiency Irrespective of the Scan Rate," *Advanced Materials*, vol. 27, pp. 3424-3430, 2015.
- [69] H. Tsai, W. Nie, P. Cheruku, N. H. Mack, P. Xu, G. Gupta, A. D. Mohite, and H.-L. Wang, "Optimizing Composition and Morphology for Large-Grain Perovskite Solar Cells via Chemical Control," *Chemistry of Materials*, vol. 27, pp. 5570-5576, 2015.
- [70] Y. Chen, Y. Zhao, and Z. Liang, "Non-Thermal Annealing Fabrication of Efficient Planar Perovskite Solar Cells with Inclusion of  $\text{NH}_4\text{Cl}$ ," *Chemistry of Materials*, vol. 27, pp. 1448-1451, 2015.
- [71] J. H. Heo, D. H. Song, and S. H. Im, "Planar  $\text{CH}_3\text{NH}_3\text{PbBr}_3$  Hybrid Solar Cells with 10.4% Power Conversion Efficiency, Fabricated by Controlled Crystallization in the Spin-Coating Process," *Advanced Materials*, vol. 26, pp. 8179-8183, 2014.
- [72] P.-W. Liang, C.-Y. Liao, C.-C. Chueh, F. Zuo, S. T. Williams, X.-K. Xin, J. Lin, and A. K. Y. Jen, "Additive Enhanced Crystallization of Solution-Processed Perovskite for Highly Efficient Planar-Heterojunction Solar Cells," *Advanced Materials*, vol. 26, pp. 3748-3754, 2014.

- [73] A. Mei, X. Li, L. Liu, Z. Ku, T. Liu, Y. Rong, M. Xu, M. Hu, J. Chen, Y. Yang, M. Grätzel, and H. Han, "A hole-conductor-free, fully printable mesoscopic perovskite solar cell with high stability," *Science*, vol. 345, pp. 295-298, 2014.
- [74] X. Li, M. Ibrahim Dar, C. Yi, J. Luo, M. Tschumi, S. M. Zakeeruddin, M. K. Nazeeruddin, H. Han, and M. Grätzel, "Improved performance and stability of perovskite solar cells by crystal crosslinking with alkylphosphonic acid  $\omega$ -ammonium chlorides," *Nat Chem*, vol. 7, pp. 703-711, 2015.
- [75] Y. Fu, F. Meng, M. B. Rowley, B. J. Thompson, M. J. Shearer, D. Ma, R. J. Hamers, J. C. Wright, and S. Jin, "Solution Growth of Single Crystal Methylammonium Lead Halide Perovskite Nanostructures for Optoelectronic and Photovoltaic Applications," *Journal of the American Chemical Society*, vol. 137, pp. 5810-5818, 2015.
- [76] S. C. Watthage, Z. Song, G. K. Liyanage, A. B. Phillips, and M. J. Heben, "Investigation on the nucleation and growth mechanisms of perovskite formation in the two-step solution process," in *2016 IEEE 43rd Photovoltaic Specialists Conference (PVSC)*, 2016, pp. 0831-0834.
- [77] W. Wu, H. Li, S. Liu, B. Zheng, Y. Xue, X. Liu, and C. Gao, "Tuning  $\text{PbI}_2$  layers by n-butanol additive for improving  $\text{CH}_3\text{NH}_3\text{PbI}_3$  light harvesters of perovskite solar cells," *RSC Advances*, vol. 6, pp. 89609-89613, 2016.
- [78] C.-G. Wu, C.-H. Chiang, Z.-L. Tseng, M. K. Nazeeruddin, A. Hagfeldt, and M. Grätzel, "High efficiency stable inverted perovskite solar cells without current hysteresis," *Energy & Environmental Science*, vol. 8, pp. 2725-2733, 2015.
- [79] S. C. Watthage, Z. Song, N. Shrestha, A. B. Phillips, G. K. Liyanage, P. J. Roland, R. J. Ellingson, and M. J. Heben, "Enhanced Grain Size, Photoluminescence, and Photoconversion Efficiency with Cadmium Addition During the Two-Step Growth of  $\text{CH}_3\text{NH}_3\text{PbI}_3$ ," *ACS Applied Materials & Interfaces*, 2016.
- [80] S. C. Watthage, Z. Song, N. Shrestha, A. B. Phillips, G. K. Liyanage, P. J. Roland, R. J. Ellingson, and M. J. Heben, "Impact of Divalent Metal Additives on the Structural and Optoelectronic Properties of  $\text{CH}_3\text{NH}_3\text{PbI}_3$  Perovskite Prepared by the Two-Step Solution Process," *MRS Advances*, pp. 1-6, 2017.
- [81] D. Bi, W. Tress, M. I. Dar, P. Gao, J. Luo, C. Renevier, K. Schenk, A. Abate, F. Giordano, J.-P. Correa Baena, J.-D. Decoppet, S. M. Zakeeruddin, M. K.

- Nazeeruddin, M. Grätzel, and A. Hagfeldt, "Efficient luminescent solar cells based on tailored mixed-cation perovskites," *Science Advances*, vol. 2, 2016.
- [82] N. Ahn, D.-Y. Son, I.-H. Jang, S. M. Kang, M. Choi, and N.-G. Park, "Highly Reproducible Perovskite Solar Cells with Average Efficiency of 18.3% and Best Efficiency of 19.7% Fabricated via Lewis Base Adduct of Lead(II) Iodide," *Journal of the American Chemical Society*, vol. 137, pp. 8696-8699, 2015.
- [83] X. Zheng, B. Chen, C. Wu, and S. Priya, "Room temperature fabrication of  $\text{CH}_3\text{NH}_3\text{PbBr}_3$  by anti-solvent assisted crystallization approach for perovskite solar cells with fast response and small J-V hysteresis," *Nano Energy*, vol. 17, pp. 269-278, 2015.
- [84] X. Fang, Y. Wu, Y. Lu, Y. Sun, S. Zhang, J. Zhang, W. Zhang, N. Yuan, and J. Ding, "Annealing-free perovskite films based on solvent engineering for efficient solar cells," *Journal of Materials Chemistry C*, vol. 5, pp. 842-847, 2017.
- [85] D. W. de Quilettes, S. M. Vorpahl, S. D. Stranks, H. Nagaoka, G. E. Eperon, M. E. Ziffer, H. J. Snaith, and D. S. Ginger, "Impact of microstructure on local carrier lifetime in perovskite solar cells," *Science*, vol. 348, pp. 683-686, 2015.
- [86] B. S. Tosun and H. W. Hillhouse, "Enhanced Carrier Lifetimes of Pure Iodide Hybrid Perovskite via Vapor-Equilibrated Re-Growth (VERG)," *The Journal of Physical Chemistry Letters*, vol. 6, pp. 2503-2508, 2015.
- [87] X. Li, D. Bi, C. Yi, J.-D. Décoppet, J. Luo, S. M. Zakeeruddin, A. Hagfeldt, and M. Grätzel, "A vacuum flash-assisted solution process for high-efficiency large-area perovskite solar cells," *Science*, vol. 353, pp. 58-62, 2016.
- [88] D. Liu and T. L. Kelly, "Perovskite solar cells with a planar heterojunction structure prepared using room-temperature solution processing techniques," *Nature Photonics*, vol. 8, pp. 133-138, 2014.
- [89] W. Ke, G. Fang, Q. Liu, L. Xiong, P. Qin, H. Tao, J. Wang, H. Lei, B. Li, J. Wan, G. Yang, and Y. Yan, "Low-Temperature Solution-Processed Tin Oxide as an Alternative Electron Transporting Layer for Efficient Perovskite Solar Cells," *Journal of the American Chemical Society*, vol. 137, pp. 6730-6733, 2015.
- [90] J. P. Correa Baena, L. Steier, W. Tress, M. Saliba, S. Neutzner, T. Matsui, F. Giordano, T. J. Jacobsson, A. R. Srimath Kandada, S. M. Zakeeruddin, A. Petrozza, A. Abate, M. K. Nazeeruddin, M. Grätzel, and A. Hagfeldt, "Highly efficient planar

perovskite solar cells through band alignment engineering," *Energy & Environmental Science*, vol. 8, pp. 2928-2934, 2015.

- [91] L. Wang, W. Fu, Z. Gu, C. Fan, X. Yang, H. Li, and H. Chen, "Low temperature solution processed planar heterojunction perovskite solar cells with a CdSe nanocrystal as an electron transport/extraction layer," *Journal of Materials Chemistry C*, vol. 2, pp. 9087-9090, 2014.
- [92] J. Liu, C. Gao, L. Luo, Q. Ye, X. He, L. Ouyang, X. Guo, D. Zhuang, C. Liao, J. Mei, and W. Lau, "Low-temperature, solution processed metal sulfide as an electron transport layer for efficient planar perovskite solar cells," *Journal of Materials Chemistry A*, vol. 3, pp. 11750-11755, 2015.
- [93] C.-H. Chiang, Z.-L. Tseng, and C.-G. Wu, "Planar heterojunction perovskite/PC<sub>71</sub>BM solar cells with enhanced open-circuit voltage via a (2/1)-step spin-coating process," *Journal of Materials Chemistry A*, vol. 2, pp. 15897-15903, 2014.
- [94] E. J. Juarez-Perez, M. Wußler, F. Fabregat-Santiago, K. Lakus-Wollny, E. Mankel, T. Mayer, W. Jaegermann, and I. Mora-Sero, "Role of the Selective Contacts in the Performance of Lead Halide Perovskite Solar Cells," *The Journal of Physical Chemistry Letters*, vol. 5, pp. 680-685, 2014.
- [95] Z. Song, A. Abate, S. C. Watthage, G. K. Liyanage, A. B. Phillips, U. Steiner, M. Graetzel, and M. J. Heben, "In-situ observation of moisture-induced degradation of perovskite solar cells using laser-beam induced current," in *2016 IEEE 43rd Photovoltaic Specialists Conference (PVSC)*, 2016, pp. 1202-1206.
- [96] Z. Song, S. C. Watthage, A. B. Phillips, G. K. Liyanage, R. R. Khanal, B. L. Tompkins, R. J. Ellingson, and M. J. Heben, "Investigation of degradation mechanisms of perovskite-based photovoltaic devices using laser beam induced current mapping," *Proc. SPIE*, vol. 9561, p. 956107, 2015.
- [97] Z. Song, A. Abate, S. C. Watthage, G. K. Liyanage, A. B. Phillips, U. Steiner, M. Graetzel, and M. J. Heben, "Perovskite Solar Cell Stability in Humid Air: Partially Reversible Phase Transitions in the PbI<sub>2</sub>-CH<sub>3</sub>NH<sub>3</sub>I-H<sub>2</sub>O System," *Advanced Energy Materials*, 6: 1600846. doi: 10.1002/aenm.201600846.
- [98] Y. Guo, C. Liu, K. Inoue, K. Harano, H. Tanaka, and E. Nakamura, "Enhancement in the efficiency of an organic-inorganic hybrid solar cell with a doped P<sub>3</sub>HT hole-

transporting layer on a void-free perovskite active layer," *Journal of Materials Chemistry A*, vol. 2, pp. 13827-13830, 2014.

- [99] K. Rakstys, A. Abate, M. I. Dar, P. Gao, V. Jankauskas, G. Jacopin, E. Kamarauskas, S. Kazim, S. Ahmad, M. Grätzel, and M. K. Nazeeruddin, "Triazatruxene-Based Hole Transporting Materials for Highly Efficient Perovskite Solar Cells," *Journal of the American Chemical Society*, vol. 137, pp. 16172-16178, 2015.
- [100] Y. Zhang, M. Elawad, Z. Yu, X. Jiang, J. Lai, and L. Sun, "Enhanced performance of perovskite solar cells with P3HT hole-transporting materials via molecular p-type doping," *RSC Advances*, vol. 6, pp. 108888-108895, 2016.
- [101] J.-Y. Jeng, K.-C. Chen, T.-Y. Chiang, P.-Y. Lin, T.-D. Tsai, Y.-C. Chang, T.-F. Guo, P. Chen, T.-C. Wen, and Y.-J. Hsu, "Nickel Oxide Electrode Interlayer in  $\text{CH}_3\text{NH}_3\text{PbI}_3$  Perovskite/PCBM Planar-Heterojunction Hybrid Solar Cells," *Advanced Materials*, vol. 26, pp. 4107-4113, 2014.
- [102] J. H. Kim, P.-W. Liang, S. T. Williams, N. Cho, C.-C. Chueh, M. S. Glaz, D. S. Ginger, and A. K. Y. Jen, "High-Performance and Environmentally Stable Planar Heterojunction Perovskite Solar Cells Based on a Solution-Processed Copper-Doped Nickel Oxide Hole-Transporting Layer," *Advanced Materials*, vol. 27, pp. 695-701, 2015.
- [103] J. H. Park, J. Seo, S. Park, S. S. Shin, Y. C. Kim, N. J. Jeon, H.-W. Shin, T. K. Ahn, J. H. Noh, S. C. Yoon, C. S. Hwang, and S. I. Seok, "Efficient  $\text{CH}_3\text{NH}_3\text{PbI}_3$  Perovskite Solar Cells Employing Nanostructured p-Type NiO Electrode Formed by a Pulsed Laser Deposition," *Advanced Materials*, vol. 27, pp. 4013-4019, 2015.
- [104] N. Li, Z. Zhu, C.-C. Chueh, H. Liu, B. Peng, A. Petrone, X. Li, L. Wang, and A. K. Y. Jen, "Mixed Cation  $\text{FA}_x\text{PEA}_{1-x}\text{PbI}_3$  with Enhanced Phase and Ambient Stability toward High-Performance Perovskite Solar Cells," *Advanced Energy Materials*, vol. 7, p. 1601307, 2017.
- [105] C. Zuo and L. Ding, "Solution-Processed  $\text{Cu}_2\text{O}$  and  $\text{CuO}$  as Hole Transport Materials for Efficient Perovskite Solar Cells," *Small*, vol. 11, pp. 5528-5532, 2015.
- [106] S. Ye, W. Sun, Y. Li, W. Yan, H. Peng, Z. Bian, Z. Liu, and C. Huang, "CuSCN-Based Inverted Planar Perovskite Solar Cell with an Average PCE of 15.6%," *Nano Letters*, vol. 15, pp. 3723-3728, 2015.

- [107] J.-P. Correa-Baena, A. Abate, M. Saliba, W. Tress, T. Jesper Jacobsson, M. Gratzel, and A. Hagfeldt, "The rapid evolution of highly efficient perovskite solar cells," *Energy & Environmental Science*, vol. 10, pp. 710-727, 2017.
- [108] C. C. Stoumpos, C. D. Malliakas, and M. G. Kanatzidis, "Semiconducting Tin and Lead Iodide Perovskites with Organic Cations: Phase Transitions, High Mobilities, and Near-Infrared Photoluminescent Properties," *Inorganic Chemistry*, vol. 52, pp. 9019-9038, 2013.
- [109] B. Chen, X. Zheng, Y. Bai, N. P. Padture, and J. Huang, "Progress in Tandem Solar Cells Based on Hybrid Organic–Inorganic Perovskites," *Advanced Energy Materials*, 2017, 7, 1602400. <https://doi.org/10.1002/aenm.201602400>.
- [110] W.-J. Yin, J.-H. Yang, J. Kang, Y. Yan, and S.-H. Wei, "Halide perovskite materials for solar cells: a theoretical review," *Journal of Materials Chemistry A*, vol. 3, pp. 8926-8942, 2015.
- [111] G. E. Eperon, S. D. Stranks, C. Menelaou, M. B. Johnston, L. M. Herz, and H. J. Snaith, "Formamidinium lead trihalide: a broadly tunable perovskite for efficient planar heterojunction solar cells," *Energy & Environmental Science*, vol. 7, pp. 982-988, 2014.
- [112] N. Pellet, P. Gao, G. Gregori, T.-Y. Yang, M. K. Nazeeruddin, J. Maier, and M. Grätzel, "Mixed-Organic-Cation Perovskite Photovoltaics for Enhanced Solar-Light Harvesting," *Angewandte Chemie International Edition*, vol. 53, pp. 3151-3157, 2014.
- [113] J.-W. Lee, D.-H. Kim, H.-S. Kim, S.-W. Seo, S. M. Cho, and N.-G. Park, "Formamidinium and Cesium Hybridization for Photo- and Moisture-Stable Perovskite Solar Cell," *Advanced Energy Materials*, 5: 1501310. doi: 10.1002/aenm.201501310.
- [114] C. Yi, J. Luo, S. Meloni, A. Boziki, N. Ashari-Astani, C. Gratzel, S. M. Zakeeruddin, U. Rothlisberger, and M. Gratzel, "Entropic stabilization of mixed A-cation ABX<sub>3</sub> metal halide perovskites for high performance perovskite solar cells," *Energy & Environmental Science*, vol. 9, pp. 656-662, 2016.
- [115] S. A. Kulkarni, T. Baikie, P. P. Boix, N. Yantara, N. Mathews, and S. Mhaisalkar, "Band-gap tuning of lead halide perovskites using a sequential deposition process," *Journal of Materials Chemistry A*, vol. 2, pp. 9221-9225, 2014.

- [116] J. H. Noh, S. H. Im, J. H. Heo, T. N. Mandal, and S. I. Seok, "Chemical Management for Colorful, Efficient, and Stable Inorganic-Organic Hybrid Nanostructured Solar Cells," *Nano Letters*, vol. 13, pp. 1764-1769, 2013.
- [117] E. Mosconi, A. Amat, M. K. Nazeeruddin, M. Grätzel, and F. De Angelis, "First-Principles Modeling of Mixed Halide Organometal Perovskites for Photovoltaic Applications," *The Journal of Physical Chemistry C*, vol. 117, pp. 13902-13913, 2013.
- [118] S. Colella, E. Mosconi, P. Fedeli, A. Listorti, F. Gazza, F. Orlandi, P. Ferro, T. Besagni, A. Rizzo, G. Calestani, G. Gigli, F. De Angelis, and R. Mosca, "MAPbI<sub>3-x</sub>Cl<sub>x</sub> Mixed Halide Perovskite for Hybrid Solar Cells: The Role of Chloride as Dopant on the Transport and Structural Properties," *Chemistry of Materials*, vol. 25, pp. 4613-4618, 2013.
- [119] Q. Chen, H. Zhou, Y. Fang, A. Z. Stieg, T.-B. Song, H.-H. Wang, X. Xu, Y. Liu, S. Lu, J. You, P. Sun, J. McKay, M. S. Goorsky, and Y. Yang, "The optoelectronic role of chlorine in CH<sub>3</sub>NH<sub>3</sub>PbI<sub>3</sub>(Cl)-based perovskite solar cells," *Nature Communications*, vol. 6, p. 7269, 2015.
- [120] N. J. Jeon, J. H. Noh, W. S. Yang, Y. C. Kim, S. Ryu, J. Seo, and S. I. Seok, "Compositional engineering of perovskite materials for high-performance solar cells," *Nature*, vol. 517, pp. 476-480, 2015.
- [121] J. Gong, S. B. Darling, and F. You, "Perovskite photovoltaics: life-cycle assessment of energy and environmental impacts," *Energy & Environmental Science*, vol. 8, pp. 1953-1968, 2015.
- [122] I. Celik, Z. Song, A. J. Cimaroli, Y. Yan, M. J. Heben, and D. Apul, "Life Cycle Assessment (LCA) of perovskite PV cells projected from lab to fab," *Solar Energy Materials and Solar Cells*, vol. 156, pp. 157-169, 2016.
- [123] N. K. Noel, S. D. Stranks, A. Abate, C. Wehrenfennig, S. Guarnera, A.-A. Haghghirad, A. Sadhanala, G. E. Eperon, S. K. Pathak, M. B. Johnston, A. Petrozza, L. M. Herz, and H. J. Snaith, "Lead-free organic-inorganic tin halide perovskites for photovoltaic applications," *Energy & Environmental Science*, vol. 7, pp. 3061-3068, 2014.
- [124] F. Hao, C. C. Stoumpos, D. H. Cao, R. P. H. Chang, and M. G. Kanatzidis, "Lead-free solid-state organic-inorganic halide perovskite solar cells," *Nat Photon*, vol. 8, pp. 489-494, 2014.

- [125] W. Ke, C. C. Stoumpos, J. L. Logsdon, M. R. Wasielewski, Y. Yan, G. Fang, and M. G. Kanatzidis, "TiO<sub>2</sub>-ZnS Cascade Electron Transport Layer for Efficient Formamidinium Tin Iodide Perovskite Solar Cells," *Journal of the American Chemical Society*, vol. 138, pp. 14998-15003, 2016.
- [126] Y. Ogomi, A. Morita, S. Tsukamoto, T. Saitho, N. Fujikawa, Q. Shen, T. Toyoda, K. Yoshino, S. S. Pandey, T. Ma, and S. Hayase, "CH<sub>3</sub>NH<sub>3</sub>Sn<sub>x</sub>Pb<sub>(1-x)</sub>I<sub>3</sub> Perovskite Solar Cells Covering up to 1060 nm," *The Journal of Physical Chemistry Letters*, vol. 5, pp. 1004-1011, 2014.
- [127] D. Zhao, Y. Yu, C. Wang, W. Liao, N. Shrestha, C. R. Grice, A. J. Cimaroli, L. Guan, R. J. Ellingson, K. Zhu, X. Zhao, R.-G. Xiong, and Y. Yan, "Low-bandgap mixed tin-lead iodide perovskite absorbers with long carrier lifetimes for all-perovskite tandem solar cells," *Nature Energy*, vol. 2, p. 17018, 2017.
- [128] P. Umari, E. Mosconi, and F. De Angelis, "Relativistic GW calculations on CH<sub>3</sub>NH<sub>3</sub>PbI<sub>3</sub> and CH<sub>3</sub>NH<sub>3</sub>SnI<sub>3</sub> Perovskites for Solar Cell Applications," *Scientific Reports*, vol. 4, p. 4467, 2014.
- [129] J. H. Noh, S. H. Im, J. H. Heo, T. N. Mandal, and S. I. Seok, "Chemical Management for Colorful, Efficient, and Stable Inorganic-Organic Hybrid Nanostructured Solar Cells," *Nano Letters*, vol. 13, pp. 1764-1769, 2013.
- [130] J. Werner, C.-H. Weng, A. Walter, L. Fesquet, J. P. Seif, S. De Wolf, B. Niesen, and C. Ballif, "Efficient Monolithic Perovskite/Silicon Tandem Solar Cell with Cell Area >1 cm<sup>2</sup>," *The Journal of Physical Chemistry Letters*, vol. 7, pp. 161-166, 2016.
- [131] S. Albrecht, M. Saliba, J. P. Correa Baena, F. Lang, L. Kegelmann, M. Mews, L. Steier, A. Abate, J. Rappich, L. Korte, R. Schlattmann, M. K. Nazeeruddin, A. Hagfeldt, M. Gratzel, and B. Rech, "Monolithic perovskite/silicon-heterojunction tandem solar cells processed at low temperature," *Energy & Environmental Science*, vol. 9, pp. 81-88, 2016.
- [132] J. P. Mailoa, C. D. Bailie, E. C. Johlin, E. T. Hoke, A. J. Akey, W. H. Nguyen, M. D. McGehee, and T. Buonassisi, "A 2-terminal perovskite/silicon multijunction solar cell enabled by a silicon tunnel junction," *Applied Physics Letters*, vol. 106, p. 121105, 2015.
- [133] T. Todorov, T. Gershon, O. Gunawan, Y. S. Lee, C. Sturdevant, L.-Y. Chang, and S. Guha, "Monolithic Perovskite-CIGS Tandem Solar Cells via In Situ Band Gap

Engineering," *Advanced Energy Materials*, 5: 1500799. doi: 10.1002/aenm.201500799.

- [134] C. D. Bailie, M. G. Christoforo, J. P. Mailoa, A. R. Bowring, E. L. Unger, W. H. Nguyen, J. Burschka, N. Pellet, J. Z. Lee, M. Gratzel, R. Noufi, T. Buonassisi, A. Salleo, and M. D. McGehee, "Semi-transparent perovskite solar cells for tandems with silicon and CIGS," *Energy & Environmental Science*, vol. 8, pp. 956-963, 2015.
- [135] T. Todorov, T. Gershon, O. Gunawan, C. Sturdevant, and S. Guha, "Perovskite-kesterite monolithic tandem solar cells with high open-circuit voltage," *Applied Physics Letters*, vol. 105, p. 173902, 2014.
- [136] G. E. Eperon, T. Leijtens, K. A. Bush, R. Prasanna, T. Green, J. T.-W. Wang, D. P. McMeekin, G. Volonakis, R. L. Milot, R. May, A. Palmstrom, D. J. Slotcavage, R. A. Belisle, J. B. Patel, E. S. Parrott, R. J. Sutton, W. Ma, F. Moghadam, B. Conings, A. Babayigit, H.-G. Boyen, S. Bent, F. Giustino, L. M. Herz, M. B. Johnston, M. D. McGehee, and H. J. Snaith, "Perovskite-perovskite tandem photovoltaics with optimized band gaps," *Science*, vol. 354, pp. 861-865, 2016.
- [137] D. P. McMeekin, G. Sadoughi, W. Rehman, G. E. Eperon, M. Saliba, M. T. Hörlantner, A. Haghighirad, N. Sakai, L. Korte, B. Rech, M. B. Johnston, L. M. Herz, and H. J. Snaith, "A mixed-cation lead mixed-halide perovskite absorber for tandem solar cells," *Science*, vol. 351, pp. 151-155, 2016.
- [138] F. Fu, T. Feurer, T. P. Weiss, S. Pisoni, E. Avancini, C. Andres, S. Buecheler, and A. N. Tiwari, "High-efficiency inverted semi-transparent planar perovskite solar cells in substrate configuration," *Nature Energy*, vol. 2, p. 16190, 2016.
- [139] Z. Yu, M. Leilaeioun, and Z. Holman, "Selecting tandem partners for silicon solar cells," *Nature Energy*, vol. 1, p. 16137, 2016.
- [140] H. Uzu, M. Ichikawa, M. Hino, K. Nakano, T. Meguro, J. L. Hernández, H.-S. Kim, N.-G. Park, and K. Yamamoto, "High efficiency solar cells combining a perovskite and a silicon heterojunction solar cells via an optical splitting system," *Applied Physics Letters*, vol. 106, p. 013506, 2015.
- [141] K. A. Bush, A. F. Palmstrom, Z. J. Yu, M. Boccard, R. Cheacharoen, J. P. Mailoa, D. P. McMeekin, R. L. Z. Hoye, C. D. Bailie, T. Leijtens, I. M. Peters, M. C. Minichetti, N. Rolston, R. Prasanna, S. Sofia, D. Harwood, W. Ma, F. Moghadam, H. J. Snaith, T. Buonassisi, Z. C. Holman, S. F. Bent, and M. D. McGehee, "23.6%-

- efficient monolithic perovskite/silicon tandem solar cells with improved stability," *Nature Energy*, vol. 2, p. 17009, 2017.
- [142] Z. Yang, A. Rajagopal, C.-C. Chueh, S. B. Jo, B. Liu, T. Zhao, and A. K. Y. Jen, "Stable Low-Bandgap Pb–Sn Binary Perovskites for Tandem Solar Cells," *Advanced Materials*, p. 1602696, 2016.
- [143] T. A. Berhe, W.-N. Su, C.-H. Chen, C.-J. Pan, J.-H. Cheng, H.-M. Chen, M.-C. Tsai, L.-Y. Chen, A. A. Dubale, and B.-J. Hwang, "Organometal halide perovskite solar cells: degradation and stability," *Energy & Environmental Science*, vol. 9, pp. 323-356, 2016.
- [144] Y. Han, S. Meyer, Y. Dkhissi, K. Weber, J. M. Pringle, U. Bach, L. Spiccia, and Y.-B. Cheng, "Degradation observations of encapsulated planar CH<sub>3</sub>NH<sub>3</sub>PbI<sub>3</sub> perovskite solar cells at high temperatures and humidity," *Journal of Materials Chemistry A*, vol. 3, pp. 8139-8147, 2015.
- [145] N. Aristidou, I. Sanchez-Molina, T. Chotchuangchutchaval, M. Brown, L. Martinez, T. Rath, and S. A. Haque, "The Role of Oxygen in the Degradation of Methylammonium Lead Trihalide Perovskite Photoactive Layers," *Angewandte Chemie International Edition*, vol. 54, pp. 8208-8212, 2015.
- [146] T. Leijtens, G. E. Eperon, S. Pathak, A. Abate, M. M. Lee, and H. J. Snaith, "Overcoming ultraviolet light instability of sensitized TiO<sub>2</sub> with meso-superstructured organometal tri-halide perovskite solar cells," *Nature Communications*, vol. 4, p. 2885, 2013.
- [147] G. Divitini, S. Cacovich, F. Matteocci, L. Cinà, A. Di Carlo, and C. Ducati, "In situ observation of heat-induced degradation of perovskite solar cells," *Nature Energy*, vol. 1, p. 15012, 2016.
- [148] S. Wang, Y. Jiang, Emilio J. Juarez-Perez, Luis K. Ono, and Y. Qi, "Accelerated degradation of methylammonium lead iodide perovskites induced by exposure to iodine vapour," *Nature Energy*, vol. 2, p. 16195, 2016.
- [149] F. Matteocci, L. Cinà, E. Lamanna, S. Cacovich, G. Divitini, P. A. Midgley, C. Ducati, and A. Di Carlo, "Encapsulation for long-term stability enhancement of perovskite solar cells," *Nano Energy*, vol. 30, pp. 162-172, 2016.

- [150] Q. Dong, F. Liu, M. K. Wong, H. W. Tam, A. B. Djurišić, A. Ng, C. Surya, W. K. Chan, and A. M. C. Ng, "Encapsulation of Perovskite Solar Cells for High Humidity Conditions," *ChemSusChem*, vol. 9, pp. 2597-2603, 2016.
- [151] S. Gholipour, J.-P. Correa-Baena, K. Domanski, T. Matsui, L. Steier, F. Giordano, F. Tajabadi, W. Tress, M. Saliba, A. Abate, A. Morteza Ali, N. Taghavinia, M. Grätzel, and A. Hagfeldt, "Highly Efficient and Stable Perovskite Solar Cells based on a Low-Cost Carbon Cloth," *Advanced Energy Materials*, vol. 6, p. 1601116, 2016.
- [152] X. Li, M. Tschumi, H. Han, S. S. Babkair, R. A. Alzubaydi, A. A. Ansari, S. S. Habib, M. K. Nazeeruddin, S. M. Zakeeruddin, and M. Grätzel, "Outdoor Performance and Stability under Elevated Temperatures and Long-Term Light Soaking of Triple-Layer Mesoporous Perovskite Photovoltaics," *Energy Technology*, vol. 3, pp. 551-555, 2015.
- [153] H. J. Snaith, A. Abate, J. M. Ball, G. E. Eperon, T. Leijtens, N. K. Noel, S. D. Stranks, J. T.-W. Wang, K. Wojciechowski, and W. Zhang, "Anomalous Hysteresis in Perovskite Solar Cells," *Journal of Physical Chemistry Letters*, vol. 5, pp. 1511-1515, 2014.
- [154] S. van Reenen, M. Kemerink, and H. J. Snaith, "Modeling Anomalous Hysteresis in Perovskite Solar Cells," *The Journal of Physical Chemistry Letters*, vol. 6, pp. 3808-3814, 2015.
- [155] T.-Y. Yang, G. Gregori, N. Pellet, M. Grätzel, and J. Maier, "The Significance of Ion Conduction in a Hybrid Organic-Inorganic Lead-Iodide-Based Perovskite Photosensitizer," *Angewandte Chemie International Edition*, vol. 54, pp. 7905-7910, 2015.
- [156] Y. Zhang, M. Liu, G. E. Eperon, T. C. Leijtens, D. McMeekin, M. Saliba, W. Zhang, M. de Bastiani, A. Petrozza, L. M. Herz, M. B. Johnston, H. Lin, and H. J. Snaith, "Charge selective contacts, mobile ions and anomalous hysteresis in organic-inorganic perovskite solar cells," *Materials Horizons*, vol. 2, pp. 315-322, 2015.
- [157] H. Zhang, C. Liang, Y. Zhao, M. Sun, H. Liu, J. Liang, D. Li, F. Zhang, and Z. He, "Dynamic interface charge governing the current-voltage hysteresis in perovskite solar cells," *Physical Chemistry Chemical Physics*, vol. 17, pp. 9613-9618, 2015.

- [158] H.-S. Kim, C.-R. Lee, J.-H. Im, K.-B. Lee, T. Moehl, A. Marchioro, S.-J. Moon, R. Humphry-Baker, J.-H. Yum, J. E. Moser, M. Gratzel, and N.-G. Park, "Lead Iodide Perovskite Sensitized All-Solid-State Submicron Thin Film Mesoscopic Solar Cell with Efficiency Exceeding 9%," *Sci. Rep.*, vol. 2, 2012.
- [159] M. A. Green, A. Ho-Baillie, and H. J. Snaith, "The emergence of perovskite solar cells," *Nat Photon*, vol. 8, pp. 506-514, 2014.
- [160] T. C. Sum and N. Mathews, "Advancements in perovskite solar cells: photophysics behind the photovoltaics," *Energy & Environmental Science*, vol. 7, pp. 2518-2534, 2014.
- [161] A. Yella, L.-P. Heiniger, P. Gao, M. K. Nazeeruddin, and M. Grätzel, "Nanocrystalline Rutile Electron Extraction Layer Enables Low-Temperature Solution Processed Perovskite Photovoltaics with 13.7% Efficiency," *Nano Letters*, vol. 14, pp. 2591-2596, 2014.
- [162] C. Bat-El, G. Shany, and Etgar Lioz, "Parameters influencing the deposition of methylammonium lead halide iodide in hole conductor free perovskite-based solar cells," *APL Materials*, vol. 2, p. 8, 2014.
- [163] J. Schlipf, P. Docampo, C. J. Schaffer, V. Körstgens, L. Bießmann, F. Hanusch, N. Giesbrecht, S. Bernstorff, T. Bein, and P. Müller-Buschbaum, "A Closer Look into Two-Step Perovskite Conversion with X-ray Scattering," *The Journal of Physical Chemistry Letters*, vol. 6, pp. 1265-1269, 2015.
- [164] S. H. Hwang, J. Roh, J. Lee, J. Ryu, J. Yun, and J. Jang, "Size-controlled SiO<sub>2</sub> nanoparticles as scaffold layers in thin-film perovskite solar cells," *Journal of Materials Chemistry A*, vol. 2, pp. 16429-16433, 2014.
- [165] S. N. Habisreutinger, T. Leijtens, G. E. Eperon, S. D. Stranks, R. J. Nicholas, and H. J. Snaith, "Carbon Nanotube/Polymer Composites as a Highly Stable Hole Collection Layer in Perovskite Solar Cells," *Nano Letters*, vol. 14, pp. 5561-5568, 2014.
- [166] T. Baikie, Y. Fang, J. M. Kadro, M. Schreyer, F. Wei, S. G. Mhaisalkar, M. Graetzel, and T. J. White, "Synthesis and crystal chemistry of the hybrid perovskite (CH<sub>3</sub>NH<sub>3</sub>)PbI<sub>3</sub> for solid-state sensitised solar cell applications," *Journal of Materials Chemistry A*, vol. 1, pp. 5628-5641, 2013.

- [167] O. Malinkiewicz, A. Yella, Y. H. Lee, G. M. Espallargas, M. Graetzel, M. K. Nazeeruddin, and H. J. Bolink, "Perovskite solar cells employing organic charge-transport layers," *Nat Photon*, vol. 8, pp. 128-132, 2014.
- [168] G. Patil, D. Kajale, V. Gaikwad, and G. Jain, "Preparation and characterization of SnO<sub>2</sub> nanoparticles by hydrothermal route," *International Nano Letters*, vol. 2, pp. 1-5, 2012.
- [169] S. Frederick and T. David, *Solid state physics* vol. 3. New York: Academic Press INC, 1956.
- [170] D. A. Porter and K. E. Easterling, *Phase Transformations in Metals and Alloys*, 2 ed.: CRC Press, 1992.
- [171] A. Peter and D. P. Julio, *Physical Chemistry*, Eight ed. New York: W. H. Freeman and Company, 2006.
- [172] F. W. Ostwald, "The formation and changes of solids," *Z. Phys. Chem*, vol. 22, p. 41, 1897.
- [173] A. M. A. Leguy, Y. Hu, M. Campoy-Quiles, M. I. Alonso, O. J. Weber, P. Azarhoosh, M. van Schilfgaarde, M. T. Weller, T. Bein, J. Nelson, P. Docampo, and P. R. F. Barnes, "Reversible Hydration of CH<sub>3</sub>NH<sub>3</sub>PbI<sub>3</sub> in Films, Single Crystals, and Solar Cells," *Chemistry of Materials*, 2015.
- [174] Z. Song, S. C. Wathage, B. L. Tompkins, G. K. Liyanage, A. B. Phillips, R. J. Ellingson, and M. J. Heben, "Spatially Resolved Characterization of Solution Processed Perovskite Solar Cells Using the LBIC Technique," presented at the IEEE 42<sup>nd</sup> Photovoltaic Specialists Conference, New Orleans, 2015.
- [175] N. Marinova, W. Tress, R. Humphry-Baker, M. I. Dar, V. Bojinov, S. M. Zakeeruddin, M. K. Nazeeruddin, and M. Grätzel, "Light Harvesting and Charge Recombination in CH<sub>3</sub>NH<sub>3</sub>PbI<sub>3</sub> Perovskite Solar Cells Studied by Hole Transport Layer Thickness Variation," *ACS Nano*, vol. 9, pp. 4200-4209, 2015.
- [176] K. Fu, C. T. Nelson, M. C. Scott, A. Minor, N. Mathews, and L. H. Wong, "Influence of void-free perovskite capping layer on the charge recombination process in high performance CH<sub>3</sub>NH<sub>3</sub>PbI<sub>3</sub> perovskite solar cells," *Nanoscale*, vol. 8, pp. 4181-4193, 2016.

- [177] C. Bi, Q. Wang, Y. Shao, Y. Yuan, Z. Xiao, and J. Huang, "Non-wetting surface-driven high-aspect-ratio crystalline grain growth for efficient hybrid perovskite solar cells," *Nat Commun*, vol. 6, 2015.
- [178] S. T. Williams, F. Zuo, C.-C. Chueh, C.-Y. Liao, P.-W. Liang, and A. K. Y. Jen, "Role of Chloride in the Morphological Evolution of Organo-Lead Halide Perovskite Thin Films," *Acs Nano*, vol. 8, pp. 10640-10654, 2014.
- [179] Y. Xu, L. Zhu, J. Shi, S. Lv, X. Xu, J. Xiao, J. Dong, H. Wu, Y. Luo, D. Li, and Q. Meng, "Efficient Hybrid Mesoscopic Solar Cells with Morphology-Controlled  $\text{CH}_3\text{NH}_3\text{PbI}_{3-x}\text{Cl}_x$  Derived from Two-Step Spin Coating Method," *ACS Applied Materials & Interfaces*, vol. 7, pp. 2242-2248, 2015.
- [180] Y. Shao, Z. Xiao, C. Bi, Y. Yuan, and J. Huang, "Origin and elimination of photocurrent hysteresis by fullerene passivation in  $\text{CH}_3\text{NH}_3\text{PbI}_3$  planar heterojunction solar cells," *Nature Communications*, vol. 5, p. 5784, 2014.
- [181] B. Wu, H. T. Nguyen, Z. Ku, G. Han, D. Giovanni, N. Mathews, H. J. Fan, and T. C. Sum, "Discerning the Surface and Bulk Recombination Kinetics of Organic-Inorganic Halide Perovskite Single Crystals," *Advanced Energy Materials*, 6: 1600551. doi: 10.1002/aenm.201600551.
- [182] T. Shi, W.-J. Yin, and Y. Yan, "Predictions for p-Type  $\text{CH}_3\text{NH}_3\text{PbI}_3$  Perovskites," *The Journal of Physical Chemistry C*, vol. 118, pp. 25350-25354, 2014.
- [183] J. Navas, A. Sanchez-Coronilla, J. J. Gallardo, E. I. Martin, N. C. Hernandez, R. Alcantara, C. Fernandez-Lorenzo, and J. Martin-Calleja, "Revealing the role of  $\text{Pb}^{2+}$  in the stability of organic-inorganic hybrid perovskite  $\text{CH}_3\text{NH}_3\text{Pb}_{1-x}\text{Cd}_x\text{I}_3$ : an experimental and theoretical study," *Physical Chemistry Chemical Physics*, vol. 17, pp. 23886-23896, 2015.
- [184] V. D'Innocenzo, A. R. Srimath Kandada, M. De Bastiani, M. Gandini, and A. Petrozza, "Tuning the Light Emission Properties by Band Gap Engineering in Hybrid Lead Halide Perovskite," *Journal of the American Chemical Society*, vol. 136, pp. 17730-17733, 2014.
- [185] H. A. Harms, N. Tetreault, N. Pellet, M. Bensimon, and M. Gratzel, "Mesoscopic photosystems for solar light harvesting and conversion: facile and reversible transformation of metal-halide perovskites," *Faraday Discussions*, vol. 176, pp. 251-269, 2014.

- [186] W. A. Dunlap-Shohl, R. Younts, B. Gautam, K. Gundogdu, and D. B. Mitzi, "Effects of Cd Diffusion and Doping in High-Performance Perovskite Solar Cells Using CdS as Electron Transport Layer," *The Journal of Physical Chemistry C*, vol. 120, pp. 16437-16445, 2016.
- [187] T. J. Trentler, K. M. Hickman, S. C. Goel, A. M. Viano, P. C. Gibbons, and W. E. Buhro, "Solution-Liquid-Solid Growth of Crystalline III-V Semiconductors: An Analogy to Vapor-Liquid-Solid Growth," *Science*, vol. 270, pp. 1791-1794, 1995.
- [188] M. Saliba, T. Matsui, J.-Y. Seo, K. Domanski, J.-P. Correa-Baena, M. K. Nazeeruddin, S. M. Zakeeruddin, W. Tress, A. Abate, A. Hagfeldt, and M. Gratzel, "Cesium-containing triple cation perovskite solar cells: improved stability, reproducibility and high efficiency," *Energy & Environmental Science*, vol. 9, pp. 1989-1997, 2016.
- [189] T. J. Jacobsson, J.-P. Correa-Baena, E. Halvani Anaraki, B. Philippe, S. D. Stranks, M. E. F. Bouduban, W. Tress, K. Schenk, J. Teuscher, J.-E. Moser, H. Rensmo, and A. Hagfeldt, "Unreacted PbI<sub>2</sub> as a Double-Edged Sword for Enhancing the Performance of Perovskite Solar Cells," *Journal of the American Chemical Society*, vol. 138, pp. 10331-10343, 2016.
- [190] C. H. Yoder, "Appendix 3: Metallic, Covalent, and Ionic Radii," in *Ionic Compounds*, ed: John Wiley & Sons, Inc., 2006, pp. 171-171.
- [191] M. Körfer, H. Fuess, J. W. Bats, and G. Klebe, "Struktur und Eigenschaften von Doppelhalogeniden von substituiertem Ammonium und Quecksilber(II). V. Die Kristallstruktur von CH<sub>3</sub>NH<sub>3</sub>HgBr<sub>3</sub> und CH<sub>3</sub>NH<sub>3</sub>HgI<sub>3</sub>," *Zeitschrift für anorganische und allgemeine Chemie*, vol. 525, pp. 23-28, 1985.
- [192] M. Daub, R. Stroh, and H. Hillebrecht, "Synthesis, Crystal Structure, and Optical Properties of (CH<sub>3</sub>NH<sub>3</sub>)<sub>2</sub>CoX<sub>4</sub> (X = Cl, Br, I, Cl<sub>0.5</sub>Br<sub>0.5</sub>, Cl<sub>0.5</sub>I<sub>0.5</sub>, Br<sub>0.5</sub>I<sub>0.5</sub>)," *Zeitschrift für anorganische und allgemeine Chemie*, vol. 642, pp. 268-274, 2016.
- [193] R. Yadav, D. Swain, P. P. Kundu, H. S. Nair, C. Narayana, and S. Elizabeth, "Dielectric and Raman investigations of structural phase transitions in (C<sub>2</sub>H<sub>5</sub>NH<sub>3</sub>)<sub>2</sub>CdCl<sub>4</sub>," *Physical Chemistry Chemical Physics*, vol. 17, pp. 12207-12214, 2015.
- [194] S. F. Hoefler, G. Trimmel, and T. Rath, "Progress on lead-free metal halide perovskites for photovoltaic applications: a review," *Monatshefte für Chemie - Chemical Monthly*, vol. 148, pp. 795-826, 2017.

- [195] Y. Yang, M. Yang, K. Zhu, J. C. Johnson, J. J. Berry, J. van de Lagemaat, and M. C. Beard, "Large polarization-dependent exciton optical Stark effect in lead iodide perovskites," *Nature Communications*, vol. 7, p. 12613, 2016.
- [196] S.-H. Chan, M.-C. Wu, K.-M. Lee, W.-C. Chen, T.-H. Lin, and W.-F. Su, "Enhancing perovskite solar cell performance and stability by doping barium in methylammonium lead halide," *Journal of Materials Chemistry A*, vol. 5, pp. 18044-18052, 2017.
- [197] J. Navas, A. Sanchez-Coronilla, J. J. Gallardo, N. Cruz Hernandez, J. C. Pinero, R. Alcántara, C. Fernandez-Lorenzo, D. M. De los Santos, T. Aguilar, and J. Martín-Calleja, "New insights into organic-inorganic hybrid perovskite  $\text{CH}_3\text{NH}_3\text{PbI}_3$  nanoparticles. An experimental and theoretical study of doping in  $\text{Pb}^{2+}$  sites with  $\text{Sn}^{2+}$ ,  $\text{Sr}^{2+}$ ,  $\text{Cd}^{2+}$  and  $\text{Ca}^{2+}$ ," *Nanoscale*, vol. 7, pp. 6216-6229, 2015.
- [198] N. Strevel, L. Trippel, and M. Gloeckler, "Performance characterization and superior energy yield of first solar PV power plants in high-temperature conditions," *Photovoltaics international*, vol. 17, pp. 148-154, 2012.
- [199] D. L. Bätzner, R. Wendt, A. Romeo, H. Zogg, and A. N. Tiwari, "A study of the back contacts on CdTe/CdS solar cells," *Thin Solid Films*, vol. 361–362, pp. 463-467, 2000.
- [200] J. Pan, M. Gloeckler, and J. R. Sites, "Hole current impedance and electron current enhancement by back-contact barriers in CdTe thin film solar cells," *Journal of Applied Physics*, vol. 100, p. 124505, 2006.
- [201] G. S. Khripunov, "Effect of a rear contact on the electrical properties of the CdS/CdTe-based thin-film solar cells," *Semiconductors*, vol. 40, pp. 113-117, 2006.
- [202] D. L. Bätzner, M. E. Öszan, D. Bonnet, and K. Bücher, "Device analysis methods for physical cell parameters of CdTe/Cds solar cells," *Thin Solid Films*, vol. 361, pp. 288-292, 2000.
- [203] C. R. Corwine, A. O. Pudov, M. Gloeckler, S. H. Demtsu, and J. R. Sites, "Copper inclusion and migration from the back contact in CdTe solar cells," *Solar Energy Materials and Solar Cells*, vol. 82, pp. 481-489, 2004.

- [204] A. Moore, T. Song, and J. Sites, "Improved CdTe Solar-Cell Performance with An Evaporated Te Layer before The Back Contact," *MRS Advances*, pp. 1-7, 2017.
- [205] W. Xia, H. Lin, H. N. Wu, C. W. Tang, I. Irfan, C. Wang, and Y. Gao, "Te/Cu bi-layer: A low-resistance back contact buffer for thin film CdS/CdTe solar cells," *Solar Energy Materials and Solar Cells*, vol. 128, pp. 411-420, 2014.
- [206] J. Zhou, X. Wu, A. Duda, G. Teeter, and S. H. Demtsu, "The formation of different phases of  $\text{Cu}_x\text{Te}$  and their effects on CdTe/CdS solar cells," *Thin Solid Films*, vol. 515, pp. 7364-7369, 2007.
- [207] X. Wu, J. Zhou, A. Duda, Y. Yan, G. Teeter, S. Asher, W. K. Metzger, S. Demtsu, S.-H. Wei, and R. Noufi, "Phase control of  $\text{Cu}_x\text{Te}$  film and its effects on CdS/CdTe solar cell," *Thin Solid Films*, vol. 515, pp. 5798-5803, 2007.
- [208] J. Perrenoud, L. Kranz, C. Gretener, F. Pianezzi, S. Nishiwaki, S. Buecheler, and A. N. Tiwari, "A comprehensive picture of Cu doping in CdTe solar cells," *Journal of Applied Physics*, vol. 114, p. 174505, 2013.
- [209] N. R. Paudel, A. D. Compaan, and Y. Yan, "Sputtered CdS/CdTe solar cells with  $\text{MoO}_{3-x}/\text{Au}$  back contacts," *Solar Energy Materials and Solar Cells*, vol. 113, pp. 26-30, 2013.
- [210] T. Song, "Design Strategies for High-Efficiency CdTe Solar Cells," Ph.D. Dissertation, Department of Physics, Colorado State University, 2017.
- [211] N. R. Paudel, K. A. Wieland, and A. D. Compaan, "Ultrathin CdS/CdTe solar cells by sputtering," *Solar Energy Materials and Solar Cells*, vol. 105, pp. 109-112, 2012.
- [212] S. Chun, S. Lee, Y. Jung, J. S. Bae, J. Kim, and D. Kim, "Wet chemical etched CdTe thin film solar cells," *Current Applied Physics*, vol. 13, pp. 211-216, 2013.
- [213] C. S. Ferekides, U. Balasubramanian, R. Mamazza, V. Viswanathan, H. Zhao, and D. L. Morel, "CdTe thin film solar cells: device and technology issues," *Solar Energy*, vol. 77, pp. 823-830, 2004.
- [214] N. Abbas Shah, A. Ali, Z. Ali, A. Maqsood, and A. K. S. Aqili, "Properties of Te-rich cadmium telluride thin films fabricated by closed space sublimation technique," *Journal of Crystal Growth*, vol. 284, pp. 477-485, 2005.

- [215] R. Ochoa-Landín, O. Vigil-Galan, Y. V. Vorobiev, and R. Ramírez-Bon, "Chemically-deposited Te layers improving the parameters of back contacts for CdTe solar cells," *Solar Energy*, vol. 83, pp. 134-138, 2009.
- [216] A. B. Phillips, R. R. Khanal, Z. Song, R. M. Zartman, J. L. DeWitt, J. M. Stone, P. J. Roland, V. V. Plotnikov, C. W. Carter, J. M. Stayancho, R. J. Ellingson, A. D. Compaan, and M. J. Heben, "Wiring-up Carbon Single Wall Nanotubes to Polycrystalline Inorganic Semiconductor Thin Films: Low-Barrier, Copper-Free Back Contact to CdTe Solar Cells," *Nano Letters*, vol. 13, pp. 5224-5232, 2013.
- [217] A. B. Phillips, Z. Song, J. L. DeWitt, J. M. Stone, P. W. Krantz, J. M. Royston, R. M. Zeller, M. R. Mapes, P. J. Roland, M. D. Dorogi, S. Zafar, G. T. Faykosh, R. J. Ellingson, and M. J. Heben, "High speed, intermediate resolution, large area laser beam induced current imaging and laser scribing system for photovoltaic devices and modules," *Review of Scientific Instruments*, vol. 87, p. 093708, 2016.
- [218] E. R. Shaaban, N. Afify, and A. El-Taher, "Effect of film thickness on microstructure parameters and optical constants of CdTe thin films," *Journal of Alloys and Compounds*, vol. 482, pp. 400-404, 2009.
- [219] A. Jarkov, S. Bereznev, O. Volobujeva, R. Traksmaa, A. Tverjanovich, A. Öpik, and E. Mellikov, "Photo-assisted electrodeposition of polypyrrole back contact to CdS/CdTe solar cell structures," *Thin Solid Films*, vol. 535, pp. 198-201, 2013.
- [220] J.-W. Liu, F. Chen, M. Zhang, H. Qi, C.-L. Zhang, and S.-H. Yu, "Rapid Microwave-Assisted Synthesis of Uniform Ultralong Te Nanowires, Optical Property, and Chemical Stability," *Langmuir*, vol. 26, pp. 11372-11377, 2010.
- [221] T. Song and J. R. Sites, "Role of Tellurium Buffer Layer on CdTe Solar Cells' Absorber/Back-Contact Interface," in *44<sup>th</sup> IEEE Photovoltaic Specialist Conference*, Washington D.C., 2017.
- [222] J. Ma, S.-H. Wei, T. A. Gessert, and K. K. Chin, "Carrier density and compensation in semiconductors with multiple dopants and multiple transition energy levels: Case of Cu impurities in CdTe," *Physical Review B*, vol. 83, p. 245207, 2011.
- [223] X. Wu, J. Zhou, A. Duda, J. C. Keane, T. A. Gessert, Y. Yan, and R. Noufi, "13.9%-efficient CdTe polycrystalline thin-film solar cells with an infrared transmission of ~50%," *Progress in Photovoltaics: Research and Applications*, vol. 14, pp. 471-483, 2006.

- [224] A. Niemegeers and M. Burgelman, "Effects of the Au/CdTe back contact on IV and CV characteristics of Au/CdTe/CdS/TCO solar cells," *Journal of Applied Physics*, vol. 81, pp. 2881-2886, 1997.
- [225] G. T. Koishiyev, J. R. Sites, S. S. Kulkarni, and N. G. Dhere, "Determination of back contact barrier height in Cu(In,Ga)(Se,S)<sub>2</sub> and CdTe solar cells," in *2008 33rd IEEE Photovoltaic Specialists Conference*, 2008, pp. 1-3.
- [226] M. Wimbor, A. Romeo, and M. Igalson, "Electrical characterisation of CdTe/CdS photovoltaic devices," *OPTOELECTRONICS REVIEW*, pp. 375-377, 2000.
- [227] N. D. Pham, V. T. Tiong, P. Chen, L. Wang, G. J. Wilson, J. Bell, and H. Wang, "Enhanced perovskite electronic properties via a modified lead(ii) chloride Lewis acid-base adduct and their effect in high-efficiency perovskite solar cells," *Journal of Materials Chemistry A*, vol. 5, pp. 5195-5203, 2017.
- [228] J. M. Kephart, "Optimization of the Front Contact to Minimize Short-Circuit Current Losses in CdTe Thin-Film Solar Cells," Ph.D. Dissertation, Department of Mechanical Engineering, Colorado State University, 2015.

# Appendix A

## Supporting Information

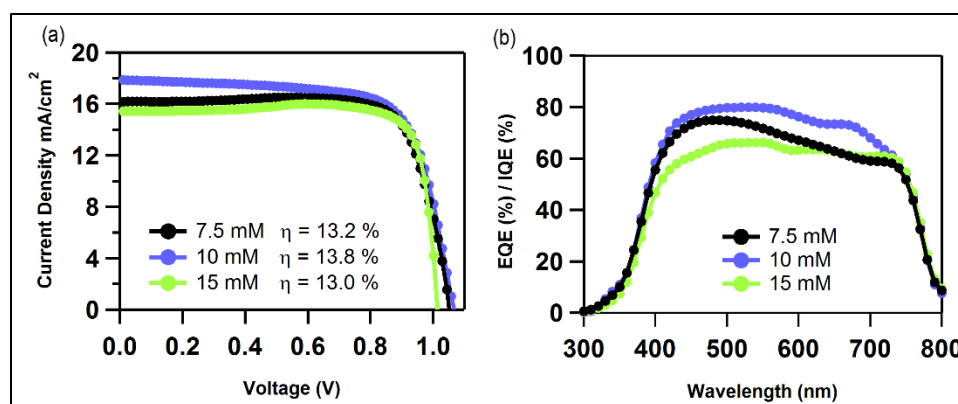


Figure A-1. (a) Current-voltage (J-V) measurements (b) External quantum efficiency (EQE) spectra of CH<sub>3</sub>NH<sub>3</sub>PbI<sub>3</sub> (MAPbI<sub>3</sub>) perovskite solar cells prepared with different CdCl<sub>2</sub> concentrations (MAI concentration is 250 mM).

## Appendix B

### List of Publications

1. **Watthage, S. C.**; Song, Z.; Shrestha, N.; Phillips, A. B.; Liyanage, G. K.; Roland, P. J.; Ellingson, R. J.; Heben, M. J. “Impact of Divalent Metal Additives on the Structural and Optoelectronic Properties of  $\text{CH}_3\text{NH}_3\text{PbI}_3$  Perovskite Prepared by the Two-Step Solution Process.” *MRS Advances* **2017**, 1-6.
2. **Watthage, S. C.**; Song, Z.; Shrestha, N.; Phillips, A. B.; Liyanage, G. K.; Roland, P. J.; Ellingson, R. J.; Heben, M. J. “Enhanced Grain Size, Photoluminescence, and Photoconversion Efficiency with Cadmium Addition During the Two-Step Growth of  $\text{CH}_3\text{NH}_3\text{PbI}_3$ .” *ACS Appl. Mater. Interfaces* **2016**.
3. Song, Z.; **Watthage, S. C.**; Phillips, A. B.; Tompkins, B. L.; Ellingson, R. J.; Heben, M. J. “Impact of Processing Temperature and Composition on the Formation of Methylammonium Lead Iodide Perovskites.” *Chem. Mater.* **2015**, 27, 4612-4619. (*ACS editor’s choice, cover article, and most downloaded in 2015*)
4. Song, Z.; **Watthage, S. C.**; Phillips, A. B.; Heben, M. J. “Pathways toward High-Performance Perovskite Solar Cells: Review of Recent Advances in Organo-Metal Halide Perovskites for Photovoltaic Applications.” *J. Photon. Energy.* **2016**, 6, 022001. (**Invited Review**)

5. Song, Z.; Werner, J.; **Watthage, S. C.**; Sahli, F.; Shrestha, N.; De Wolf, S.; Niesen, B.; Phillips, A. B.; Ballif, C.; Ellingson, R. J.; Heben, M. J. “Imaging the Spatial Evolution of Degradation in Perovskite/Si Tandem Solar Cells after Exposure to Humid Air.” *IEEE Journal of Photovoltaics*. **2017**.
6. Song, Z.; Abate, A.; **Watthage, S. C.**; Liyanage, G. K.; Phillips, A. B.; Steiner, U.; Graetzel, M.; Heben, M. J. “Perovskite Solar Cell Stability in Humid Air: Partially Reversible Phase Transitions in the  $\text{PbI}_2\text{-CH}_3\text{NH}_3\text{I-H}_2\text{O}$  System.” *Adv. Energy Mater.* **2016**, *6*, 1600846.
7. Song, Z.; Werner, J.; Shrestha, N.; Sahli, F.; De Wolf, S.; Niesen, B.; **Watthage, S. C.**; Phillips, A. B.; Ballif, C.; Ellingson, R. J.; Heben, M. J. “Probing Photocurrent Nonuniformities in the Subcells of Monolithic Perovskite/Silicon Tandem Solar Cells.” *J. Phys. Chem. Lett.* **2016**, *7*, 5114-5120.
8. Phillips, A. B.; Khanal, R. R.; Song, Z.; **Watthage, S. C.**; Kormanyos, K. R.; Heben, M. J. “Simultaneous Shunt Protection and Back Contact Formation for CdTe Solar Cells with Single Wall Carbon Nanotube Layers.” *Appl. Phys. Lett.* **2015**, *107*, 253901.
9. Song, Z.; McElvany, C. L.; Phillips, A. B.; Celik, I.; Krantz, P.W.; **Watthage, S. C.**; Liyanage, G. K.; Apul, D.; Heben, M.J.; “A techno-economic analysis of perovskite solar module manufacturing with low-cost materials and techniques,” *Energy & Environmental Science*. **2017**.
10. Haugen, N. O.; Phillips, A. B.; Dykstra, T. E.; **Watthage, S. C.**; Heben, M. J.; Ellingson, R. J. “Intraexciton Transitions Observed in High Stability Doped Single-

Wall Carbon Nanotube Films and Solutions.” *J. Phys. Chem. C* **2014**, *118*, 25253-25260.

***Submitted:***

1. **Wathhage, S. C.**; Song, Z.; Phillips, A. B.; Heben, M. J. Evolution of Perovskite Solar Cells, in “Perovskite Photovoltaics - Basic to Advanced Concepts and Implementation”, Thankappan A. and Thomas S. Eds., ed: *Elsevier*, 2018. (**Invited Book Chapter**)

***In-progress:***

1. **Wathhage, S. C.**; Phillips, A. B.; Liyanage, G. K. ; Song, Z.; Gibbs, J. M.; Alfadhili, F.K.; Alkhayat, R. B.; Ahangharnejhad, R. H.; Bhandari K.P.; Almutawah, Z. S.; Ellingson, R. J.; Heben, M. J. “Selective Cd Removal from CdTe for High Efficiency Te Back Contact Formation”.
2. **Wathhage, S. C.**; Song, Z.; Phillips, A. B.; Tompkins, B. L.; Heben, M. J. “Understanding the Nucleation and Growth Behaviors of Methylammonium Lead Iodide Perovskites in the Two-Step Solution Process”.
3. Bhandari K.P.; **Wathhage, S. C.**; Song, Z.; Phillips, A. B.; Heben, M. J. ; Ellingson, R. J. “Inexpensive, Earth-Abundant, and Tunable Hole Transport Material for CdTe Solar Cells”.

***Conference publications:***

1. **Suneth C. Wathhage**, Geethika K. Liyanage, Zhaoning Song, Fadhil K. Alfadhili, Rabee B. Alkhayat, Khagendra P. Bhandari, Randy J. Ellingson, Adam B. Phillips, and Michael J. Heben, “Novel, Facile Back Surface Treatment for CdTe Solar Cells” PVSC 44 (2017).

2. **Suneth C. Wathhage**, Zhaoning Song, Geethika K. Liyanage, Adam B. Phillips, and Michael J. Heben, “Investigation on the nucleation and growth mechanisms of perovskite formation in the two-step solution process,” PVSC 43 (2016).
3. Niraj Shrestha, **Suneth C. Wathhage**, Zhaoning Song, Paul J. Roland, Adam B. Phillips, Michael J. Heben, and Randall J. Ellingson, “Influence of Mono- and Di-valent Metal Additives on Morphology and Charge Carrier Dynamics of  $\text{CH}_3\text{NH}_3\text{PbI}_3$  Perovskite,” PVSC 44 (2017).
4. Khagendra P. Bhandari, **Suneth C. Wathhage**, Zhaoning Song, Adam B. Phillips, Michael J. Heben, and Randy J. Ellingson, “Applications of Hybrid Organic-Inorganic Metal Halide Perovskite Thin Film as a Hole Transport Layer in CdTe Thin Film Solar Cells,” PVSC 44 (2017).
5. Zhaoning Song, Antonio Abate, **Suneth C. Wathhage**, Geethika K. Liyanage, Adam B. Phillips, Michael Graetzel, and Michael J. Heben, “In-situ observation of moisture-induced degradation of perovskite solar cells using laser-beam induced current,” PVSC 43 (2016).
6. Geethika K. Liyanage, Corey R. Grice, Adam B. Phillips, Zhaoning Song, **Suneth C. Wathhage**, Nicholas D. Franzer, Sean Garner, Yanfa Yan, and Michael J. Heben, “RF-sputtered amorphous  $\text{Cd}_2\text{SnO}_4$  for flexible glass CdTe solar cells,” PVSC 43 (2016).
7. Zhaoning Song, **Suneth C. Wathhage**, Adam B. Phillips, Geethika K. Liyanage, Rajendra R. Khanal, Brandon L. Tompkins, Randy J. Ellingson, and Michael J. Heben, “Investigation of degradation mechanism of perovskite-based photovoltaic devices using laser beam induced current mapping,” Proceedings of SPIE (2015).

8. Zhaoning Song, **Suneth C. Wathhage**, Geethika K. Liyanage, Adam B. Phillips, and Michael J. Heben, “Spatially resolved characterization of solution processed perovskite solar cells using the LBIC technique,” PVSC 42 (2015).